Characterization and Optimization of Sulfurized Poly(acrylonitrile) Cathodes and Silicon Anodes

Von der Fakultät Chemie der Universität Stuttgart

zur Erlangung der Würde eines

Doktors der Naturwissenschaften (Dr. rer. nat.)

genehmigte Abhandlung

Vorgelegt von

Stefan Niesen

Aus Köln

Hauptberichter: Prof. Dr. Michael R. Buchmeiser

Mitberichter: Prof. Dr. Oliver Clemens

Prüfungsvorsitzender: Prof. Dr. Frank Gießelmann

Tag der mündlichen Prüfung: 01.03.2023

Institut für Polymerchemie der Universität Stuttgart

2023

Vorwort

Die vorliegende Dissertation entstand unter der akademischen Leitung von Herrn Prof. Dr. Michael R. Buchmeiser am Institut für Polymerchemie der Universität Stuttgart und der Daimler AG in der Zeit von November 2018 bis Dezember 2021.

Die praktische Ausführung dieser Dissertation erfolgte zum größten Teil am Institut für Polymerchemie der Universität Stuttgart.

Im Rahmen dieser Arbeit wurden folgende Publikationen vorab veröffentlicht:

- S. Niesen; A. M. Fox; S. Murugan; G. Richter; M. R. Buchmeiser, Multifunctional Copolymer as Self-Cross-Linkable Binder for High-Loading Silicon Anodes. ACS Appl. Energy Mater. 2022, 5, 11386-11391.
- S. Niesen; J. Trück; C. Seidl; K. Renger; M. R. Buchmeiser, Lithium-Sulfur Batteries Based on Sulfurized Poly(acrylonitrile) Cathodes: Impact of Electrode Density on Cell Performance. J. Electrochem. Soc. 2021, 168, 110513.
- S. Niesen; J. M. Kappler, J. Trück; L. Veith; T. Weil; T. Soczka-Guth, M. R. Buchmeiser, Influence of the Drying Temperature on the Performance and Binder Distribution of Sulfurized Poly(acrylonitrile) Cathodes. J. Electrochem. Soc. 2021, 168, 050510.

Publikationen, welche nicht Teil dieser Doktorarbeit sind:

- A. M. Fox, S. Niesen, Q. Du, N. Keim, D. Vrankovic, M. R. Buchmeiser, Polyethylene Imine Crosslinked Sodium Alginate Binder for Micro-Silicon/Graphite Composite Anodes. J. Electrochem. Soc. 2022, 169, 100507.
- J. Trück; P. Wang; E. Buch; J. Groos; S. Niesen; M. R. Buchmeiser, Lithium Titanate as Mg-Ion Insertion Anode for Mg-Ion Sulfur Batteries Based on Sulfurated Poly(acrylonitrile) Composite. J. Electrochem. Soc. 2022, 169, 010505.
- S. Murugan; S. Niesen; J. M. Kappler; K. Küster; U. Starke; M. R. Buchmeiser, Ultra-Stable Cycling of High Capacity Room Temperature Sodium-Sulfur Batteries Based on Sulfurated Poly(acrylonitrile). Batteries & Supercaps 2021 4, 1636-1646.
- P. Wang; J Trück; S. Niesen; J. Kappler; K. Küster; U. Starke; F. Ziegler; A. Hinntenach; M. R. Buchmeiser, High-Performance Magnesium-Sulfur Batteries Based on a Sulfurated Poly(acrylonitrile) Cathode, a Borohydride Electrolyte and a High-Surface Area Magnesium Anode. Batteries & Supercaps 2020, 3, 1239-1247.

Erklärung über die Eigenständigkeit der Dissertation

Hiermit versichere ich, dass die Arbeit mit dem Titel

"Characterization and Optimization of Sulfurized Poly(acrylonitrile) Cathodes and Silicon Anodes**"**

eigenständig verfasst wurde und keine anderen als die gekennzeichneten Quellen und Hilfsmittel benutzt wurden; die digitale Version stimmt mit den anderen Exemplaren überein.

Declaration of Authorship

Hereby, I certify that the dissertation with the title

"Characterization and Optimization of Sulfurized Poly(acrylonitrile) Cathodes and Silicon Anodes**"**

has been written independently except stated otherwise. Ideas and passages from other sources have been indicated. The digital version is identical to all hard copies.

Name/Name: Stefan Niesen

Unterschrift/Signed: _____

Datum/Date: _____

Danksagung

An allererster Stelle möchte ich mich bei meinem Doktorvater Herrn Prof. Dr. Michael R. Buchmeiser bedanken für die Aufnahme im Arbeitskreis, die exzellente Betreuung und das stets sehr schnelle Korrekturlesen meiner Manuskripte. Besonders dankbar bin ich für die sehr gut ausgestatteten Labore sowie das sehr produktive Arbeitsklima am Lehrstuhl, dies hat maßgeblich zu dem Erfolg meiner Arbeit beigetragen. Herzlich danke ich Herrn Prof. Dr. Oliver Clemens für die Rolle als Zweitgutachter und Herrn Prof. Dr. Frank Gießelmann für die Übernahme des Prüfungsvorsitzes.

Des Weiteren möchte ich mich bei Herrn Prof. Dr. Dr. Andreas Hintennach für die Einstellung bei der Daimler AG, die Möglichkeit der Promotion im Unternehmen sowie die fachliche Betreuung seitens der Daimler AG bedanken. Besonders möchte ich bei Dr. Thomas Soczka-Guth und Dr. Martin Frey für die herzliche Übernahme in die Abteilung RD/EBZ sowie die Unterstützung bei fachlichen und bürokratischen Themen danken.

Großer Dank gilt dem gesamten Arbeitskreis für die herzliche Aufnahme und die stets sehr gute Arbeitsatmosphäre. Besonders großen Dank bin ich Dr. Dongren Wang verpflichtet für die herausragende Organisation des Arbeitskreises, die nette Gesellschaft sowie für spannende Gespräche. Für die gute Zusammenarbeit im Labor und die professionelle Büroatmosphäre danke ich Dr. Tim Lebherz, Dr. Alina Fox, Dr. Janina Trück, Alexander Balint, Dr. Saravanakumar Murugan, Julian Kappler, Qian Du und Dr. Peiwen Wang. Zudem bedanke ich mich bei meinen Forschungspraktikanten Martin Siodlaczek und Noah Keim für das motivierte Arbeiten im Labor und das Einbringen von eigenen Ideen. Außerhalb des Labors bedanke ich mich für Handwerkshilfe, Trainingstipps, indisches/italienisches Essen, den Verzehr von Kaltgetränken und unzählige lustige Momente bei Julian Kappler, Dr. Janis Musso, Alexander Balint, Dr. Philipp Hauser, Dr. Alina Fox, Francesco Ceccini, Patrick Probst und Dr. Saravanakumar Murugan. Für das Korrekturlesen bin ich Dr. Alina Fox und Dr. Janis Musso zu erneutem Dank verpflichtet.

Zu guter Letzt gilt der größte Dank meiner Familie und Freunden, die mich in allen Lebenslagen immer unterstützt haben. Ohne euch wäre diese Promotion nicht möglich gewesen.

Table of Contents

List of Abbreviations

A	Chemical activity
E	Dielectric constant
P	Density
σ_0	Electrolyte conductivity
T	Tortuosity
Φ	Phase shift
Ω	Radial frequency
A	Electrode surface area
AM	Acryl amide
BMS	Battery Management System
C	Capacitor
c_{dl}	Double-layer capacitance
c_{spec}	Specific capacity
CE	Coulombic efficiency
CPE	Constant phase element
CMC	Carboxymethyl cellulose
CNT	Carbon nanotubes
D	Ion pathway
D	Pore size
DEC	Diethyl carbonate
DMC	Dimethyl carbonate
DME	1,2-Dimethoxyethane
DMF	*N*,*N*-Dimethyl formamide
DMSO	Dimethyl sulfoxide
DOL	1,3-Dioxolane
E	Electrode potential
E^0	Standards electrode potential
EC	Ethylene carbonate
EIS	Electrochemical Impedance Spectroscopy
EV	Electric vehicle
F	Frequency

F	Faraday constant
FEC	Fluoroethylene carbonate
I	Current
L	Inductor
LCO	Lithium cobalt oxide
LFP	Lithium iron phosphate
LIB	Lithium-ion Battery
Li-S	Lithium-Sulfur
LiTFSI	Lithium bis(trifluoromethanesulfonyl)imide
LMO	Lithium manganese oxide
LMP	Lithium manganese phosphate
LTO	Lithium titanium oxide
m_{cell}	Weight of cell components
M	Metal
M_n	Molar mass
MBAA	*N*,*N*-Methylenebisacrylamide
N	Number of exchanged electrons
NCA	Nickel cobalt aluminum oxide
NMC	Nickel manganese oxide
OCV	Open-circuit voltage
P	Porosity
PAA	Poly(acrylic acid)
PAM	Poly(acryl amide)
PAN	Poly(acrylonitrile)
PC	Propylene carbonate
PEDOT:PSS	Poly(3,4-ethylenedioxythiophene) poly(styrene sulfonate)
PEG	Polyethylene glycol
PEO	Poly(ethylene oxide)
PMMA	Poly(methyl methacrylate
PVA	Poly(vinyl alcohol)
PVDF	Poly(vinylidene fluoride)
Q	CPE coefficient
NMP	*N*-Methyl-2-pyrrolidone

Na-alginate	Sodium alginate
NaPAA	Sodium polyacrylate
R	Resistor
R^0	Gas constant
R_{ct}	Charge-transfer resistance
R_{el}	Electrical resistance
R_{pore}	Pore resistance
R_{sol}	Solution resistance
R_w	Diffusion resistance
SBR	Styrene-butadiene rubber
SEI	Solid electrolyte interface
SEM	Scanning electron microscope
Si	Silicon
SiNP	Silicon nanoparticles
SiO	Silicon oxide
SoC	State-of-Charge
SPAN	Sulfurized poly(acrylonitrile)
TMSP	Tris(trimethylsilyl)phosphite
T	Temperature
T_b	Boiling point
T_f	Flash point
T_m	Melting point
ToF-SIMS	Time-of-Flight Secondary Ion Mass Spectroscopy
U	Voltage
U_A	Voltage amplitude
V	Volume
VC	Vinylene carbonate
w	Gravimetric energy density
W	Warburg impedance
XAS	X-ray absorption spectroscopy
Z	Complex impedance

Motivation

In recent years, the demand for electrochemical energy storage devices has sharply increased and will continue to raise in the future. Besides finding application in portable devices, batteries are regarded as a crucial element in our future energy economy.[1] For instance, the transport sector is responsible for roughly 24 % of the total global CO_2 emissions.[2] By replacing fossil-fueled automobiles with battery electric vehicles (BEVs), a large share of these emissions can be avoided. Additionally, for replacing the share of fossil fuels in electricity production, batteries and other storage solutions are required to compensate for the fluctuating electricity supply of renewable energy sources.[3-4] Several studies have estimated that the stationary and transport sector alone will require a globally installed storage capacity of 1.5 - 2.5 TWh in 2030.[5-6] To manage this projected massive demand for energy storage devices in the future, not only the energy density and other performance characteristics of batteries need to be improved. Rather, the focus should be laid on developing sustainable, recyclable and cost-effective batteries.[7] Figure 1 summarizes the main battery cell components (anode, electrolyte and cathode), which are applied today, and their projected future development steps regarding energy density, eco-friendliness and safety.

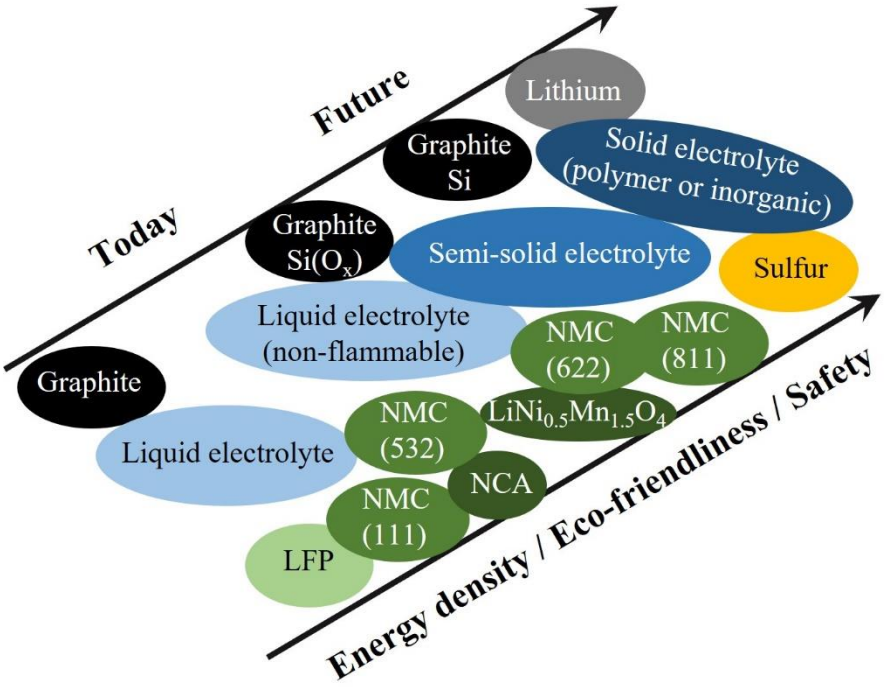

Figure 1: Main battery cell components (anode, electrolyte and cathode) applied today and their projected future development steps (based on ref.[7]).

The Li-ion battery (LIB) with a silicon (Si) or Si/graphite (high Si content) anode and the Lithium-Sulfur (Li-S) battery are battery systems, which are promising candidates for replacing today´s applied LIBs in the future. Si as an anode material is abundant and offers a more than ten times higher capacity than graphite. The merits of the Li-S battery include its remarkably high theoretical capacity as well as the high abundance, eco-friendliness and low cost of sulfur. Nonetheless, intensive research efforts are required for Si anodes and Li-S batteries to have commercial success.[8-9] Focus should especially be laid on optimizing electrode processability and electrode formulation (e.g., conductive additives, binder system) of these electrode materials. This thesis addresses the characterization of processing parameters of Li-S cathode materials and the optimization of the electrode formulation of Si anodes.

Zusammenfassung

Die Nachfrage nach elektrischen Speichermedien hat in den letzten zwei Jahrzehnten stark zugenommen. Neben ihrer Anwendung in tragbaren elektronischen Geräten werden Batterien in Energiespeichersystemen zur Stabilisierung des Stromnetzes sowie als Stromspeicher für Elektrofahrzeuge eingesetzt. Da die heute verwendeten Li-Ionen Batterien (LIB) auf begrenzt verfügbaren und umweltkritischen Aktivmaterialien mit begrenzter theoretischer Kapazität (z. B.: Lithium-Nickel-Kobalt-Oxide) basieren, müssen neue Batterietechnologien auf Grundlage umweltfreundlicher und kostengünstiger Aktivmaterialien mit hoher Kapazität auf den Markt gebracht werden.

Die Lithium-Schwefel Batterie (Li-S) mit sulfuriertem Poly(acrylnitril) (SPAN) als Kathodenmaterial ist eine vielversprechende Alternative für die derzeit verwendete LIB, da die Li-SPAN Batterie eine hohe theoretische Kapazität bietet und auf reichlich vorhandenen und kostengünstigen Rohstoffen basiert. Im Vergleich zu den meisten anderen Li-S Kathodenmaterialien ist der Schwefel in der SPAN-Struktur kovalent gebunden, was eine Auflösung des Schwefels im Elektrolyten verhindert und somit eine ausgezeichnete Langzeitzyklisierbarkeit ermöglicht. Nichtsdestotrotz müssen noch einige Produktionsparameter untersucht werden bevor die Li-SPAN Batterie im großen Maßstab kommerziell produziert werden kann.

Im ersten Teil dieser Arbeit wurden sowohl die Auswirkungen der Trocknungstemperatur der Kathodenbeschichtung als auch der Einfluss der Elektrodendichte auf die elektrochemische Performanz der Li-SPAN Zellen untersucht. Zur Untersuchung des Einflusses der Trocknungstemperatur wurden SPAN Beschichtungen, die mit zwei gängigen Bindersystemen Poly(vinylidenfluorid) (PVdF) und Poly(acrylsäure) (PAA) hergestellt wurden, bei verschiedenen Trocknungstemperaturen (30, 60 und 90 °C) getrocknet. Der Einfluss der Trocknungstemperatur auf die elektrochemischen Eigenschaften der hergestellten SPAN Kathoden wurde mittels Zyklisierung in Halbzellen und referenzgestützter elektrochemischer Impedanzspektroskopie (EIS) untersucht. Zudem wurde Flugzeit-Sekundärionen-Massenspektrometrie (ToF-SIMS) eingesetzt, um die Binderverteilung innerhalb der Beschichtungen zu ermitteln. Der Einfluss der Trocknungstemperatur auf die Zyklisierbarkeit der SPAN Kathoden war stark von dem verwendeten Bindersystem abhängig. Für die SPAN Kathoden, welche mit PVdF als Binder hergestellt wurden, zeigte sich mittels ToF-SIMS Messungen, dass der

PVdF Binder zur Elektrodenoberfläche wanderte, wenn die Elektroden bei höheren Temperaturen (≥ 60 °C) getrocknet wurden. Die Migration des PVdF Binders zur Elektrodenoberfläche erhöhte den Ladungsübertragungswiderstand, was zu einer Verringerung der erreichbaren Kapazität bei hohen Raten führte. Im Gegensatz zu den PVdF-basierten Kathoden war die elektrochemische Performanz der PAA-basierten Elektroden nicht von der Trocknungstemperatur abhängig.

Das Kalandrieren von Batterieelektroden zu niedrigeren Elektrodendichten wird häufig angewandt, um die Energiedichte zu erhöhen, hat aber bekanntermaßen auch Auswirkungen auf die elektrochemische Leistung der Zelle. Um den Einfluss der Elektrodendichte auf die elektrochemische Leistungsfähigkeit zu untersuchen, wurden die SPAN Kathoden zu drei unterschiedlichen Elektrodendichten komprimiert und mit (elektro)chemischen Methoden charakterisiert. Mit Hilfe von referenzgestützten EIS Messungen konnte gezeigt werden, dass das Kalandrieren der SPAN Kathode zu einer Verringerung des elektrischen Widerstandes führte, aber auch den Ladungsübertragungswiderstand erhöhte, wenn die Elektrodendichte einen Wert von 1,05 g cm^{-3} überstieg. Quecksilberintrusionsmessungen ergaben, dass der Anstieg des Ladungsübertragungswiderstandes bei sehr hohen Elektrodendichten durch eine kompressionsbedingte Abnahme an aktiven Reaktionsstellen verursacht wurde.

Ein weiterer Ansatz zur Erhöhung der Energiedichte von LIB besteht darin, die traditionell verwendete Graphitanode durch Silizium zu ersetzen. Silizium bietet eine mehr als zehnmal höhere Kapazität als Graphit, leidet aber unter einer starken teilweise irreversiblen Volumenveränderung, während der kontinuierlichen (De-)Lithiierung, was zu einer unzureichenden Lebensdauer führt. Eine vielversprechende Möglichkeit die irreversible Volumenänderung zu begrenzen ist die Verwendung von quervernetzenden Bindersystemen. Im zweiten Teil dieser Arbeit wurde das selbstvernetzende Copolymer Poly(acrylamid)-*co*-Poly(hydroxymethylacrylat) (p(AM-*co*-HMA)) als Binder für Si Anoden hergestellt und untersucht. Das p(AM-*co*-HMA) Bindersystem war in der Lage durch eine thermisch induzierte Selbstvernetzungsreaktion eine 3D-Netzwerkstruktur auszubilden. Silizium Elektroden, welche mit p(AM-*co*-HMA) als Binder hergestellt wurden, wiesen eine bessere Haftung am Stromableiter, einen geringeren Kapazitätsabfall und eine höhere Leistungsfähigkeit im Vergleich zu traditionell verwendeten Bindersystemen (z. B.: Natriumalginat) auf. Es zeigte sich, dass der p(AM-*co*-HMA) Binder die irreversible Volumenexpansion der Si Partikel einschränken konnte,

wodurch die mechanische Integrität der Elektrode, während der Zyklisierung verbessert und somit die Lebensdauer der Anode gesteigert wurde.

Abstract

The demand for electrical storage devices has strongly increased in the previous two decades. Besides their application in portable electronic devices, batteries find application in grid-scale energy storage systems and are highly needed as the power source for electric vehicles (EVs). As today´s applied LIB technology is based on non-abundant and non-ecofriendly active materials with limited theoretical capacity (e.g., lithium nickel cobalt oxides), novel battery technologies based on eco-friendly, cost-effective active materials with high capacities need to be commercialized to enable the mass-market adaption of EVs and the replacement of fossil fuels by renewable energy in the electricity generation.

The Li-S battery with sulfurized poly(acrylonitrile) (SPAN) as cathode material is a promising alternative for the well-established LIB as it offers high capacity and is based on abundant and cost-effective raw materials. Compared to most other Li-S cathode materials, the sulfur is covalently bound in the SPAN structure, which prevents sulfur dissolution and thereby enables excellent long-time cycling ability. Nonetheless, several production parameters need to be investigated before SPAN electrodes are produced at a large scale.

In the first part of this thesis, both the impact of the coating drying temperature and the effect of the electrode density on the electrochemical performance were examined. The impact of the coating drying temperature was analyzed by drying SPAN electrodes prepared with two commonly used binder systems (poly(vinylidene fluoride) (PVdF) and poly(acrylic acid) (PAA)) at various temperatures (30, 60 and 90 °C) and measuring their electrochemical performance against lithium metal. Besides evaluating the cycling performance of the prepared SPAN cathodes, reference-assisted Electrochemical Impedance Spectroscopy (EIS) and Time-of-Flight Secondary Ion Mass Spectrometry (ToF-SIMS) were applied as analytical techniques. It was shown that the effect of the drying temperature on the cycling performance strongly depended on the used binder system. For the PVdF-based SPAN cathodes, the ToF-SIMS measurements revealed that the PVdF binder migrated towards the electrode surface when the electrodes were dried at elevated temperatures. The migration of PVdF towards the electrode surface increased the charge-transfer resistance, which consequently led to a decrease in the rate capability.

In contrast to the PVdF-based cathodes, the electrochemical performance of the PAA-based electrodes showed no dependence on the drying temperature.

Calendering of battery electrodes towards lower electrode densities is widely applied to increase the energy density but is also known to affect the electrochemical performance of the resulting cell. To elucidate the influence of the electrode density on the electrochemical performance, SPAN cathodes were compressed to three different electrode densities and characterized by various (electro)chemical methods. With the aid of reference-assisted EIS measurements, it was demonstrated that calendering of the SPAN cathodes led to a decrease in the electrical resistance and an increase in the charge-transfer resistance when the electrodes were compressed to electrode densities greater than 1.05 g cm^{-3}. Mercury intrusion measurements revealed that the increase in the charge-transfer resistance at higher electrode densities, which strongly reduced the rate capability, was caused by a compression-induced decrease of active reaction sites.

An additional approach to increase the energy density of LIBs is to replace the traditionally applied graphite anode with silicon. Si offers a more than ten times higher capacity than graphite but suffers from severe volume changes during continuous (de)lithiation, which results in insufficient cycle life. Previous studies have shown that the usage of binders that form a 3D network can sufficiently restrict volume changes. Unfortunately, most reported crosslinked binder systems are based on two or more components, which increases production complexity. In the second part of this thesis, the self-cross-linkable copolymer poly(acrylamide)-*co*-poly(hydroxymethylacrylate), p(AM-*co*-HMA) was developed and applied as a binder for high-loading Si anodes. The p(AM-*co*-HMA) novel binder was capable of forming a 3D network structure via a thermal-induced self-crosslinking reaction. Si electrodes prepared with p(AM-*co*-HMA) exhibited better adhesion to the current collector, lower capacity fading and higher rate capability compared to commonly applied binder systems (e.g., sodium alginate). It was revealed that the superior electrochemical performance of the p(AM-*co*-HMA)-based Si anodes stemmed from the improved ability of the p(AM-*co*-HMA) crosslinked binder matrix to restrict the irreversible volume expansion of the Si particles, which enhanced the mechanical integrity of the electrode during cycling.

1 Theoretical Survey

1.1 Basic Concept of a Battery

In 1866, Georges Leclanché patented an energy storage device consisting of a zinc anode and a manganese dioxide cathode dipped in an ammonium chloride solution. Due to its broad application in electric bell work as well as telegraphy, Leclanché`s invention was one of the first commercial battery cells. In the following decades, several battery inventions such as the lead-acid battery or the nickel-cadmium accumulator followed until today`s widely applied Li-ion battery was introduced in 1991 by Sony. Today`s battery systems are still based on the working mechanism of the electrochemical cells invented in the 19th century.[10-11] In Table 1-1, reaction mechanism, theoretical voltage and theoretical capacity of today's used battery cells are depicted.

Table 1-1: Reaction mechanism, theoretical voltage and theoretical capacity of prominent secondary battery cells (based on ref.[12]).

Battery type	**Reaction mechanism**	**Th. Voltage [V]**	**Th. Capacity [Ah kg^{-1}]**
Pb-acid	$Pb+PbO_2+2H_2SO_4 \rightarrow 2PbSO_4+2H_2O$	2.1	120
Ni-Cd	$Cd+2NiOOH+2H_2O \rightarrow 2Ni(OH)_2+Cd(OH)_2$	1.4	244
Ni-Zi	$Zn+2NiOOH+2H_2O \rightarrow 2Ni(OH)_2+Zn(OH)_2$	1.7	372
Ni-metal hydride	$MH+2NiOOH \rightarrow 2Ni(OH)_2$	1.4	240
Li-ion	$Li_xC_6+Li_{(1-x)}CoO_2 \rightarrow LiCoO_2+C_6$	4.1	280
Li-S	$16Li+S_8 \rightarrow 8Li_2S$	2.2	1675

In general, a battery consists of two or more galvanostatic cells that convert stored chemical energy into electrical energy. Depending on the cell`s ability to recharge, it can be divided into primary and secondary cells. Primary cells (e.g., Leclanché`s cell) irreversibly transform chemical energy into electrical energy. The reconversion of reactants to their initial state by electrical energy is not possible. By supplying electrical energy to a secondary battery cell (e.g., lead-acid or Li-ion battery cells), its original chemical composition can be restored.[10]

All battery cells consist of the following basic components:[12-14]

- Negative electrode: As the cell discharges a chemical compound (e.g., a metal (M)) is electrochemically oxidized ($M \rightarrow M^+ + e^-$) on the negative electrode. As shown in Figure 1-1a, the generated electrons move through the external circuit to the positive electrode. The electrode where the oxidation takes place during discharge is called the anode.
- Positive electrode: The electrons coming from the negative electrode lead to an electrochemical reduction ($X + e^- \rightarrow X^-$). During the discharge, the positive electrode is called the cathode.

  If the cell is rechargeable, the reactions occurring on the negative and positive electrodes are reversed (Figure 1-1b). The electrons flow from the positive to the negative electrode as the cell charges. Thus, the reduction takes place on the negative electrode (now cathode) and the oxidation occurs on the positive electrode (now anode). In battery research, the labeling of the electrodes is referring to the cell`s discharged state. Hence, negative electrode and positive electrode are always defined as anode and cathode, respectively.

- Electrolyte: To balance the charges, anions and cations move within the electrolyte phase towards the electrode of the opposite polarization. A liquid electrolyte composes of salts, bases or acids in a (non)aqueous solution. Besides liquid electrolytes, solid or polymeric electrolytes are widely applied.
- Separator: The separator keeps the electrodes spatially apart to prevent short circuits while still enabling the transport of ionic charge carriers.

The potential difference between the electrodes defines the voltage of the cell. In case that no external load is connected it can be calculated with the following equation:

$$E_{cell} = E_+ - E_- \tag{1.1}$$

Since measuring individual potentials is not possible, an electrode potential is defined as the potential difference relative to a standard electrode (usually the hydrogen electrode). Commonly, these electrode potentials are measured in standard conditions and are therefore called standard electrode potentials (E^0). The standard potentials of various redox pairs are given in the electrochemical series. In the ideal case, the

electrode pair is chosen in a way that the potential difference is the highest, which would result in the highest cell voltage.[15-16]

The potential of active materials can be calculated under real conditions (e.g., varying temperature and concentration) with the aid of the Nernst equation:[15]

$$E = E^0 - \frac{R^0 T}{nF} ln \frac{\alpha(Red)}{\alpha(Ox)} \quad (1.2)$$

in which R^0 is the universal gas constant, T is the temperature, E^0 is the standard electrode potential, n is the number of electrons exchanged in the reaction, F is the Faraday constant and α is the chemical activity of the reduced or oxidized species.

Depending on the connection of the cells in the battery, the voltage or current can be adjusted according to the customers' needs. Connecting the cells in serial increases the voltage of the battery and the parallel connection enhances its current. Besides several cells, a battery pack contains a battery management system (BMS), which controls and monitors the charge state, current flow and temperature.[10]

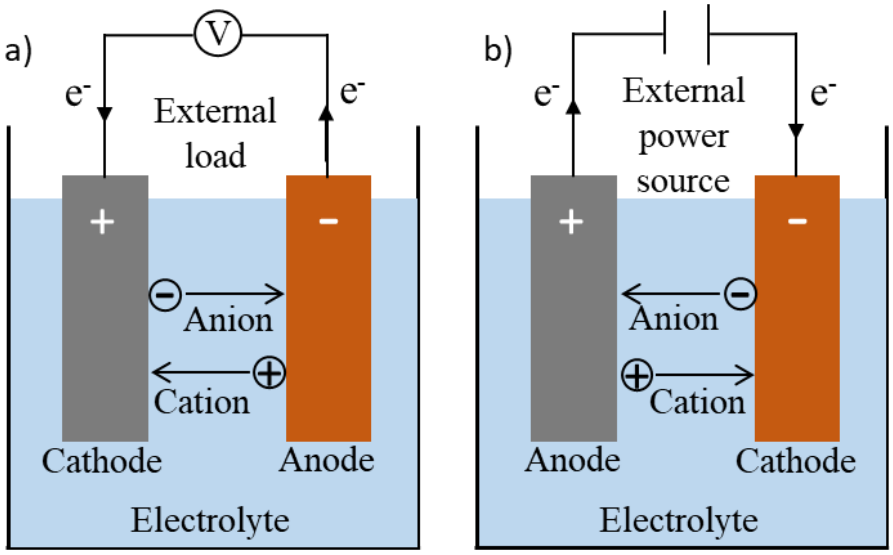

Figure 1-1: Schematic illustration of a battery cell during discharging (a) and charging (b) (based on ref.[12]).

1.2 The Li-ion Battery

The Li-ion battery is currently the most advanced rechargeable battery and finds broad application as a power source for portable electronic devices and electric vehicles. The development of Li-ion batteries started roughly 20 years before its commercialization in 1991 by Sony. First rechargeable Li-ion batteries were based on lithium as the negative electrode (e.g., Li/MoS_2 or Li/TiS_2 systems). However, their mass-market application was hindered due to dendrite formation on the lithium anode and the instability of the electrolyte used.[17-18] The Goodenough group[19] discovered the ability of lithiated transition metal oxides (e.g., $LiCoO_2$) to reversible (de)intercalate Li-ions at high potentials. Their patented material ($LiCoO_2$) was later used as the positive electrode in Sony`s Li-ion battery. For the negative electrode, research focused on finding a suitable and safe alternative for lithium metal. Several researchers showed that graphite and other carbonaceous materials can reversibly (de)intercalate Li-ions.[20] In 1985, Yoshino and coworkers[21] successfully combined a $LiCoO_2$ negative electrode with a carbonaceous positive electrode. Their prototype cell made way for the commercialization of the Li-ion battery. In the 1990s, Li-ion batteries found fast application in handheld devices and are therefore considered to be the enabler of the portable electronic revolution. However, it took two more decades until the first electric vehicle powered by a LIB entered the market in 2011. Nowadays, Li-ion batteries are commonly used to power electric vehicles, trucks, buses and bikes.[18, 22]

1.2.1 Working Principle

In Figure 1-2, a schematic illustration of a Li-ion battery cell during charge is shown. A typical Li-ion battery consists of two intercalation electrodes, which are coated on metallic current collectors, a separator and an ionic conductive non-aqueous electrolyte. In a typical Li-ion battery, graphite is used as the anode material (negative electrode) and a transition metal oxide as the cathode material (positive electrode). Both electrodes are prepared by coating the active material (graphite or transition metal oxide) together with a conductive additive (mostly carbon) and a polymeric binder on a current collector. Commonly, poly(vinylidene fluoride) (PVdF) processed in *N*-Methyl-2-pyrrolidone (NMP) is applied as the binder for cathode materials. For graphite anodes, an aqueous binder system is mostly used (e.g., a mixture of carboxymethylcellulose (CMC) and styrene-butadiene rubber (SBR)).[18, 23] As the current collectors, copper and aluminum foils are used for the anode and cathode, respectively. Between the electrodes, a separator

(shown as a dashed line) is placed to avoid short circuits. State-of-the-art separators are made of nonwoven fibers (e.g., glass, nylon, cotton) or microporous polymers (e.g., poly(ethylene), poly(propylene)).[14]

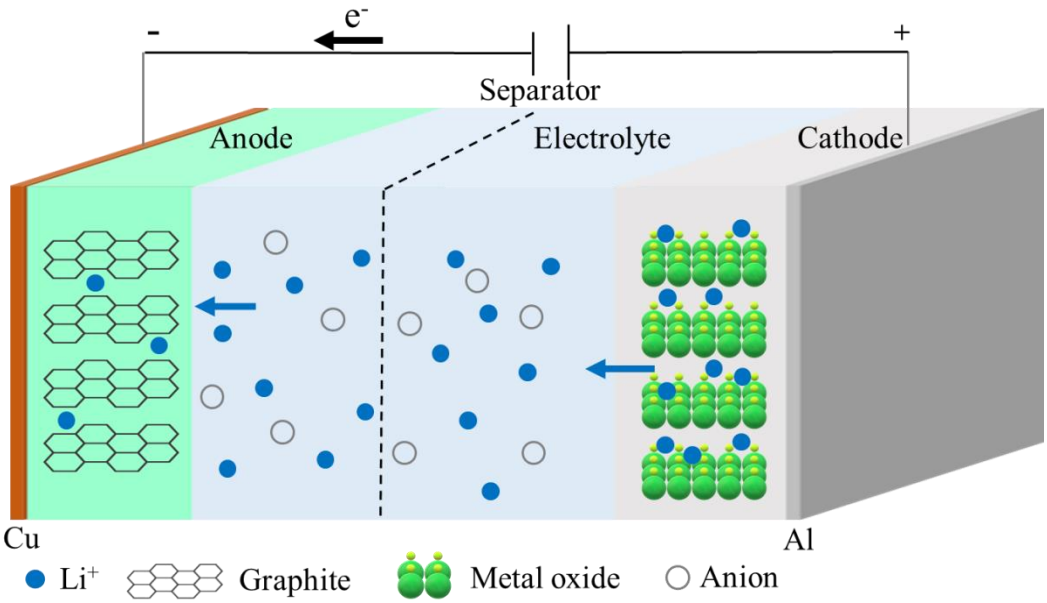

Figure 1-2: Schematic illustration of a Li-ion battery cell during charge.

Since lithiated transition metal oxide electrodes are stable in air, commercial Li-ion batteries are typically assembled in the discharged state. Hence, the cell is first charged after assembly. Upon charging of the cell, the electron flow from the metal oxide cathode to the graphite anode. The metal in the metal oxide is oxidized leading to the deintercalation of lithium ions (Li^+). The generated lithium ions move from the cathode site through the ionic conductive electrolyte to the graphite anode. At the anode, lithium is intercalated in the graphite structure up to a stoichiometry of LiC_6. During the discharge, the opposite reaction occurs. The metal oxide is reduced resulting in the intercalation of lithium and the graphite anode is delithiated. The reactions occurring at the anode and cathode can be summarized by the following chemical equations.[10, 16]

$$C_6 + x\ Li^+ + x\ e^- \rightleftharpoons Li_xC_6 \quad \text{with } x < 1$$

$$LiMO_2 \rightleftharpoons Li_{1-x}MO_2 + x\ Li^+ + x\ e^- \quad \text{with } x < 0.5$$

1.2.2 Electrolytes for Li-ion Batteries

In a Li-Ion battery, the electrolyte provides sufficient ionic conductivity to enable charge transport between the electrodes while being electrically insulating to prevent short circuits. The following three types of electrolytes are commonly applied: (i) liquid

systems (lithium salts diluted in an aprotic solvent), (ii) polymer electrolytes (solid or gel systems) and (iii) solid ionic conductors (e.g., glasses or ceramics).[24]

This section solely focuses on introducing liquid electrolytes. Typically, liquid electrolytes consist of a lithium salt diluted in a mixture of two or more solvents. Generally, the electrolyte solvent should meet the following requirements: (i) be inert to all cell components, in particular the charged electrode surfaces, (ii) dissolve lithium salts in an adequate concentration (high dielectric constant ε), (iii) exhibit a low viscosity to ensure fast ion transport, (iv) be able to sufficiently wet the electrodes and the separator, (v) remain liquid at a wide temperature range (low melting point T_m and high boiling point T_b) and (vi) possess low flammability (high flash point T_f). In addition, the electrolyte solvent must remain stable in a broad voltage range due to the very low discharged potential of the anode (0.0 - 0.2 V) and the high charged potential of the cathode (3.0 - 4.5 V). Since protic solvents are unstable at low potentials, mainly organic esters or ethers are applied because they still possess good salt solvating ability despite being aprotic. Table 1-2 summarizes some of the applied organic carbonates and ethers along with their basic physical properties.[10, 25]

Due to the limited anodic stability of ethers and the wide application of high voltage cathode materials, today's Li-ion electrolytes are predominantly carbonate based. Cyclic carbonates such as ethylene carbonate (EC) and propylene carbonate (PC) were early identified as suitable solvents due to their excellent stability towards oxidation (up to 5 V vs Li/Li^+) and high dielectric constants. However, these compounds exhibit high viscosities and have relatively high melting points (Table 1-2). On the other hand, linear carbonates (e.g., DMC, DEC) have low viscosities and low melting points but suffer from a low salvation power towards lithium salts.[25] Tarascon and coworkers[26] added DMC as a cosolvent to an EC-based electrolyte and thereby showed that a synergistic effect was achieved by mixing these two solvents. The resulting mixture remained stable up to 5 V on a cathode surface, had high solvation power towards lithium salts and displayed low viscosity for sufficient ion transport. This solvent mixture based on cyclic and linear carbonates was quickly adopted by researchers as well as manufacturers and still is used today for state-of-the-art LIB electrolytes.

Table 1-2: Structure, melting point (*Tm*), boiling point (*Tb*), flash point (*Tf*), viscosity (η) and dielectric constant (ε) of some organic electrolyte solvents. Cyclic carbonates: ethylene carbonate (EC), propylene carbonate (PC); Linear carbonates: dimethyl carbonate (DMC), diethyl carbonate (DEC); Ethers: dimethoxyethane (DME), 1,3-dioxolane (DOL) (based on ref.[25]).

	Structure	Tm [°C]	Tb [°C]	Tf [°C]	η [cp] (25°C)	ε (25°C)
EC	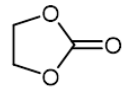	36	248	160	1.90 (40°C)	89.8
PC	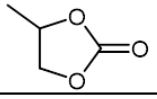	-49	242	132	2.53	64.9
DMC	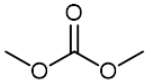	4.6	91	18	0.59 (20°C)	3.1
DEC	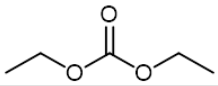	-74	126	31	0.75	2.8
DME	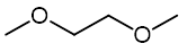	-58	84	0	0.46	7.2
DOL		-95	78	1	0.60	6.8

During the operation of the cell, a lithium salt is needed in the electrolyte solution for transporting ions between the electrodes. Finding a suitable lithium salt is rather challenging as it must completely dissolve in aprotic solvents while being stable against oxidative decomposition at the cathode and inert towards all other cell components. Most used lithium salts are composed of anions that consist of a simple anion core (e.g., F^-) stabilized by a Lewis acid (e.g., PF_5). In this kind of anion, the formal negative charge is well-distributed by the electron withdrawing Lewis acid ligand, which facilitates excellent solubility in aprotic solvents.[27] The structures of exemplary lithium salts as electrolyte solutes are depicted in Figure 1-3.

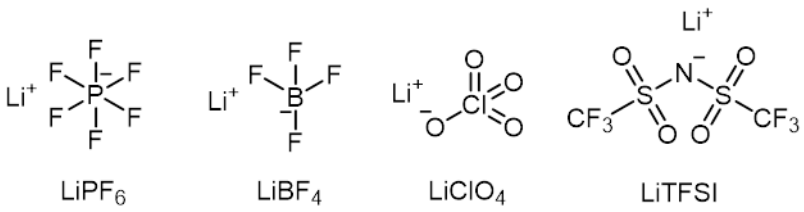

Figure 1-3: Structures of lithium hexafluorophosphate ($LiPF_6$), lithiumtrifluoromethanesulfonate ($LiBF_4$), lithium perchlorate ($LiClO_4$) and lithium bis(trifluoromethane sulfone)imide (LiTFSI).

Among numerous researched salts $LiPF_6$ is predominantly applied in commercial Li-ion electrolytes. $LiPF_6$ was chosen due to its well-balanced properties and characteristics. The salt shows excellent resistance against oxidation (up to 5.1 V vs Li/Li^+) and contrary to

other lithium salts (e.g., lithium bis(trifluoromethanesulfonyl)imide (LiTFSI)) it forms a stable passivation layer on the aluminum current collector to prevent corrosion. However, $LiPF_6$ decomposes at elevated temperatures to LiF and PF_5, which is known to initiate the decomposition of carbonates. Additionally, contact of $LiPF_6$ with moisture leads to the formation of toxic hydrogen fluoride (HF) gas:

$$LiPF_6 + H_2O \rightarrow POF_3 + LiF + 2\ HF$$

The formed HF can further initiate undesired site reactions with the active materials and bears a safety risk upon cell leakage. Due to the sensitivity of $LiPF_6$ towards moisture, $LiPF_6$ as well as all other electrolyte components must be manufactured in high purity and handled in a dry atmosphere.[27-28]

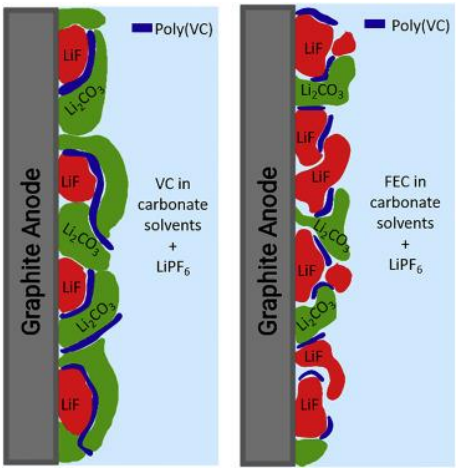

Figure 1-4: Schematic illustration of the SEI layer on a graphite anode formed in electrolytes containing VC (left) or FEC (right) (reprinted with the permission of ref.[29]).

Due to the low potential of the graphite anode, electrolyte solvents decompose reductively on the graphite surface during charging. The formed decomposition products form a solid electrolyte interphase (SEI) layer on the anode, which is ionically conductive but an electronic insulator. The film prevents further electrolyte reduction once the anode surface is fully covered with decomposition products. A commonly applied method to improve the performance of Li-ion batteries is the usage of electrolyte additives. Electrolyte additives facilitate the formation of a more stable SEI on the graphite anode, reduce active material dissolution on the cathode and improve the physical properties of the electrolyte (e.g., viscosity or wettability).[28] To facilitate the formation of a high-quality SEI layer, the electrolyte additive must get preferentially reduced during the first charge cycle. A prominent additive that is commonly used in Li-ion batteries is vinylene carbonate (VC).[30] The reduction of VC at ~ 1 V vs Li/Li^+ leads to the formation of a

flexible polymeric film on the anode surface. Besides VC, fluoroethylene carbonate (FEC) and lithium-bis(oxalato)borate find wide application as film-forming additives in Li-ion and post-Li-ion batteries.[28, 31-32] Figure 1-4 illustrates the composition of SEI layers, which are formed in electrolytes consisting of VC or FEC as additive. In both electrolyte systems, the SEI layer is mainly composed of lithium fluoride (LiF), lithium carbonate (Li_2CO_3) and a polymeric species (poly(VC)), which is formed by the polymerization of VC.[29] As the additive determines the SEI composition, the additive choice has a strong impact on the electrochemical performance of the overall battery cell. For instance, Jaumann et al.[33] reported that the SEI layer on Si anodes in FEC-based electrolytes contains more LiF compared to the SEI layer in electrolytes with VC as an additive. The higher LiF amount in the SEI layer led to better power capability but lower cycle life.

1.2.3 Cathode Materials for Li-ion Batteries

Cathode materials are critical cell components as they limit energy density and strongly dictate battery costs.[34] In this section, the structure, electrochemical characteristics, advantages and drawbacks of commonly applied Li-ion cathode materials will be discussed.

Table 1-3: Characteristics of commercially available cathode materials (based on ref.[35]).

Crystal structure	Compund	Specific capacity [mAh g^{-1}] (theoretical/experimental)	Av. Voltage [V]
Layered	$LiCoO_2$ (LCO)	274/148	3.8
	$LiNi_{0.33}Mn_{0.33}Co_{0.33}O_2$ (NMC)	280/160	3.7
	$LiNi_{0.8}Co_{0.15}Al_{0.05}O_2$ (NCA)	279/199	3.7
Spinel	$LiMn_2O_4$ (LMO)	148/120	4.1
Olivine	$LiFePO_4$ (LFP)	170/165	3.4
	$LiMnPO_4$ (LMP)	171/168	3.8

In the 1980s, Goodenough`s group discovered three classes of cathode materials namely layered metal oxides, spinel oxides and phosphor-olivines.[36] Even today`s Li-ion batteries are solely based on these materials. Table 1-3 summarizes most of the commercially available cathode materials along with their basic electrochemical properties.

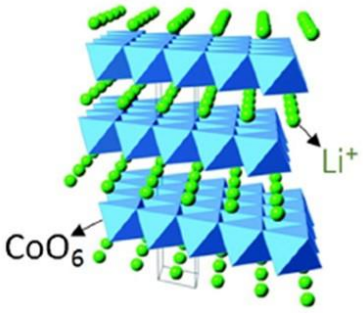

Figure 1-5: Crystal structure of the layered $LiCoO_2$ (reprinted with permission from ref.[35]).

The first investigated layered metal oxide with the general formula unit $LiMO_2$ was $LiCoO_2$ (LCO). In the crystal structure of LCO, the cations (Li^+, Co^{3+}) occupy the octahedrally coordinated position in between sheets of close-packed oxide ions. Li^+ and Co^{3+} are placed in alternating layers between the oxide anions (Figure 1-5). LCO is a very potent cathode material due to its high discharge voltage, high theoretical capacity (274 mAh g^{-1}) and good cycling characteristics. Unfortunately, the theoretical capacity cannot be fully reached as delithiation below 50 % induces lattice distortions that in turn reduce cycling stability. Coating metal oxides (e.g., Al_2O_3, B_2O_3, TiO_2) on LCO can effectively enhance the stability and performance during deep delithiation. Further limitations include the high cost of cobalt and the low thermal stability of LCO. When LCO is heated above a certain temperature, an exothermic release of oxygen occurs, which potentially leads to a dangerous thermal runaway reaction. Following LCO, the use of $LiNiO_2$ (LNO) as cathode material has gained much research attention as the material is cheaper than its analogous cobalt-based material. Nevertheless, pure LNO electrodes suffer from severe capacity fading due to the blockage of Li^+ diffusion pathways. Ni^{2+} ions tend to occupy Li^+ sites during synthesis and delithiation, which as a result lessens Li-ion diffusion. Additionally, the LNO cathode has even lower thermal stability than LCO. It was found that the partial replacement of nickel with cobalt and aluminum can effectively reduce the cationic disorder and enhance thermal stability. This observation led to the introduction of $LiNi_{0.80}Co_{0.15}Al_{0.05}O_2$ (NCA) as a cathode material. Nowadays, NCA is widely used as cathode material in Li-ion batteries. Since manganese is more abundant and cheaper than cobalt and nickel (Co: 53 \$ kg^{-1}, Ni: 19 \$ kg^{-1}, Mn: 3 \$ kg^{-1})[37], $LiMnO_2$ was also tested as a potential cathode material. Unfortunately, the cycling ability of $LiMnO_2$ is unsatisfying due to the dissolution of active material and structural change during delithiation. During lithium extraction, the layered structure of $LiMnO_2$ changes to the thermodynamically more stable spinel structure (Mn_2O_4). Further

research led to the combination of Co, Ni and Mn in a mixed metal layered oxide. In $LiNi_xMn_yCo_z$ (NMC) with x+y+z=1, the specific electrochemical characteristics of the individual transition metals are combined. The cobalt in the structure increases the electrical conductivity and reduces the lithium-nickel disorder. Manganese stabilizes the structure and thereby enhances the cycling stability and safety of the material. By enhancing the amount of nickel in the structure, the specific capacity of the NMC material can be increased. Analogous to LCO, NMC cannot be fully delithiated as deep cycling induces structure deterioration.[35, 38-39] Therefore, the practical achievable capacity is below the theoretical value (see Table 1-3). Ongoing research focuses on increasing the nickel content to enhance the specific obtainable capacity and reduce costs. For example, $LiNi_{0.8}Mn_{0.1}Co_{0.1}$ (NMC811) which has a practical obtainable capacity of ~ 200 mAh g^{-1} was recently introduced to the market. Today NMC is the predominately used cathode material in Li-ion batteries.[40]

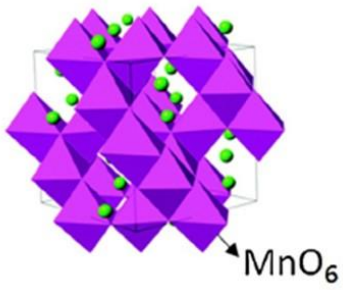

Figure 1-6: Crystal structures of the spinel $LiMn_2O_4$ (reprinted with permission from ref.[35]).

A promising high voltage cathode material is the spinel $LiMn_2O_4$ (LMO). In the spinel structure, Li^+ occupies tetrahedral sites and Mn cations occupy octahedral sites in a cubic close-packed oxygen array (Figure 1-6). This material profits from the high abundance, low cost and eco-friendliness of manganese. LMO has a capacity of 148 mAh g^{-1} and operates at a flat potential of 4.1 V. Unfortunately, LMO suffers from severe capacity fading induced by the dissolution of Mn^{2+} (formed by the disproportionation reaction of Mn^{3+} to Mn^{2+} and M^{4+}) and the generation of new phases during cycling. To tackle these issues several strategies have been attempted such as the partial substitution of Mn^{3+} by foreign cations (e.g., Ni^{2+}, Zn^{2+}, Al^{3+}) or modifying the surface with a protective coating (e.g., Al_2O_3, TiO_2, ZnO, SiO_2).[35, 41-42]

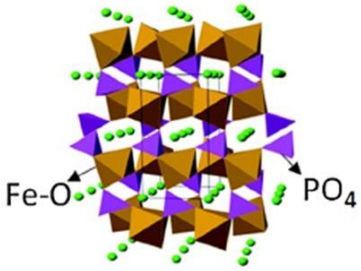

Figure 1-7: Crystal structure of the olivine $LiFePO_4$ (reprinted with permission from ref.[35]).

In 1997, a phospho-olivine was first used as a cathode material in Li-ion batteries.[43] In this type of structure, Li^+ and M^{2+} (M = Fe, Mn, Co) are located at octahedral sites while P occupies tetrahedral sites in a distorted hexagonal packed oxygen array (Figure 1-7). Lithium iron phosphate (LFP) with the chemical formula $LiFePO_4$ is the most prominent representative of this structure. Contrary to most other cathode materials, LFP is based on abundant, sustainable and inexpensive materials. Additionally, due to the strong covalent P-O bond, LFP offers higher thermal stability and improved safety compared to metal oxide cathode materials. However, LFP suffers from poor electronic and ionic conductivity, which limits its electrochemical performance at higher C-rates. Methods to enhance the conductivity include the reduction of LFP particle size and applying a carbon coating on the LFP particles.[35, 44] Due to the lower voltage plateau of LFP compared to metal oxides (Table 1-3), LFP is less suited for applications where high energy densities are required. Therefore, ongoing research focuses on investigating other olivine-type materials such as LMP ($LiMnPO_4$) and LCP ($LiCoPO_4$) which have higher operating voltages. For example, replacing LFP with LMP increases the average voltage of a full cell by ~ 0.4 V.[45-46]

1.2.4 Anode Materials for Li-ion Batteries

In this section, commercial applied and potential future anode materials for Li-ion batteries will be introduced. This includes lithium metal, intercalation anodes (carbon-based materials, $Li_4Ti_5O_{12}$) and silicon. Table 1-4 summarizes the physical and electrochemical properties of these anode materials.

Table 1-4: Characteristics of common Li-ion anode materials (based on ref.[47]).

Material	Density [g cm^{-3}]	Th. specific capacity [mAh g^{-1}]	Operating potential vs Li/Li$^+$
Lithium metal	0.53	3860	0
Graphite	2.25	372	0.1
LTO ($Li_4Ti_5O_{12}$)	3.50	175	1.6
Silicon	2.30	3579 ($Li_{15}S_4$)	0.4

1.2.4.1 Lithium metal:

Elemental lithium is the most potent anode material as lithium has a high theoretical capacity (3860 mAh g^{-1}) and the lowest potential (-3.04 V vs standard hydrogen electrode) of all lithium storage materials.

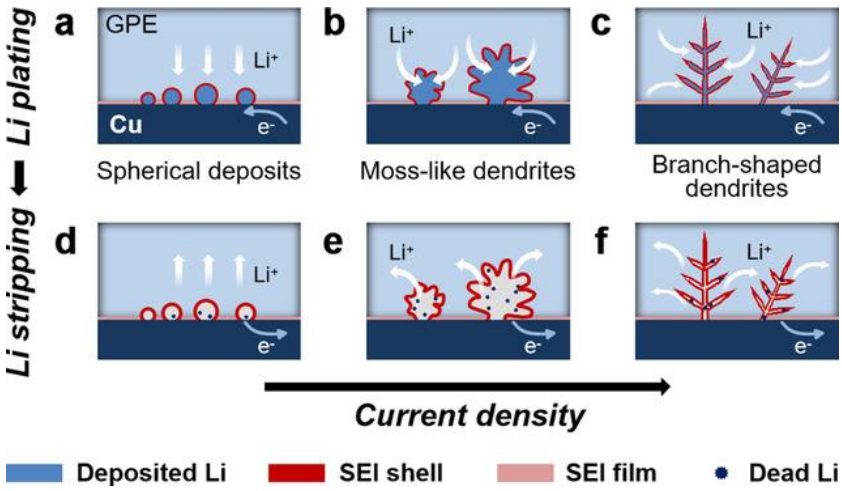

Figure 1-8: Schematical illustration of the evolution of Li plating (a-c) and stripping (d-f) (reprinted with the permission of ref.[48]).

However, metallic lithium has not yet been commercialized as anode material. Cells with lithium as the counter electrode (so called half-cells) suffer from severe safety risks and low cycling life. Repeated plating and stripping of lithium leads to the formation of dendrites on the Li surface. The formed Li dendrites can penetrate the separator and thereby short-circuit the cell. The breakage of the Li dendrites can further lead to the formation of inactive (dead) lithium. Additionally, lithium metal anodes are unable to form a stable SEI layer as the surface area of the lithium metal repeatedly changes. The inability to form a stable SEI layer results in continuous electrolyte consumption, which severely reduces the cycle life.[47-48] Figure 1-8 illustrates the formation of dendrites on the Li metal anode surface during continuous (dis)charge cycles. Safety concerns and the

non-satisfying cycling performance of Li metal anodes led to the investigation of alternative anode materials.

1.2.4.2 Carbonaceous materials:

Carbonaceous materials as negative electrodes exhibit several advantages such as high ionic/electrical conductivity, low cost, abundance and decent thermal/mechanical properties. The most applied Li-ion anode material is graphite. Graphite consists of graphene layers stabilized by van-der-Waals forces and π-π interactions of delocalized electron orbitals. Each monolayer of graphene is composed of sp^2 carbons that are bonded in a hexagonal arrangement extending in the 2D plane. During lithiation (charge of the full-cell), the lithium ions enter the plane that is perpendicular to the graphite layer and intercalate between the graphite sheets to give LiC_6 (Figure 1-9). The complete conversion to LiC_6 contributes to a theoretical capacity of 372 mAh g^{-1} and leads to a small expansion (~ 10 %) of the structure. The stability of the electrolyte towards the graphite anode is achieved by the formation of an SEI layer during the initial charge. Besides preventing continuous electrolyte decomposition, the SEI layer stops the co-intercalation of solvent molecules in the graphite structure. Unfortunately, the formation of the protective SEI layer leads to a 10 – 20 % irreversible capacity loss. An additional drawback of the graphite anode is the inability to charge at high C-rates. Charging the graphite anode with rates exceeding 1C results in capacity reduction and safety hazards. As the lithium intercalation potential is very close to the Li plating potential (0 V vs Li/Li^+), the overpotentials associated with the high rate charging process may reduce the intercalation potential below the critical 0 V and thereby induce dendrite formation. Research efforts focus on reducing the resistance of the graphite anode to lower the overpotential at higher C-rates.[20, 49] For example, Cai et al.[50] coated a nanoscale carbon layer on a graphite anode and showed that the carbon layer significantly improved the Li^+ diffusion rate, which as a result enhanced the rate capability. Besides graphite, disordered carbons (e.g., soft/hard carbon) find application as anode materials in Li-ion batteries. Compared to graphite, hard carbons exhibit higher theoretical capacity and better rate performance but suffer from higher irreversible capacity loss, higher voltage hysteresis and lower packaging density.[51-52]

Figure 1-9: Schematic illustration of the intercalation of lithium ions between the graphite sheets (reprinted with permission from ref.[53]).

1.2.4.3 Lithium titanate (LTO):

The spinel lithium titanate (LTO) is a commercial anode material. As visible in the following chemical equation, one mole of LTO can intercalate three moles of lithium ions resulting in a theoretical capacity of 175 mAh g^{-1}.

$$Li_4Ti_5O_{12} + 3\ Li^+ + 3\ e^- \rightleftharpoons Li_7Ti_5O_{12}$$

The main advantages of LTO are its low cost, high safety, excellent electrochemical stability and the occurrence of almost no volume changes during cycling. Due to the relatively high charge-discharge potential (~ 1.6 V vs Li/Li^+, Figure 1-10), the LTO anode is stable against the electrolyte and harmful lithium plating is evaded. However, due to the lower capacity and relatively high (de)lithiation potential relative to carbon-based anode materials, LTO is rather irrelevant for applications where high energy densities are required (e.g., EV batteries). In addition, the preparation of nano-sized LTO is needed to achieve high (dis)charge rates as the ionic/electrical conductivity of pristine LTO is rather low (Figure 1-10).[54-55]

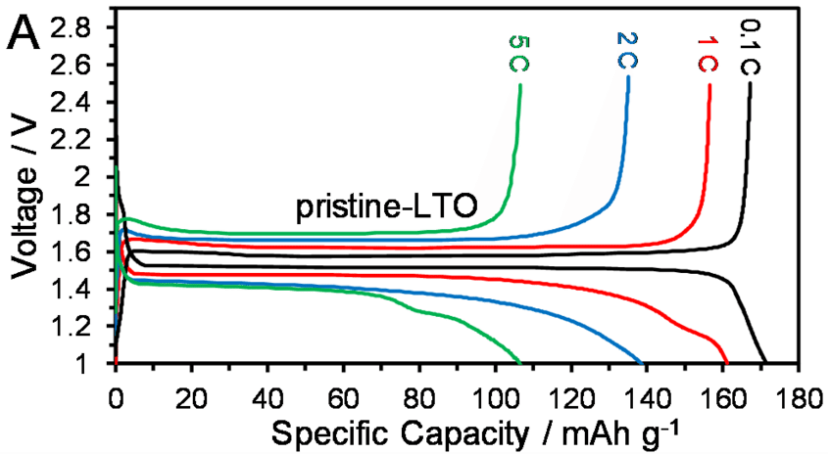

Figure 1-10: Typical voltage profile of LTO measured at various C-rates (0.1 C – 5 C) (reprinted with permission from ref.[56]).

1.2.4.4 Silicon-based materials:

Silicon, which has a ten times higher theoretical capacity than graphite, gained tremendous research interest in both academics and industry.[57] At low potentials, Si forms an alloy with lithium. Figure 1-11 shows the lithiation (1st and 2nd cycle) and delithiation (1st cycle) curves of a Si anode.

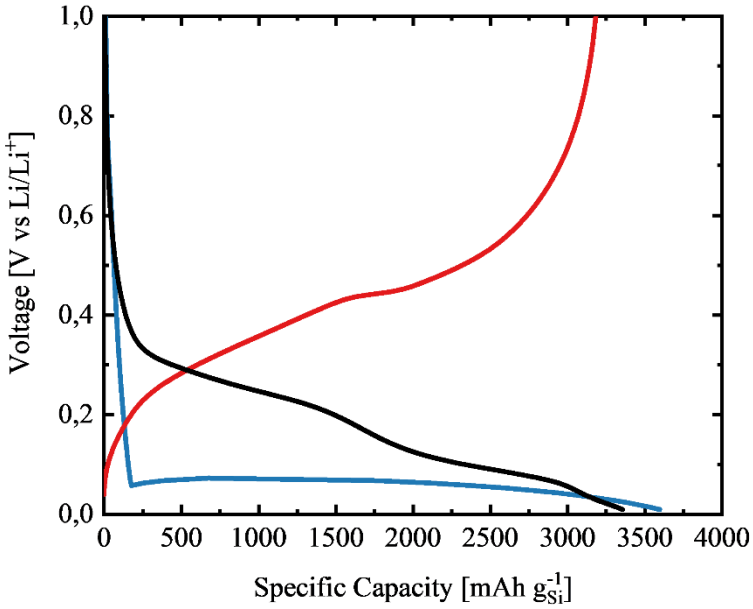

Figure 1-11: 1st cycle lithiation (blue), 1st delithiation (red) and 2nd cycle lithiation (black) curve of a Si anode at room temperature.

During the first lithiation (blue line), a two-phase region (flat plateau) is visible corresponding to the conversion of crystalline silicon to partially lithiated amorphous silicon. Below 50 mV the crystallization of the amorphous silicon to $Li_{15}Si_4$ occurs. At room temperature, $Li_{15}Si_4$ is the fully lithiated phase of Si, corresponding to a theoretical specific capacity of 3579 mAh g^{-1}. During delithiation (red line), the potential increases quickly to 0.4 V. Then a single flat plateau is visible, which corresponds to the conversion of $Li_{15}Si_4$ back to amorphous silicon. In the second lithiation cycle (black line), three sloping plateaus can be observed. At the second and during the following lithiation cycles, amorphous silicon is lithiated and the $Li_{15}Si_4$ phase forms again when the potential is below 50 mV.[58-59] Compared to graphite and LTO, Si exhibits the more attractive operating voltage (~ 0.2 – 0.4 V vs Li/Li^+) as the potential is high enough to prevent lithium plating while still being low enough to avoid an energy density penalty. Additional merits include the abundance and low cost of silicon as well as the already well-developed Si processing infrastructure. Unfortunately, the alloying process is accompanied by severe volume changes. During the lithiation, the volume of the Si

particles expands by ~ 280 % (for $Li_{15}Si_4$). The huge mechanical stress generated throughout the repeated (de)lithiation cycles leads to severe repercussions. Cracking and pulverization of active particles induced by the large volume changes result in the disconnection of the Si particles from the conductive matrix (Figure 1-12). The electrical isolation of particles strongly increases the internal resistance and results in irreversible capacity loss as the isolated particles are not electrochemical addressable. The low intrinsic electrical conductivity of Si makes this effect even more severe. Due to the continuous volume changes, Si anodes are not able to form a stable SEI layer. The repeated SEI breakage-reformation process causes ongoing electrolyte decomposition and irreversible consumption of lithium ions. In addition, the continuous growth of the non-electrically conductive SEI layer further reduces the electrical conductivity between the particles.[60-61]

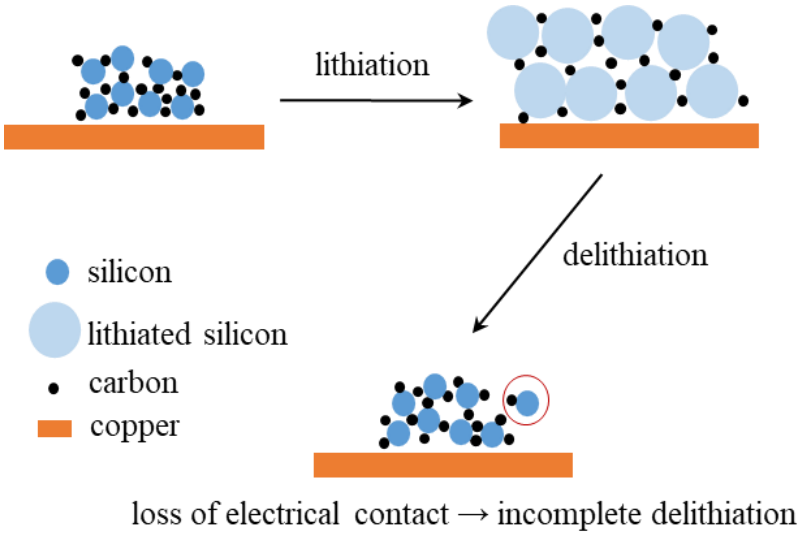

Figure 1-12: Schematic illustration of particle isolation occurring during cycling.

To restrict the volume changes, several approaches have been developed. Most applied are the following strategies: (i) Si composites: a composite matrix into which Si particles are dispersed is used to accommodate the volume expansion. To maintain ionic and electrical contact between the particles, the composite matrix must be highly conductive for electrons and ions. Most filling materials are carbon-based as carbon materials are cheap and exhibit high electrical conductivity. For example, Si/graphite composites are widely applied as graphite is low in price and the composite can easily be prepared by well-known processes.[62-63] (ii) Particle size control: several studies showed that reducing the Si particle size to nanometer range (< 150 nm) significantly enhances the cycling performance.[64-65] As can be observed in Figure 1-13, the boost in cycling ability can be

attributed to the higher tendency of large particles (< 150 nm) to crack.[66-67] In addition, particle size reduction lowers the transport distance of ions and electrons, which in turn positively affects the rate capability.[68] (iii) Voltage limitation: capacity fading of alloy materials can be reduced by restricting the upper or lower cutoff voltage.[69-70] For example, it has been shown that setting the Si lithiation potential above 50 mV strongly enhances the cycling life of a silicon anode. By increasing the lower cutoff voltage, the high stress induced by the sudden conversion of lithiated amorphous Si into the crystalline $Li_{15}S_4$ phase is prevented.[58] Nevertheless, shortening the voltage window is accompanied by a capacity reduction. (iv) Particle functionalization: several researchers proved that coating Si particles with a protective shell or encapsulating Si in a carbon matrix strongly improves the cycling ability. [71-72] Since these tests were mostly conducted in laboratory-type cells with high electrolyte amounts, applicability in practical cells still needs to be proved. (v) Electrolyte additives: to prevent ongoing SEI breakage/reformation, an electrolyte additive is needed that facilitates the formation of a flexible SEI layer. For instance, a heavily investigated and commonly applied additive for Si-containing anodes is FEC.[57] According to a study conducted by Jung et al.,[73] decomposition of FEC leads to the formation of a crosslinked lithium-conductive polymer. (vi) Additional research efforts focus on designing polymeric binders, which are capable of buffering large volume changes.

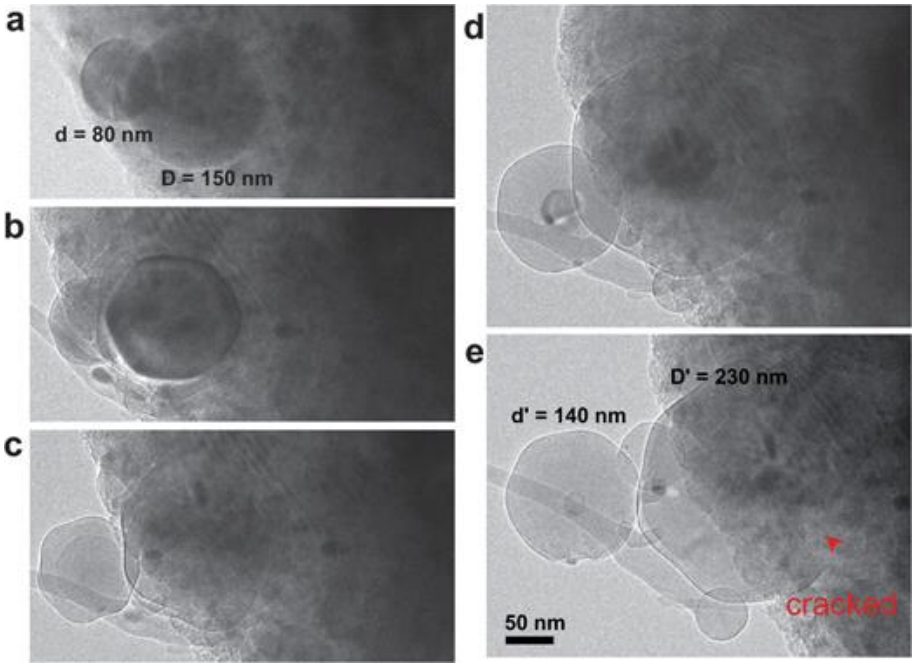

Figure 1-13: Expansion behavior of Si nanoparticles (SiNPs) with two different diameters (80 nm and 150 nm) during lithiation (a-e) (reprinted with permission from ref.[67]).

Silicon oxide (SiO_x, $0 < x \leq 2$) was recently introduced as a potential replacement for elemental Si. Applied silicon oxides include silicon monoxide (SiO), silicon dioxide (SiO_2), silicon oxycarbide (Si-O-C) and non-stoichiometric SiO_x. Compared to Si, silicon oxide is cheaper, easier to synthesize and possesses a lower volume expansion (~ 118 % for SiO_x vs ≥ 300 % for Si).[74-75] Depending on the oxygen content in SiO_x, the specific capacity, capacity retention and voltage hysteresis can be adjusted. For example, a high oxygen content enhances cycle life and results in a high voltage hysteresis but reduces rate capability and initial Coulombic efficiency.[75,76] Nowadays, blend materials of SiO_x ($x \leq 1$) and graphite with low SiO_x contents (lower than 10 wt.%) are commercially applied in Li-ion batteries.[77]

1.2.5 State-of-the-Art Binders for Si Anodes

In a battery electrode, the binder is utilized to tightly glue active material, conductive carbon and current collector together. In order to avoid a negative effect on cycling performance, the binder must be electrochemically stable, prevent particle agglomeration and must ensure strong binding and good adhesion to both the electrode materials and the current collector.[78] Besides these properties, a binder applied for Si anodes must be able to buffer large volume changes.[79] Table 1-5 shows the electrochemical performance of Si anodes prepared with different binder systems.

Table 1-5: Capacity retention of Si anodes with various binders (based on Ref.[80]).

Binder	**Binder content [wt.%]**	**Capacity retention**
PVdF	8	>600 mAh g^{-1} after 50 cycles at 150 mA g^{-1}
CMC	15	2373 mAh g^{-1} after 55 cycles at 0.2C
PAA	15	~ 3100 mAh g^{-1} after 20 cycles at C/20
Na-alginate	19	1822 mAh g^{-1} after 120 cycles at 420 mA g^{-1}
PAA-PVA	20	2283 mAh g^{-1} after 100 cycles at 400 mA g^{-1}
PAA-CMC	20	~2100 mAh g^{-1} after 100 cycles at 300 mA g^{-1}

The capability of a polymeric binder to accommodate the mechanical stress induced by the volume changes depends on its tensile strength, flexibility and elasticity. In addition, it has been shown that electrostatic interactions and covalent bonds between the functional groups of the binder and the Si-OH bonds on the Si surface further assist in

mitigating the volume expansion of the Si particles.[79] Many researchers have reported that the cycle performance of Si anodes prepared with PVdF, which is traditionally applied as a binder for many LIB active materials, is rather poor. The non-existence of functional groups that can interact with the Si particles within the PVdF structure is often described as the reason for the poor electrochemical performance of PVdF-based Si anodes.[81-82] This led to the investigation of many different synthetic and nature-derived binder systems with polar functionalities. For instance, Hochgatterer et al.[83] applied CMC as a binder and found that Si-OH surface groups form a covalent bond with the carboxyl groups of CMC. They claimed that the binder's chemical interaction with Si is important to obtain long cycling life and not necessarily its mechanical properties. Similarly, Komaba et al.[84] reported that Si anodes prepared with sodium polyacrylate (NaPAA) showed superior performance compared to PVdF-based anodes. Hence, the presence of functional groups (e.g., carboxylate, hydroxyl, amide) in the polymer is crucial for obtaining sufficient cycling performance. Besides CMC and NaPAA, other linear binders with polar moieties such as Na-alginate[85], chitosan[86], poly(vinyl alcohol)[87] and guar gum[88] have been investigated.

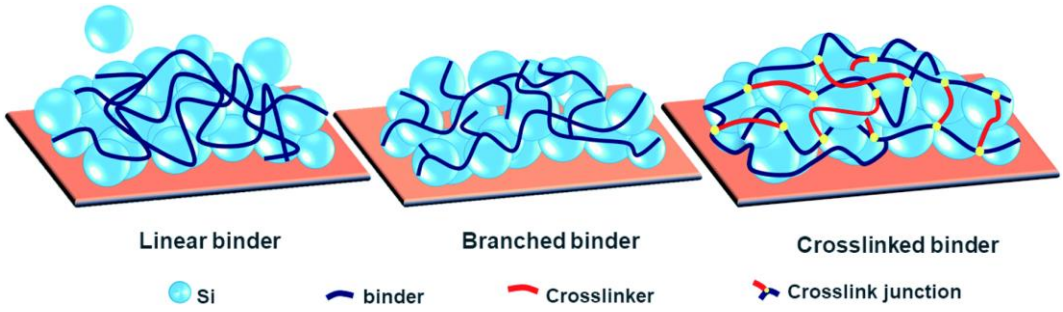

Figure 1-14: Schematic illustration of different binder types (linear, branched and cross-linked) and their response to the volume expansion of Si particles (reprinted with permission from ref.[89]).

Nevertheless, the one-dimensional interaction of the above-described linear binders with the active material is insufficient to compensate for the severe volume changes. To introduce additional contact points between the binder and the Si particles, grafted polymers have been examined.[89,90] For example, Wei et al.[91] prepared NaPAA-grafted CMC by grafting acrylic acid onto the CMC backbone. The Si anodes prepared with NaPAA-g-CMC polymer possessed a far superior cycling performance than those made from PAA and CMC binders. However, even with branched binders the slippage of polymer chains still occurs upon expansion of the Si particles. Binders with a 3D network structure formed by multiple interchain connections between the polymer chains have been introduced to further enhance mechanical integrity.[89] Figure 1-14 illustrates the

distinctions between different binder types (linear, branched and cross-linked) and their response to the volume expansion of Si particles. Generally, 3D interconnected polymer binders are either cross-linked by covalent bonds or dynamic interactions (e.g., hydrogen bonding, metal ion coordination).[90] Covalent cross-linking between binder chains are mostly constructed by a thermal- or light-induced esterification reaction. For instance, Koo et al.[92] prepared Si anodes with a crosslinked PAA/CMC binder. The in-situ cross-linking reaction was conducted by heating the electrodes at 150 °C under vacuum. As visible in Figure 1-15, the PAA/CMC-based electrodes exhibited superior capacity retention and rate capability compared to Si anodes prepared with linear PVdF and PAA binders. A similar approach was followed by Wang and coworkers[93]. They prepared a cross-linked PVA-PAA binder system and further demonstrated that the usage of a 3D-network binder is beneficial for the electrochemical performance of Si anodes. Cross-linked binders for Si anodes have also been fabricated by reacting -OH with anhydride, boronic acid and sulfonic acid groups. In addition to esterification reactions, Schiff base reactions between $-NH_2$ and -CHO as well as reactions involving epoxy and -OH or $-NH_2$ groups have been used to prepare 3D structured binders.[90] For instance, Lee et al.[94] prepared a cross-linked binder for SiNP-based anodes by cross-linking poly(ethylene glycol diglycidyl ether) and CMC. The electrode with their binder system showed improved adhesion and long-term cyclability (2000 mAh g_{Si}^{-1} after 350 cycles) compared to electrodes fabricated with CMC. Cross-linked binder systems can also be prepared by combining a polymer with a cross-linking agent. For example, Wang et al.[95] demonstrated that a cross-linked binder can be obtained by adding borax to a PAA-based electrode slurry. The 3D network of the PAA-borax binder is formed by a condensation reaction between the carboxyl groups of PAA and the hydroxy groups in borax. By using the PAA-borax binder, the capacity retention of SiNPs was increased by more than 30 % relative to the PAA-based Si samples. An alternative approach to fabricate a 3D binder network is to in situ polymerize cross-linkable monomers. Woo et al.[96] fabricated a cross-linked binder by in situ polymerizing acrylamide (AM) in presence of *N*,*N*-methylenebisacrylamide (MBAA). The degree of cross-linking in the synthesized poly(acryl amide) hydrogel was controlled by varying the AM to MBAA ratio. Compared to linear poly(acryl amide) (PAM), the cross-linked PAM hydrogel exhibited improved adhesion, better stretchability and superior capacity retention (up to 90 % after 100 cycles).

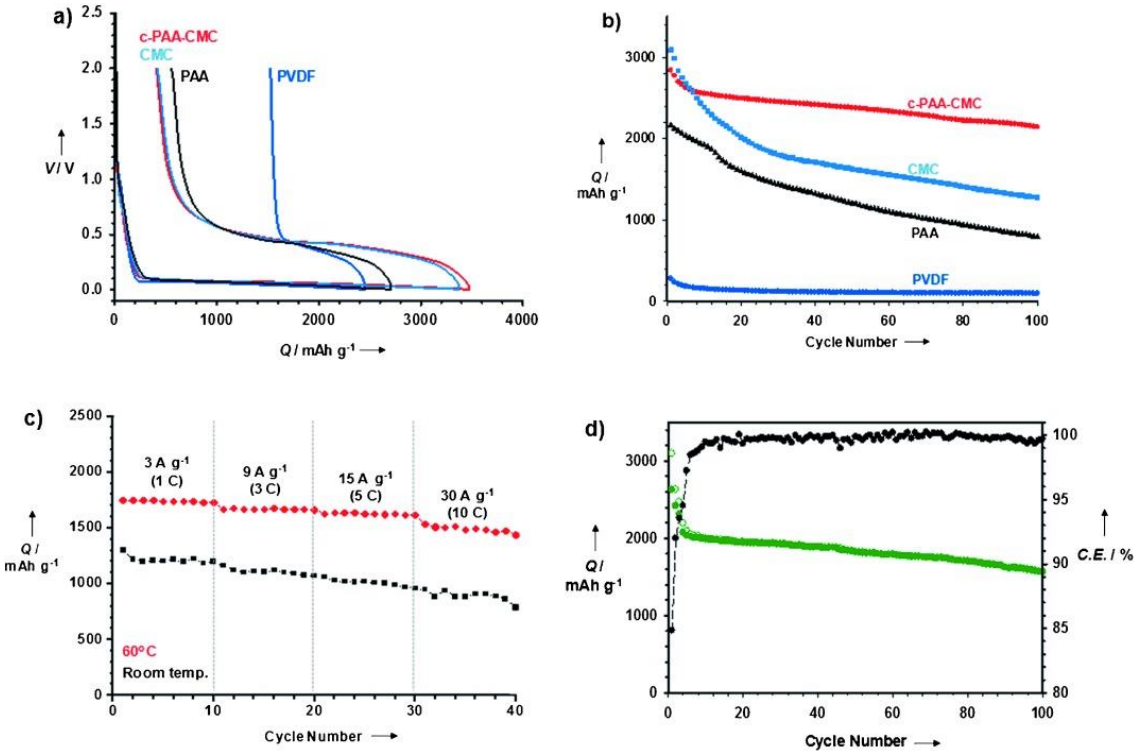

Figure 1-15: Electrochemical performance of the c-PAA-CMC-based Si anodes compared to Si anodes prepared with various linear binders (PAA, CMC, PVdF) (reprinted with permission from ref.[92]).

1.3 The Lithium-Sulfur Battery

Lithium-Sulfur (Li-S) batteries were first discovered in the 1960s. However, it took almost 50 more years until the battery society noticed the potential of the Li-S battery for energy storage applications. The increasing demand for cheap and sustainable batteries as well as a breakthrough by Nazar and coworkers[97] revived the development of Li-S batteries in recent years. The biggest merit of the Li-S battery is the more than five times greater theoretical specific capacity of sulfur (1675 mAh g^{-1}) relative to traditional Li-ion cathode materials (e.g., 280 mAh g^{-1} for NMC). This enables a practical energy density of up to 500 Wh kg^{-1} for a 4 mAh cm^{-2} pouch cell with a sulfur content of 70 wt.%, which is two to three times higher than the gravimetric energy density of commercial Li-ion batteries. Additionally, sulfur as a raw material is abundant, eco-friendly and low in price. These characteristics make the Li-S battery appealing for a broad range of energy storage applications.[98] In the following sections, the working principle of the Li-S battery, complications of the system and possible solutions to solve these issues will be summarized. Special focus will be laid on cathode materials, electrolytes and binders.

1.3.1 Working Principle

In a Li-S cell, metallic lithium is the negative electrode while sulfur is applied as the positive electrode. As current collectors' copper and aluminum are commonly applied on the negative and positive electrodes, respectively. Figure 1-16 illustrates a Li-S battery during discharge. After cell assembly, the cell is in its charged state when a sulfur-based cathode is used. Upon discharge, lithium is oxidized on the anode forming Li^+ ions and electrons. The produced Li^+ ions move through the electrolyte while the electrons flow over the external electric circuit from the negative to the positive electrode. At the positive electrode, sulfur is reduced by the uptake of electrons and lithium ions. During discharge, the following reactions take place while the reverse reaction processes occur during charge:[99]

Negative electrode: $16\ Li \rightarrow 16\ Li^+ + 16\ e^-$

Positive electrode: $S_8 + 16\ Li^+ + 16\ e^- \rightarrow 8\ Li_2S$

Overall reaction: $16\ Li + S_8 \rightarrow 8\ Li_2S$

The reduction of sulfur to lithium sulfide (Li_2S) is a multistep process that involves several intermediate species. These intermediates are lithium polysulfides with the general composition of Li_2S_x. In general, the discharge process begins with the formation

of long-chained polysulfides (Li_2S_x with $x \leq 4$) and continues with the reduction of long-chained polysulfides to short-chained polysulfides (Li_2S_x with $x \geq 4$). Once the final discharge products (Li_2S or Li_2S_2) are formed, the reduction process is completed.[100]

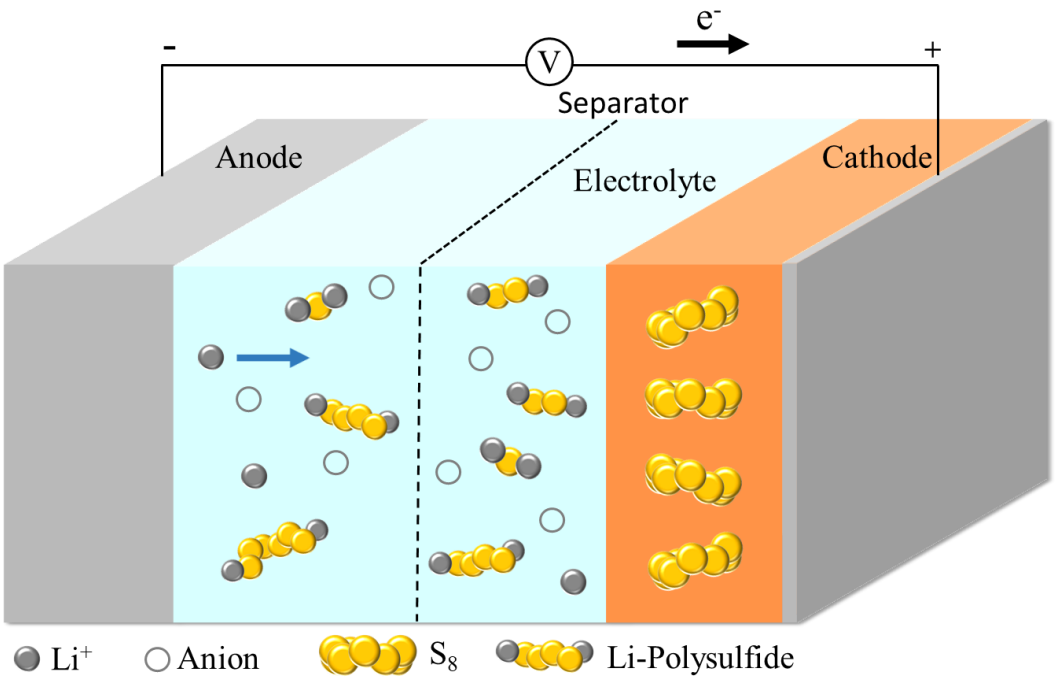

Figure 1-16: Schematic illustration of a Li-S battery cell during discharge.

The used electrolyte solvent determines which specific polysulfide species are formed. Commonly applied as electrolyte solvents are mixtures of tetraethylene glycol and dimethyl ether as well as mixtures of 1,3-dioxolane (DOL) and 1,2-dimethoxyethane (DME). Dimethyl sulfoxide (DMSO) and dimethyl formamide (DMF) are also used as electrolyte solvents.[101-102] Generally, the ability of a solvent to stabilize charged species depends on its dielectric constant. In electrolyte solvents that possess high dielectric constants such as DMSO and DMF, multiple polysulfide species (S_8^{2-}, S_6^{2-}, S_4^{2-} and $S_3^{\cdot-}$) are formed. While in electrolytes that contain solvents with low dielectric constants such as DOL:DME, simpler reaction pathways occur with S_4^{-2} as the main polysulfide species.[103]

In Figure 1-17, a discharge curve of a Li-S cell with a carbon/S-composite electrode in a DOL:DME-based electrolyte is depicted. The potential curve can be divided into four distinct reduction regions.[104]

(I): Between 2.4 – 2.2 V a two-phase reduction from S_8 to Li_2S_8, which is visible as the first reduction plateau, occurs. The produced liquid Li_2S_8 dissolves into the liquid electrolyte.

(II): In this region, a single-phase reduction from Li_2S_8 to shorter-chained polysulfides takes place. The potential sharply decreases during this reduction process.

(III): During the second plateau (2.1 – 2.0 V), various disproportion reactions involving Li_2S_4 as the dominant species occur, which end in the formation of Li_2S_2 or Li_2S. This region contributes to most of the cell´s capacity.

(IV): The remaining insoluble Li_2S_2 is reduced in a solid-solid reduction to Li_2S. Since Li_2S_2 is insoluble and non-conductive, mostly a mixture of Li_2S_2 and Li_2S remains as the final discharge product.

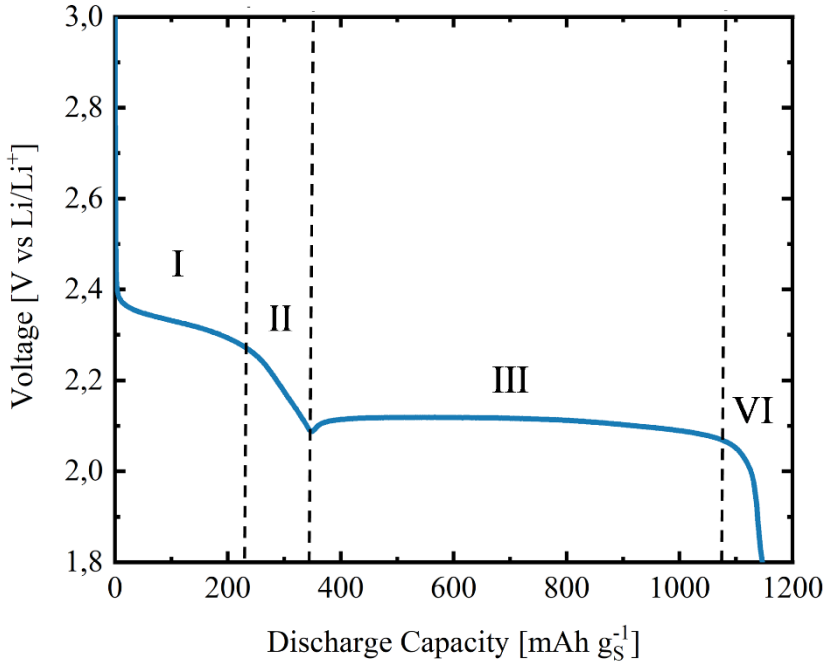

Figure 1-17: Discharge curve of a Li-S cell with a carbon/S-composite electrode (4 mAh cm^{-2}) at C/10 (based on Ref.[105]).

1.3.2 Key Challenges of Li-S Batteries

Despite the above mentioned merits, the Li-S battery suffers from several complications, which lead to low active material utilization, severe capacity fading and unsatisfying cycle life.[8]

Sulfur itself exhibits poor electrical and ionic conductivity. That´s why the usage of pure sulfur as an active material would result in low sulfur utilization and insufficient rate

capability. Hence, the addition of a large amount of conductive carbon additive is required to obtain a satisfactory conductive network. The relatively high amount of conductive additive in the cathode (up to 20 – 30 %, compared to 2 – 4 % in LIBs) reduces the obtainable energy density and creates a porous structure, which is prone to collapse during ongoing sulfur dissolution and deposition. To increase the ionic conductivity, electrolytes that possess high polysulfide solubility are used.[106]

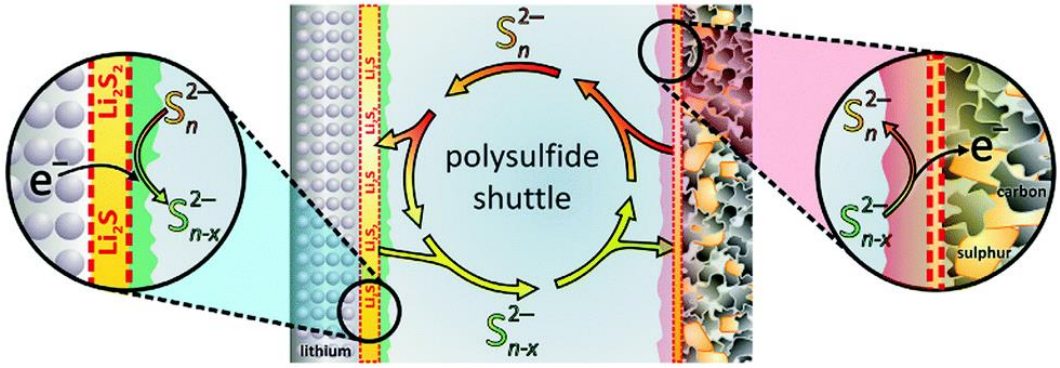

Figure 1-18: Schematic illustration of the polysulfide shuttle (reprinted with permission from ref.[107]).

Unfortunately, the high solubility of polysulfides in the electrolyte facilitates capacity loss from the sulfur cathode and creates another well-known challenge for Li-S batteries. The ongoing reduction of polysulfides on the Li anode and the re-oxidation on the S cathode during charging creates an internal shuttle phenomenon. This so-called polysulfide shuttle reduces the cell´s Coulombic efficiency and facilitates the formation of a passivation layer (Li_2S) on the Li anode (Figure 1-18).[108] Efforts to reduce polysulfide shuttling include the usage of non-active materials in the S cathode (see section 1.3.4) or the usage of separators that anchor polysulfides and thereby prevent the polysulfide diffusion to the Li anode. In addition, the application of active materials consisting of covalently bonded sulfur inhibits the formation of soluble polysulfides in the first place.[109-111] By applying these methods, academic researchers have achieved promising results in laboratory-type cells such as a long-life span with more than 1000 cycles and high rate capability. Nevertheless, practical pouch cells with low electrolyte amounts and carbon materials that are suitable for large-scale production have only achieved low cycling performance. Therefore, the applicability of the Li-S battery in commercial cells still needs to be proven.[112-113]

Since S_8 (2.03 g cm^{-3}) exhibits a higher density than Li_2S (1.66 g cm^{-3}), the active material expands during discharge (up to 80 %). The ongoing volume changes occurring during (dis)charging can cause active material pulverization and thus induce capacity fading.[112,

[114] Another performance limiting factor is the lithium anode itself. As explained earlier, the very low reduction potential of lithium and the inability to form a stable SEI on its surface lead to severe electrolyte degradation. Many researchers focus on developing a protective film on the lithium surface, which prevents contact with the bulk electrolyte while being Li^+ ion conductive.[115-116] The replacement of lithium by e.g., graphite, silicon or tin has also been investigated. However, replacing lithium with less electronegative anode materials further decreases the already relatively low cell voltage of the Li-S battery (~ 2.1 V compared to ~ 3.8 V for Li-ion batteries).[8]

Despite the current challenges, the Li-S battery still is the most promising post-Li-ion technology for applications where a high gravimetric energy density is desired.

1.3.3 Electrolytes for Li-S Batteries

As the electrolyte strongly dictates the solubility of polysulfide intermediates, the electrolyte choice is crucial for the overall cell performance. On the one hand, effective polysulfide solvation facilitates fast reaction kinetics and high sulfur utilization, on the other hand, it enables the loss of active material and the polysulfide shuttle.[117] In contrast to Li-ion batteries, a smaller electrochemical stability widow is required for Li-S batteries. This allows the usage of ether-based electrolyte solvents and other electrolyte salts besides $LiPF_6$. For example, LiTFSI is the commonly applied salt in Li-S electrolytes. In contrast to $LiPF_6$, LiTFSI possess a higher ionic conductivity and does not form Lewis acids which decompose the solvents.[118-119]

The usage of carbonate-based electrolytes is inappropriate for most S cathodes as carbonates undergo a parasitic side reaction with polysulfide species. Gao et al.[120] conducted an X-ray absorption spectroscopy (XAS) measurement on a Li-S battery with a carbonate-based electrolyte solvent. They observed almost no obtainable capacity and proposed based on the in-situ XAS measurement that polysulfides undergo a nucleophilic addition or substitution with carbonates, which yields the formation of thiocarbonates. In 2013, Yim et al.[121] investigated the reaction of polysulfides with two commonly applied carbonate solvents (EC and ethylene methyl carbonate). In the case of EC, they proposed that EC reacts with high-ordered polysulfides via a nucleophilic substitution to form a ring-opened intermediate, which then undergoes a second nucleophilic substitution to form ethylene glycol and a thiocarbonate (Figure 1-19). Therefore, common Li-S electrolytes traditionally consist of ethers such DOL, DME or tetraethylene glycol dimethyl ether. For ether-based electrolytes, lithium nitrate ($LiNO_3$) is widely applied as

an additive. It forms a passivation layer on the Li anode and thereby significantly reduces the extent of the polysulfide shuttle.[122-123]

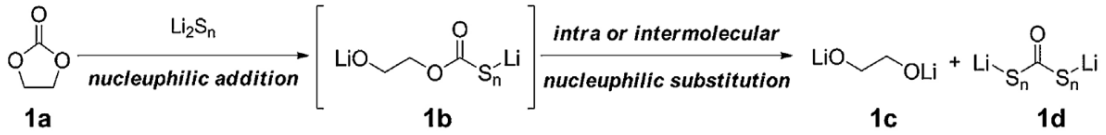

Figure 1-19: Proposed reaction mechanism of EC with high-ordered polysulfides (reprinted with permission from ref.[121]).

In addition to ethers, several ionic liquids and short-chained polyethylene glycol (PEG) have also been investigated as potential electrolyte solvents. Ionic liquids as electrolyte solvents exhibit several merits such as high ionic conductivity, non-flammability, wide electrochemical stability and non-volatility. Additionally, several groups have shown that ionic liquids possess reduced polysulfide solubility relative to common solvents, which hampers active material dissolution and polysulfide shuttling.[98,118] For example, Park et al.[124] used the ionic liquid *N*,*N*-diethyl-*N*-methyl-*N*-(2-methoxyethyl)ammonium bis((trifluoromethyl)sulfonyl)-amide ([DEME][TFSA]) as electrolyte solvent, which exhibited superior cycling stability compared to a TEGDME-based electrolyte. They revealed that the low donor ability owned to the low Lewis basicity of the [$TFSA^-$] anion decreased the polysulfide solubility. The suppressed polysulfide dissolution led to longer cycling life and better Coulombic efficiency.

Compared to liquid electrolytes, solid-state electrolytes can potentially more effectively reduce sulfur dissolution and lithium dendrite formation. Common solid-state electrolytes are based on polymers, ceramics or polymer/ceramic composites.[125-126] For example, Zhang et al.[127] used an all-solid-state electrolyte based on poly(ethylene oxide), which retained a reversible discharge capacity of 634 mAh g^{-1} after 100 cycles. However, until now the unsatisfying electrochemical characteristics of solid electrolytes such as low ionic conductivity especially at lower temperatures and interfacial instability prevent their widespread application.[98,125,128]

1.3.4 Cathode Materials

To enhance the low electrical conductivity of sulfur-based cathodes, researchers have focused on combining sulfur with materials that exhibit high electrical conductivity. The addition of conductive carbons and conductive polymers yields the formation of sulfur-carbon composites and sulfur-polymer composites, respectively.[129]

1.3.4.1 Carbon-based materials:

Most of the cathode materials applied in Li-S batteries are in some way based on carbon. In general, carbon materials enhance the electrical conductivity of the S cathode by forming a conductive carbon network as well as establishing intimate contact between the conductive matrix and the insulating sulfur particles. In addition, porous carbons can absorb sulfur species in their pores. Trapping polysulfide species in the pores of the carbon host reduces active material dissolution and restricts the polysulfide shuttle.[98,129]

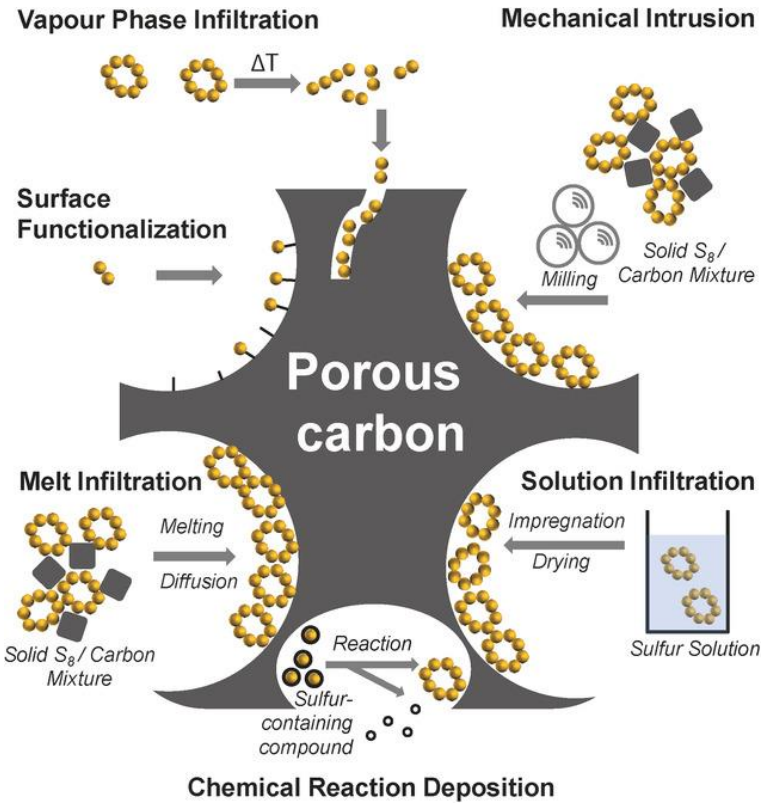

Figure 1-20: Commonly applied approaches for introducing sulfur into porous carbon materials (reprinted with permission from ref.[130]).

Commonly applied methods to combine sulfur with a carbon host are illustrated in Figure 1-20. The simplest approach to prepare carbon/sulfur composites is to mix carbon and sulfur under mechanical force (e.g., by ball milling or pestling). However, in carbon/sulfur composites prepared by mechanical intrusion the confinement effect of sulfur in the porous carbon matrix is rather poor. Melt infiltration is a technique that does not require complex equipment and is easily scalable. The melt infiltration of sulfur into carbon is carried out slightly above the melting point of sulfur (~ 120 °C), followed by an after-treatment at 300 °C to remove non-absorbed sulfur species. Vapor phase infiltration is conducted at 550 °C. At this temperature, smaller allotropes of sulfur (S_2 – S_4) are formed in the vapor phase that infiltrate into the pores of the carbon matrix. Since

the solubility of sulfur in organic substances is limited, solvent-aided infiltration can only be carried out in a small number of solvents (e.g., toluene, carbon disulfide). After the infiltration, the solvent is evaporated and needs to be recycled to ensure the sustainability of the process. Chemical reaction deposition avoids the usage of organic solvents as many sulfur-containing precursor compounds are water-soluble. In this process, liquid sulfur precursors infiltrate the pores and are oxidized to elemental sulfur in a subsequent reaction step. An example of the in situ formation of sulfur is the reaction between sodium thiosulfate and hydrochloric acid in an aqueous solution.[130,131]

To minimize the resistance of the cathode and to achieve full active material utilization, the sulfur must be packed as tight as possible in the pores of the carbon material. Therefore, the pore size (D) as well as the morphology of the carbon strongly affect the electrochemical properties of the resulting cathode material. In the following paragraphs, some of the predominantly used carbon materials will be introduced.[98]

C/S composite derived from porous carbons can be classified according to their pore size as microporous, mesoporous and macroporous. Microporous carbon materials ($D < 2$ nm) exhibit excellent cycling stability. The long cycling life is caused by the strong polysulfide adsorption within the narrow pores. Xin et al.[132] showed that due to the limited space in the small pores (≤ 0.5 nm) predominantly short-chained polysulfides are formed ($S_{2\text{-}4}^{2-}$). The absence of the transition from S_8^{2-} to S_4^{2-} prevents active material dissolution and the formation of the polysulfide shuttle. In addition, Li et al.[133] demonstrated the ability to cycle a microporous carbon-based ($D = 0.46$ nm) sulfur cathode in a carbonate-based electrolyte. Since the pore diameter of their carbon material was well below the theoretically calculated diameter of common carbonates (e.g., 0.57 nm and 0.79 nm for EC and DMC), they concluded that the (de)lithiation reactions inside a micropore must occur as a solid-solid process. Unfortunately, the sulfur uptake of microporous carbon materials is limited to less than 40 wt.%.[130,134] Mesoporous carbon materials ($2\text{ nm} < D < 50$ nm) can encapsulate sulfur and enhance Li^+ transport. Compared to microporous carbons, mesoporous carbon materials tolerate higher sulfur loadings as the fillable pore size is larger. C/S composites prepared with mesoporous carbons possess an excellent initial capacity and decent capacity retention. In macropores ($D > 50$ nm), the electrical contact between the encapsulated sulfur is quite low, which potentially leads to an incomplete discharge. However, microporous carbon materials exhibit very good electrolyte absorbability, which reduces polysulfide migration. It has been shown that

combining different pore structures in one carbon material can be beneficial for the electrochemical properties of the resulting C/S composite.[98,135] For example, Liang et al.[136] achieved high sulfur loading while maintaining good electrochemical performance by immobilizing sulfur into a bimodal porous carbon with hierarchically structured meso/microporosity.

Carbon nanotubes (CNTs), which have a one-dimension elongated structure were first used by Han et al.[137] as a conductive additive in a sulfur-based cathode. Since then, several groups have utilized CNT/S composites as cathode materials. Generally, CNTs exhibit excellent electrical conductivity and stable mechanical properties. However, as the sulfur is immobilized on the outer surface of the carbon nanotubes, additional treatment is needed to prevent sulfur dissolution. For example, introducing pores or holes to the walls of the CNTs enables the active material to infiltrate the interior of the CNTs and thereby restrict the formation of soluble polysulfides. Another method to reduce sulfur dissolution is to functionalize the carbon host (e.g., by nitrogen doping), which promotes the adsorption of polysulfides.[130,138,139]

Graphene is a 2D carbon monolayer that is ultralight and exhibits exceptional electrical conductivity. Wang et al.[140] used a graphene/S composite, which was prepared by melt infiltration, as a sulfur-based cathode. Their cathode material had a high initial discharge capacity but suffered from severe capacity fading. To obtain satisfactory capacity retention, protective polymer layers are usually coated onto the graphene/S composites. Additionally, several groups showed that by functionalizing graphene or by replacing graphene with graphene oxide the capacity retention of the graphene-based sulfur cathodes can be strongly enhanced.[98,141]

Due to the low cost and high abundance of carbon nanoparticles such as carbon black, the application of carbon black/S composites is of high commercial interest. As the sulfur is immobilized on the exterior surface of the carbon particles, the sulfur shell thickness grows with increasing sulfur loading. This leads to homogeneous sulfur distribution as well as high S/C ratios. Unfortunately, the lack of sulfur confinement and the reduction of the electrical conductivity of the carbon particles by the sulfur layer leads to low sulfur addressability and capacity fading. These issues can be overcome by utilizing carbon hollow spheres as carbon host materials. The void space within the conductive carbon shell ensures high electrical conductivity and restricts the dissolution of active material in the electrolyte. [130,134]

1.3.4.2 Sulfur-Polymer composites:

Polymers are not only applied as binders or barriers for blocking polysulfides. To reduce polysulfide dissolution and enhance sulfur utilization, several sulfur-polymer composites have been synthesized and used as cathode materials. In contrast to C/S composites, the sulfur in most sulfur-polymer composites is covalently bonded to the polymer backbone, which reduces active material dissolution and enables the usage of non-ether-based electrolytes. Common methods to prepare sulfur-polymer hybrid materials include copolymerization of suitable monomers and sulfur as well as heating a polymer in the presence of sulfur.[98,142]

The strategy of applying sulfur-polymers as active materials was initially presented by de Jonghe et al.[143] They tested a selection of polymers with disulfide linkage, which were prepared by oxidizing the corresponding di-/trithiol monomer with iodine, for usage as cathode materials in solid-state Li-S batteries. Evaluation of the electrochemical tests showed that the cells with 2,5-dimercapto-1,3,4-thiadiazole as active material exhibited the highest sulfur utilization (75 %) and longest cycle life (up to 83 cycles).

The vulcanization of rubber with sulfur as the co-reactant is a well-known process to alter the physical and chemical characteristics of rubber. During the thermal-induced reaction of sulfur with rubber, some C-H groups are replaced by sulfur chains and bridges are formed between the polysulfides.[144] This process has been adapted by battery material researchers to utilize polymer-sulfur composites with longer sulfur chains (S_x, $x>2$) as electroactive materials. Trofimov et al.[145-146] were the first to investigate sulfurized polymeric materials in Li-S cells. They reacted different polymers such as poly(styrene), poly(acetylene) and poly(vinylpyridine) with sulfur at elevated temperatures. The resulting sulfurized polymers had sulfur contents of up to 80 %. The cells with sulfurized poly(acetylene) as active material showed the best performance with a capacity higher than 400 mAh g_S^{-1}. Yang et al.[147] modified this approach and prepared a sulfurized polyyene-analogous electroactive material via the basic treatment of poly(vinylidene chloride) and subsequent heating in the presence of elemental sulfur. The resulting polymer (termed as carbyne polysulfide) had a sulfur content of 54 wt.% and cycled for 200 cycles in an ether-based electrolyte with a capacity greater than 800 mAh g_S^{-1}.

The most prominent representative of sulfur-polymer composites is sulfurized poly(acrylonitrile) (SPAN). SPAN was initially described as potential cathode material by Wang et al.[148] in 2002. They prepared SPAN by reacting poly(acrylonitrile) (PAN)

with sulfur at ~ 300 °C (Figure 1-21). The resulting composite contained 53 wt.% of sulfur and showed good electrochemical performance.

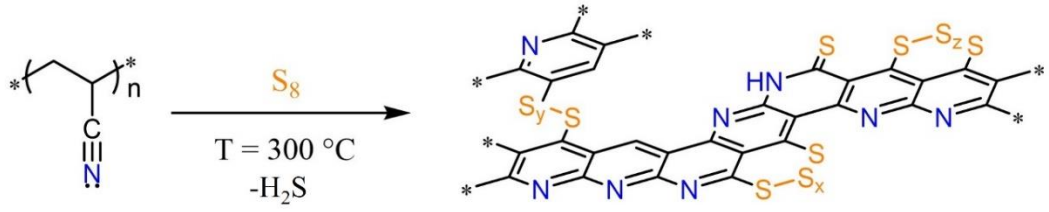

Figure 1-21: Reaction scheme and structure (as proposed by Fanous et al.[149]) of SPAN.

In a follow-up study, Wang et al.[150] cycled a SPAN material with 45 wt.% of sulfur in a gel-based electrolyte and reported a stable capacity of 1545 mAh g_S^{-1} over 50 cycles, which equaled to a remarkable sulfur utilization of 92 % relative to the theoretical capacity of sulfur.

Initially, it was assumed that the heterocyclic PAN served as a host for elemental sulfur. Later, this hypothesis was proven wrong by Yu et al.[151] By utilizing XPS and Raman spectroscopy, they proved the existence C-S and S-S bonds. They proposed that the obtainable capacity mainly stemmed from the cleavage and formation of S-S as well as the (de)intercalation of Li^+ ions in the cyclic-PAN backbone. Additionally, they demonstrated that increasing the annealing temperature enhances cycling stability. During the reaction, the triple bonds of the nitrile groups convert into C=N bonds and a cyclized ladder-structure polymer is formed. Additionally, the S-S bonds of S_8 break, which results in the formation of C-S and S-S bonds in the side chain of the cyclized PAN. The sulfur acts both as a mild oxidant to dehydrogenate PAN and a sulfurization agent.[152]

Buchmeiser and coworkers[149] further proved the existence of C-S and S-S bonds by detecting their related fragments with ToF-SIMS. They suggested that sulfur exclusively bounds to carbon by forming C-S_x-C, C=S and 2-pyridylthiolate groups (Figure 1-21).

Many groups have detected a strong relationship between the electrochemical performance of SPAN cathodes and the synthesis parameters such as reaction time, temperature, and pressure. For example, a higher synthesis temperature and longer reaction time resulted in lower sulfur content and better cycling stability.[149,153,154,155] The lower sulfur content and enhanced electrochemical performance likely result from the

formation of shorter sulfur chains and a higher degree of graphitization at elevated synthesis temperatures.[149]

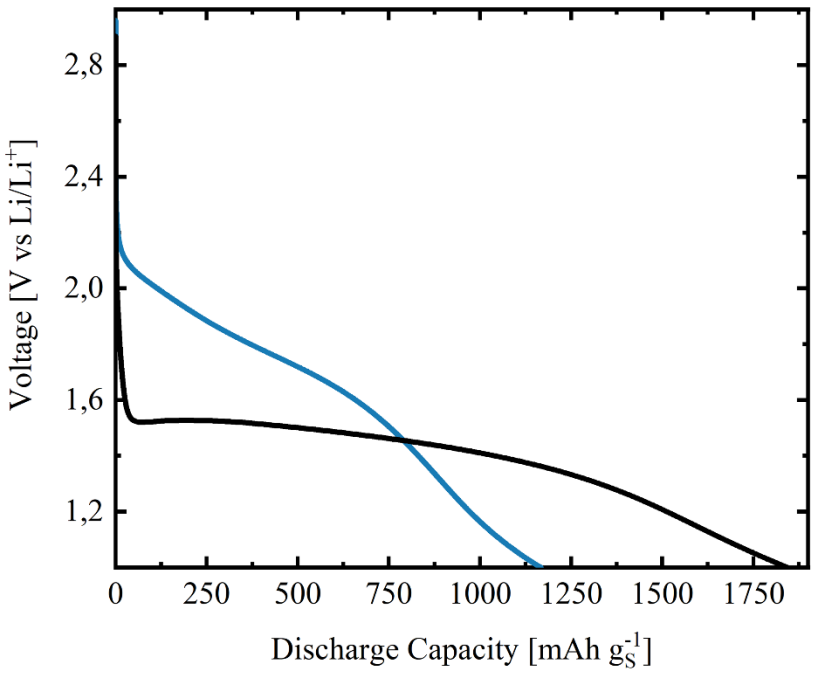

Figure 1-22: Discharge curve (1st (black) and 2nd (blue) cycle) of a Li-S cell with a SPAN electrode (~ 2.5 mAh cm^{-2}) at C/4.

Contrary to traditional C/S-composites-based cathodes, SPAN cathodes undergo a different (de)lithiation process. As can be seen by comparing Figures 1-17 and 1-22, the discharge curve of the SPAN cathodes shows a single one-step plateau whereas within the discharge profiles of traditional C/S-composites-based cathodes two distinct voltage plateaus (starting at ~ 2.4 V and ~ 2.1 V) are visible.[156] In 2019, Wang et al.[157] proved the existence of a solid-solid conversion mechanism and revealed Li_2S as the sole discharge product. Therefore, the absence of voltage plateaus during the (de)lithiation of SPAN cathodes can be attributed to the occurrence of a direct solid-solid conversion, which prevents the formation of soluble polysulfide intermediates. The non-existing formation of liquid polysulfide species enables the usage of carbonate-based electrolytes, which are standard in Li-ion batteries. As visible in Figure 1-22, the discharge capacity exceeds the theoretical capacity of sulfur (1675 mAh g^{-1}) in the first cycle. Zhang et al.[154] and Wei et al.[158] elucidated this effect and proposed that the excessive discharge capacity in the first cycle is caused by irreversible C-S bond cleavage as well as the irreversible storage of Li^+ ions in the cyclic-PAN backbone. Hence, the redox reaction of S-S bonds is the major source of reversible capacity in the subsequent cycles.

Additional research efforts with a focus on conductive additives, active material design and electrolyte optimization further improved the rate capability and cycle life of SPAN-based Li-S batteries. For instance, Wang et. al[157] increased the electrical conductivity of cathodes prepared with SPAN by in situ polymerizing or spray drying various conductive additives such as multiwalled carbon nano tubes, graphene microspheres or graphene oxide sheets in the cathode material. Yang et al.[159] demonstrated that using an electrolyte, which main component is the film-forming additive FEC, prevents dendrite formation and enables a Li/SPAN to cycle for up to 4000 cycles at C-rate of 6C. Buchmeiser and coworkers[160] presented a fiber-based SPAN composite with high sulfur content (44 wt.%) and excellent rate capability (up to 8 C). Their composite was prepared by utilizing a simple and cost-effective process with a PAN/PMMA (poly(methyl methacrylate) fiber blend as the raw material.

1.3.5 Binders for Li-S Batteries

In contrast to the strong focus of researchers on cathode design and electrolyte additives, less attention has been paid to improving non-active cathode components such as the binder. Although the amount of binder incorporated in an S cathode is low (typically less than 10 wt.%), several groups have shown that the binder strongly affects both capacity retention and rate capability. Besides ensuring close contact between the active material and conductive additive, as well as sufficient addition to the current collector, functional binders for S cathodes, can interact with polysulfides. They are capable of reducing active material dissolution by trapping soluble sulfur species or accelerating the redox reaction kinetics of polysulfides.[161,162] The chemical structures of typical binders that find application in Li-S batteries are summarized in Figure 1-23.

PVdF is commonly applied in most Li-ion cathode materials mainly due to its high thermal stability and broad electrochemical stability window. However, utilizing PVdF as a binder in S cathodes has been often described as problematic. PVdF can only interact via weak van-der-Walls interactions with the electrode materials and is incapable of buffering large volume changes. In S electrodes, the limited interaction between PVdF and sulfur can result in pulverization and detachment of the active material from the current collector. In addition, the preparation of PVdF-based electrodes involves the handling of NMP, which is a toxic and non-ecofriendly organic solvent.[162,163] As a result, a broad range of aqueous polymers such as poly(ethylene glycol) (PEO) and sodium alginate (Na-alginate) have been introduced as binders in sulfur cathodes. The utilization

of aqueous binders avoids the usage of organic solvents and reduces electrode slurry processing costs. In addition, the oxygen, nitrogen, and sulfur-containing functional groups, which exist in aqueous binders, can interact with active sulfur species and thereby likely reduce active material dissolution.[164] For instance, Manthiram and coworkers[165] prepared high-loading S cathodes (10 mg cm^{-2}) consisting of elemental sulfur, carbon and chitosan as the binder. Their cells exhibited remarkable capacity retention (91 % after 50 cycles). With the aid of UV-VIS measurements, they confirmed that the -NH_2 and -OH groups of chitosan firmly bind to the active sulfur species.

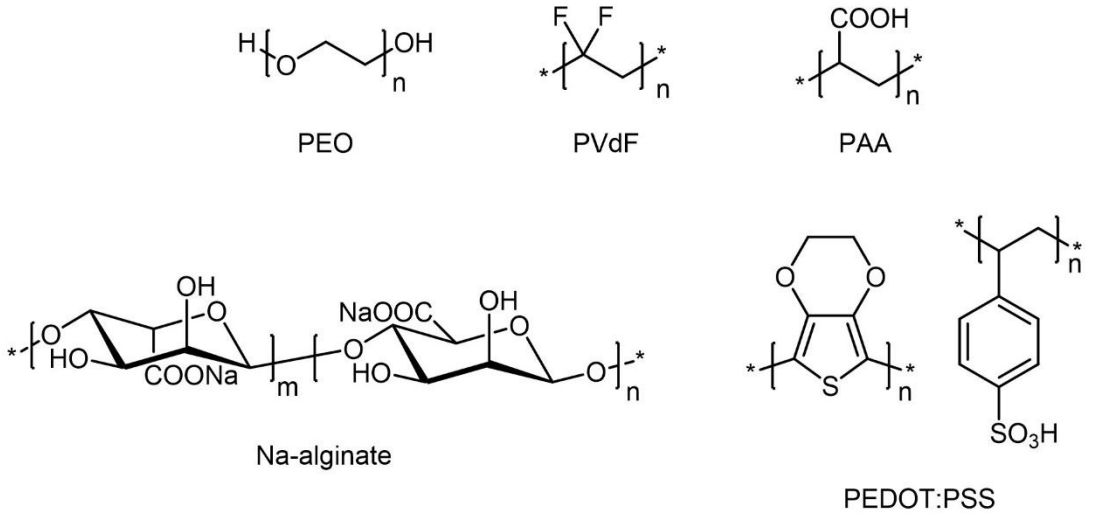

Figure 1-23: Chemical structures of commonly applied binders in Li-S batteries.

Similar observations have been made for SPAN cathodes. For example, Wang et al.[166] showed that cells with carbonyl-β-cyclodextrin as a water-soluble binder exhibit far superior electrochemical performance than cells prepared with PVdF. Kim et al.[167] compared the cycling characteristics of SPAN electrodes prepared with PAA and PVdF. Like Wang et al., they elucidated that the application of a more polar binder than PVdF is advantageous for adhesion, rate capability and cycling life.

In addition, polymers with special functionalities such as electrical conductivity or polysulfide regulation have been introduced as binders in S electrodes. For instance, the use of the conductive polymer poly(3,4-ethylenedioxythiophene) poly(styrene sulfonate) (PEDOT:PSS) as a binder reduces the electrical resistance of the electrode and accelerates the transfer of electrons.[168,169] Redox-active polymers such as poly(2,2,6,6-tetramethyl-1-piperidinyloxy-4-yl methacrylate) were further introduced as binders in S electrodes. They improve the redox kinetics of soluble polysulfides and thereby promote their

conversion to the final discharge products.[170] Nevertheless, these unique binder systems are mostly applied in laboratory-type cells as their synthesis is rather complex and costly.

1.4 Processing of Battery Electrodes

Besides the active material and the general electrode composition, the processing of battery electrodes is essential for achieving sufficient energy densities and performance. Hence, the underlying process steps must be carefully engineered. In recent years, significant energy density gains have been made by optimizing electrode processing parameters such as increasing the electrode loading or reducing the electrode density. Additionally, as the process contributes to the overall battery costs, the involved production steps must be carefully designed to achieve cost-effectiveness and high throughput.[171-173] In general, state-of-the-art manufacturing of LIB and most post-Li-ion (e.g., Li-S) battery electrodes include the following four processing steps: (i) mixing, (ii) coating, (iii) drying and (iv) calendering (Figure 1-24). In this section, these processing steps will be described in detail.

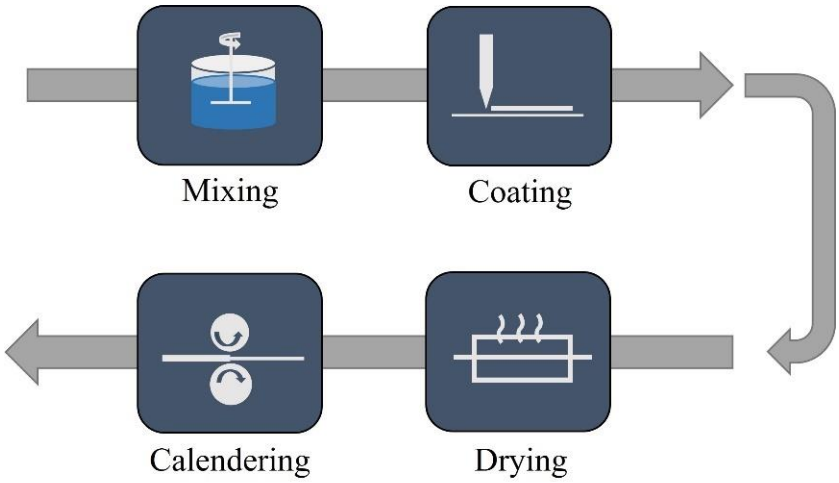

Figure 1-24: Schematic illustration of battery electrode processing.

In the first mixing step, the active material, binder and conductive additives are mixed with the help of a rotating tool in the dry state, followed by dispersing and mixing the dry mixture in a solvent. Depending on the active material water or an organic solvent (mostly NMP) is used as the dispersant. The mixing sequence and dispersing method strongly depend on the cell chemistry and must be wisely chosen to reach the performance targets. To ensure sufficient stability and processability of the slurry, its flow behavior is constantly monitored via rheology. In a commercial process, the produced slurry is transported to the following coating step in sealed storage tanks or by pipework.[171-172, 174,175]

The slurry is coated on a current collector foil utilizing an application tool such as a doctor blade or a slot die. Aluminum or copper foils with a thickness ranging between 5 µm – 25 µm are usually applied as current collectors. In general, the slurry is coated on both sides of the foil. After the slurry is applied to the first side of the foil, the one-sided coated foil is dried and continuously fed back to the coating system to coat the remaining blank side of the foil. A less often applied alternative to the consequent coating process is to coat the top and bottom sides of the foil simultaneously. The wet layer thickness is used to control the electrode loading in such a way as to reach the desired power and energy density targets of the electrode. To monitor the electrode thickness, a thickness measurement is commonly conducted in situ during the process.[171-172, 175-177]

The drying of the coating is performed by continuously transporting the coated foil through an oven, which consists of different temperature zones. During this process, the solvent is thermally removed from the electrode coating. To reduce the processing cost, organic solvent vapors are commonly recovered. The temperature profile in the oven chambers as well as the drying speed is adjusted depending on the cell chemistry to ensure good coating quality.[176, 178]

Calendering is the final step of the electrode manufacturing process. During this step, the coated foil is transported through two a pair of rollers, which compacts the electrode coating. Before calendering, the coated foils are statically discharged and cleaned by air flow or a brusher to prevent contamination of the substrate layer by foreign particles. The line pressure is adjusted by varying the gap between the two rollers. By controlling the line pressure, the final electrode density and porosity of the electrode foil are adjusted. For instance, the electrode density of an NMC cathode is increased from 0.9 – 1.2 g cm^{-3} (before calendering) to 1.4 – 1.7 g cm^{-3} (after calendering) by applying a line load of 1000 N mm^{-1}. After this process step, the electrode foil is rolled up and submitted to the following cell production steps.[175, 177]

1.4.1 Effect of the Coating Drying Temperature on the Electrochemical Performance

Within the wet-electrode processing, conducting a drying step is mandatory to completely remove the solvent. As a large amount of energy is required to evaporate and recover the solvent, the drying process is a cost intensive process especially when organic solvents with high boiling points (e.g., NMP) are used. Thus, a cost model for an NCA-based LIB

cell prepared with NMP-based slurries showed that an estimated 40 % of the overall electrode preparation costs stem from the coating and drying step.[177, 179]

Mainly driven by the ambitions to reduce manufacturing costs and optimize the performance of LIBs, intensive experimental research has been conducted on the drying process of LIB electrodes in recent years. Interestingly, many studies concluded that changes in the drying process parameters (e.g., drying temperature, time or radiation intensity) drastically influences the electrode microstructure and thereby the final mechanical properties and electrochemical performance of the electrode. In particular, it has been noted that high drying rates result in the migration of the binder to the surface of the electrode. The consequences of the enrichment of the binder at the electrode surface include higher internal resistance and lower obtainable capacity. In addition, as the binder migration induces depletion of the binder at areas close to the current collector, the adhesion between the electrode coating and the current collector decreases.[180-186] For instance, Jaiser et al.[182] investigated the effect of the drying rate on the electrode homogeneity and electrochemical performance of PVdF-based graphite anodes. Increasing the drying rate resulted in a migration of the PVdF binder towards the electrode surface and a reduction of the rate capability. They argued that the poor rate performance of the anodes dried at higher drying rates was induced by a surface binder layer that increases the charge-transfer resistance or poor electrical conductivity at areas close to the current collector due to the migration of carbon black.

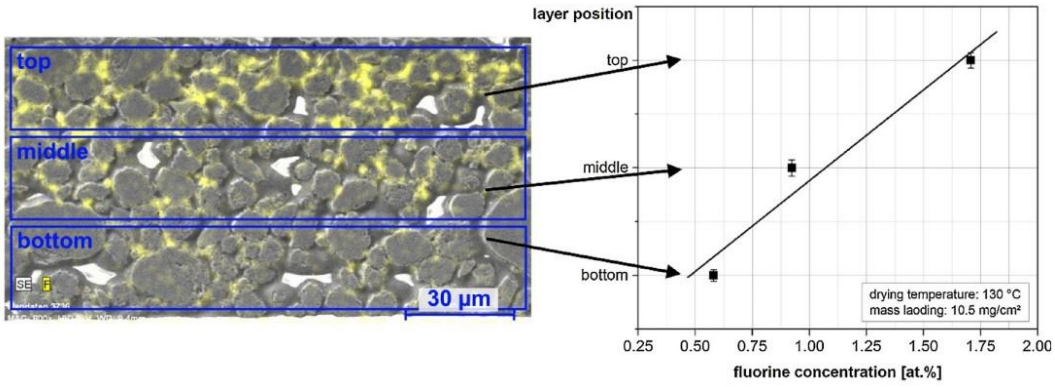

Figure 1-25: Binder distribution within a graphite anode, which was dried at 130 °C, measured via SEM-EDX at the cross-section (reprinted with permission from ref.[183]).

Westphal et al.[183] used SEM-EDX to detect the binder distribution within PVdF-based graphite anodes, which had different mass loadings and were dried at various drying temperatures. By monitoring the fluorine concentration in the electrode cross-sections,

they observed higher binder concentrations at areas close to the electrode surface for anodes that were dried at higher drying temperatures (Figure 1-25). Based on their results, they were able to define drying conditions (temperature, time) for various mass loadings below which the migration of non-active components does not occur. Kumberg et al.[181] made a similar observation for CMC-SBR-based graphite anodes. They demonstrated that increasing the drying rate results in the enrichment of the binder at the electrode surface and they stated that the loss of adhesion of the anodes, which were dried at higher rates, likely resulted from the migration of both SBR and CMC.

Figure 1-16 illustrates the mechanism of the electrode drying process according to today´s understanding. Before the drying step begins, the active and inactive components are homogeneously dispersed in the wet-film of the electrode coating. Once the drying starts, the solvent evaporates and the film thickness begins to decrease. During the ongoing solvent evaporation, the particles move closer together until the film cannot shrink anymore and the final electrode porosity is reached. In the following drying stage, the solvent in the partially filled capillary network is carried by capillary transport and evaporated at the film surface. The remaining liquid in the pores, which is not reachable by capillary transport, is removed via vapor diffusion. According to different studies, the binder and conductive additives are likely dragged upwards along with the solvent during the capillary transport phase (early drying stages).[178, 180-181]

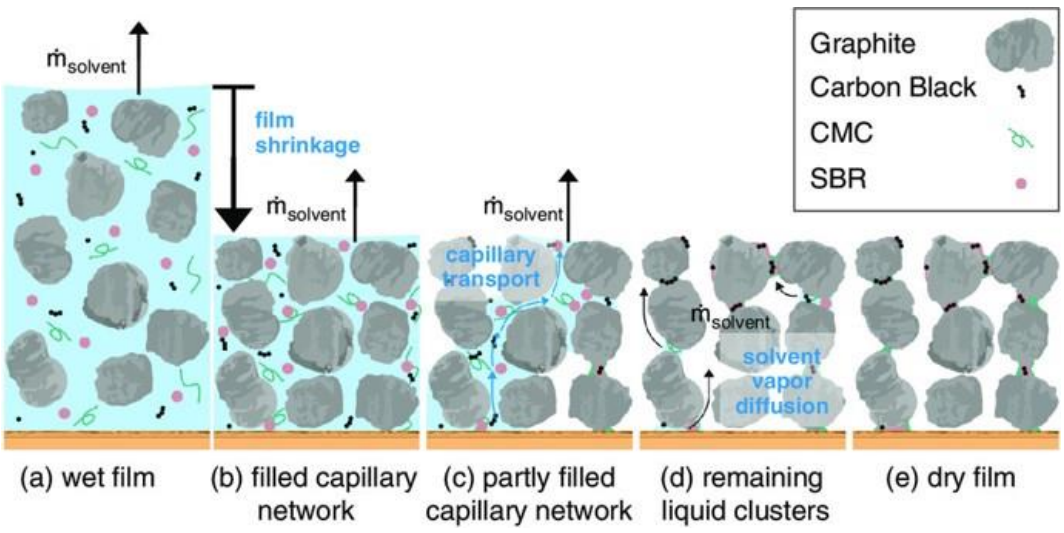

Figure 1-26: Schematic illustration of the different drying stages that occur during the drying process of a particulate wet-film coating (reprinted with permission from ref.[181]).

1.4.2 Influence of the Calendering Step on the Electrochemical Performance

As reported by numerous publications, this process is known to impact the physical and electrochemical properties of the electrode. Depending on the applied active material and the general electrode composition, compacting the particle composite film can improve the electronic percolation network, enhance the mechanical stability of the electrode, improve the adhesion of the film to the current collector, reduce active reaction sites or increase ionic diffusion pathways (tortuosity).[187-193] For instance, van Bommel et al.[193] compared the electrochemical performance of uncalandered and calendered LFP cathodes. They demonstrated that calendering sharply reduced the contact resistance at the interphase between the electrode layer and the current collector. The reduction in the contact resistance led to a severe increase in capacity retention at higher current densities. Similarly, Kang et al.[194] investigated the influence of compression on the performance of NMC cathodes. Calendering of the NMC cathodes reduced the charge-transfer resistance by enhancing the electrochemically active area, which increased the rate capability. However, compression to very high electrode densities (≥ 3.0 g cm^{-3}) resulted in NMC particle crushing, which as a result reduced the power performance (Figure 1-17a). According to their study, compressing NMC electrodes to an electrode density of 3.0 g cm^{-3} resulted in the best compromise between power density and energy density (Figure 1-27b).

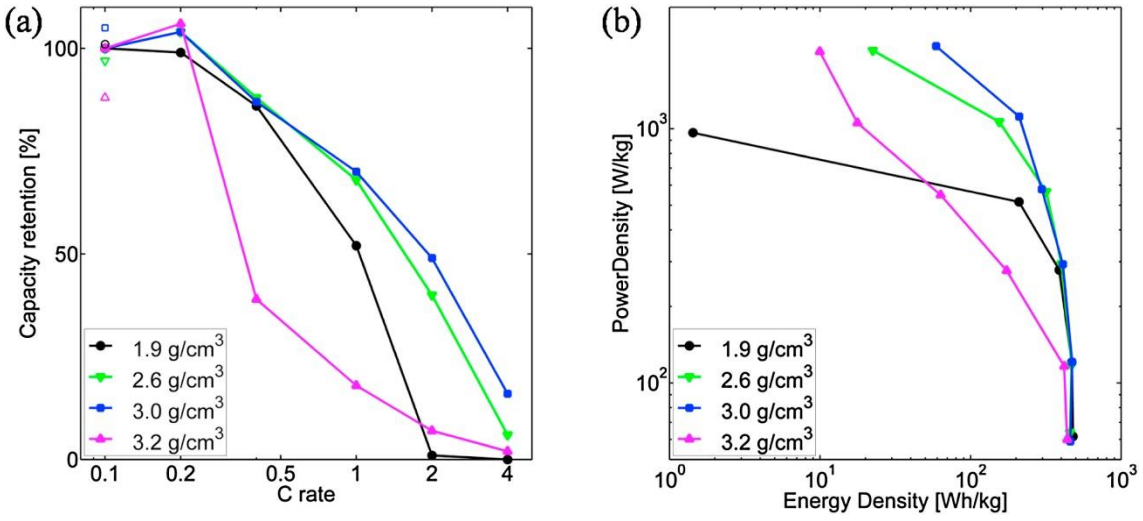

Figure 1-27: Rate capability (a) and Ragone plot (b) of NMC cathodes, which were compressed to different electrode densities (reprinted with permission from ref.[194]).

Gnanaraj et al.[195] and Novak et al.[196] investigated the impact of compression on the electrochemical performance of graphite anodes. Calendering the graphite anodes at high pressures reduced both the first cycle efficiency and cycling performance. They explained

that these effects were caused by Li-ion transport limitation and the occurrence of particle break-up at very high compressions.

One of the drawbacks of the Li-S battery is its low volumetric energy density compared to the LIB, which is caused by the relatively low density of sulfur. Calendering is an option to reduce the gap in volumetric energy density between the Li-S battery and the LIB. Several studies have investigated the compressibility of C/S-composite Li-S cathode materials. For example, Kim et al.[188] compressed C/S-composite cathodes to various electrode densities and discussed the effect of porosity on the rate capability. The electrodes were compressed from 0.6 g cm^{-3} (pristine state) to 1.1 g cm^{-3} and 1.7 g cm^{-3}, respectively. In their study, they demonstrated that the electrodes with the medium density showed no difference in performance from the uncompressed samples, while compression to the highest electrode density resulted in a decrease in the rate capability (Figure 1-28). Interestingly, calendering the electrodes at 70 °C to the highest degree of compaction noticeably enhanced the capacity retention. They argued that calendering at evaluated temperature improved the mechanical integrity, which helped to accommodate mechanical stress induced by morphology changes.

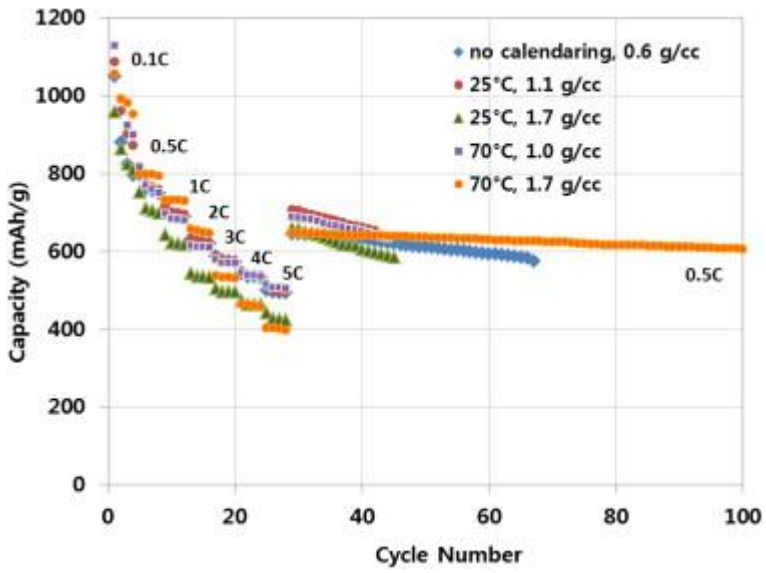

Figure 1-28: Rate and capacity retention test of C/S-composite cathodes compressed to various electrode densities (reprinted with permission from Ref.[188]).

Lv et al.[197] calendered C/S-composite cathodes under varying pressure conditions (0 – 16 MPa) and made similar observations. Applying higher pressures (> 9 MPa) led to the blockage of electrolyte pathways and thereby strongly reduced the obtainable capacity. The effect of porosity on the dissolution/deposition behavior of C/S-composites was investigated by Kang et al[198]. In their study, they compressed C/S composite cathodes

with two different loadings to porosities ranging from 70 % to 40 %. Reducing the electrode porosity to 50 % or less resulted in shrinkage of the second discharge plateau, which as a consequence reduced the capacity retention (Figure 1-29a and 1-29b). They explained with the aid of EIS measurements that the compression of the 2nd discharge plateau was caused by a reduction of active reaction sites, which was visible by an increase in the charge-transfer resistance (Figure 1-29c) During cycling, the active surface area of the compressed electrodes (porosity < 50 %) was blocked due to the deposition of insulating discharge products (Li_2S_2/Li_2S), which led to the observed increase in resistance and the sharp voltage drop in the 2nd discharge plateau. Interestingly, electrode compaction seems to be more suitable for S cathodes, which follow a solid-solid conversion mechanism (e.g., SPAN electrodes). Wang et al.[199] reported that decreasing the porosity of SPAN cathodes is beneficial for cycling performance due to reduced electrical resistance in the electrode.

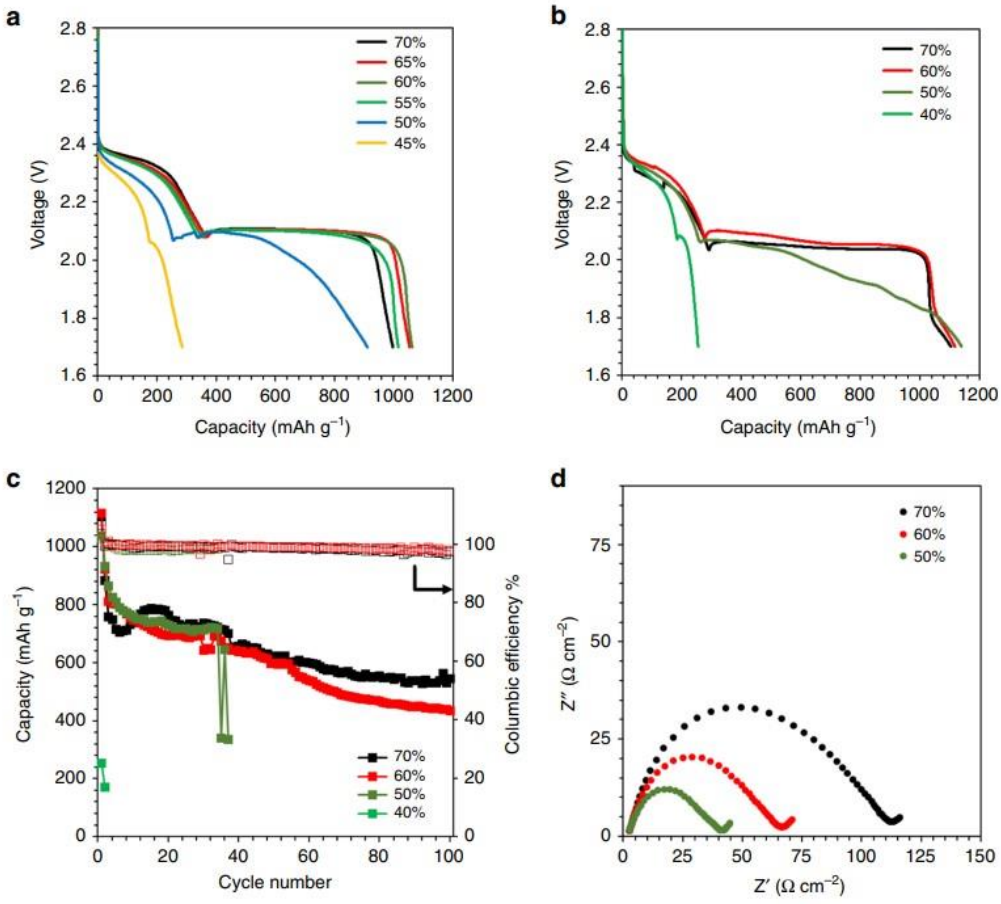

Figure 1-29: Electrochemical performance of C/S-composite cathodes with two different mass loadings and various porosities. Voltage profiles (a,b), cycling test (c) and EIS measurements (d) (reprinted with permission from Ref.[198]).

1.5 General Battery-related Terms and Definitions

Battery users have high expectations; among other things they look for long cycle life, high energy density and short charging times. To compare different battery systems, several parameters were defined such as specific capacity, energy density, C-rate and Coulombic efficiency. In the following paragraph, these parameters will be introduced according to literature from Julien[11], Kurzweil[15], Huggins[200] and Wen Ng[201].

Specific capacity:

The specific capacity (generally in mAh g^{-1}) describes the amount of charge stored per unit mass in a particular active material:

$$C_{spec} = \frac{n \cdot F}{M_n} \tag{1.3}$$

F is the Faraday constant; n is the number of exchanged electrons per unit formula and M_n is the molar mass (in g mol^{-1}) of the active material.

Energy density:

The energy density is a practical measuring unit describing the amount of energy a battery can store per weight or volume. With known theoretical voltage (U_{th}), the gravimetrical energy density (w_{th}) of an active material can be calculated as follows:

$$w_{th} = C_{spec} \cdot U_{th} = \frac{n \cdot F}{M_n} \cdot U_{th} \tag{1.4}$$

Since almost every cell potential depends on the state-of-charge of the battery, U_{th} is not constant. A more practical energy density (w_{pr}) can be calculated by fully discharging the cell and monitoring the cell voltage (U_{cell}) as well as the discharge current ($I_{discharge}$) as a function of time:

$$w_{pr} = \frac{\int_{t_0}^{t_{end}} \left(U_{cell} \cdot I_{discharge}\right) dt}{m_{cell}} = \frac{\overline{U}_{cell} \cdot I_{discharge}}{m_{cell}} \tag{1.5}$$

As a battery cell also includes non-active components (e.g., binder, separator or current collector), m_{cell} equals to the total cell weight. To calculate the volumetric energy density, the energy density can also be related to the total cell volume.

C-rate:

The C-rate is defined as the relationship between the current I (in A) and the nominal capacity of the cell C_n (in Ah):

$$C - rate = \frac{I}{C_n} \tag{1.6}$$

Depending on the tested battery cell, C_n is given by the manufacturer, measured or calculated with the theoretical capacity of the active material. The unit of the C-rate is h^{-1} and indicates how many times a cell is (dis)charged within one hour. For example, a C-rate of C/2 means that the cell is formally fully (dis)charged within 2 h. With the aid of the C-rate, comparing cells with varying active material content is possible.

Coulombic Efficiency:

The ratio of the discharge capacity ($C_{discharge}$) to the charge capacity (C_{charge}) is defined as the Coulombic efficiency (CE):

$$CE = \frac{C_{discharge}}{C_{charge}} \tag{1.7}$$

Assuming completely reversible reactions on the electrodes, the Coulombic efficiency equals to 100 %. However, in practical cells side reactions between electrodes and electrolytes occur leading to Coulombic efficiency below 100 %.[202]

1.6 Applied Characterization Methods

1.6.1 Electrochemical Impedance Spectroscopy (EIS)

EIS is a powerful measurement technique to investigate reaction mechanisms and identify loss processes, which limit the performance of electrochemical storage devices. A fundamental advantage of this method is the ability to characterize a complex electrochemical system with a single non-destructive measurement. The measurement principle is based on the frequency dependency of electrochemical loss processes (e.g., resistance, capacitance and induction).[203,204]

1.6.1.1 Measuring Principle of EIS

This section is based on literature from Lasia[203], Barsoukov[205] and Lvovich[206]. EIS measurements can be carried out by applying a potential (potentiostatic EIS) or a current (galvanostatic EIS). In the potentiostatic mode, an AC voltage (U) with an amplitude (U_A) and a frequency (f) is applied. The time-dependent voltage can be described with the following expression:

$$U(t) = U_A \cdot \sin(\omega t) \tag{1.8}$$

ω is the radial frequency and is defined as $\omega = 2\pi f$. Depending on the properties of the tested system, the current response signal is shifted in phase. The current response in a time-dependent form that is shifted in phase (Φ) can be expressed with the following equation:

$$I(t) = I_A \cdot \sin(\omega t + \Phi) \tag{1.9}$$

With Euler´s formula $U(t)$ and $I(t)$ can be rewritten in their complex notation:

$$U(t) = U_A \cdot e^{i\omega t} \tag{1.10}$$

$$I(t) = I_A \cdot e^{i\omega t - i\Phi} \tag{1.11}$$

With the aid of Ohm`s Law, the complex impedance (Z) can be obtained by dividing the input voltage ($U(t)$) by the output current ($I(t)$):

$$Z = \frac{U(t)}{I(t)} = \frac{U_A \cdot e^{i\omega t}}{I_A \cdot e^{i\omega t - i\Phi}} = Z_A \cdot e^{i\Phi} = Z_A \cdot (cos\Phi + i\, sin\Phi) = Z^{real} + iZ^{im} \quad (1.12)$$

The complex impedance consists of a real (Z^{real}) and an imaginary (Z^{im}) component. An impedance spectrum is constructed by measuring the impedance over a broad frequency range and plotting $-Z^{im}$ as a function of Z^{real} for each measured frequency (so-called Nyquist plot). To analyze the measured impedance spectrum of an electrochemical system, the impedance response of the system is modeled with equivalent electric circuits, which consist of well-known basic electric elements (mainly resistor, capacitor and inductor). Table 1.6 shows the impedance equations and phase shifts of a resistor, capacitor and inductor.

Table 1-6: Impedance equations and phase shifts of resistor and capacitor. R = resistance, C = capacitance and L = inductance.

Element	Impedance	Phase shift
Resistor	$Z_R = R$	$\Phi = 0$
Capacitor	$Z_C = \frac{1}{i\omega C}$	$\Phi = \frac{\pi}{2}$
Inductor	$Z_L = i\omega L$	$\Phi = -\frac{\pi}{2}$

Since the impedance of the resistor is independent of frequency, the real part equals to the resistance *R* and the imaginary part of the impedance is zero. Therefore, the current flowing through a resistor is always in phase with the voltage. In the Nyquist plot, the resistor resembles a point on the real axis (Figure 1-30a). Resistors are frequently used to model the solution resistance of a battery cell. The impedance of the capacitor is frequency dependent and is phase-shifted by π/2. The real part is zero and the imaginary part of the impedance reduces with increasing frequency. In the Nyquist representation, the capacitor is visible as a line for several measured frequencies on the imaginary axis (Figure 1-30b). The connection of a resistor and capacitor would be visible as a straight line that is shifted by the value of the resistor on the x-axis (Figure 1-30c). By the parallel connection of a resistor and a capacitor (R/C element), an electrochemical interface can be modeled. Within the R/C element, the resistor represents the charge-transfer-resistance and the capacitor is used to model the electrochemical double-layer capacitance. In the Nyquist representation, the R/Q element becomes visible as a semicircle (Figure 1-30d).

The inductor has only an imaginary component and the voltage to the current signal is phase-shifted by -π/2. In contrast to the capacitor, the impedance of the inductor raises with increasing frequency.

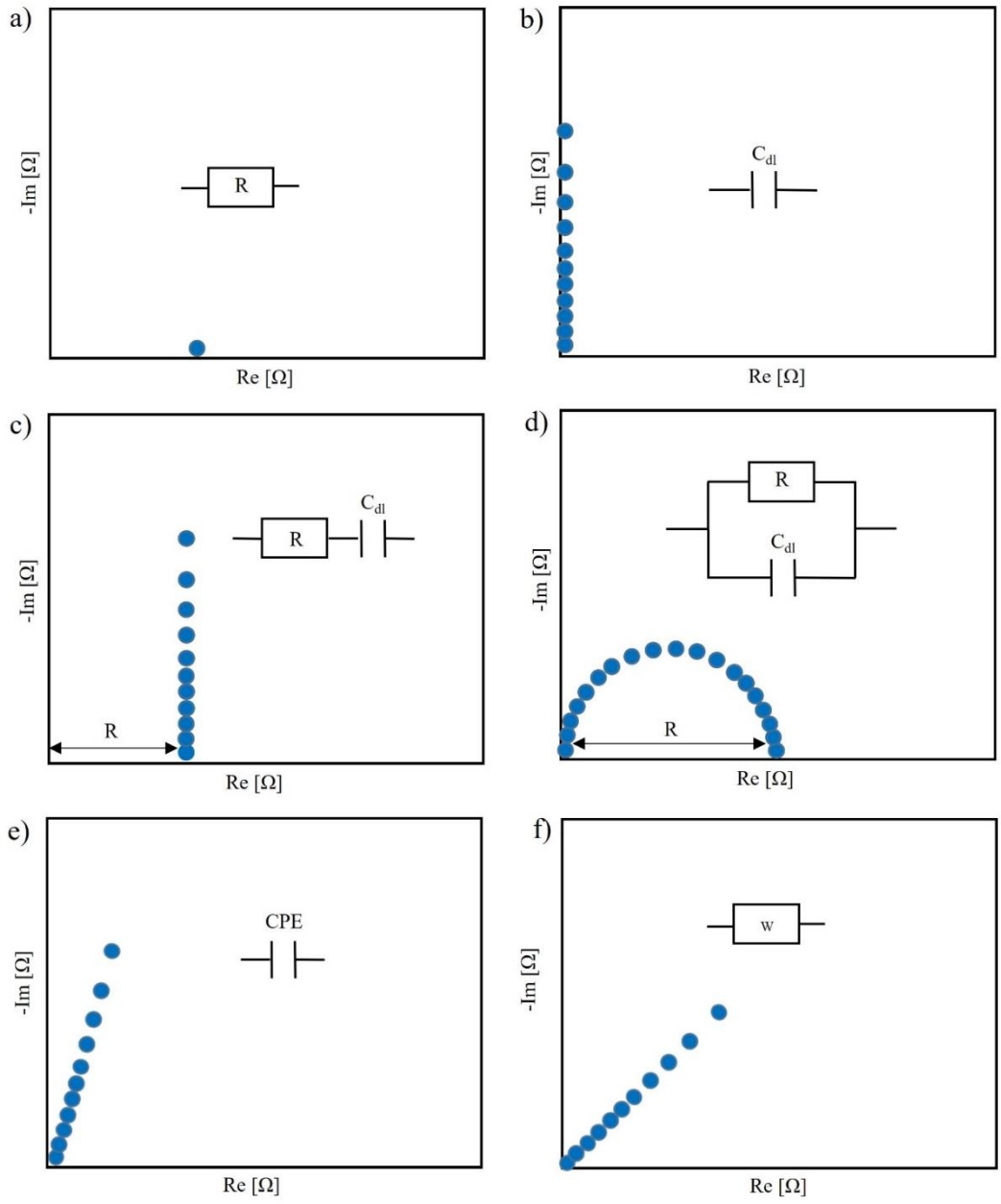

Figure 1-30: Simplified illustration of the Nyquist plots and equivalent circuit models of resistor (a), capacitor (b), resistor and capacitor in serial (c), resistor and capacitor in parallel (d), CPE (e) and Warburg element (f).

Since impedance tries to represent a complex system consisting of chemical, physical, mechanical and electrical components, additional non-ideal circuit elements are required

to describe the impedance response of a real system. Two of these elements are the constant phase element (CPE) and the Warburg diffusion (*W*). Due to electroactive species and the distribution of currents many capacitors such as the double-layer capacitor, do not behave ideally. Therefore, the constant phase element was introduced to model non-ideal capacitive behavior:

$$Z_{CPE} = \frac{1}{Q \cdot (i\omega)^{\alpha}} \tag{1.13}$$

Q is the effective CPE coefficient. If α = 1 and *Q* = *C*, the equation describes the impedance of a pure ideal capacitor. Given α = 0 the equation expresses the impedance of a pure resistor. In the Nyquist plot, a single constant phase element is visible as a straight line that has an angle of -90°α with the x-axis (Figure 1-30e). The parallel connection of a resistor with a constant phase element leads to the formation of a plot with a depressed semicircle. The Warburg impedance (W) for a homogenous semi-infinitive diffusion is given for α = 0:

$$Z_W = \frac{R_W}{\sqrt{i\omega}} \tag{1.14}$$

in which R_w is the diffusion resistance.

As can be seen in Figure 1-30f, the Warburg element is visible as a line with a 45° angle to the x-axis.

In Figure 1-31, a simplified equivalent circuit of an ideally polarizable electrode in solution and the schematic illustration of the corresponding Nyquist plot are depicted. The equivalent circuit includes a solution resistance (R_{sol}), which describes the electrolyte bulk resistance, an in parallel connected R/C element (R_{ct}/C_{dl}) modeling the charge-transfer reaction and the capacitance at the electrode/electrolyte interphase, and a Warburg element (*W*) representing diffusion. The total impedance of the equivalent circuit equals to the following equation:

$$Z = R_{sol} + \frac{R_{ct}}{i\omega C_{dl}} + \frac{W}{\sqrt{i\omega}} \tag{1.15}$$

The Nyquist plot (shown in Figure 1-31) consists of a semi-circle, which is shifted on the x-axis by the value of R_{sol}. Within an impedance spectrum, the lengths of the vector |Z| (blue dotted line), which is the ratio of voltage and current amplitude, and the phase shift

(Φ) determine each measured point. At the highest frequency (around 100 kz), the impedance consists solely of the solution resistances (R_{sol}) as the impedance of the capacitor (R_{sol}) is zero. With decreasing frequency, the impedance of the capacitor increases and the current flow is distributed between the charge-transfer resistance (R_{ct}) and C_{dl}. Once the frequency approaches zero, the impedance of the capacitor raises towards infinity and the current flows exclusively through R_{sol} + $R_{ct.}$ At very low frequencies, a Warburg element (W) can be observed (visible by the 45° line). The values of R_{sol} and R_{sol} + R_{ct} can be obtained from the real intercepts. With the radial frequency at the high point of the semicircle (ω_{max}), the value of C_{dl} can be calculated:

$$\omega_{max} = \frac{1}{R_{ct} \cdot C_{dl}} \tag{1.16}$$

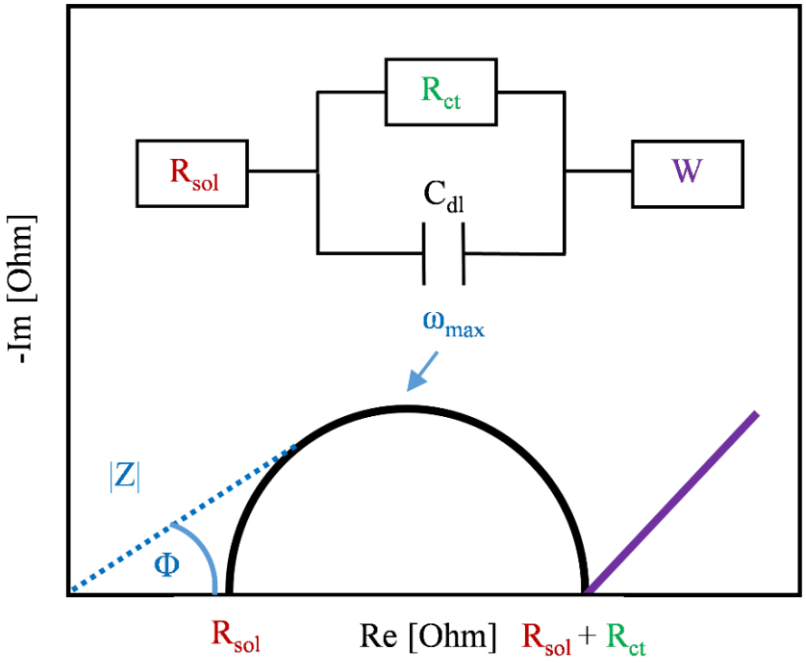

Figure 1-31: Exemplary equivalent circuit of an ideally polarizable electrode in solution and schematic illustration of the corresponding Nyquist plot.

1.6.1.2 Deconvolution of Anode and Cathode Impedance Signals

Generally, the sum of the anode and cathode impedance signals is visible in an impedance spectrum of a battery cell. Unfortunately, the separation of their contribution is challenging as their characteristic frequency often overlaps.[207] Due to the large impedance contribution of lithium metal anodes, this effect is even more severe for cells with lithium metal as the counter electrode (e.g., Li-S battery).[208] Therefore, deconvolution of the

anode and cathode impedance signals is compulsory to fully understand the impedance response of a battery cell. A possible approach first introduced by Chen et al.[209] to neglect the contribution of the countering electrode is measuring the impedance in symmetrical cells. A symmetrical cell consists of two identical electrodes and the impedance of a single electrode equals to one-half of the overall impedance. This ex situ measurement is rather complicated as it involves additional (dis)assembly steps.

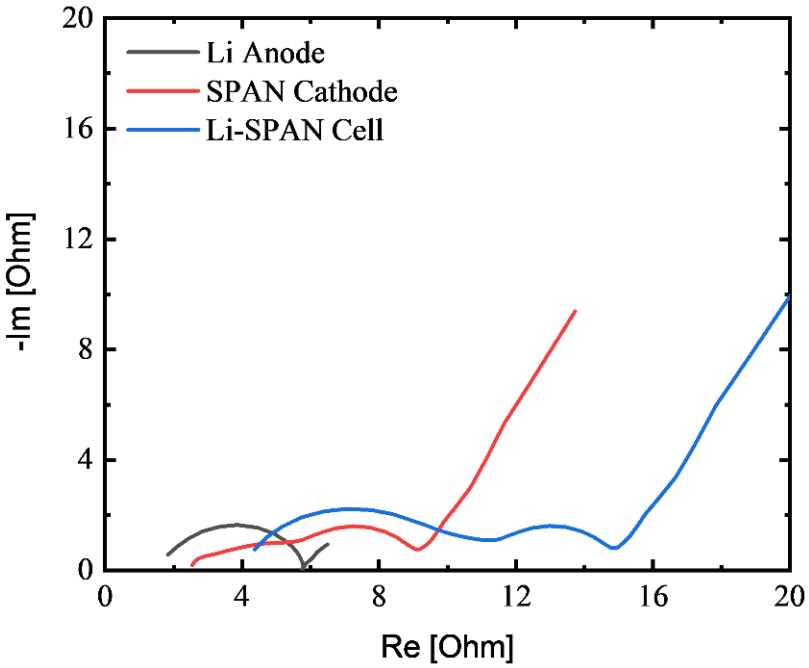

Figure 1-32: Impedance spectrum of a Li-SPAN cell measured with a lithiated stainless steel finger-shaped reference electrode. EIS was acquired at 50 % SOC after cycling for five cycles. The full impedance of the Li-SPAN cell is shown in blue, the Li anode in black and the SPAN cathode in red.

By applying a reference electrode, separation of the impedance response of the anode and cathode can be carried out in situ. In a three-electrode cell set-up, the reference electrode acts as a spectator and does not interfere with cell cycling.[210] Conventional reference electrodes are usually placed at the outer edge of the stack. Since even minor misalignments of the electrodes bias the electric field around the reference electrode, placing the reference electrode at the edge of the stack can lead to severe measurement artifacts.[211] This issue can be overcome by the usage of a micro-reference electrode or a mesh-type reference electrode. A micro-reference electrode is a partially insulated wire, which extends to the center of the cell and is placed between the electrodes and two separators. Only the wire tip is exposed to the ionic current flow of the electrodes. To activate the micro-reference electrode, the wire is lithiated by applying a small current between the wire and the lithium-containing electrode (e.g., lithium metal, LFP, NMC).

Depending on the wire material, a lithium-wire alloy is formed or lithium is plated on the surface of the wire tip.[212-213] Used wire materials include e.g., copper[212], tin[214-215] and gold[216]. As the plated or alloyed lithium can dissolve over time by self-discharge reactions, verifying the potential stability of the lithiated micro-reference electrode in the tested cell setup is important. Further potential drifts of the reference electrode during the impedance measurement can lead to distortions in the measured EIS spectrum.[216]

Besides alignment errors, electrochemical asymmetry such as large distinctions in the surface areas of the electrodes can also cause a biased impedance signal. By adding up the individual impedance responses of the electrodes and comparing them to the full-cell impedance, the validity of a measurement setup can be verified.[213, 217]

In this thesis, a finger-shaped stainless steel reference electrode was used. The reference electrode was lithiated by applying a small current vs the lithium metal anode. Figure 1-32 shows the application of a finger-shaped stainless steel reference electrode in a Li-SPAN cell measured at 50 % SOC after cycling for five cycles. The impedance of the Li anode (shown in black) is smaller than the cathode impedance and consists of one semi-circle. For the cathode impedance (shown in blue), two semi-circles are visible. Since the anode impedance overlaps the first semi-circle of the cathode impedance, utilizing a reference electrode helps to gain a much better understanding of the impedance of the SPAN cathode.

1.6.1.3 Determination of Tortuosity by EIS

The transport of ions within the pores of an electrode strongly influences the rate capability of battery cells. Therefore, an open electrode structure is required and a parameter, which can quantify the ability of ions to move within a porous structure, is of strong interest.[204,218] The tortuosity (τ) is a microscopic approach to evaluate the ion movement within a porous medium. τ is defined as the quotient of the lengths of the effective ion pathway (d_{eff}) through a porous medium to the direct pathway (d_0):[219]

$$\tau = \frac{d_{eff}}{d_0} \tag{1.17}$$

The tortuosity of a battery electrode can be determined by various methods. In the field of electrochemistry commonly applied are impedance-based techniques with blocking electrolytes[220-222], polarization-interrupts methods[222-223], methods based on gas

diffusion[224] and 3D imaging techniques based on X-ray tomography or focused-ion beam scanning electron microscopy.[208, 225-226]

In the following paragraph, the tortuosity determination with electrochemical impedance spectroscopy based on the work of Landesfeind et al.[220] is described. With known ionic resistance (R_{pore}) of the electrode, electrolyte conductivity (σ_0), electrode surface area (A), electrode thickness (d) and porosity (p), the tortuosity of a battery electrode can be calculated:

$$\tau = \frac{R_{pore} \cdot A \cdot \sigma_o \cdot p}{d} \tag{1.18}$$

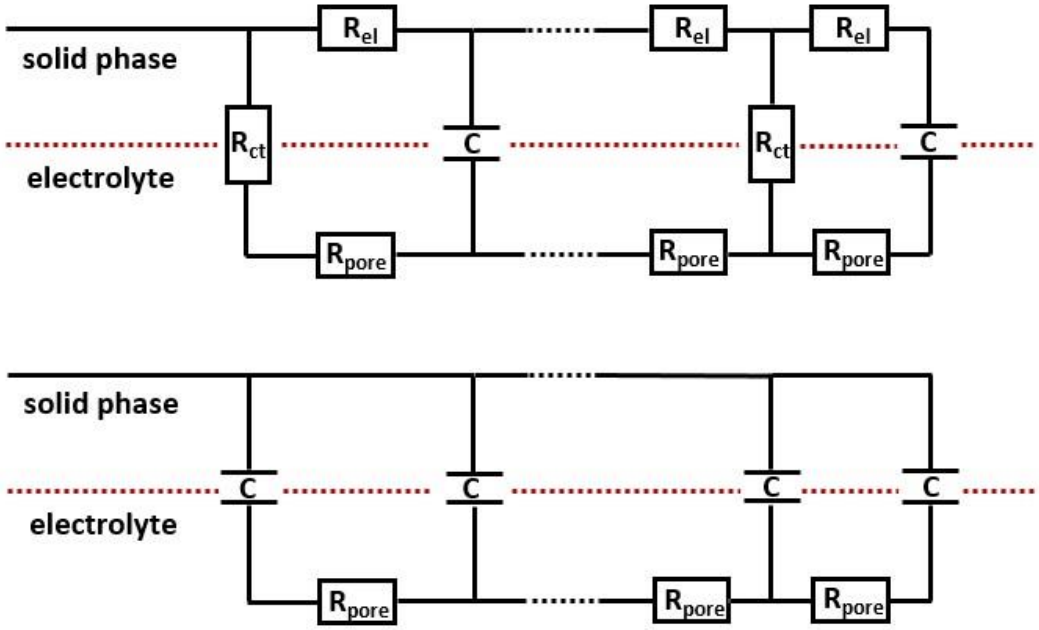

Figure 1-33: Equivalent circuit of the general (upper panel) and simplified (lower panel) transmission line model (based on ref.[220]).

The determination of R_{pore} can be conducted via measuring EIS of symmetrical cells and fitting the obtained plot with a transmission line model, which describes the total impedance of a porous electrode filled with electrolyte. Figure 1-33 (upper panel) shows the equivalent circuit of a transmission line model describing a porous battery electrode. The serial connection of ohmic resistors (R_{el}) represents the electronic resistance in the solid phase. Accordingly, ohmic resistors model the ionic resistance of the electrode (R_{pore}) in the liquid phase. Between the solid and electrolyte phase, a charge can be transferred via faradaic (R_{ct}) or capacitive (C) reactions. Within a battery, an electrically

insulating separator is placed on the surface of the electrodes and the electrical and ionic rails are connected to separate ends. Therefore, electrons are only mobile in the solid phase. Due to the presence of conductive carbon additives in a battery electrode, the electrical conductivity of the solid phase is noticeably higher than the ionic conductivity within the electrolyte phase. Thus, the assumption $R_{pore} >> R_{el}$ is generally true and R_{el} can be omitted (Figure 1-33, lower panel). By measuring the impedance under blocking conditions, R_{ct} can be neglected and the transmission-line model further simplified. Blocking conditions can be realized by measuring at 0 % or 100 % state-of-charge (SOC). For intercalation-type electrodes, blocking conditions can further be achieved by using non-intercalating electrolytes. The equivalent circuit of the simplified transmission line model is depicted in the lower panel of Figure 1-26.

Figure 1-34 illustrates the Nyquist plot of a symmetrical SPAN-SPAN cell. The SPAN electrodes were measured at 100 % SOC under blocking conditions. In the high-frequency region, the plot is linear with a ~ 45° slope and deviates towards a line with a slope slightly lower than 90° at low frequencies. R_{pore} can be determined by extrapolating the real intercepts of the high and low-frequency branches.

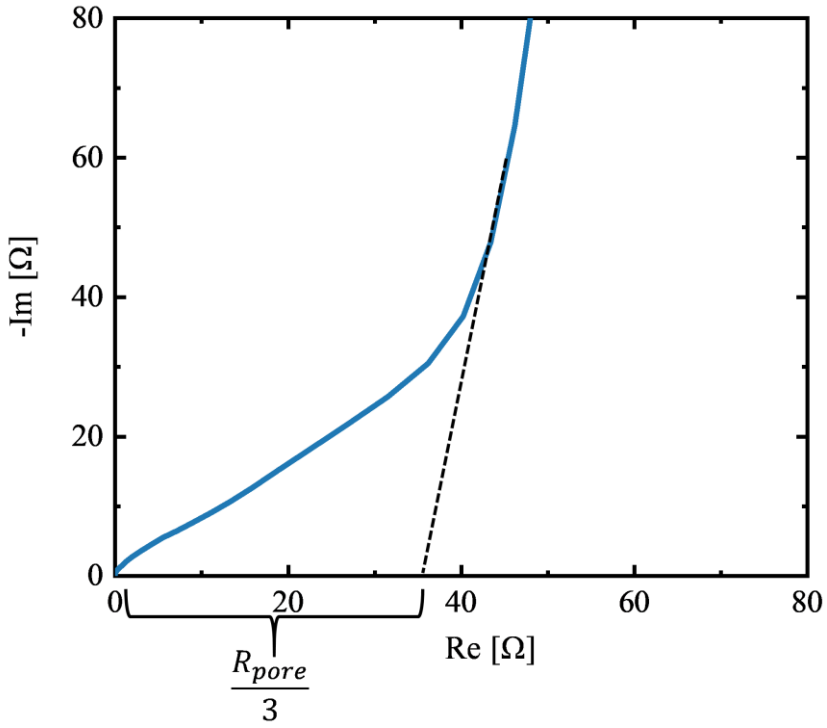

Figure 1-34: Nyquist plot of symmetrical SPAN-SPAN cells under blocking conditions. Determination of R_{pore} by extrapolation of the x-axis intercept

1.6.2 Time-of-Flight Secondary Ion Spectroscopy (ToF-SIMS)

For more than 50 years, ToF-SIMS has been intensively used to investigate the chemical composition of material surfaces. The unique characteristics of this technique such as the ability to measure all elements on the periodic table, the high sensitivity (in ppb range for many elements) as well as the high depth (0.3 - 1.0 nm) and lateral resolution (down to 50 nm) make ToF-SIMS a powerful analytical method.[227-228]

1.6.2.1 Working Principle

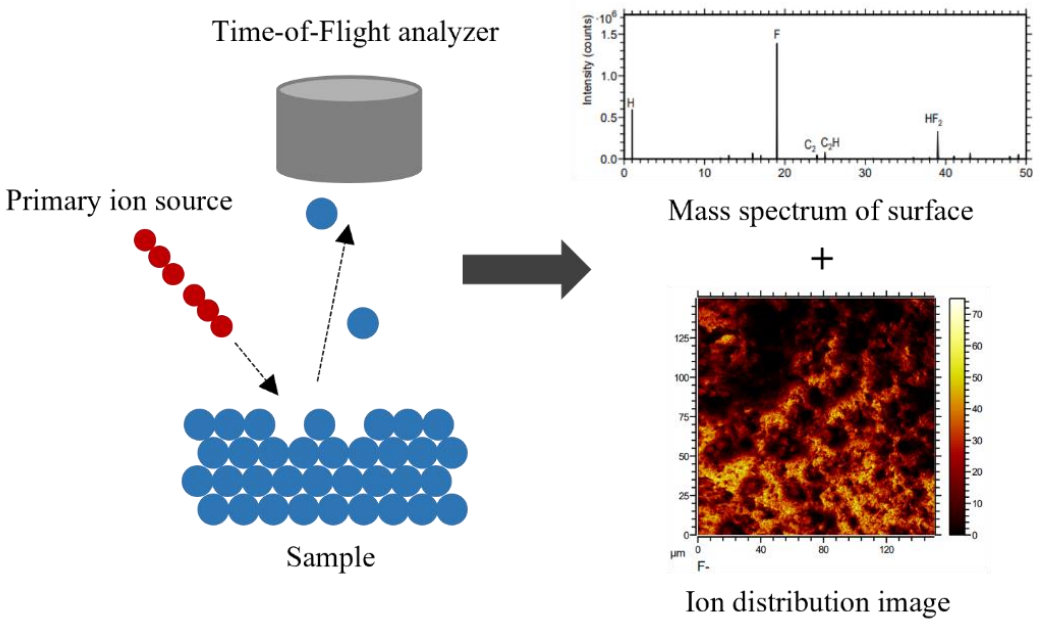

Figure 1-35: Schematic illustration of the working principle of ToF-SIMS.

Figure 1-35 illustrates the working mechanism of ToF-SIMS and the valuable information it provides. ToF-SIMS combines Secondary Ion Mass Spectroscopy (SIMS) and Time-of-Flight (ToF) mass analysis in one analytical method. The measuring principle of SIMS is to detect ionized species with a mass spectrometer that are generated when a targeted surface is blasted with a primary ion beam (typically Cs or Ga). The kinetic energy of the striking ions of the primary ion beam is transferred to the surface of the sample via atomic collisions, which generate a collision cascade process. Once the transferred energy surpasses the surface binding energy, the emission of secondary particles from the surface of the sample occurs. SIMS can be operated in a non-destructive operation mode by using an ion beam with a very low dose of primary ions ($< 10^{-13}$ ions cm^{-2}), which ensures that only less than 1 % of the sample surface is bombarded with ions during the experiment. This guarantees that the detected fragments are solely formed on an undamaged surface. Most of the emitted fragments are neutral in

charge but a small percentage (< 1 %) is charged (positively or negatively). In the subsequent time-of-flight analysis, the mass to charge ratio (*m/z*) of the emitted ions is detected.[229-230] The ToF analyzer detects the masses of the emitted species by measuring their flight time. Advantages of this type of analyzer over others include high transmission, parallel detection of masses and very high mass range. Based on the information provided by the ToF-SIMS experiment, a mass spectrum of the surface as well as 2D and 3D ion distribution images can be created (Figure 1-35).[231-232]

1.6.2.2 Application in Battery Research

Besides its application in material science, ToF-SIMS has been intensively used to solve many research questions related to batteries. Since the detection of lithium is very challenging with standard techniques (e.g., energy dispersive x-ray (EDX) or scanning electron microscope (SEM)), ToF-SIMS has been applied to monitor the lithium distribution within electrodes.[233-236] Besides detecting lithium gradients, ToF-SIMS has also been utilized to verify the binder distribution within an electrode coating.[237-238] As explained earlier, the SEI layer consists of many different types of inorganic and organic compounds, which makes the determination of its composition challenging. Due to the wide elemental detection range of this analytical technique, ToF-SIMS has been widely applied to analyze the chemical composition of the SEI layer.[239-242]

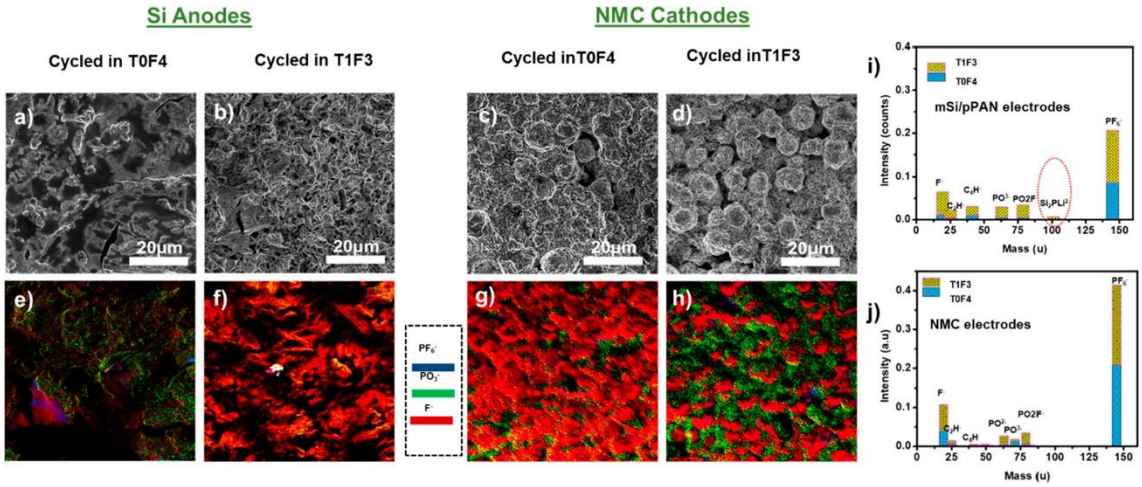

Figure 1-36: (a-h) SEM images and ToF-SIMS ion distribution images of the surface of Si anodes and NMC cathodes after cycling for two cycles. (i-j) ToF-SIMS mass spectra of the cycled electrodes (reprinted with permission from ref.[241]).

For instance, Haridas et al.[241] used ToF-SIMS to investigate the influence of two different electrolyte additives on the chemical compositions of the SEI layers of Si-NMC full cells. They showed that TMSP as an additive forms a more fluoride-rich SEI layer on the Si

anode and a more phosphor-rich layer on the NMC cathode compared to when FEC was used as the additive (Figure 1-36). Furthermore, the electrochemical reaction of many conversion-type battery technologies such as the Li-S battery is often a multistep process that involves many intermediate species. As their identification is quite intriguing, ToF-SIMS has been utilized to identify these intermediates and thereby helped to uncover reaction mechanisms.[243-244]

2 Summary of Research

As outlined earlier, the Li-SPAN battery and the Li-ion battery with a Si anode are often regarded as energy storage technologies of the future. However, to enable the commercial success of these technologies, electrode formulation and processability of SPAN cathodes and Si anodes need to be optimized. This thesis focuses on characterizing the electrode drying process and calendering step of SPAN cathodes as well as improving the electrode formulation of Si anodes by applying a novel binder design. The obtained results were the base for three publications (Publication I[245], Publication II[246] and Publication III[247]), which will be outlined and discussed in this chapter.

2.1 Effect of the Drying Temperature on the Performance and Binder Distribution of SPAN Cathodes (Publication I)

Before Li-SPAN batteries find commercial application, the processability of SPAN cathodes needs to be evaluated. As outlined earlier (section 1.4), electrode film drying and calendering are two important processing steps. Since both production steps strongly affect the electrochemical performance, optimal processing parameters ought to be obtained. Even though the drying process has been intensively studied for LIB electrodes, the impact of the drying step on the binder distribution and electrochemical performance has not yet been investigated for SPAN electrodes or any other Li-S cathode material. This section summarizes and discusses my findings concerning the influence of the drying temperature on the electrochemical performance and binder distribution of SPAN cathodes.

2.1.1 Effect of the Drying Temperature on the Electrochemical Performance

The influence of the drying temperature on the electrochemical performance was investigated by drying SPAN electrodes (~ 2.4 mAh cm^{-2}) prepared with two commonly used binder systems (PVdF and PAA) at three different temperatures (30 °C, 60 °C and 90 °C) and measuring their electrochemical performance against lithium metal. Both electrode types were prepared with NMP as the solvent. First, the rate capabilities of the prepared SPAN cathodes were measured by cycling the electrodes in half-cells at various C-rates (C/4 - 4C). As visible in Figure 2.1, at higher rates (> C/2) the discharge capacities of the PVdF-based cathodes decreased with elevating drying temperature of the coating. For instance, increasing the drying temperature from 30 °C to 90 °C resulted in a 56 % loss in the obtainable discharge capacity at 4C. In contrast to the cycling behavior of the PVdF-based cathodes at higher rates, no drying temperature effect on the electrochemical

performance was observed at lower rates (< 1C). Since the obtainable capacities at lower rates (C/4 and C/2) remained the same prior and after cycling at higher rates (> C/2), the drop in discharge capacity is not caused by cell degradation and is expected to be induced by an increase in the internal resistance.

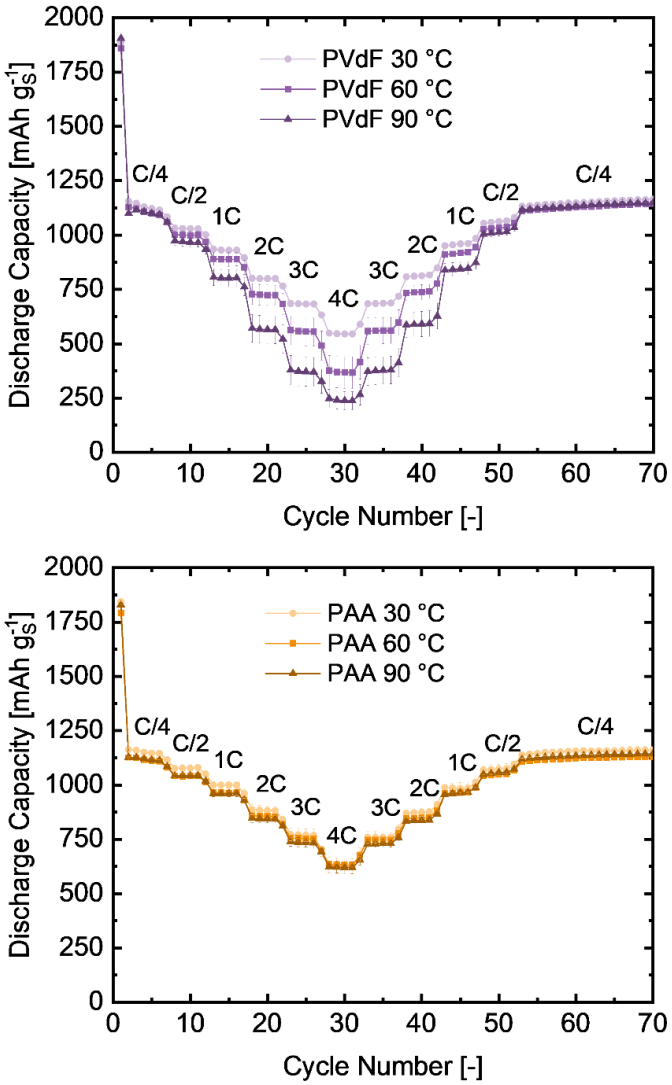

Figure 2-1: Rate capabilities of PVdF- (upper panel) and PAA-based (lower panel) SPAN cathodes, which were dried at various coating drying temperatures (30 °C, 60 °C and 90 °C). The galvanostatic cycling was conducted with applied currents ranging from C/4 (~ 0.6 mA cm^{-2}) to 4C (~ 9.6 mA cm^{-2}). The standard deviation of at least two independent measurements is represented by the error bars (reprinted with permission from ref.[245]).

Contrary to the PVdF-based cathodes, with PAA as binder, no influence of the drying temperature on the rate capability was observed (Figure 2-1, lower panel). The obtained results from the rate tests further suggest that the lower rate capability of the PVdF-based electrodes was solely caused by a drying temperature effect as the rate capability of the PVdF-based electrodes, which were dried at 30 °C, was similar to the rate capability of the PAA-based electrodes.

In addition to verifying the dependence of the drying step on the rate capability, the prepared SPAN electrodes were cycled at 1C for 500 cycles to assess the influence of the drying temperature on capacity retention. Figure 2-2 illustrates the dependence of the coating drying temperature on the long-term cycling performance of the PVdF-based electrodes. The obtained results indicate that the drying temperature only affects the rate capability as no clear changes in the capacity retention after cycling for 500 cycles were observed when the coating drying temperature was increased.

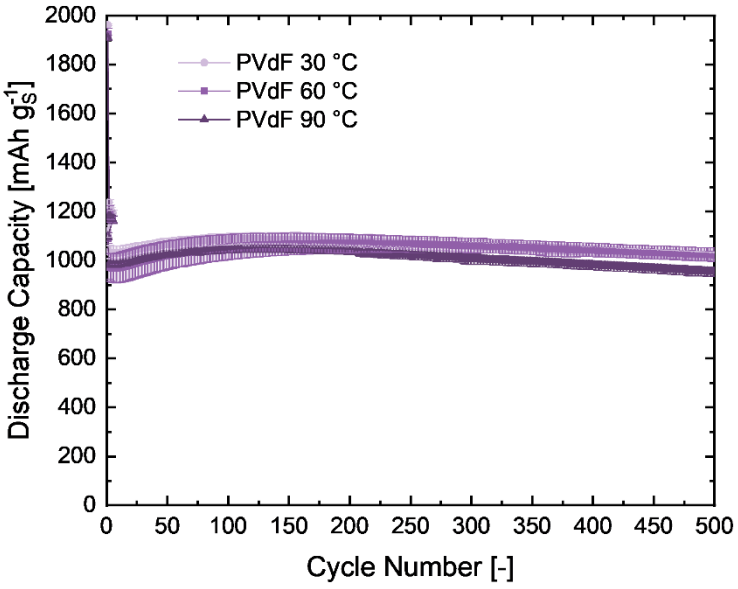

Figure 2-2: Long-term cycling performance of PVdF-based SPAN cathodes, which were dried at various coating drying temperatures. The electrodes were cycled at 1C (~ 2.4 mA cm^{-2}) after five preformation cycles at C/4 (~ 0.6 mA cm^{-2}). The standard deviation of at least two independent measurements is represented by the error bars (reprinted with permission from ref.[245]).

Besides half-cell cycling tests, reference-assisted EIS was employed as an analytical technique to determine the drying temperature effect on the cathode resistance. With this advanced analytical EIS method, it was possible to measure the cathode impedance without disturbance of the lithium metal anode impedance signal or any misalignment errors. Noticeably, this was the first time the reference-assisted EIS approach was used within the field of Li-S batteries. As described in section 1.6, the cathode impedance was measured by placing a lithiated stainless steel finger-shaped reference electrode in the geometrical center between anode and cathode and measuring the impedance at 50 % SOC after five C/4 preformation cycles. Figure 2-3 illustrates the Nyquist plots of the prepared PVdF- and PAA-based SPAN cathodes, which were dried at different drying rates. To fit the obtained Nyquist plots, the equivalent electrical circuit model shown in Figure 2-4 was applied.

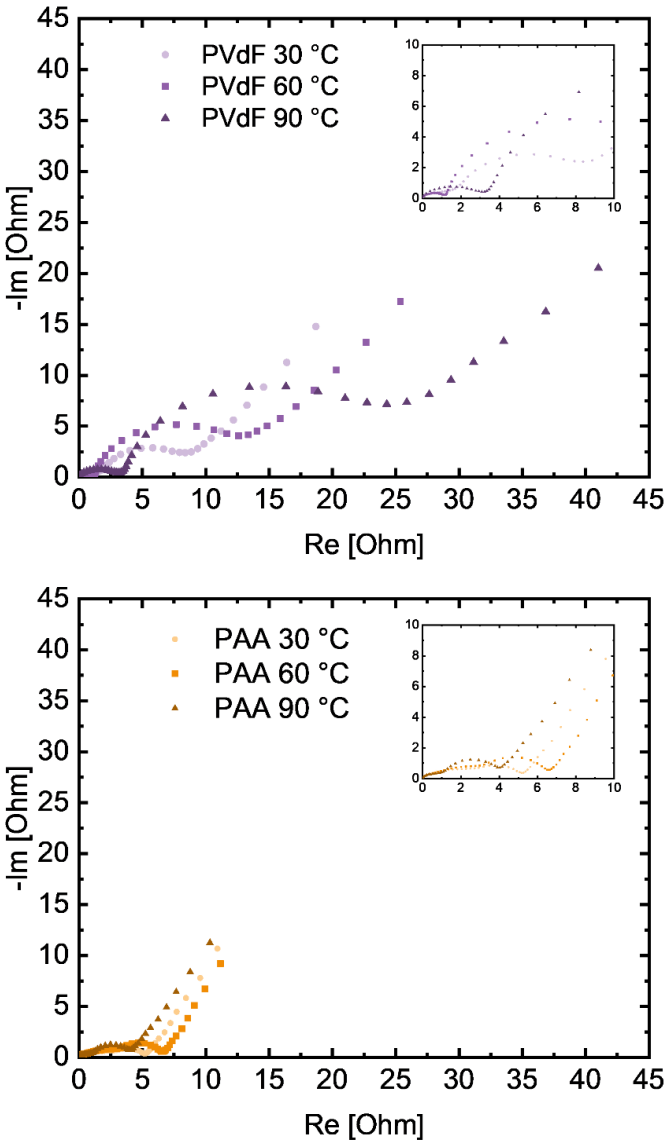

Figure 2-3: Nyquist plots of PVdF- (upper panel) and PAA-based (lower panel) SPAN cathodes, which were dried at different drying temperatures. EIS measurements were conducted with a lithiated stainless steel finger-shaped reference electrode and measured at 50 % SOC after five preformation cycles at C/4. To enable better comparability the high-frequency resistance (R_1) was subtracted from all the measurements (reprinted with permission from ref.[245]).

The equivalent circuit model consisted of a high-frequency resistance (R_1), two R/Q elements (R_2Q_1, R_3/Q_2) and a Warburg element connected in series. The first R/Q element was assigned to the contact resistance at the coating and current collector interphase (R_2Q_1) and the second R/Q element was used to represent the charge-transfer resistance (R_3/Q_2). The Li^+ ion diffusion was modeled by a Warburg element. As the fitted contact resistances (R_2) were almost identical for all tested samples (~ 2 Ω), the following discussion focuses on the differences in the R_3 values and distinctions in the low frequency region of the Nyquist plots (Warburg element). For the PVdF-based SPAN cathodes, the charge-transfer resistance increased severely with an increased drying rate.

For instance, the charge-transfer resistance increased by a factor of three when the coating drying temperature was increased from 30 °C to 90 °C (Table 2-1). Further, a decrease in the angle of the low frequency branch became visible when the coating drying temperature of the PVdF-based electrodes was increased (Figure 2-3, upper panel). In contrast to the PVdF-based cathodes, the charge-transfer resistance of the PAA-based electrodes remained almost independent of the applied coating drying temperature (~ 3 Ω for all tested samples) and no changes in the angle of the Warburg element were observed. Hence, the obtained impedance results indicate that the observed decrease in the rate capability of PVdF-based electrodes could be traced back to a drying temperature-induced increase in the charge-transfer resistance and a more pronounced Li^+ ion diffusion limitation at higher drying rates.

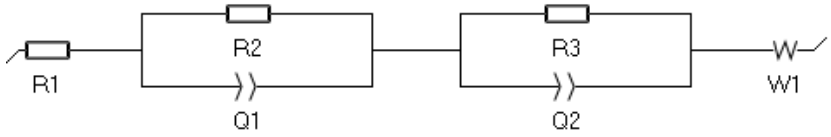

Figure 2-4: Equivalent electric circuit model used to model the obtained Nyquist plots (reprinted with permission from ref.[245])

Table 2-1: Exact fitted resistance values obtained from the Nyquist plots shown in Figure 2-3. The standard deviation of at least two independent measurements is represented by the error bars (reprinted with permission from ref.[245]).

	R_2 [Ω]	R_3 [Ω]
PAA 30°C	1.5 ± 0.1	3.3 ± 0.3
PAA 60°C	2.3 ± 0.2	4.0 ± 0.3
PAA 90°C	2.0 ± 1.0	2.7 ± 0.4
PVdF 30°C	1.7 ± 0.6	5.2 ± 0.3
PVdF 60°C	1.7 ± 0.6	9.8 ± 0.6
PVdF 90°C	2.9 ± 0.7	14.3 ± 2.4

2.1.2 Effect of the Drying Temperature on the Binder Distribution

Since previous studies conducted on LIB electrode materials have shown that higher drying rates lead to an inhomogeneous PVdF distribution (as explained in section 1.4.1), the effect of the drying temperature on the binder distribution within the PVdF- and PAA-based SPAN cathodes was evaluated. In this study, ToF-SIMS was the analytical method of choice to analyze the binder distribution. As PAA does not contain any detectable elements, which are not evident in the other electrode materials (SPAN and C65 carbon),

SEM/EDX could not be used as an analytical tool to provide information on the binder distribution. Instead, ToF-SIMS, which detects fragments rather than elements, was applied. First, suitable characteristic fragments for each electrode component were determined by measuring ToF-SIMS spectra of the electrode bulk materials. Figure 2-5 illustrates exemplary ToF-SIMS spectra of PAA. Since no C_2HO^- and $C_3H_3O_2^-$ ions were detected for SPAN, PVdF and C65 carbon, C_2HO^- and $C_3H_3O_2^-$ ions were chosen as diagnostic ions to detect the PAA distribution within the PAA-based SPAN cathodes. Similarly, CN^-, C_2^- and F^- were identified as detectable diagnostic ions for SPAN, C65 carbon and PVdF, respectively.

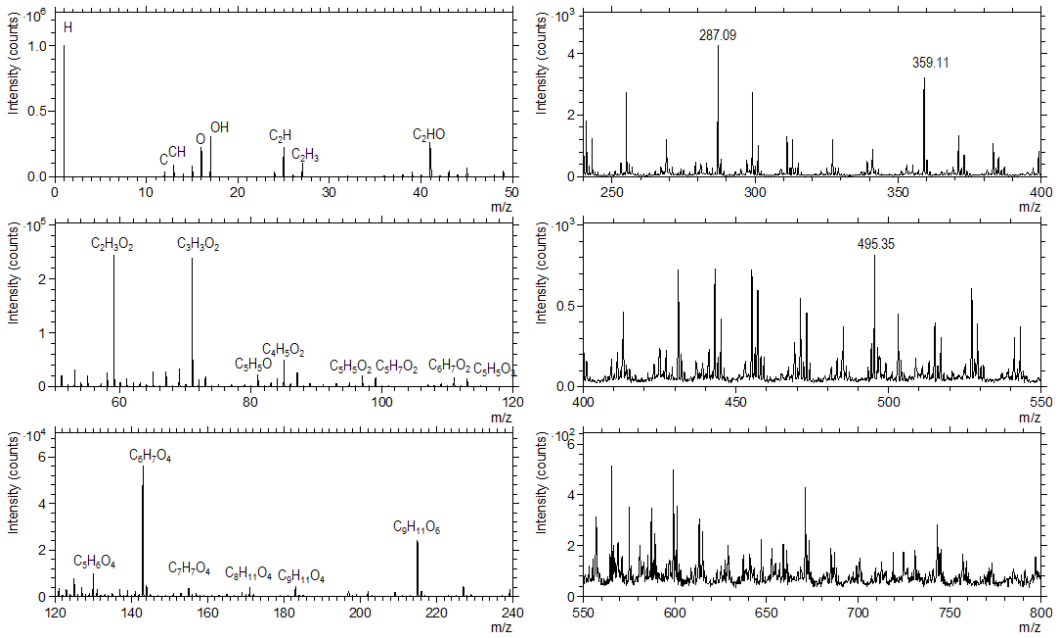

Figure 2-5: ToF-SIMS spectra of the negative fragments of PAA (reprinted with permission from ref.[245]).

The first ToF-SIMS measurements were conducted on the surface of the pristine SPAN cathodes. Figure 2-6 shows the ToF-SIMS images of the surface of the SPAN cathodes. The detected fragments of SPAN (CN^-), C65 carbon (C_2^-) and binder (F-, C_2HO^-) are visible in red, green and blue, respectively. To enable the comparison between the electrodes, the intensity scales were adjusted to an equal minimum and maximum value. For the PVdF-based cathodes, a sharp increase in the F^- intensity (shown in blue) on the electrode surface with elevating coating drying temperature was observed. At higher drying temperatures (≥ 60 °C), the F^- signal intensities almost completely overlapped the signal intensities of the other electrode components (CN^- and C_2^-). This indicates that a dense PVdF layer was formed on the electrode surface when the coating drying temperature was increased above 30 °C. As visible in Figure 2-6 (lower panel), no clear

enrichment of the binder was observed in the PAA-based SPAN cathodes. Even at the highest coating drying temperature (90 °C), clear signal intensities of the other electrode components (CN^- for SPAN and C_2^- for C65 carbon) were still visible in the ToF-SIMS images of the PAA-based electrode surfaces.

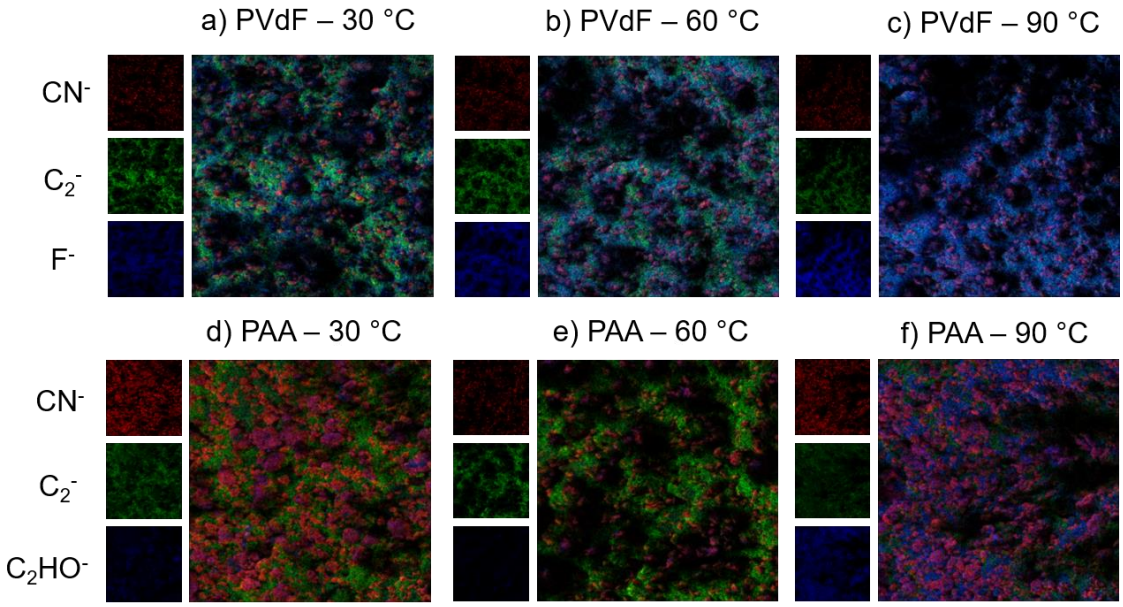

Figure 2-6: ToF-SIMS images of the surface of the PVdF- (a-c) and PAA-based (d-f) SPAN cathodes, which were dried at various drying temperatures (30 °C, 60 °C and 90 °C). CN^- (SPAN, red), C_2^- (C65 carbon, green), F^- (PVdF, blue) and C_2HO^- (PAA, blue) were the detected fragments (reprinted with permission from ref.[245]).

To analyze the drying temperature dependent binder migration of the PAA- and PVdF-based cathodes in greater detail, ToF-SIMS measurements were additionally conducted on the electrode cross-sections. Figure 2-7 illustrates the ToF-SIMS images of the PVdF- and PAA-based electrode cross-sections. The signals corresponding to PVdF (F^-) and PAA ($C_3H_3O_2^-$) are shown in green. O^- and AlO^- fragments were used to detect the aluminum current collector and are visible in red at the top of the images. As depicted in the upper panel of Figure 2-6, the F^- signal intensities are homogenously distributed in the sample, which was dried at 30 °C. Once the temperature was increased to 60 °C and above, various spots with increased F^- signal intensities (visible in brighter green) were observed especially in areas close to the electrode surface (marked with red circles). This indicates that the increase in the drying rate led to an agglomeration of PVdF and migration of the PVdF binder to the surface of the electrodes. As PVdF possesses only poor ionic conductivity and is an electrical insulator, agglomeration of PVdF and formation of a PVdF surface layer likely leads to higher ionic and electrical resistances. Therefore, the obtained ToF-SIMS results indicate that the formation of a dense PVdF

layer on the electrode surface was the most feasible cause for the drying temperature-induced increase in both charge-transfer resistance and Li^+ ion diffusion limitation of the PVdF-based SPAN cathodes, which consequently had a detrimental effect on the rate capability. As described in section 1.4.1, similar observations have been made for other LIB electrode materials. In contrast to the PVdF-based cathodes, the signal intensities of the detected PAA binder fragment ($C_3H_3O_2^-$) were mostly homogenously distributed for all investigated samples. Only at areas close to the current collector, spots with elevated $C_3H_3O_2^-$ intensities were visible in the PAA-based electrodes dried at 30 °C and 90 °C.

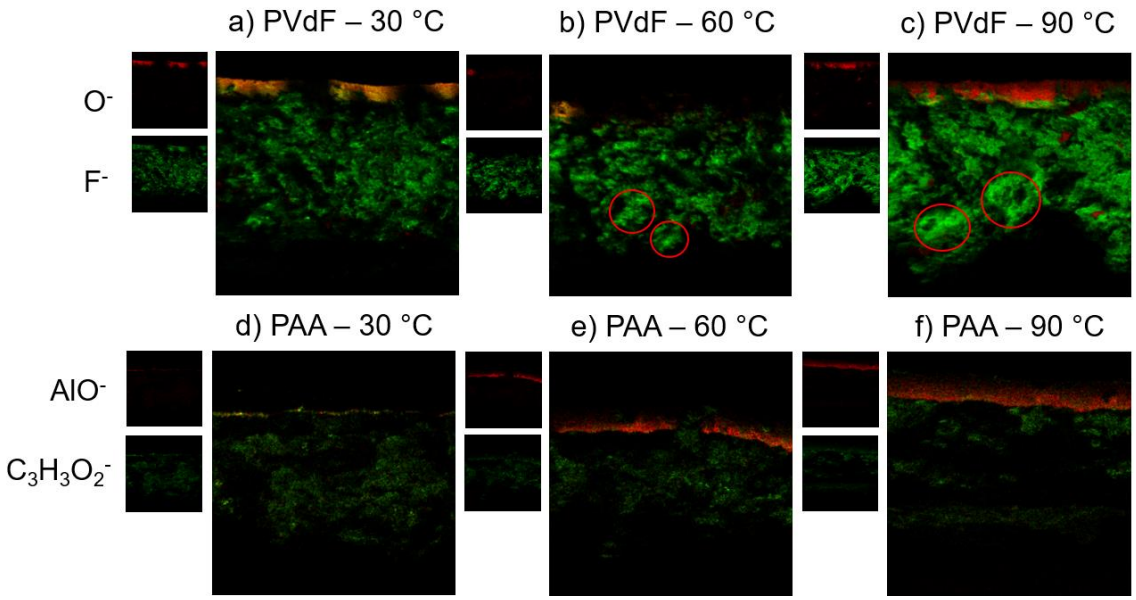

Figure 2-7: ToF-SIMS images of the electrode cross-sections of PVdF- (a-c) and PAA-based (d-f) cathodes, which were dried at various drying temperatures (30 °C, 60 °C and 90 °C). O^- (current collector, red), AlO^- (current collector, red), F^- (PVdF, green) and $C_3H_3O_2^-$ (PAA, green) were the detected fragments (reprinted with permission from ref.[245]).

The increased $C_3H_3O_2^-$ signal intensities were potentially caused by the interaction of PAA with the carbon-coated aluminum current collect as both PAA and the carbon coating of the current collector contain oxygen moieties, which can interact via hydrogen bonds. Taking into account that no harmful effect of the coating drying temperature on the electrochemical performance was observed, the enrichment of PAA at the current collector has no negative effect on the cyclability of the PAA-based cathodes and can therefore be neglected. The distinctions in the drying behavior of the PAA- and PVdF-based electrodes can potentially be explained by the difference in the binder structures. In contrast to PVdF, PAA contains polar functional groups, which can interact via hydrogen bonds with the current collector, active material and conductive additive. As PVdF can only form weak van-der-Waals interactions with the other electrode

components, the more pronounced solvent evaporation at higher drying temperatures potentially leads to the migration of PVdF to the electrode surface. Apart from the insufficient adhesion between PVdF and the other electrode material, a more pronounced interaction between PVdF and NMP relative to the interaction of PAA and NMP may be an additional root for the observed mobility of PVdF.

In conclusion, this study led to the following findings and suggestions which are beneficial for the future mass-production of SPAN cathodes: (i) The influence of the drying step strongly depends on the applied binder system, which indicates that the drying behavior should be tested before the final binder selection. (ii) PVdF, which is commonly applied as a binder for LIB, is not a suitable binder for SPAN electrodes when high drying rates are desired as the interaction between the PVdF binder and the other electrode components (SPAN, conductive carbon) is likely too weak. (iii) Based on the obtained results PAA can be recommended as a suitable binder for SPAN cathodes.

2.2 Influence of the Electrode Density on the Performance of SPAN Cathodes (Publication II)

The process taking place after the electrode drying step in which the electrode sheet is compressed between rollers is called calendering. Calendering enhances the volumetric capacity of the battery electrodes, which is essential for increasing the energy density of the resulting battery cell. Since the Li-S battery possesses a lower volumetric energy density than the LIB, calendering of Li-S cathodes is very important to minimize the gap in volumetric energy between the two battery systems. Besides a positive effect on the energy density, many studies conducted on both Li-S and LIB electrodes have shown that the calendering step strongly affects the cell´s electrochemical performance (section 1.4.2). However, up to now a clear understanding of how the compression of SPAN cathodes affects their performance is still missing in the literature. Similar to the previous section, which shed light on the influence of the drying step, this section investigates the effect of the calendering step on the electrochemical performance of SPAN cathodes.

2.2.1 Physical and Electrochemical Characterization of the SPAN Cathodes

To evaluate the influence of the electrode density on the performance of SPAN cathodes, pristine SPAN electrodes (0.80 g cm^{-3}) were calendered to result in three additional electrode densities (0.95 g cm^{-3}, 1.05 g cm^{-3} and 1.20 g cm^{-3}). Table 2-2 summarizes the physical properties of the pristine and compressed electrodes. By varying the line gap between the rollers of the calender, the coating density was decreased from 59 µm (pristine state) to 49 µm, 43 µm and 38 µm, respectively.

Table 2-2: Physical properties of the SPAN cathodes, which were compressed to different electrode densities. The standard deviation of at least two independent measurements is represented by the error bars (reprinted with permission from ref.[246]).

Sample	Coating weight [mg]	Coating thickness [µm]	Electrode density [g cm^{-3}]	Porosity [%]
Pristine	10.1 ± 0.2	59 ± 1	0.80 ± 0.02	56 ± 1
1	10.1 ± 0.2	49 ± 1	0.95 ± 0.02	48 ± 1
2	10.1 ± 0.2	43 ± 1	1.05 ± 0.02	41 ± 1
3	10.1 ± 0.2	38 ± 1	1.20 ± 0.02	33 ± 1

The electrode porosity was calculated with equation 2.1 to evaluate the impact of electrode density on the porosity. For calculating the electrode porosity (p), coating mass (m), material bulk densities (ρ) and coating volume (V) need to be known.

$$p = \frac{m_{coating}}{\rho_{material}} \cdot \frac{1}{V_{coating}} \tag{2.1}$$

By compressing the electrodes to higher electrode densities, the porosity was reduced from 56 % (pristine state) to 48 %, 41 % and 33 % for the electrodes with densities of 0.95 g cm^{-3}, 1.05 g cm^{-3} and 1.20 g cm^{-3}, respectively.

SEM measurements on the surface of the prepared electrodes were conducted to investigate compression-induced changes in the electrode morphology. As depicted in Figure 2-8, increasing the electrode density resulted in a closer packing of the particles and a reduction of the void volume within the electrode structure. At the highest electrode density (1.20 g cm^{-3}), several particle agglomerates became visible. Mercury intrusion porosity measurements were conducted to further follow up on the compression-induced changes in the pore structure.

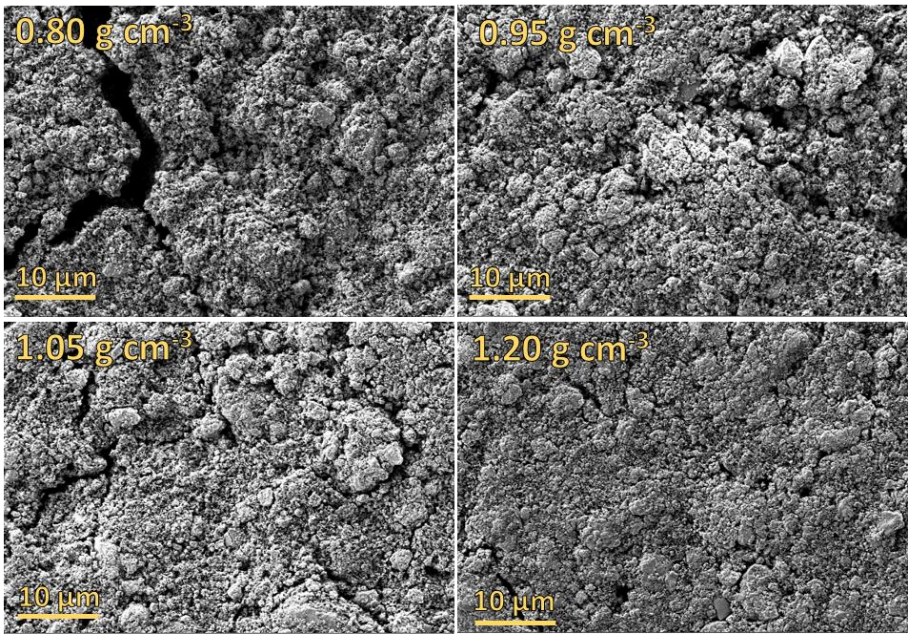

Figure 2-8: SEM images (top view) of the SPAN electrodes that were compressed to different electrode densities (reprinted with permission from ref.[246]).

Figure 2-9 illustrates the results of the mercury intrusion porosity measurements. Increasing the electrode densities reduced the pore size and the overall obtainable pore volume. This effect was most pronounced for the SPAN cathodes that were compressed

to the highest electrode density. By increasing the electrode density from 0.80 g cm^{-3} to 1.20 g cm^{-3} the specific pore volume was reduced by 50 % and the average pore size was lowered from 0.43 µm to 0.22 µm. Both the SEM images and mercury intrusion measurements indicate that calendering to higher electrode densities (> 1.05 g cm^{-3}) has a severe effect on the pore size and overall pore volume. As described in section 1.4.2, previous studies conducted on Li-S cathode materials have shown that a high overall pore volume is needed to ensure fast Li^+ ion transport and high conversion rates.[197-198] Therefore, compressing the SPAN electrodes to higher electrode densities potentially harms the overall electrochemical performance.

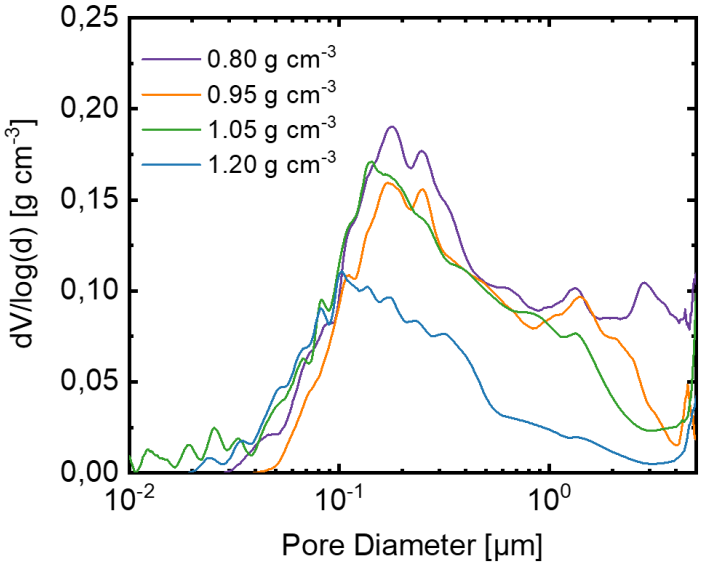

Figure 2-9: Pore size distribution of the SPAN cathodes, which were compressed to various electrode densities, determined by mercury intrusion porosity measurements (reprinted with permission from ref.[246]).

To verify the impact of the calendering step on the transport of Li^+ ions, the tortuosity values of the investigated SPAN cathodes were determined by using an EIS-based approach. Generally, tortuosity, which is defined as the quotient of the effective pathway to the direct pathway in porous media, has often been applied to quantify the ability of Li^+ ions to move within a porous electrode. The theory behind the impedance-based methodology, which was used to obtain the tortuosity values, is described in section 1.6.1.3. The obtained tortuosity values for the tested SPAN electrodes are depicted in Table 2-3. By compressing the SPAN cathodes, the tortuosity increased from 2.4 (pristine state) to 2.6, 2.9 and 3.1 for the SPAN electrodes with densities of 0.95 g cm^{-3}, 1.05 g cm^{-3} and 1.20 g cm^{-3}, respectively. Surprisingly, the increase in tortuosity was rather linear and no sharp increase in the tortuosity was observed when the electrodes were compressed to

the highest electrode density (Figure 2-10a). This indicates that the determined severe reduction in the obtainable pore volume of the SPAN cathodes, which were compressed to the highest electrode density (1.20 g cm^{-3}), likely had no significant impact on the Li^+ ion transport pathways.

Table 2-3 Porosities and tortuosity values of the investigated SPAN electrodes. The standard deviation of at least two independent measurements is represented by the error bars (reprinted with permission from ref.[246]).

Electrode density [g cm^{-3}]	Porosity [%]	Tortuosity [-]
0.80	56 ± 1	2.4 ± 0.1
0.95	47 ± 1	2.6 ± 0.1
1.05	41 ± 1	2.9 ± 0.1
1.20	33 ± 1	3.1 ± 0.1

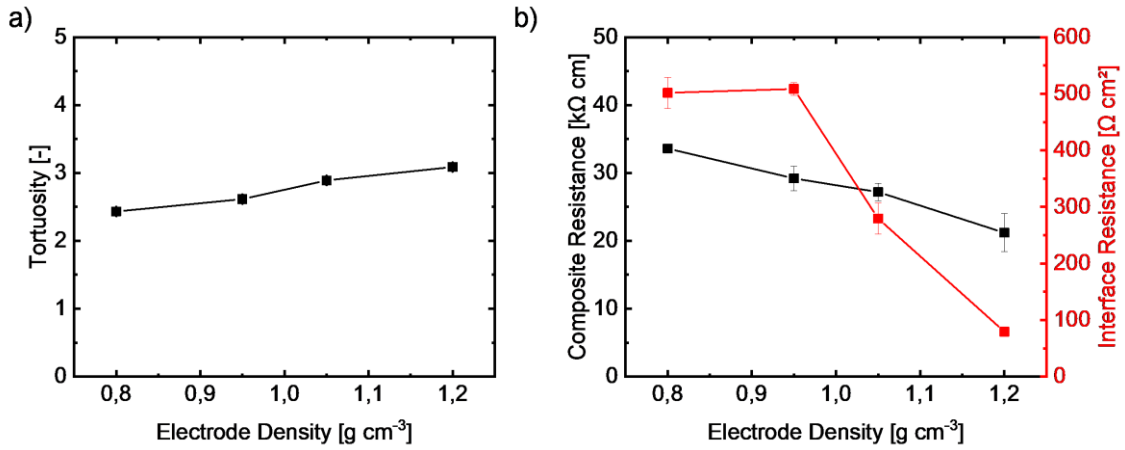

Figure 2-10: . a) Tortuosity values, which were obtained from the measurements as a function of the SPAN electrode density The standard deviation of at least two independent measurements is represented by the error bars. b) Composite resistance (black line) and interphase resistance (red line) plotted over the electrode density of the SPAN cathodes (reprinted with permission from ref.[246]).

Besides influencing the ionic resistance, the calendering step can also affect the electrical resistance of the electrode. The electrical resistances of the prepared SPAN electrodes were assessed by utilizing a multipoint probe electrode resistance measurement system, which quantified the electrical resistance within the coating (composite resistance) as well as the resistance at the interphase between the coating and current collector (interphase resistance). Figure 2-10b shows both composite resistance (black line) and interphase resistance (red line) as a function of the electrode density. For the composite resistance, a slight decrease with increasing electrode density was visible. In contrast, a sharp decline

in the interphase resistance was observed for the SPAN electrodes, which were compressed to densities ≥ 1.05 g cm^{-3}. For instance, compressing the cathodes from 0.80 g cm^{-3} to 1.20 g cm^{-3} reduced the contact resistance at the interphase between the coating and current collector by a factor of six. Hence, calendering of the electrodes should most possibly have a positive effect on the electrochemical performance if the electrical resistance contributes the most to the total impedance of the SPAN cathodes.

2.2.2 Influence of the Electrode Density on the Electrochemical Performance

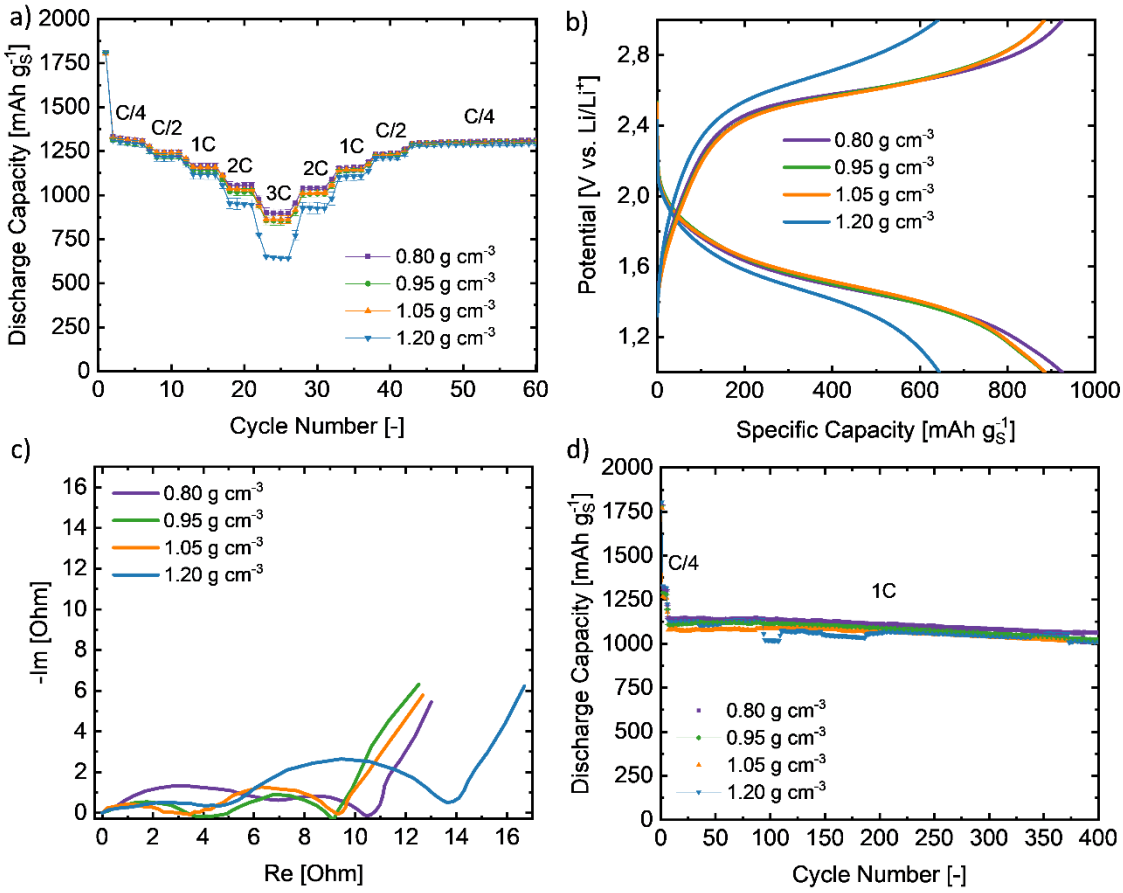

Figure 2-11: a) Rate capabilities of SPAN cathodes, which were compressed to various electrode densities. The galvanostatic cycling was conducted with applied currents ranging from C/4 (~ 0.7 mA cm^{-2}) to 3C (~ 8.1 mA cm^{-2}). The standard deviation of at least two independent measurements is represented by the error bars. b) Voltage profiles at 3C. c) Nyquist plots of the investigated SPAN cathodes. EIS measurements were conducted with a lithiated stainless steel finger-shaped reference electrode and measured at 50 % SOC after five preformation cycles at C/4. To enable better comparability the high-frequency resistance (R_1) was subtracted from all the measurements. d) Long-term cycling performance of the investigated SPAN cathodes at 1C (~ 2.7 mA cm^{-2}) (reprinted with permission from ref.[246]).

First, the prepared SPAN electrodes were cycled against Li metal at alternating current densities (C/4 – 3C) to verify the impact of the electrode density on the rate capability. As visible in Figure 2-11a, no distinction in the rate performance was observed for SPAN electrodes compressed to densities below 1.20 g cm^{-3}. However, compressing the SPAN

cathodes to the highest electrode density (1.20 g cm^{-3}) resulted in a sharp decrease in the obtainable discharge capacity at higher rates (≥ 2C). For instance, increasing the electrode density from 1.05 g cm^{-3} to 1.20 g cm^{-3} reduced the obtainable capacity from 864 mAh g_S^{-1} to 647 mAh g_S^{-1}. Figure 2-11b depicts the voltage profiles of the tested SPAN cathodes at 4C. Compressing the electrodes to a density of 1.20 g cm^{-3} resulted in a shift of the voltage profile to lower potentials during discharge and higher potentials during charge. The shift of the voltage curves indicates that the lower rate capability of the most compressed SPAN electrode (1.20 g cm^{-3}) was caused by an overpotential, which resulted in an incomplete dis(charge) at higher rates. Similar to the previous study (section 2.1), reference-assisted impedance spectroscopy was applied to assess the impact of the electrode density on the internal resistance of the SPAN cathodes. The EIS measurements were performed at 50 % SOC after cycling for five preformation cycles at C/4. Figure 2-11c shows the Nyquist plots of the SPAN electrodes, which were calendered to various electrode densities. The impedance results were modeled with the equivalent electric circuit model depicted in Figure 2-12. Within the proposed circuit model, R_1 was the high-frequency resistance, R_2/Q_1 was used to model the electrical resistance at the grain boundary between the particles as well as the contact resistance at the interphase between the coating and current collector, R_3/Q_2 was assigned to the charge transfer resistance and Q_3 represented the Li^+ ion diffusion. The exact fitted values of R_1, R_2 and R_3 are summarized in Table 2-4. Compressing of the SPAN electrodes to > 0.80 g cm^{-3} resulted in a slight decrease (~ 2-3 Ω) of the electrical resistances (R_2) between the SPAN particles and at the interface between the coating and the current collector. The decrease in the R_2 value is in good agreement with the obtained resistivity measurement (Figure 2-10a). This further suggests that compressing of the electrodes decreases the contact resistance both at the grain boundary between the particles and at the coating / current collector interphase. The SPAN cathodes, which were compressed to the highest electrode density (1.20 g cm^{-3}), had a more than two times higher charge-transfer resistance (R_3) than the electrodes with lower electrode density (≤ 1.05 g cm^{-3}). The sharp increase of the R_3 value likely was the origin of the lower rate capability observed for the cathode with the highest degree of compression. Considering the earlier observed reduction in pore volume (Figure 2-9), it can be assumed that the higher charge-transfer resistance of the electrode with a density of 1.20 g cm^{-3} originated from a compression-induced reduction of active reduction sites and/or a decline in void spaces for electrolyte uptake. The obtained results agree with previous studies conducted on S-based electrodes. For instance, Kang et al.

showed that calendering of C/S-composite cathodes to lower porosity resulted in a reduction of active reaction sites, which harmed the electrochemical performance at higher rates.[198] Besides investigating the impact of the calenderation step on the rate capability, the long-term cycling ability of the SPAN electrodes with different electrode densities was evaluated. During the long-term cycling test, no distinctions in capacity retention were observed (Figure 2-11d). All cells had capacity fade of 0.05 % per cycle.

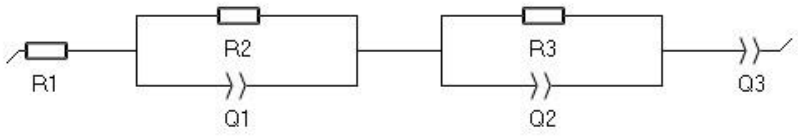

Figure 2-12: Equivalent circuit model used to fit the obtained Nyquist plots in Figure 2-11c (reprinted with permission from ref.[246]).

Table 2-4: Exact fitted resistance values obtained from the Nyquist plots shown in Figure 2-11c. (reprinted with permission from ref.[246]).

Electrode density [g cm^{-3}]	**R_1 [Ω]**	**R_2 [Ω]**	**R_3 [Ω]**
0.80	7.6	8.3	2.9
0.95	7.1	6.0	4.8
1.05	8.3	5.8	4.4
1.20	6.5	5.2	9.4

2.2.3 Dependence of the Energy Density on the Electrode Density

Since calendering can significantly increase the volumetric capacity of battery electrodes, the effect of the electrode density on the volumetric energy density was estimated for a multi-layer Li-SPAN pouch cell. The energy densities were calculated based on a simplified model from Liu et al. using equation 2-2 and the parameters illustrated in Table 2-5.

$$E_v = \frac{U \cdot x \cdot c_{areal}}{d_{cathode} + d_{Li} + d_{Al} + d_{Cu} + d_{separator}} \qquad (2.2)$$

where U is the voltage of the cell, E_v is the volumetric energy density, c_{areal} is the areal capacity, x is the capacity utilization, d_i is the thickness of the cathode, anode, current collector foils and separator.

Table 2-5: Parameters used for calculating the volumetric energy densities of Li//SPAN stacked cells (reprinted with permission from ref.[246]).

Li // SPAN (90 wt%)	
Capacity utilization (x)	80 % (536 mAh g^{-1}_{SPAN})
Cell voltage (U)	1.69 V
Anode current collector thickness (d_{anode})	8 µm
Cathode current collector thickness ($d_{cathode}$)	12 µm
Separator thickness ($d_{separator}$)	20 µm
Lithium excess	100 %

As visible in equation 2.5, the energy densities were calculated neglecting the additional volume of the pouch foil and potential excess electrolyte.

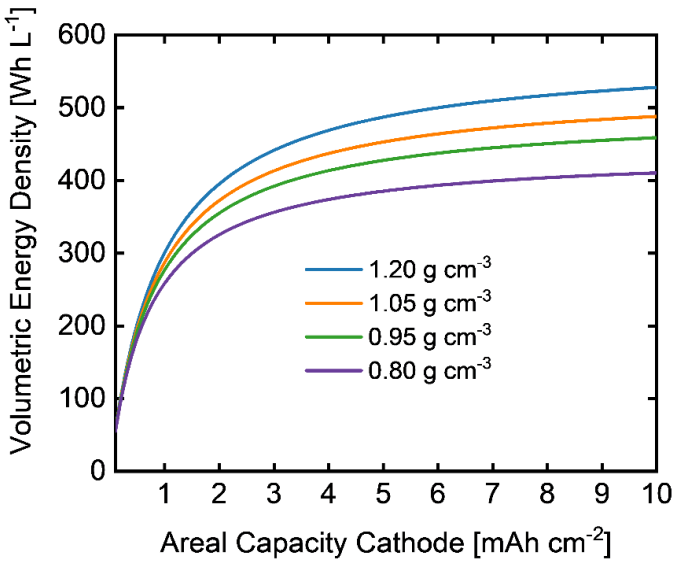

Figure 2-13: Volumetric energy density as a function of the areal loading calculated for different SPAN electrode densities (reprinted with permission from ref.[246]).

In Figure 2-13, the calculated volumetric energy density values as a function of the areal cathode capacity calculated for different electrode densities are depicted. The obtained results clearly show that increasing the density of the SPAN cathodes can strongly improve the energy density of a Li-SPAN pouch cell. For instance, compressing an SPAN cathode with areal loading of 3.0 mAh cm^{-2} from its pristine state to an electrode density of 1.05 g cm^{-3} would increase the volumetric energy density by 16 %. Additionally, the calculated energy density curves point out that the cathode loading should be above 2.5 mAh cm^{-2} to achieve sufficiently high energy densities as the volume contribution of current collector foils is high at low areal capacities.

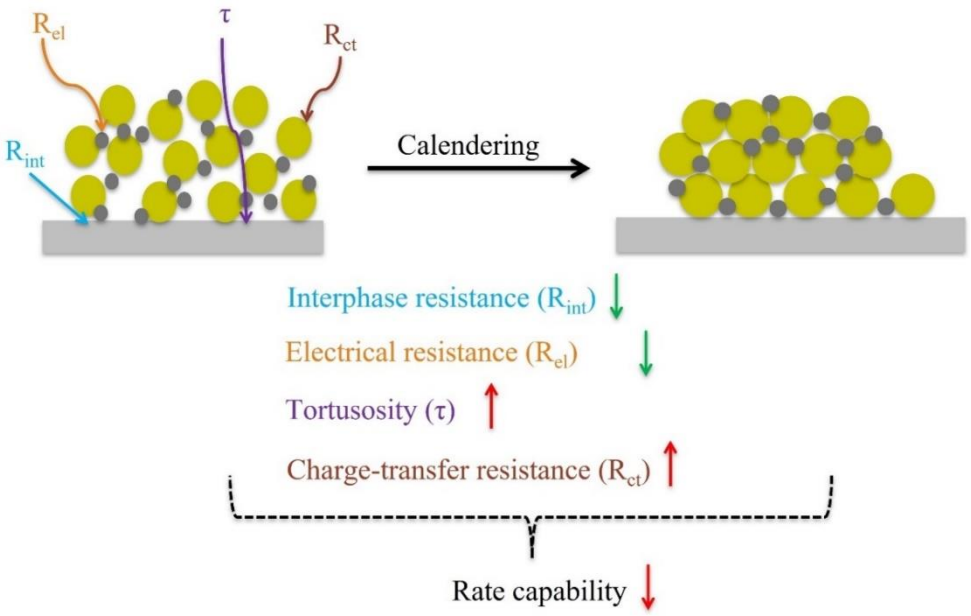

Figure 2-14: Schematic illustration of the impact of the calendering step on the electrochemical performance of SPAN-based cathodes.

Figure 2-14 summarizes the effect that calendering has on the electrochemical properties of SPAN cathodes. Calendering of SPAN cathodes decreased both the contact resistance at the coating / current collector interphase but increased both the tortuosity and charge-transfer resistance. At electrode densities of 1.20 g cm^{-3}, the increase in the charge-transfer resistance was most severe and had a detrimental effect on the rate capability.

This study led to the following conclusions, which are useful for the future commerciuallization of SPAN cathodes: (i) Calendering of SPAN electrodes strongly improves the energy density. For instance, it was revealed that compressing the SPAN cathodes from their pristine state (0.80 g cm^{-3}) to 1.05 g cm^{-3} would increase the energy density of a multi-layer Li-SPAN pouch cell by 16 %. (ii) Compressing of SPAN cathodes to very high electrode densities (1.20 g cm^{-3}) is not recommend as this results in poorer rate capablilty. (iii) The results of this study suggest that compressing the SPAN cathodes to an electrode density of 1.05 g cm^{-3} is desirable as this is the best tradeoff between obtainable energy density and performance.

2.3 Self-Cross-Linked Binder for Silicon Anodes (Publication III)

Besides the Li-SPAN battery, LIBs that apply Si instead of graphite as anode material are often regarded as future battery technology. Nevertheless, the severe volume expansion of the Si anode limits the cycling life of the cell and thereby prevents its commercial application. Hence, similar to SPAN cathodes (sections 2.1 & 2.2) the electrode composition as well as processing conditions need to be optimized and understood in detail to improve the cycle performance and commercialize LIBs with Si anodes. As described in section 1.2.5, the electrode formulation and especially the binder choice strongly affect the electrochemical performance of Si anodes. Particularly, cross-linked binder systems have shown the ability to strongly compensate for the volume expansion and thereby significantly enhance the cycle life. Nevertheless, these binder systems are often based on multi-component systems, which complicates their commercial application. In this section, an self-cross-linked binder, which is easy-to-prepare and process will be introduced as a novel binder for high-loading Si anodes.

2.3.1 Preparation and Physical Properties of p(AM-*co*-HMA)

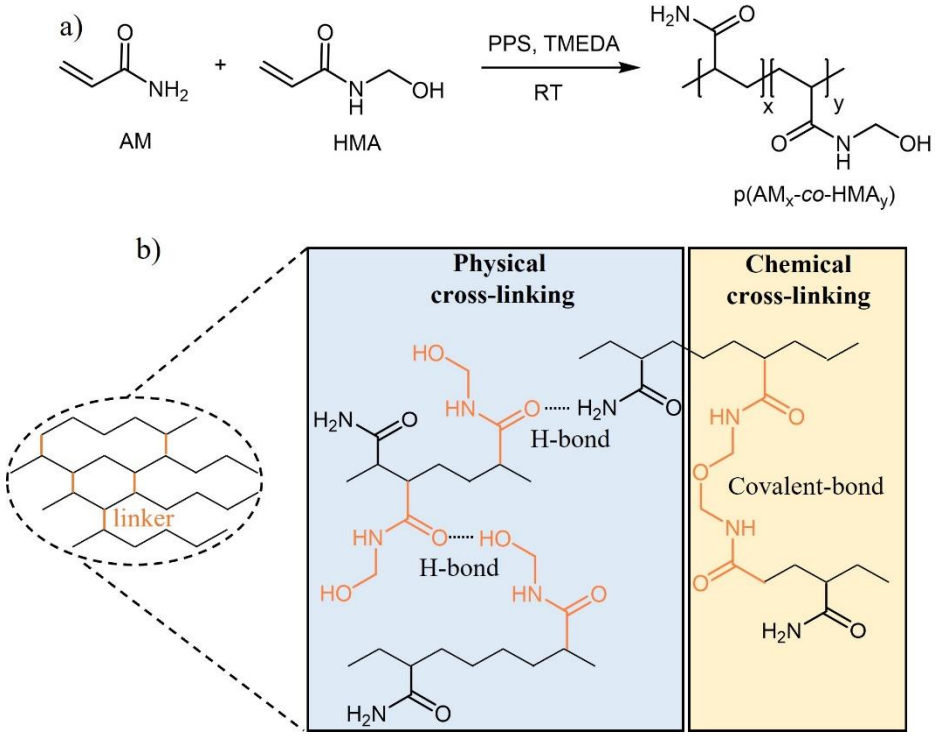

Figure 2-15: a) Preparation of p(AM-*co*-HMA) by redox-initiated copolymerization. b) Schematic illustration of the physical and chemical cross-linking taking place in p(AM-*co*-HMA) (reprinted with permission from ref.[247]).

Poly(acrylamide)-*co*-poly(hydroxymethylacrylate) (p(AM-*co*-HMA)) was synthesized as a potential binder for Si anodes by copolymerization of acryl amide (AM) and *N*-

(hydroxymethyl)-acrylamide (HMA) (Figure 2-15a). As described in literature, the hydroxymethyl groups within an HMA-based polymer self-cross-link via a thermally-induced condensation of two methylol groups. At temperatures above 90 °C, the methylol groups of two HMA units condense to form a bis(methylene) ether (Figure 2-16).[248]

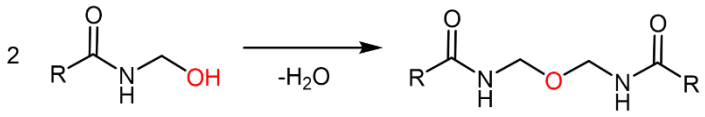

Figure 2-16: Self-cross-linking reaction of the HMA-based polymer.

By constructing a polymeric binder, which contains HMA units, a one-component self-cross-linking binder can be prepared. AM was additionally incorporated in the polymer structure as AM is abundant, water-soluble and able to form hydrogen bonds. As depicted in Figure 2-15b, additional to chemical cross-linking of two HMA units, also physical cross-linking can occur, which is induced by the formation of hydrogen bonds. Hence, this novel binder design should possess superior interaction between the binder and the other electrode components (Si, conductive additive) as well as facilitate good adhesion between the coating and the current collector. In this study, p(AM-co-HMA) was synthesized in three different AM:HMA ratios (p(AM_{90}-*co*-HMA_{10}, p(AM_{70}-*co*-HMA_{30}), p(AM_{60}-*co*-HMA_{40}).

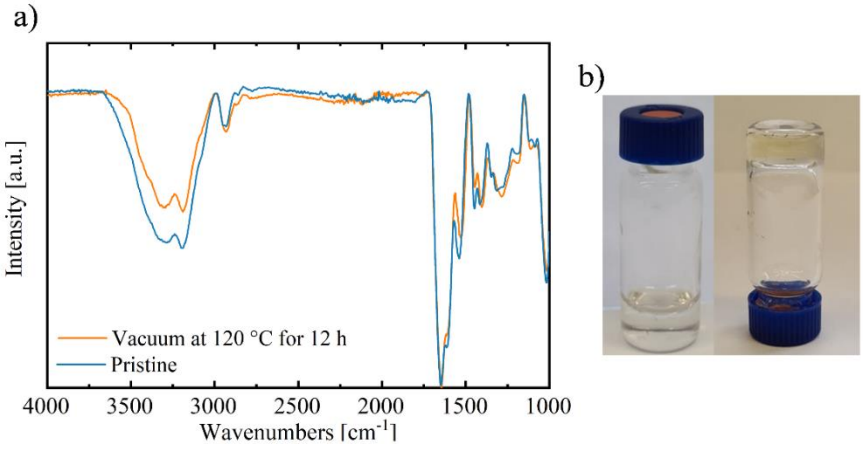

Figure 2-17: a) FTIR spectra of a p(AM-*co*-HMA) film before (blue) and after heating under vacuum (orange). b) Images of p(AM-*co*-HMA) dispersed in ethylene glycol before (left) and after heating at 100 °C (right) (reprinted with permission from ref.[247]).

To evaluate the cross-linking ability of the prepared p(AM-*co*-HMA) copolymers, FTIR spectra were measured of a p(AM-*co*-HMA)-based film before and after heating at 100 °C under vacuum. Heating the film under vacuum resulted in a reduction in the peak intensity of the OH-band (3250 - 3686 cm^{-1}), while the intensity of the band at 1600 cm^{-1}

(C=O stretching) remained unchanged (Figure 2-17a). This confirmed the occurrence of a cross-linking reaction involving the condensation of two OH groups.

The cross-linking was further proven by heating a solution of p(AM-*co*-HMA) in ethylene glycol at 100 °C under vacuum. After heating under vacuum the solution turned into a gel with high viscosity (Figure 2-17b).

High-loading Si anodes (3.6 mAh cm^{-2}) with a Si content of 60 wt.% were prepared with p(AM_{70}-*co*-HMA_{30}) as the binder to examine the impact of the binder on the coating quality. Na-alginate and PAM were applied as reference binder systems. Figure 2-18 illustrates the SEM images of the pristine Si anode surfaces. The SEM images of the Si anodes fabricated with the p(AM_{70}-*co*-HMA_{30}) exhibited a smoother surface morphology with fewer cracks relative to the reference binder systems. In addition to observing the surface quality of the anodes, peel tests were conducted to investigate the influence of the binder on the adhesion. The adhesion tests were performed on p(AM_{70}-*co*-HMA_{30})- and Na-alginate-based Si electrode sheets.

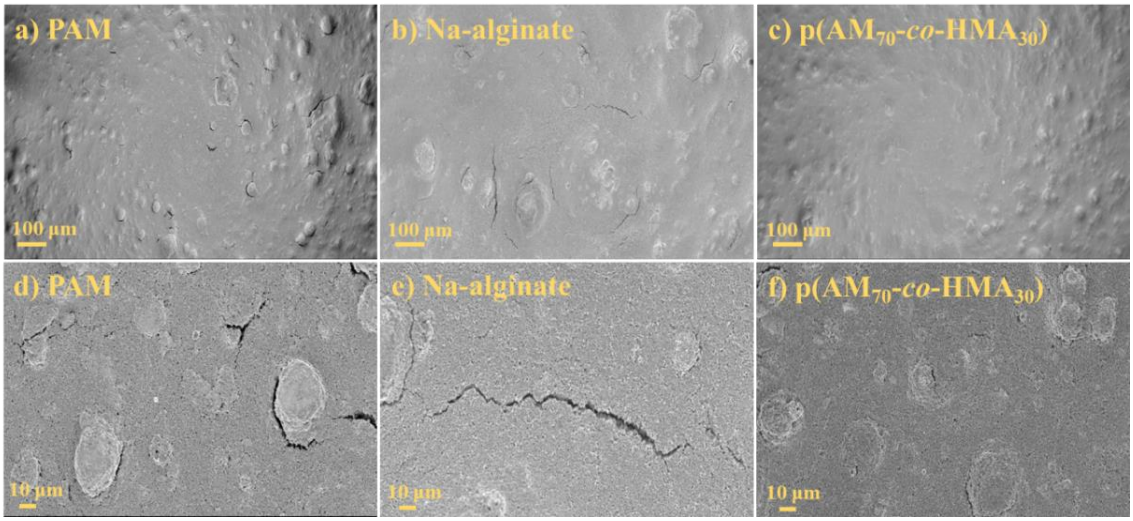

Figure 2-18: SEM images (top view) of the pristine Si anodes that were prepared with (a, d) PAM, (b, e) Na-alginate and (c, f) p(AM_{70}-*co*-HMA_{30}). The scale bars are 100 µm or 10 µm in size (reprinted with permission from ref.[247]).

As visible in Figure 2-19, the p(AM_{70}-*co*-HMA_{30})-based electrode sheet remained almost completely undamaged while large parts of the Na-alginate-based coating were ripped off from the current collector after performing the peel test. Both the SEM images and the adhesion test showed that the p(AM_{70}-*co*-HMA_{30})-based anodes exhibited superior coating quality and adhesion to the current collector, which could be attributed to the self-cross-linked structure of the p(AM_{70}-*co*-HMA_{30}) binder. In conclusion, the p(AM-*co*-

HMA) binder possessed promising physical properties as well as superior binding ability, which should be beneficial for the electrochemical performance of high-loading Si anodes.

Figure 2-19: Images of Si coatings with Na-alginate (upper panel) and p(AM_{70}-*co*-HMA_{30}) (lower panel) as binder after the adhesion test (reprinted with permission from ref.[247]).

2.3.2 Influence on the Electrochemical Performance

To verify the electrochemical characteristics of the synthesized p(AM-*co*-HMA) copolymers, Si electrodes were prepared and characterized in half-cells. Na-alginate- and PAM-based Si anodes were applied as reference samples. In the first cycling test, the cycling performance was evaluated by cycling the Si electrodes prepared with different binders at C/5 after conducting three formation cycles at C/20. All tested cells showed specific capacities above 3500 mAh g_{Si}^{-1} and similar Coulombic efficiencies (~ 89 %) in the first preformation cycle (2-20b). As shown in Figure 2-20a, the electrodes fabricated with p(AM_{70}-co-HMA_{30}) and p(AM_{60}-*co*-HMA_{40}) exhibited far superior capacity retention than the anodes, which were prepared with p(AM_{90}-*co*-HMA_{10}) and the reference binder systems (Na-alginate, PAM). The positive effect of p(AM_{70}-*co*-HMA_{30}) and p(AM_{60}-*co*-HMA_{40}) on capacity retention was especially noticeable in the first ten cycles. At the end of the cycling test, the capacity retentions were 70 %, 67 %, 45 % and 39 % for the anodes prepared with p(AM_{70}-*co*-HMA_{30}), p(AM_{60}-*co*-HMA_{40}), Na-alginate and PAM, respectively. The results of the cycling test indicate that copolymerizing the self-cross-linking HMA monomer (HMA content ≥ 30 %) into the polymeric binder structure is beneficial for the capacity retention of high-loading Si anodes. For the following electrochemical tests, p(AM_{70}-*co*-HMA_{30})-, PAM- and Na-alginate-based Si electrodes were used.

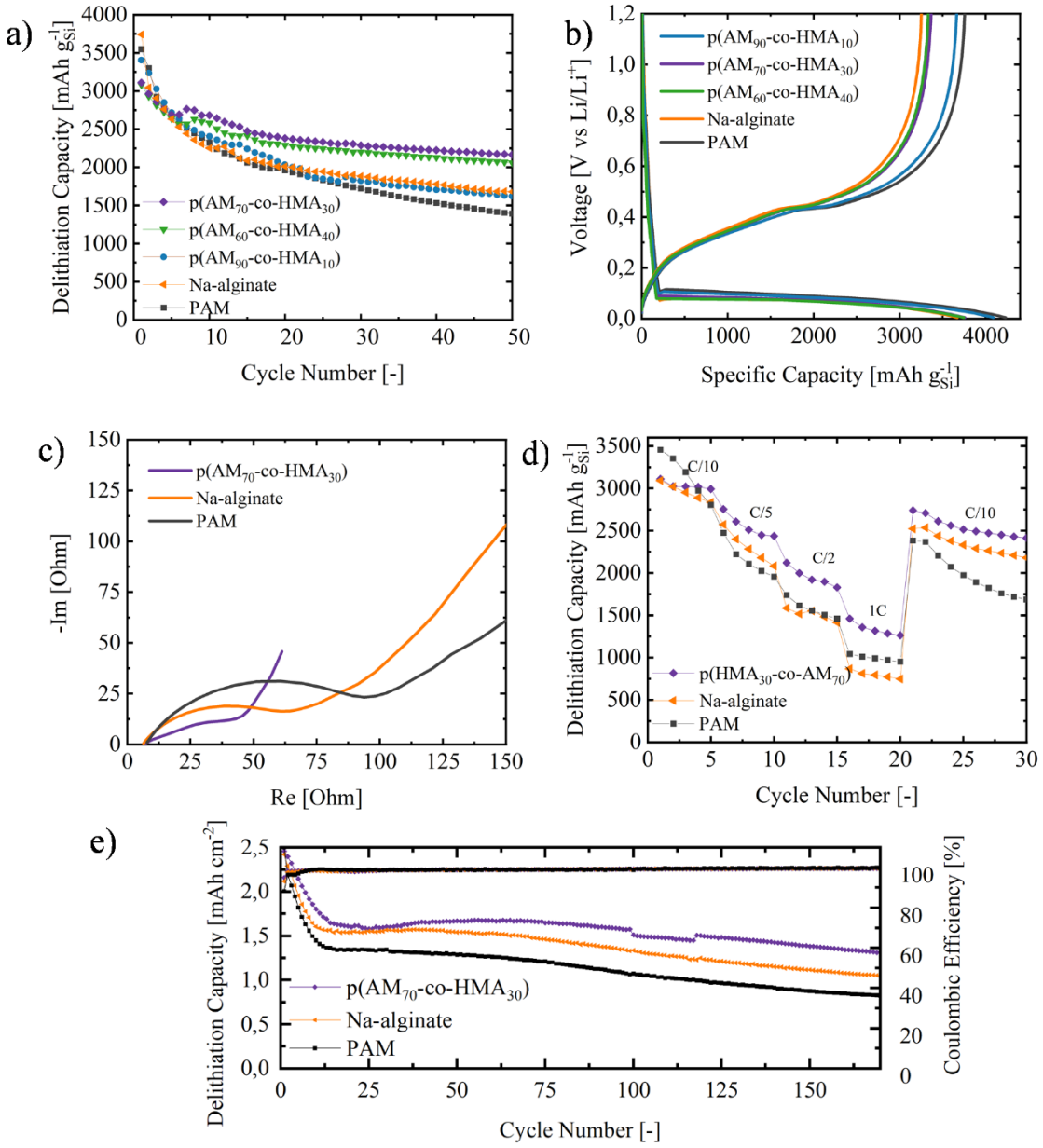

Figure 2-20: a) Cycling performance of Si anodes prepared with different binders at C/5 (~ 0.7 A g^{-1}). b) Voltage curves of the formation cycle at C/20. c) Nyquist plots of the Si electrodes after ten C/5 cycles. d) Cycling performance of the Si anodes at alternating rates (C/10 – 1C). e) Electrochemical performance of the Si electrodes at C/2 (1.8 A g^{-1}) (reprinted with permission from ref.[247]).

Besides cycling the Si anodes at C/5, the electrodes were additionally cycled at a higher rate (C/2). Similar to the cycling test at C/5, the p(AM$_{70}$-*co*-HMA$_{30}$)-based anodes exhibited a far lower capacity decay during the first ten cycles compared to electrodes fabricated with the reference binders, which strongly improved the overall capacity retention of the p(AM$_{70}$-*co*-HMA$_{30}$)-based anode. To gain a better understanding of how the p(AM$_{70}$-*co*-HMA$_{30}$) binder affects the capacity drop in the initial cycles, EIS measurements were acquired after cycling the cells for ten cycles at C/5. Figure 2-20c illustrates the Nyquist plots of the Si anodes fabricated with p(AM$_{70}$-*co*-HMA$_{30}$), Na-

alginate and PAM as a binder, which were fitted with the equivalent circuit model shown in Figure 2-21. The applied circuit model consisted of a high-frequency resistance (R_1), two R/Q elements (R_2/Q_1, R_3/Q_2) and a Warburg element (W_1), which represented the Li^+ ion diffusion, in serial connection. The R/Q elements were used to model the resistance of the SEI layer (R_2/Q_1) and the charge transfer resistance of the Si electrodes (R_3/Q_1). Table 2-6 summarizes the fitted values of R_1, R_2 and R_3. The sum of R_2 and R_3 was labeled as the interphase resistance as both the SEI layer resistance and the charge-transfer resistance occur on the interphase of the electrodes. As visible in Table 2-6, the anode fabricated with the reference binder systems had significantly higher interphase resistances (R_2+R_3) compared to the p(AM_{70}-*co*-HMA_{30})-based electrode. For the p(AM_{70}-*co*-HMA_{30})-, Na-alginate- and PAM-based anodes the interphase resistances were 45 Ω, 82 Ω and 103 Ω, respectively. As explained in the literature, continuous expansion/shrinkage of the Si particles causes a reduction in the electrical and ionic contact and the creation of a thick SEI layer. Both effects increase the interphase resistance.[249] Hence, the cross-linked binder structure within the p(AM_{70}-*co*-HMA_{30})-based anodes likely helped to limit the volume changes and thereby restricted the increase of interphase resistance during cycling, which was beneficial for the capacity retention. Figure 2-20d depicts the cycle test conducted at alternating rates (C/10 – 1C). Compared to the anodes prepared with the reference binder, the p(AM_{70}-*co*-HMA_{30})-based anode possessed superior rate capability. For instance, at a rate of 1C, the p(AM_{70}-*co*-HMA_{30})-based anodes reached at specific capacity of 1316 mAh g_{Si}^{-1} while the obtained capacity of the Na-alginate-based electrode was 795 mAh g_{Si}^{-1}. The enhanced rate capability can likely be attributed to a lower internal resistance of the anode containing p(AM_{70}-*co*-HMA_{30}) as the binder. In summary, all electrochemical experiments point out that using a binder, which consists of the self-cross-linking HMA monomer (≥ 30 wt.%), is beneficial for the cyclability of Si anodes.

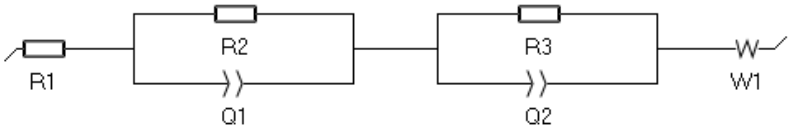

Figure 2-21: Equivalent circuit model used to fit the obtained Nyquist plots in Figure 2-20c (reprinted with permission from ref.[247]).

Table 2-6: Exact fitted resistance values obtained from the Nyquist plots shown in Figure 2-20c (reprinted with permission from ref.[247]).

Sample	R_1 [Ω]	R_2 [Ω]	R_3 [Ω]
PAM	4.7	1.2	101.9
Na-alginate	8.5	2.6	79.5
p(AM_{70}-*co*-HMA_{30})	7.0	3.2	41.5

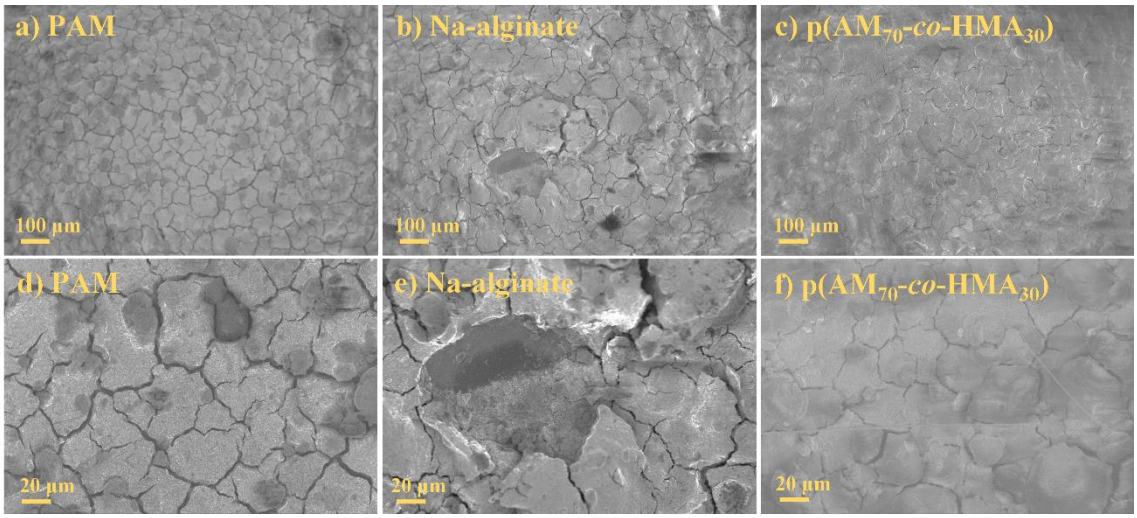

Figure 2-22: SEM images (top view) of the cycled Si anodes that were prepared with (a, d) PAM, (b, e) Na-alginate and (c, f) p(AM_{70}-*co*-HMA_{30}). The scale bars are 100 µm or 20 µm in size (reprinted with permission from ref.[247]).

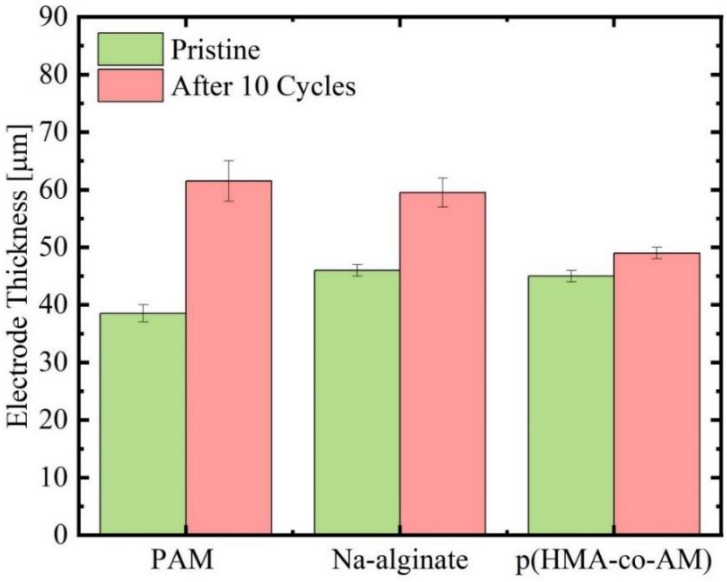

Figure 2-23: Thickness of the Si electrodes with PAM, Na-alginate and p(AM_{70}-*co*-HMA_{30}) as binder before and after cycling (reprinted with permission from ref.[247]).

To gain a better understanding of how the cross-linked structure of the p(AM_{70}-*co*-HMA_{30}) helps to restrict the morphology changes of the Si anodes, both SEM measurements and thickness measurements were conducted after cycling the electrodes for ten cycles at C/5. As visible in Figure 2-22, the anodes fabricated with p(AM_{70}-*co*-HMA_{30}) showed a generally smoother surface with less visible cracks compared to the anodes containing the reference binders. The thickness measurements revealed that the p(AM_{70}-*co*-HMA_{30})-based electrodes exhibited a significantly lower irreversible expansion than the Na-alginate and PAM-based Si anodes. For p(AM_{70}-*co*-HMA_{30})-, Na-alginate and PAM-based anodes, the thickness increased by 8 %, 20 % and 34 %, respectively. As proven by SEM measurements and post-mortem thickness measurements, the superior electrochemical performance of the p(AM-*co*-HMA)-based Si anodes can be attributed to the ability of the cross-linked polymer matrix to restrict the volume changes of the Si particles, which helped to preserve the mechanical integrity of the electrode during cycling.

In summary, a novel one-component binder for high-loading Si anodes was prepared, which exhibited superior electrochemical characteristics compared to conventional applied binder systems. This study showed that incorporation of HMA as a self-cross-linking monomer in the binder structure induced the formation of a cross-linked network, which severely improved the performance of the Si anodes. In contrast to other future active materials (e.g., SPAN), the electrode formulation is not completely obtimized to enable commercial application. However, the application of HMA-based polymers is a promising pathway to make way for the commercial application of Si anodes. Future work could focus on incorporating the self-cross-linkable HMA monomer into different polymeric binder designs to further improve the performance of Si anodes.

3 Conclusions

In conclusion, SPAN cathodes as well as Si anodes were characterized and optimized to bring these active materials one step closer to commercialization. Both electrode materials possess promising electrochemical characteristics. Nonetheless, before these materials can be commercially applied, their electrode formulation and processability need to be optimized. In the first part of this thesis, the processability of SPAN electrodes was evaluated. The focus was placed on two major electrode processing steps. First, the influence of the electrode drying step was investigated via various analytical and electrochemical methods. The effect of the drying temperature was evaluated for both PAA- and PVdF-based SPAN cathodes. It was revealed that an increase in the drying temperature led to a sharp decrease in the rate capability of the PVdF-based electrodes. The reduction in the rate capability was induced by the migration of the PVdF binder towards the electrode surface, which led to a sharp increase in the charge-transfer resistance. Surprisingly, the performance of the PAA-based SPAN electrodes was independent of the applied drying rate. In the following study, the effect of the calendering step on the performance of SPAN electrodes was investigated. The SPAN cathodes were compressed from their pristine state (0.80 g cm^{-3}) to three different electrode densities (0.95, 1.05, 1.20 g cm^{-3}). Compressing the electrodes to the highest electrode density resulted in a decrease in the rate capability, which was rooted by a growth in the charge-transfer resistance. As proven by mercury intrusion measurements, the increase in the internal resistance was caused by a compression-induced reduction of active reaction sites. Nevertheless, increasing the electrode density up to 1.05 g cm^{-3} was possible without a penalty in power performance. Calculations revealed that the increase in electrode density from the pristine state (0.80 g cm^{-3}) to 1.05 g cm^{-3} would lead to a 16 % increase in the volumetric energy density for a multi-layer Li-SPAN pouch cell. Based on the results of these studies, the following recommendation can be made for the processing of SPAN cathodes: (i) The commonly applied PVdF binder should not be used when high drying rates are required. (ii) PAA can be used as an alternative to PVdF. (iii) SPAN electrodes should be compressed to an electrode density of 1.05 g cm^{-3} as this is the best tradeoff between reachable energy density and performance. In the third part of this thesis, p(AM-*co*-HMA) was introduced as a self-cross-linking binder for high-loading Si anodes. Electrodes prepared with the p(AM-*co*-HMA) exhibited better adhesion to the current collector, superior capacity retention and higher rate capability compared to commonly applied binder systems (e.g., Na-alginate). The superior

electrochemical performance of the p(AM-co-HMA)-based Si anodes can be ascribed to the ability of the cross-linked polymer matrix to restrict the volume changes of the Si particles during cycling. This study clearly showed that optimizing the electrode composition is a powerful tool to improve the performance of Si anodes.

4 References

1. Zubi, G.; Dufo-López, R.; Carvalho, M.; Pasaoglu, G., The lithium-ion battery: State of the art and future perspectives. *Renew. Sust. Energ. Rev.* **2018,** *89*, 292-308.
2. Solaymani, S., CO2 emissions patterns in 7 top carbon emitter economies: The case of transport sector. *Energy* **2019,** *168*, 989-1001.
3. Martins, L. S.; Guimaraes, L. F.; Botelho Junior, A. B.; Tenorio, J. A. S.; Espinosa, D. C. R., Electric car battery: An overview on global demand, recycling and future approaches towards sustainability. *J. Environ. Manage.* **2021,** *295*, 113091.
4. Hesse, H.; Schimpe, M.; Kucevic, D.; Jossen, A., Lithium-Ion Battery Storage for the Grid—A Review of Stationary Battery Storage System Design Tailored for Applications in Modern Power Grids. *Energies* **2017,** *10*, 2107.
5. Zhao, Y.; Pohl, O.; Bhatt, A. I.; Collis, G. E.; Mahon, P. J.; Rüther, T.; Hollenkamp, A. F., A Review on Battery Market Trends, Second-Life Reuse, and Recycling. *Sustainable Chemistry* **2021,** *2*, 167-205.
6. Curry, C. *Lithium-Ion Battery Costs and Market*; Bloomberg NEF: 2017.
7. Fichtner, M.; Edström, K.; Ayerbe, E.; Berecibar, M.; Bhowmik, A.; Castelli, I. E.; Clark, S.; Dominko, R.; Erakca, M.; Franco, A. A.; Grimaud, A.; Horstmann, B.; Latz, A.; Lorrmann, H.; Meeus, M.; Narayan, R.; Pammer, F.; Ruhland, J.; Stein, H.; Vegge, T.; Weil, M., Rechargeable Batteries of the Future—The State of the Art from a BATTERY 2030+ Perspective. *Adv. Energy Mater.* **2021,** *12*, 2102904.
8. Fotouhi, A.; Auger, D.; O'Neill, L.; Cleaver, T.; Walus, S., Lithium-Sulfur Battery Technology Readiness and Applications—A Review. *Energies* **2017,** *10*, 1937.
9. Ma, D.; Cao, Z.; Hu, A., Si-Based Anode Materials for Li-Ion Batteries: A Mini Review. *Nano-Micro Lett.* **2014,** *6*, 347-358.
10. Korthauer, R., *Handbuch Li-Ionen-Batterien* Springer: Heidelberg, 2013.
11. Julien, C.; Mauger, A.; Vijh, A.; Zaghib, K., *Lithium Batteries Science and Technologies*. Springer: Switzerland, 2016.
12. Pistoia, G., *Batteries for Portable Devices*. Elsevier: 2005.
13. Kanamura, K., *Next Gerneration Batteries*. Springer: Tokyo, 2021.
14. Deimede, V.; Elmasides, C., Separators for Lithium-Ion Batteries: A Review on the Production Processes and Recent Developments. *Energy Technol.* **2015,** *3*, 453-468.
15. Kurzweil, P., *Angewandte Elektrochemie*. Springer: Wiesbaden, 2020.
16. S., P., *Battery Technology Crash Course*. Switzerland, 2021.
17. Blomgren, G. E., The Development and Future of Lithium Ion Batteries. *J. Electrochem. Soc.* **2017,** *164*, A5019.
18. Deng, D., Li-ion batteries: basics, progress, and challenges. *Energy Sci. Eng.* **2015,** *3*, 385-418.
19. Mizushima, K.; Jones, P. C.; Wiseman, P. J.; Goodenough, J. B., LixCoO2 (0<x<-1): A new cathode material for batteries of high energy density. *Mater. Res. Bull.* **1980,** *15*, 783-789.
20. Asenbauer, J.; Eisenmann, T.; Kuenzel, M.; Kazzazi, A.; Chen, Z.; Bresser, D., The success story of graphite as a lithium-ion anode material – fundamentals, remaining challenges, and recent developments including silicon (oxide) composites. *Sustain. Energy & Fuels* **2020,** *4*, 5387-5416.
21. Yoshino, A., The birth of the lithium-ion battery. *Angew. Chem.* **2012,** *51*, 5798-800.
22. Hannan, M. A.; Hoque, M. M.; Mohamed, A.; Ayob, A., Review of energy storage systems for electric vehicle applications: Issues and challenges. *Renew. Sust. Energ. Rev.* **2017,** *69*, 771-789.
23. Zou, F.; Manthiram, A., A Review of the Design of Advanced Binders for High-Performance Batteries. *Adv. Energy Mater.* **2020,** *10*, 2002508.

24. Marcinek, M.; Syzdek, J.; Marczewski, M.; Piszcz, M.; Niedzicki, L.; Kalita, M.; Plewa-Marczewska, A.; Bitner, A.; Wieczorek, P.; Trzeciak, T.; Kasprzyk, M.; P.Łężak; Zukowska, Z.; Zalewska, A.; Wieczorek, W., Electrolytes for Li-ion transport – Review. *Solid State Ion* **2015,** *276*, 107-126.
25. Kang, X., Nonaqueous Liquid Electrolytes for Lithium-Based Rechargeable Batteries. *Chem. Rev.* **2004,** *104*, 4303.
26. Tarascon, J. M.; Guyomard, D., New electrolyte compositions stable over the 0 to 5 V voltage range and compatible with the Li1+xMn2O4/carbon Li-ion cells. *Solid State Ion* **1994,** *69*, 293-305.
27. Aravindan, V.; Gnanaraj, J.; Madhavi, S.; Liu, H. K., Lithium-ion conducting electrolyte salts for lithium batteries. *Chem. Eur. J.* **2011,** *17*, 14326-46.
28. Zhang, S. S., A review on electrolyte additives for lithium-ion batteries. *J. Power Sources* **2006,** *162*, 1379-1394.
29. Heiskanen, S. K.; Kim, J.; Lucht, B. L., Generation and Evolution of the Solid Electrolyte Interphase of Lithium-Ion Batteries. *Joule* **2019,** *3*, 2322-2333.
30. An, S. J.; Li, J.; Daniel, C.; Mohanty, D.; Nagpure, S.; Wood, D. L., The state of understanding of the lithium-ion-battery graphite solid electrolyte interphase (SEI) and its relationship to formation cycling. *Carbon* **2016,** *105*, 52-76.
31. Haregewoin, A. M.; Wotango, A. S.; Hwang, B.-J., Electrolyte additives for lithium ion battery electrodes: progress and perspectives. *Energy Environ. Sci.* **2016,** *9*, 1955-1988.
32. Zhao, H.; Yu, X.; Li, J.; Li, B.; Shao, H.; Li, L.; Deng, Y., Film-forming electrolyte additives for rechargeable lithium-ion batteries: progress and outlook. *J. Mater. Chem. A* **2019,** *7*, 8700-8722.
33. Jaumann, T.; Balach, J.; Langklotz, U.; Sauchuk, V.; Fritsch, M.; Michaelis, A.; Teltevskij, V.; Mikhailova, D.; Oswald, S.; Klose, M.; Stephani, G.; Hauser, R.; Eckert, J.; Giebeler, L., Lifetime vs. rate capability: Understanding the role of FEC and VC in high-energy Li-ion batteries with nano-silicon anodes. *Energy Stor. Mater.* **2017,** *6*, 26-35.
34. Gröger, O.; Gasteiger, H. A.; Suchsland, J.-P., Review—Electromobility: Batteries or Fuel Cells? *J. Electrochem. Soc.* **2015,** *162*, A2605.
35. Nitta, N.; Wu, F.; Lee, J. T.; Yushin, G., Li-ion battery materials: present and future. *Mater. Today* **2015,** *18*, 252-264.
36. Manthiram, A., A reflection on lithium-ion battery chemistry. *Nat. Commun.* **2020**.
37. Rohstoffe, B. f. G. u., Deutsche Rohstoffagentur, Preismonitor. Hannover, 2021.
38. Dou, S., Review and prospect of layered lithium nickel manganese oxide as cathode materials for Li-ion batteries. *J. Solid State Electrochem.* **2013,** *17*, 911-926.
39. Whittingham, M. S., Lithium Batteries and Cathode Material. *Chem. Rev.* **2004,** *104*, 4271-4301.
40. Tolganbek, N.; Yerkinbekova, Y.; Kalybekkyzy, S.; Bakenov, Z.; Mentbayeva, A., Current state of high voltage olivine structured LiMPO4 cathode materials for energy storage applications: A review. *J. Alloys Compd.* **2021,** *882*, 160774.
41. Yamada, A.; Hosoya, M.; Chung, S.-C.; Kudo, Y.; Hinokuma, K.; Liu, K.-Y.; Nishi, Y., Olivine-type cathodes. *J. Power Sources* **2003,** *119-121*, 232-238.
42. Bhandari, A.; Bhattacherya, J., Review—Manganese Dissolution from Spinel Cathode: Few Unanswered Questions. *J. Electrochem. Soc.* **2017,** *164*, A106-A127.
43. Padhi, A. K.; Nanjudaswamy, K. S.; Goodenough, J. B., Phospho-olivines as Positive-Electrode Materials for Rechargeable Lithium Batteries. *J. Electrochem. Soc.* **1997,** *144*, 1188-1194.
44. Yang, Z.; Dai, Y.; Wang, S.; Yu, J., How to make lithium iron phosphate better: a review exploring classical modification approaches in-depth and proposing future optimization methods. *J. Mater. Chem. A* **2016,** *4*, 18210-18222.
45. Aravindan, V.; Gnanaraj, J.; Lee, Y.-S.; Madhavi, S., LiMnPO4 – A next generation cathode material for lithium-ion batteries. *J. Mater. Chem. A* **2013,** *1*, 3518.

46. Yang, L.; Deng, W.; Xu, W.; Tian, Y.; Wang, A.; Wang, B.; Zou, G.; Hou, H.; Deng, W.; Ji, X., Olivine LiMnxFe1−xPO4 cathode materials for lithium ion batteries: restricted factors of rate performances. *J. Mater. Chem. A* **2021,** *9*, 14214-14232.
47. Zhang, L.; Zhu, C.; Yu, S.; Ge, D.; Zhou, H., Status and challenges facing representative anode materials for rechargeable lithium batteries. *J. Energy Chem.* **2022,** *66*, 260-294.
48. Shi, Y.; Wan, J.; Liu, G. X.; Zuo, T. T.; Song, Y. X.; Liu, B.; Guo, Y. G.; Wen, R.; Wan, L. J., Interfacial Evolution of Lithium Dendrites and Their Solid Electrolyte Interphase Shells of Quasi-Solid-State Lithium-Metal Batteries. *Angew. Chem.* **2020,** *59*, 18120-18125.
49. Zhang, H.; Yang, Y.; Ren, D.; Wang, L.; He, X., Graphite as anode materials: Fundamental mechanism, recent progress and advances. *Energy Stor. Mater.* **2021,** *36*, 147-170.
50. Marom, R.; Amalraj, S. F.; Leifer, N.; Jacob, D.; Aurbach, D., A review of advanced and practical lithium battery materials. *J. Mater. Chem.* **2011,** *21*, 9938.
51. Zhang, Z.; Zhang, S., *Rechargeable Batteries Materials, Technologies and New Trends*. Springer: 2015.
52. Xie, L.; Tang, C.; Bi, Z.; Song, M.; Fan, Y.; Yan, C.; Li, X.; Su, F.; Zhang, Q.; Chen, C., Hard Carbon Anodes for Next-Generation Li-Ion Batteries: Review and Perspective. *Adv. Energy Mater.* **2021,** *11*, 2101650.
53. Wang, S.; Wang, C.; Ji, X., Towards understanding the salt-intercalation exfoliation of graphite into graphene. *RSC Advances* **2017,** *7*, 52252-52260.
54. Zhao, B.; Ran, R.; Liu, M.; Shao, Z., A comprehensive review of Li4Ti5O12-based electrodes for lithium-ion batteries: The latest advancements and future perspectives. *Mater.* **2015,** *98*, 1-71.
55. Sandhya, C. P.; John, B.; Gouri, C., Lithium titanate as anode material for lithium-ion cells: a review. *Ionics* **2014,** *20*, 601-620.
56. Nasara, R. N.; Tsai, P.-c.; Lin, S.-k., One-Step Synthesis of Highly Oxygen-Deficient Lithium Titanate Oxide with Conformal Amorphous Carbon Coating as Anode Material for Lithium Ion Batteries. *Adv. Mater. Interfaces* **2017,** *4*, 1700329.
57. Eshetu, G. G.; Figgemeier, E., Confronting the Challenges of Next-Generation Silicon Anode-Based Lithium-Ion Batteries: Role of Designer Electrolyte Additives and Polymeric Binders. *ChemSusChem* **2019,** *12*, 2515-2539.
58. Obrovac, M. N.; Christensen, L., Structural Changes in Silicon Anodes during Lithium Insertion/Extraction. *Electrochem. Solid-State Lett.* **2004,** *7*, A93.
59. Li, J.; Dahn, J. R., An In Situ X-Ray Diffraction Study of the Reaction of Li with Crystalline Si. *J. Electrochem. Soc.* **2007,** *154*, A156.
60. Zuo, X.; Zhu, J.; Müller-Buschbaum, P.; Cheng, Y.-J., Silicon based lithium-ion battery anodes: A chronicle perspective review. *Nano Energy* **2017,** *31*, 113-143.
61. Zhang, C.; Wang, F.; Han, J.; Bai, S.; Tan, J.; Liu, J.; Li, F., Challenges and Recent Progress on Silicon-Based Anode Materials for Next-Generation Lithium-Ion Batteries. *Small Structures* **2021,** *2*, 2100009.
62. Zhang, W.-J., A review of the electrochemical performance of alloy anodes for lithium-ion batteries. *J. Power Sources* **2011,** *196*, 13-24.
63. Zhao, X.; Lehto, V. P., Challenges and prospects of nanosized silicon anodes in lithium-ion batteries. *Nanotechnology* **2021,** *32*, 042002.
64. Ding, N.; Xu, J.; Yao, Y.; Wegner, G.; Lieberwirth, I.; Chen, C., Improvement of cyclability of Si as anode for Li-ion batteries. *J. Power Sources* **2009,** *192*, 644-651.
65. Li, H.; Huang, X.; Chen, L.; Wu, Z.; Liang, Y., A High Capacity Nano Si Composite Anode Material for Lithium Rechargeable Batteries. *Electrochem. Solid-State Lett.* **1999,** *2*, 547.
66. Liu, X. H.; Zhong, L.; Huang, S.; Mao, S. X.; Zhu, T.; Huang, J. Y., Size-Dependent Fracture of Silicon Nanoparticles During Lithiation. *ACS Nano* **2012,** *2*, 1522.

67. Liu, X. H.; Huang, J. Y., In situ TEM electrochemistry of anode materials in lithium ion batteries. *Energy Environ. Sci.* **2011,** *4*, 3844.
68. Liu, W.-R.; Guo, Z.-Z.; Young, W.-S.; Shieh, D.-T.; Wu, H.-C.; Yang, M.-H.; Wu, N.-L., Effect of electrode structure on performance of Si anode in Li-ion batteries: Si particle size and conductive additive. *J. Power Sources* **2005,** *140*, 139-144.
69. Chan, C. K.; Ruffo, R.; Hong, S. S.; Huggins, R. A.; Cui, Y., Structural and electrochemical study of the reaction of lithium with silicon nanowires. *J. Power Sources* **2009,** *189*, 34-39.
70. Wetjen, M.; Solchenbach, S.; Pritzl, D.; Hou, J.; Tileli, V.; Gasteiger, H. A., Morphological Changes of Silicon Nanoparticles and the Influence of Cutoff Potentials in Silicon-Graphite Electrodes. *J. Electrochem. Soc.* **2018,** *165*, A1503.
71. Lee, D.-S.; Lee, D.-M.; Yoo, S.-W.; Kim, J.-H.; Jeong, H.-D., Effects of surface functionalization and polymerization on anode characteristics of plasma-synthesized silicon nanocrystal active materials for lithium ion battery anode. *Ind. Eng. Chem. Res.* **2019,** *80*, 479-489.
72. Fox, A. M.; Vrankovic, D.; Buchmeiser, M. R., Influence of the Silicon-Carbon Interface on the Structure and Electrochemical Performance of a Phenolic Resin-Derived Si@C Core-Shell Nanocomposite-Based Anode. *ACS Appl. Mater. Interfaces* **2022,** *14*, 761-770.
73. Jung, R.; Metzger, M.; Haering, D.; Solchenbach, S.; Marino, C.; Tsiouvaras, N.; Stinner, C.; Gasteiger, H. A., Consumption of Fluoroethylene Carbonate (FEC) on Si-C Composite Electrodes for Li-Ion Batteries. *J. Electrochem. Soc.* **2016,** *163*, A1705.
74. Pan, K.; Zou, F.; Canova, M.; Zhu, Y.; Kim, J.-H., Systematic electrochemical characterizations of Si and SiO anodes for high-capacity Li-Ion batteries. *J. Power Sources* **2019,** *413*, 20-28.
75. Liu, Z.; Yu, Q.; Zhao, Y.; He, R.; Xu, M.; Feng, S.; Li, S.; Zhou, L.; Mai, L., Silicon oxides: a promising family of anode materials for lithium-ion batteries. *Chem. Soc. Rev.* **2019,** *48*, 285-309.
76. Kim, M. K.; Jang, B. Y.; Lee, J. S.; Kim, J. S.; Nahm, S., Microstructures and electrochemical performances of nano-sized SiOx ($1.18 \leq x \leq 1.83$) as an anode material for a lithium(Li)-ion battery. *J. Power Sources* **2013,** *244*, 115-121.
77. Choi, J. W.; Aurbach, D., Promise and reality of post-lithium-ion batteries with high energy densities. *Nat. Rev. Mater.* **2016,** *1*.
78. Li, J.-T.; Wu, Z.-Y.; Lu, Y.-Q.; Zhou, Y.; Huang, Q.-S.; Huang, L.; Sun, S.-G., Water Soluble Binder, an Electrochemical Performance Booster for Electrode Materials with High Energy Density. *Adv. Energy Mater.* **2017,** *7*, 1701185.
79. Yang, Y.; Wu, S.; Zhang, Y.; Liu, C.; Wei, X.; Luo, D.; Lin, Z., Towards efficient binders for silicon based lithium-ion battery anodes. *Chem. Eng. J.* **2021,** *406*, 126807.
80. Zhu, W.; Zhou, J.; Xiang, S.; Bian, X.; Yin, J.; Jiang, J.; Yang, L., Progress of Binder Structures in Silicon-Based Anodes for Advanced Lithium-Ion Batteries: A Mini Review. *Front. Chem.* **2021,** *9*, 712225.
81. Hays, K. A.; Ruther, R. E.; Kukay, A. J.; Cao, P.; Saito, T.; Wood, D. L.; Li, J., What makes lithium substituted polyacrylic acid a better binder than polyacrylic acid for silicon-graphite composite anodes? *J. Power Sources* **2018,** *384*, 136-144.
82. Huang, W.; Wang, W.; Wang, Y.; Qu, Q.; Jin, C.; Zheng, H., Overcoming the fundamental challenge of PVDF binder use with silicon anodes with a super-molecular nano-layer. *J. Mater. Chem. A* **2021,** *9*, 1541-1551.
83. Hochgatterer, N. S.; Schweiger, M. R.; Koller, S.; Raimann, P. R.; Wöhrle, T.; Wurm, C.; M., W., Silicon/Graphite Composite Electrodes for High-Capacity Anodes: Influence of Binder Chemistry on Cycling Stability. *Electrochem. Solid-State Lett.* **2008,** *11*, A76.

84. Komaba, S.; Ozeki, T.; Yabuuchi, N.; Shimomura, K., Polyacrylate as Functional Binder for Silicon and Graphite Composite Electrode in Lithium-Ion Batteries. *Electrochemistry* **2011,** *79*, 6-9.
85. Kovalenko, I.; Zdyrko, B.; Magasinski, A.; Hertzberg, B.; Milicev, Z.; Burtovyy, R.; Luzinov, I.; Yushin, G., A major constituent of brown algae for use in high-capacity Li-ion batteries. *Science* **2011,** *334*, 75-9.
86. Yue, L.; Zhang, L.; Zhong, H., Carboxymethyl chitosan: A new water soluble binder for Si anode of Li-ion batteries. *J. Power Sources* **2014,** *247*, 327-331.
87. Park, H.-K.; Kong, B.-S.; Oh, E.-S., Effect of high adhesive polyvinyl alcohol binder on the anodes of lithium ion batteries. *Electrochem. commun.* **2011,** *13*, 1051-1053.
88. Liu, J.; Zhang, Q.; Zhang, T.; Li, J.-T.; Huang, L.; Sun, S.-G., A Robust Ion-Conductive Biopolymer as a Binder for Si Anodes of Lithium-Ion Batteries. *Adv. Funct. Mater.* **2015,** *25*, 3599-3605.
89. Preman, A. N.; Lee, H.; Yoo, J.; Kim, I. T.; Saito, T.; Ahn, S.-k., Progress of 3D network binders in silicon anodes for lithium ion batteries. *J. Mater. Chem. A* **2020,** *8*, 25548-25570.
90. Zhao, Y. M.; Yue, F. S.; Li, S. C.; Zhang, Y.; Tian, Z. R.; Xu, Q.; Xin, S.; Guo, Y. G., Advances of polymer binders for silicon-based anodes in high energy density lithium-ion batteries. *InfoMat* **2021,** *3*, 460-501.
91. Wei, L.; Chen, C.; Hou, Z.; Wei, H., Poly (acrylic acid sodium) grafted carboxymethyl cellulose as a high performance polymer binder for silicon anode in lithium ion batteries. *Sci Rep* **2016,** *6*, 19583.
92. Koo, B.; Kim, H.; Cho, Y.; Lee, K. T.; Choi, N. S.; Cho, J., A highly cross-linked polymeric binder for high-performance silicon negative electrodes in lithium ion batteries. *Angew. Chem.* **2012,** *51*, 8762-7.
93. Song, J.; Zhou, M.; Yi, R.; Xu, T.; Gordin, M. L.; Tang, D.; Yu, Z.; Regula, M.; Wang, D., Interpenetrated Gel Polymer Binder for High-Performance Silicon Anodes in Lithium-ion Batteries. *Adv. Funct. Mater.* **2014,** *24*, 5904-5910.
94. Lee, D.; Park, H.; Goliaszewski, A.; Byeun, Y.-k.; Song, T.; Paik, U., In Situ Cross-linked Carboxymethyl Cellulose-Polyethylene Glycol Binder for Improving the Long-Term Cycle Life of Silicon Anodes in Li Ion Batteries. *Ind. Eng. Chem. Res.* **2019,** *58*, 8123-8130.
95. Wang, S.; Duan, Q.; Lei, J.; Yu, D. Y. W., Slime-inspired polyacrylic acid-borax crosslinked binder for high-capacity bulk silicon anodes in lithium-ion batteries. *J. Power Sources* **2020,** *468*, 228365.
96. Woo, H.; Park, K.; Kim, J.; Yun, A. J.; Nam, S.; Park, B., 3D Meshlike Polyacrylamide Hydrogel as a Novel Binder System via in situ Polymerization for High-Performance Si-Based Electrode. *Adv. Mater. Interfaces* **2019,** *7*, 1901475.
97. Ji, X.; Lee, K. T.; Nazar, L. F., A highly ordered nanostructured carbon-sulphur cathode for lithium-sulphur batteries. *Nat. Mater.* **2009,** *8*, 500-6.
98. Manthiram, A.; Fu, Y.; Chung, S. H.; Zu, C.; Su, Y. S., Rechargeable lithium-sulfur batteries. *Chem. Rev.* **2014,** *114*, 11751-87.
99. Lin, Z.; Liang, C., Lithium–sulfur batteries: from liquid to solid cells. *J. Mater. Chem. A* **2015,** *3*, 936-958.
100. Barghamadi, M.; Kapoor, A.; Wen, C., A Review on Li-S Batteries as a High Efficiency Rechargeable Lithium Battery. *J. Electrochem. Soc.* **2013,** *160*, A1256.
101. Cao, R.; Xu, W.; Lv, D.; Xiao, J.; Zhang, J.-G., Anodes for Rechargeable Lithium-Sulfur Batteries. *Adv. Energy Mater.* **2015,** *5*, 1402273.
102. Lin, Y.; Huang, S.; Zhong, L.; Wang, S.; Han, D.; Ren, S.; Xiao, M.; Meng, Y., Organic liquid electrolytes in Li-S batteries: actualities and perspectives. *Energy Stor. Mater.* **2021,** *34*, 128-147.

103. Bieker, G.; Wellmann, J.; Kolek, M.; Jalkanen, K.; Winter, M.; Bieker, P., Influence of cations in lithium and magnesium polysulphide solutions: dependence of the solvent chemistry. *Phys. Chem. Chem. Phys.* **2017,** *19*, 11152-11162.
104. Zhang, S. S., Liquid electrolyte lithium/sulfur battery: Fundamental chemistry, problems, and solutions. *J. Power Sources* **2013,** *231*, 153-162.
105. Niesen, S. Optimization and Characterization of Sulfur-Cathodes and Silicon-Graphite Anodes for post Li-Ion Batteries. Technical University of Munich, Munich, 2017.
106. Liang, J.; Sun, Z.-H.; Li, F.; Cheng, H.-M., Carbon materials for Li–S batteries: Functional evolution and performance improvement. *Energy Stor. Mater.* **2016,** *2*, 76-106.
107. Yang, Q.; Zhang, Z.; Sun, X. G.; Hu, Y. S.; Xing, H.; Dai, S., Ionic liquids and derived materials for lithium and sodium batteries. *Chem. Soc. Rev.* **2018,** *47*, 2020-2064.
108. Kang, W.; Deng, N.; Ju, J.; Li, Q.; Wu, D.; Ma, X.; Li, L.; Naebe, M.; Cheng, B., A review of recent developments in rechargeable lithium-sulfur batteries. *Nanoscale* **2016,** *8*, 16541-16588.
109. Dirlam, P. T.; Glass, R. S.; Char, K.; Pyun, J., The use of polymers in Li-S batteries: A review. *J. Polym. Sci. A Polym. Chem.* **2017,** *55*, 1635-1668.
110. Mukkabla, R.; Buchmeiser, M. R., Cathode materials for lithium–sulfur batteries based on sulfur covalently bound to a polymeric backbone. *J. Mater. Chem. A* **2020,** *8*, 5379-5394.
111. Zhou, L.; Danilov, D. L.; Eichel, R. A.; Notten, P. H. L., Host Materials Anchoring Polysulfides in Li–S Batteries Reviewed. *Adv. Energy Mater.* **2020,** *11*, 2001304.
112. Zhu, K.; Wang, C.; Chi, Z.; Ke, F.; Yang, Y.; Wang, A.; Wang, W.; Miao, L., How Far Away Are Lithium-Sulfur Batteries From Commercialization? *Front. Energy Res.* **2019,** *7*, 1.12.
113. Dörfler, S.; Althues, H.; Härtel, P.; Abendroth, T.; Schumm, B.; Kaskel, S., Challenges and Key Parameters of Lithium-Sulfur Batteries on Pouch Cell Level. *Joule* **2020,** *4*, 539-554.
114. Yang, Y.; Zheng, G.; Cui, Y., Nanostructured sulfur cathodes. *Chem. Soc. Rev.* **2013,** *42*, 3018-32.
115. Zhao, H.; Deng, N.; Yan, J.; Kang, W.; Ju, J.; Ruan, Y.; Wang, X.; Zhuang, X.; Li, Q.; Cheng, B., A review on anode for lithium-sulfur batteries: Progress and prospects. *Chem. Eng. J.* **2018,** *347*, 343-365.
116. Yan, C.; Zhang, X.-Q.; Huang, J.-Q.; Liu, Q.; Zhang, Q., Lithium-Anode Protection in Lithium–Sulfur Batteries. *Trends in Chemistry* **2019,** *1*, 693-704.
117. Liu, Y.; Elias, Y.; Meng, J.; Aurbach, D.; Zou, R.; Xia, D.; Pang, Q., Electrolyte solutions design for lithium-sulfur batteries. *Joule* **2021,** *5*, 2323-2364.
118. Angulakshmi, N.; Stephan, A. M., Efficient Electrolytes for Lithium-Sulfur Batteries. *Front. Energy Res.* **2015,** *3*, 1-8.
119. Scheers, J.; Fantini, S.; Johansson, P., A review of electrolytes for lithium–sulphur batteries. *J. Power Sources* **2014,** *255*, 204-218.
120. Gao, J.; Lowe, M. A.; Kiya, Y.; Abruña, H. D., Effects of Liquid Electrolytes on the Charge–Discharge Performance of Rechargeable Lithium/Sulfur Batteries: Electrochemical and in-Situ X-ray Absorption Spectroscopic Studies. *J. Phys. Chem. C* **2011,** *115*, 25132-25137.
121. Yim, T.; Park, M.-S.; Yu, J.-S.; Kim, K. J.; Im, K. Y.; Kim, J.-H.; Jeong, G.; Jo, Y. N.; Woo, S.-G.; Kang, K. S.; Lee, I.; Kim, Y.-J., Effect of chemical reactivity of polysulfide toward carbonate-based electrolyte on the electrochemical performance of Li–S batteries. *Electrochim. Acta* **2013,** *107*, 454-460.
122. Barghamadi, M.; Best, A. S.; Bhatt, A. I.; Hollenkamp, A. F.; Musameh, M.; Rees, R. J.; Rüther, T., Lithium–sulfur batteries—the solution is in the electrolyte, but is the electrolyte a solution? *Energy Environ. Sci.* **2014,** *7*, 3902-3920.

123. Aurbach, D.; Pollak, E.; Elazari, R.; Salitra, G.-.; Kelly, C. S.; Affinito, J., On the Surface Chemical Aspects of Very High Energy Density, Rechargeable Li–Sulfur Batteries. *J. Electrochem. Soc.* **2009,** *156*, A694.
124. Park, J.-W.; Yamauchi, K.; Takashima, E.; Tachikawa, N.; Ueno, K.; Dokko, K.; Watanabe, M., Solvent Effect of Room Temperature Ionic Liquids on Electrochemical Reactions in Lithium–Sulfur Batteries. *J. Phys. Chem. C* **2013,** *117*, 4431-4440.
125. Lei, D.; Shi, K.; Ye, H.; Wan, Z.; Wang, Y.; Shen, L.; Li, B.; Yang, Q.-H.; Kang, F.; He, Y.-B., Progress and Perspective of Solid-State Lithium-Sulfur Batteries. *Adv. Funct. Mater.* **2018,** *28*, 1707570.
126. Yao, P.; Yu, H.; Ding, Z.; Liu, Y.; Lu, J.; Lavorgna, M.; Wu, J.; Liu, X., Review on Polymer-Based Composite Electrolytes for Lithium Batteries. *Front. Chem.* **2019,** *7*, 522.
127. Zhang, Y.; Zhao, Y.; Gosselink, D.; Chen, P., Synthesis of poly(ethylene-oxide)/nanoclay solid polymer electrolyte for all solid-state lithium/sulfur battery. *Ionics* **2014,** *21*, 381-385.
128. Pan, H.; Cheng, Z.; He, P.; Zhou, H., A Review of Solid-State Lithium–Sulfur Battery: Ion Transport and Polysulfide Chemistry. *Energy Fuels* **2020,** *34*, 11942-11961.
129. Eftekhari, A.; Kim, D.-W., Cathode materials for lithium–sulfur batteries: a practical perspective. *J. Mater. Chem. A* **2017,** *5*, 17734-17776.
130. Borchardt, L.; Oschatz, M.; Kaskel, S., Carbon Materials for Lithium Sulfur Batteries-Ten Critical Questions. *Chemistry* **2016,** *22*, 7324-51.
131. Rao, M.; Li, W.; Cairns, E. J., Porous carbon-sulfur composite cathode for lithium/sulfur cells. *Electrochem. commun.* **2012,** *17*, 1-5.
132. Xin, S.; Gu, L.; Zhao, N. H.; Yin, Y. X.; Zhou, L. J.; Guo, Y. G.; Wan, L. J., Smaller sulfur molecules promise better lithium-sulfur batteries. *J. Am. Chem. Soc.* **2012,** *134*, 18510-3.
133. Li, Z.; Yuan, L.; Yi, Z.; Sun, Y.; Liu, Y.; Jiang, Y.; Shen, Y.; Xin, Y.; Zhang, Z.; Huang, Y., Insight into the Electrode Mechanism in Lithium-Sulfur Batteries with Ordered Microporous Carbon Confined Sulfur as the Cathode. *Adv. Energy Mater.* **2014,** *4*, 1301473.
134. Wang, D.-W.; Zeng, Q.; Zhou, G.; Yin, L.; Li, F.; Cheng, H.-M.; Gentle, I. R.; Lu, G. Q. M., Carbon–sulfur composites for Li–S batteries: status and prospects. *J. Mater. Chem. A* **2013,** *1*, 9382.
135. Li, S.; Jin, B.; Zhai, X.; Li, H.; Jiang, Q., Review of Carbon Materials for Lithium-Sulfur Batteries. *ChemistrySelect* **2018,** *3*, 2245-2260.
136. Liang, C.; Dudney, N. J.; Howe, J. Y., Hierarchically Structured Sulfur/Carbon Nanocomposite Material for High-Energy Lithium Battery. *Chem. Mater.* **2009,** *21*, 4724-4730.
137. Han, S.-C.; Song, M.-S.; Lee, H.; Kim, H.-S.; Ahn, H.-J.; Lee, J.-Y., Effect of Multiwalled Carbon Nanotubes on Electrochemical Properties of Lithium-Sulfur Rechargeable Batteries. *J. Electrochem. Soc.* **2003,** *150*.
138. Ji, X.; Nazar, L. F., Advances in Li–S batteries. *J. Mater. Chem.* **2010,** *20*, 9821.
139. Zheng, M.; Chi, Y.; Hu, Q.; Tang, H.; Jiang, X.; Zhang, L.; Zhang, S.; Pang, H.; Xu, Q., Carbon nanotube-based materials for lithium–sulfur batteries. *J. Mater. Chem. A* **2019,** *7*, 17204-17241.
140. Wang, J.-Z.; Lu, L.; Choucair, M.; Stride, J. A.; Xu, X.; Liu, H.-K., Sulfur-graphene composite for rechargeable lithium batteries. *J. Power Sources* **2011,** *196*, 7030-7034.
141. Yu, M.; Li, R.; Wu, M.; Shi, G., Graphene materials for lithium–sulfur batteries. *Energy Stor. Mater.* **2015,** *1*, 51-73.
142. Zhang, Q.; Huang, Q.; Hao, S. M.; Deng, S.; He, Q.; Lin, Z.; Yang, Y., Polymers in Lithium-Sulfur Batteries. *Adv. Sci.* **2021**, e2103798.
143. Visco, S. J.; Liu, M.; Armand, M. B.; de Jonghe, L. C., *Mol. Cryst. Liq. Cryst.* **1990,** *190*, 185.

144. Akiba, M.; Hashim, A. S., Vulcanization and crosslinking in elastomers. *Prog. Polym. Sci.* **1997,** *22*, 475.
145. Tromfimov, B. A.; Myachina, G. F.; Korzhova, S. A.; Malkina, A. G.; Sokolyanskaya, L. V.; Vakulskaya, T. I.; Skotheim, T. A., New Electrochemically Active Highly Sulfurized Polyconjugated Polymers. *Russ. J. Electrochem.* **2002,** *38*, 188.
146. Tromfimov, B. A.; Vasiltsov, A. M.; Petrova, O. V.; Mikhaleva, A. I.; Myachina, G. F.; Korzhova, S. A.; Skotheim, T. A.; Mikhailik, Y. V.; Yakulskays, T. I., Sulfurization of polymers. 6. Poly(vinylene polysulfide), poly(thienothiophene), and related structures from polyacetylene and elemental sulfur. *Russ. J. Electrochem.* **2002,** *51*, 1709.
147. Duan, B.; Wang, W.; Wang, A.; Yuan, K.; Yu, Z.; Zhao, H.; Qiu, J.; Yang, Y., Carbyne polysulfide as a novel cathode material for lithium/sulfur batteries. *J. Mater. Chem. A* **2013,** *1*, 13261.
148. Wang, J.; Wang, Y.; He, X.; Ren, J.; Jiang, C.; Wan, C., A Novel Conductive Polymer-Sulfur Composite Cathode Material for Rechargeable LithiumBatteries. *Adv. Mater.* **2002,** *14*, 13.
149. Fanous, J.; Wegner, M.; Grimminger, J.; Andresen, Ä.; Buchmeiser, M. R., Structure-Related Electrochemistry of Sulfur-Poly(acrylonitrile) Composite Cathode Materials for Rechargeable Lithium Batteries. *Chem. Mater.* **2011,** *23*, 5024-5028.
150. Wang, J.; Wang, Y.; He, X.; Ren, J.; Jiang, C.; Wan, C., Electrochemical characteristics of sulfur composite cathode materials in rechargeable lithium batteries. *J. Power Sources* **2004,** *138*, 271-273.
151. Yu, X.-g.; Xie, J.-y.; Yang, J.; Huang, H.-j.; Wang, K.; Wen, Z.-s., Lithium storage in conductive sulfur-containing polymers. *J. Electroanal. Chem.* **2004,** *573*, 121-128.
152. Zhang, S. S., Sulfurized Carbon: A Class of Cathode Materials for High Performance Lithium/Sulfur Batteries. *Front. Energy Res.* **2013,** *1*.
153. He, X.-M.; Wang, L.; Pu, W. H.; Ren, J.-G.; Wu, W.; Jiang, C.-Y.; Wan, C.-R., Thermal Analysis of sulfurization of polyacrylonitrile with elemetal sulfur. **2008,** *94*, 151.
154. Zhang, S., Understanding of Sulfurized Polyacrylonitrile for Superior Performance Lithium/Sulfur Battery. *Energies* **2014,** *7*, 4588-4600.
155. Liu, Y.; Wang, W.; Wang, A.; Jin, Z.; Zhao, H.; Yang, Y., Effect of vapor pressure on performance of sulfurized polyacrylonitrile cathodes for Li/S batteries. *RSC Advances* **2016,** *6*, 106625-106630.
156. Zhao, X.; Wang, C.; Li, Z.; Hu, X.; Abdul Razzaq, A.; Deng, Z., Sulfurized polyacrylonitrile for high-performance lithium sulfur batteries: advances and prospects. *J. Mater. Chem. A* **2021,** *9*, 19282-19297.
157. Wang, X.; Qian, Y.; Wang, L.; Yang, H.; Li, H.; Zhao, Y.; Liu, T., Sulfurized Polyacrylonitrile Cathodes with High Compatibility in Both Ether and Carbonate Electrolytes for Ultrastable Lithium–Sulfur Batteries. *Adv. Funct. Mater.* **2019,** *29*, 1902929.
158. Wei, S.; Ma, L.; Hendrickson, K. E.; Tu, Z.; Archer, L. A., Metal-Sulfur Battery Cathodes Based on PAN-Sulfur Composites. *J. Am. Chem. Soc.* **2015,** *137*, 12143-52.
159. Yang, H.; Naveed, A.; Li, Q.; Guo, C.; Chen, J.; Lei, J.; Yang, J.; Nuli, Y.; Wang, J., Lithium sulfur batteries with compatible electrolyte both for stable cathode and dendrite-free anode. *Energy Stor. Mater.* **2018,** *15*, 299-307.
160. Frey, M.; Zenn, R. K.; Warneke, S.; Müller, K.; Hintennach, A.; Dinnebier, R. E.; Buchmeiser, M. R., Easily Accessible, Textile Fiber-Based Sulfurized Poly(acrylonitrile) as Li/S Cathode Material: Correlating Electrochemical Performance with Morphology and Structure. *ACS Energy Lett.* **2017,** *2*, 595-604.
161. Yuan, H.; Huang, J.-Q.; Peng, H.-J.; Titirici, M.-M.; Xiang, R.; Chen, R.; Liu, Q.; Zhang, Q., A Review of Functional Binders in Lithium-Sulfur Batteries. *Adv. Energy Mater.* **2018,** *8*, 1802107.

162. Zhang, J.; Li, M.; Younus, H. A.; Wang, B.; Weng, Q.; Zhang, Y.; Zhang, S., An overview of the characteristics of advanced binders for high-performance Li–S batteries. *Nano Materials Science* **2021,** *3*, 124-139.
163. Zhang, Z.; Bao, W.; Lu, H.; Jia, M.; Xie, K.; Lai, Y.; Li, J., Water-Soluble Polyacrylic Acid as a Binder for Sulfur Cathode in LithiumSulfur Battery. *ECS Electrochem. Lett.* **2012,** *1*, A34.
164. Qi, Q.; Lv, X.; Lv, W.; Yang, Q.-H., Multifunctional binder designs for lithium-sulfur batteries. *J. Energy Chem.* **2019,** *39*, 88-100.
165. Kim, H. M.; Sun, H.-H.; Belharouak, I.; Manthiram, A.; Sun, Y.-K., An Alternative Approach to Enhance the Performance of High Sulfur-Loading Electrodes for Li–S Batteries. *ACS Energy Lett.* **2016,** *1*, 136-141.
166. Wang, J.; Yao, Z.; Monroe, C. W.; Yang, J.; Nuli, Y., Carbonyl-β-Cyclodextrin as a Novel Binder for Sulfur Composite Cathodes in Rechargeable Lithium Batteries. *Adv. Funct. Mater.* **2013,** *23*, 1194-1201.
167. Kim, H. M.; Hwang, J. Y.; Aurbach, D.; Sun, Y. K., Electrochemical Properties of Sulfurized-Polyacrylonitrile Cathode for Lithium-Sulfur Batteries: Effect of Polyacrylic Acid Binder and Fluoroethylene Carbonate Additive. *J. Phys. Chem. Lett.* **2017,** *8*, 5331-5337.
168. Yan, L.; Gao, X.; Thomas, J. P.; Ngai, J.; Altounian, H.; Leung, K. T.; Meng, Y.; Li, Y., Ionically cross-linked PEDOT:PSS as a multi-functional conductive binder for high-performance lithium–sulfur batteries. *Sustain. Energy & Fuels* **2018,** *2*, 1574-1581.
169. Wang, Z.; Chen, Y.; Battaglia, V.; Liu, G., Improving the performance of lithium–sulfur batteries using conductive polymer and micrometric sulfur powder. *Journal of Materials Research* **2014,** *29*, 1027-1033.
170. Chen, H.; Wang, C.; Dai, Y.; Ge, J.; Lu, W.; Yang, J.; Chen, L., In-situ activated polycation as a multifunctional additive for Li-S batteries. *Nano Energy* **2016,** *26*, 43-49.
171. Li, J.; Fleetwood, J.; Hawley, W. B.; Kays, W., From Materials to Cell: State-of-the-Art and Prospective Technologies for Lithium-Ion Battery Electrode Processing. *Chem. Rev.* **2022,** *122*, 903-956.
172. Liu, Y.; Zhang, R.; Wang, J.; Wang, Y., Current and future lithium-ion battery manufacturing. *iScience* **2021,** *24*, 102332.
173. Mohanty, D.; Hockaday, E.; Li, J.; Hensley, D. K.; Daniel, C.; Wood, D. L., Effect of electrode manufacturing defects on electrochemical performance of lithium-ion batteries: Cognizance of the battery failure sources. *J. Power Sources* **2016,** *312*, 70-79.
174. Hawley, W. B.; Li, J., Electrode manufacturing for lithium-ion batteries—Analysis of current and next generation processing. *J. Energy Storage* **2019,** *25*, 100862.
175. Heimes, H. H.; Kampker, A.; Lienemann, C.; Locke, M.; Offermanns, C.; Michaelis, S.; Rahimzei, E., *Lithium-Ion Battery Cell Production*. VDA: Frankfurt, 2019.
176. Gonçalves, R.; Lanceros-Méndez, S.; Costa, C. M., Electrode fabrication process and its influence in lithium-ion battery performance: State of the art and future trends. *Electrochem. commun.* **2022,** *135*, 107210.
177. Wood, D. L.; Quass, J. D.; Li, J.; Ahmed, S.; Ventola, D.; Daniel, C., Technical and economic analysis of solvent-based lithium-ion electrode drying with water and NMP. *Dry. Technol.* **2017,** *36*, 234-244.
178. Zhang, Y. S.; Courtier, N. E.; Zhang, Z.; Liu, K.; Bailey, J. J.; Boyce, A. M.; Richardson, G.; Shearing, P. R.; Kendrick, E.; Brett, D. J. L., A Review of Lithium-Ion Battery Electrode Drying: Mechanisms and Metrology. *Adv. Energy Mater.* **2021,** *12*, 2102233.
179. J., R.; Barnett, B.; Hyung, Y. E. In *PHEV battery cost assessment*, DOE Annual Merit Review Meeting, Washington DC, Washington DC, 2013.
180. Jaiser, S.; Kumberg, J.; Klaver, J.; Urai, J. L.; Schabel, W.; Schmatz, J.; Scharfer, P., Microstructure formation of lithium-ion battery electrodes during drying – An ex-situ study using cryogenic broad ion beam slope-cutting and scanning electron microscopy (Cryo-BIB-SEM). *J. Power Sources* **2017,** *345*, 97-107.

181. Kumberg, J.; Müller, M.; Diehm, R.; Spiegel, S.; Wachsmann, C.; Bauer, W.; Scharfer, P.; Schabel, W., Drying of Lithium-Ion Battery Anodes for Use in High-Energy Cells: Influence of Electrode Thickness on Drying Time, Adhesion, and Crack Formation. *Energy Technol.* **2019,** *7*, 1900722.
182. Jaiser, S.; Müller, M.; Baunach, M.; Bauer, W.; Scharfer, P.; Schabel, W., Investigation of film solidification and binder migration during drying of Li-Ion battery anodes. *J. Power Sources* **2016,** *318*, 210-219.
183. Westphal, B. G.; Kwade, A., Critical electrode properties and drying conditions causing component segregation in graphitic anodes for lithium-ion batteries. *J. Energy Storage* **2018,** *18*, 509-517.
184. Font, F.; Protas, B.; Richardson, G.; Foster, J. M., Binder migration during drying of lithium-ion battery electrodes: Modelling and comparison to experiment. *J. Power Sources* **2018,** *393*, 177-185.
185. Lombardo, T.; Ngandjong, A. C.; Belhcen, A.; Franco, A. A., Carbon-Binder Migration: A Three-Dimensional Drying Model for Lithium-ion Battery Electrodes. *Energy Stor. Mater.* **2021,** *43*, 337-347.
186. Rollag, K.; Juarez-Robles, D.; Du, Z.; Wood, D. L.; Mukherjee, P. P., Drying Temperature and Capillarity-Driven Crack Formation in Aqueous Processing of Li-Ion Battery Electrodes. *ACS Appl. Energy Mater.* **2019,** *2*, 4464-4476.
187. Chien, Y. C.; Li, H.; Lampkin, J.; Hall, S.; Garcia-Araez, N.; Brant, W. R.; Brandell, D.; Lacey, M. J., Impact of Compression on the Electrochemical Performance of the Sulfur/Carbon Composite Electrode in Lithium-Sulfur Batteries. *Batteries & Supercaps* **2022,** *5*, e202200058.
188. Kim, C. S.; Guerfi, A.; Hovington, P.; Trottier, J.; Gagnon, C.; Barray, F.; Vijh, A.; Armand, M.; Zaghib, K., Importance of open pore structures with mechanical integrity in designing the cathode electrode for lithium–sulfur batteries. *J. Power Sources* **2013,** *241*, 554-559.
189. Meyer, C.; Bockholt, H.; Haselrieder, W.; Kwade, A., Characterization of the calendering process for compaction of electrodes for lithium-ion batteries. *J. Mater. Process. Technol.* **2017,** *249*, 172-178.
190. Sim, R.; Lee, S.; Li, W.; Manthiram, A., Influence of Calendering on the Electrochemical Performance of LiNi0.9Mn0.05Al0.05O2 Cathodes in Lithium-Ion Cells. *ACS Appl. Mater. Interfaces* **2021,** *13*, 42898-42908.
191. Karkar, Z.; Jaouhari, T.; Tranchot, A.; Mazouzi, D.; Guyomard, D.; Lestriez, B.; Roué, L., How silicon electrodes can be calendered without altering their mechanical strength and cycle life. *J. Power Sources* **2017,** *371*, 136-147.
192. Haselrieder, W.; Ivanov, S.; Christen, D. K.; Bockholt, H.; Kwade, A., Impact of the Calendering Process on the Interfacial Structure and the Related Electrochemical Performance of Secondary Lithium-Ion Batteries. *ECS Trans.* **2013,** *50*, 59-70.
193. Van Boomel, A.; Divigalpitiya, R., Effect of Calendering $LiFePO_4$ Electrode. *J. Electrochem. Soc.* **2012,** *159*, A1791-A1795.
194. Kang, H.; Lim, C.; Li, T.; Fu, Y.; Yan, B.; Houston, N.; De Andrade, V.; De Carlo, F.; Zhu, L., Geometric and Electrochemical Characteristics of LiNi1/3Mn1/3Co1/3O2 Electrode with Different Calendering Conditions. *Electrochim. Acta* **2017,** *232*, 431-438.
195. Gnanaraj, J. S.; Yaron, S.; Cohen, S.; Levi, M. D.; Aurbach, D., The effect of pressure on the electroanalytical response of graphite anodes and LiCoO2 cathodes for Li-ion batteries. *J. Electroanal. Chem.* **2001,** *516*, 89-102.
196. Novak, P.; Scheifele, W.; Winter, M.; Haas, O., Graphite electrodes with tailored porosity for rechargeable ion-transfer batteries. *J. Power Sources* **1997,** *68*, 267-270.
197. Lv, D.; Zheng, J.; Li, Q.; Xie, X.; Ferrara, S.; Nie, Z.; Mehdi, L. B.; Browning, N. D.; Zhang, J.-G.; Graff, G. L.; Liu, J.; Xiao, J., High Energy Density Lithium-Sulfur Batteries: Challenges of Thick Sulfur Cathodes. *Adv. Energy Mater.* **2015,** *5*, 1402290.

198. Kang, N.; Lin, Y.; Yang, L.; Lu, D.; Xiao, J.; Qi, Y.; Cai, M., Cathode porosity is a missing key parameter to optimize lithium-sulfur battery energy density. *Nat. Commun.* **2019,** *10*, 4597.
199. Chen, J.; Zhang, H.; Yang, H.; Lei, J.; Naveed, A.; Yang, J.; Nuli, Y.; Wang, J., Towards practical Li–S battery with dense and flexible electrode containing lean electrolyte. *Energy Stor. Mater.* **2020,** *27*, 307-315.
200. Huggins, R. A., *Energy Storage: Fundamentals, Materials and Applications*. Springer: Switzerlad, 2016.
201. Wen Ng, X., *Concise Guide to Electrochemical Methods and Voltammetry*. Springer: Singapore, 2022.
202. Xiao, J.; Li, Q.; Bi, Y.; Cai, M.; Dunn, B.; Glossmann, T.; Liu, J.; Osaka, T.; Sugiura, R.; Wu, B.; Yang, J.; Zhang, J.-G.; Whittingham, M. S., Understanding and applying coulombic efficiency in lithium metal batteries. *Nat. Energy* **2020,** *5*, 561-568.
203. Lasia, A., *Electrochemical Impedance Spectroscopy and its Applications*. Springer: 2004.
204. Andre, D.; Meiler, M.; Steiner, K.; Wimmer, C.; Soczka-Guth, T.; Sauer, D. U., Characterization of high-power lithium-ion batteries by electrochemical impedance spectroscopy. I. Experimental investigation. *J. Power Sources* **2011,** *196*, 5334-5341.
205. Barsoukov, E.; Macdonald, R. J., *Impedance Spectroscopy: Theory, Experiment, and Applications*. Wiley: 2005.
206. Lvovich, V. F., *Impedance Spectroscopy: Applications to Electrochemical and Dielectric Phenomena*. Wiley: 2012.
207. Li, J.; Murphy, E.; Winnick, J.; Kohl, P. A., Studies on the cycle life of commercial lithium ion batteries during rapid charge–discharge cycling. *J. Power Sources* **2001,** *102*, 294.
208. Hutzenlaub, T.; Asthana, A.; Becker, J.; Wheeler, D. R.; Zengerle, R.; Thiele, S., FIB/SEM-based calculation of tortuosity in a porous LiCoO2 cathode for a Li-ion battery. *Electrochem. commun.* **2013,** *27*, 77-80.
209. Chen, C. H.; Liu, J.; Amine, K., Symmetric cell approach and impedance spectroscopy of high power lithium-ion batteries. *J. Power Sources* **2001,** *96*, 321.
210. Middlemiss, L. A.; Rennie, A. J. R.; Sayers, R.; West, A. R., Characterisation of batteries by electrochemical impedance spectroscopy. *Energy Rep.* **2020,** *6*, 232-241.
211. Dees, D. W.; Jansen, A. N.; Abraham, D. P., Theoretical examination of reference electrodes for lithium-ion cells. *J. Power Sources* **2004,** *174*, 1001.
212. Zhou, J.; Notten, P. H. L., Development of Reliable Lithium Microreference Electrodes for LongTerm In Situ Studies of Lithium-Based Battery Systems. *J. Electrochem. Soc.* **2004,** *151*, A2173.
213. Costard, J.; Ender, M.; Weiss, M.; Ivers-Tiffee, E., Three-Electrode Setups for Lithium-Ion Batteries. *J. Electrochem. Soc.* **2017,** *164*, A80.
214. Abraham, D. P.; Poppen, S. D.; Jansen, A. N.; Liu, J.; Dees, D. W., Application of a lithium–tin reference electrode to determine electrode contributions to impedance rise in high-power lithium-ion cells. *Electrochim. Acta* **2004,** *49*, 4763-4775.
215. Linsenmann, F.; Pritzl, D.; Gasteiger, H. A., A Reference Electrode for In Situ Impedance Measurements in Sodium-Ion Batteries. *J. Electrochem. Soc.* **2019,** *166*, A3668.
216. Solchenbach, S.; Pritzl, D.; Kong, E. J. Y.; Landesfeind, J.; Gasteiger, H. A., A Gold Micro-Reference Electrode for Impedance and Potential Measurements in Lithium Ion Batteries. *J. Electrochem. Soc.* **2016,** *163*, A2265.
217. Hsieh, G.; Ford, S. J.; Mason, T. O.; Pederson, L. R., Experimental limitations in impedance spectroscopy: Part I of reference electrode artifacts in three-point measurements. *Solid State Ion* **1996,** *91*, 191.
218. Delattre, B.; Amin, R.; Sander, J.; De Coninck., J.; P., T. A.; Chiang, Y.-M., Impact of Pore Tortuosity on Electrode Kinetics in Lithium Battery Electrodes: Study in Directionally Freeze-Cast LiNi0.8Co0.15Al0.05O2 (NCA). *J. Electrochem. Soc.* **2018**, A388.

219. Pouraghajan, F.; Knight, H.; Wray, M.; Mazzeo, B.; Subbaraman, R.; Christensen, J.; Wheeler, D., Quantifying Tortuosity of Porous Li-Ion Battery Electrodes: Comparing Polarization-Interrupt and Blocking-Electrolyte Methods. *J. Electrochem. Soc.* **2018,** *165*, A2644.
220. Landesfeind, J.; Hattendorff, J.; Ehrl, A.; Wall, W. A.; Gasteiger, H. A., Tortuosity Determination of Battery Electrodes and Separators by Impedance Spectroscopy *J. Electrochem. Soc.* **2016,** *163*, A1373-A1387.
221. Ogihara, N.; Kawauchi, S.; Okuda, C.; Itou, Y.; Takeuchi, Y.; Ukyo, Y., Theoretical and Experimental Analysis of Porous Electrodes for Lithium-Ion Batteries by Electrochemical Impedance Spectroscopy Using a Symmetric Cell. *J. Electrochem. Soc.* **2012,** *159*, A1034-A1039.
222. Thorat, I. V.; Stephenson, D. E.; Zacharias, N. A.; Zaghib, K.; Harb, J. N.; Wheeler, D. R., Quantifying tortuosity in porous Li-ion battery materials. *J. Power Sources* **2009,** *188*, 592-600.
223. Chen, H.; Pei, A.; Wan, J.; Lin, D.; Vilá, R.; Wang, H.; Mackanic, D.; Steinrück, H.-G.; Huang, W.; Li, Y.; Yang, A.; Xie, J.; Wu, Y.; Wang, H.; Cui, Y., Tortuosity Effects in Lithium-Metal Host Anodes. *Joule* **2020,** *4*, 938-952.
224. DuBeshter, T.; Sinha, P. K.; Sakars, A.; Fly, G. W.; Jorne, J., Measurement of Tortuosity and Porosity of Porous Battery Electrodes. *J. Electrochem. Soc.* **2014,** *161*, A599-A605.
225. Ebner, M.; Wood, V., Tool for Tortuosity Estimation in Lithium Ion Battery Porous Electrodes. *J. Electrochem. Soc.* **2015,** *162*, A3064.
226. Bae, C. J.; Erdonmez, C. K.; Halloran, J. W.; Chiang, Y. M., Design of battery electrodes with dual-scale porosity to minimize tortuosity and maximize performance. *Adv. Mater.* **2013,** *25*, 1254-8.
227. Smentkowski, V.; Ostrowski, S., Applications of ToF-SIMS in a Research and Development Laboratory. *Microsc. Microanal.* **2006,** *12*, 1226-1227.
228. Fearn, S., *An Introduction to Time-of-Flight Secondary Ion Mass Spectrometry (ToF-SIMS) and its Application to Materials Science*. Morgan & Claypool Publishers: USA, 2015.
229. Chan, C. M.; Weng, L. T., Surface Characterization of Polymer Blends by XPS and ToF-SIMS. *Materials* **2016,** *9*, 655.
230. Vieckerman, J. C.; Briggs, D., *ToF-SIMS Surface Analysis by Mass Spectrometry*. Surface Spectra/IMPublications: London, 2001.
231. Saha, B.; Chakraborty, P., MCsn+-SIMS: An Innovative Approach for Direct Compositional Analysis of Materials without Standards. *Energy Procedia* **2013,** *41*, 80-109.
232. Weickhardt, C.; Moritz, F.; Grotemeyer, J., Time-of-flight mass spectrometry State-of the-art in chemical analysis and molecular science. *Mass Spectrom* **1996,** *15*, 139-162.
233. Miller, D. J.; Zapotok, D.; Hiller, J.; Juracka, Z.; Schmidt, U.; Ezell, T.; Senabulya, N.; Kerns, B.; Fonseca Rodrigues, M.-T.; Maroni, V. A.; Abraham, D. P., Exploring Heterogeneity in Li Battery Electrodes using FIB-SEM Integrated with Raman and TOF-SIMS. *Microsc. Microanal.* **2019,** *25*, 862-863.
234. Miller, D. J.; Zapotok, D.; Anzalone, P.; Samofil, T.; Hladik, L.; Tesafova, H.; Yao, K. P. C.; Maroni, V. A.; Abraham, D. P., Exploring Li distribution in Li-ion batteries with FIB-SEM and TOF-SIMS. *Microsc. Microanal.* **2018,** *24*, 370-371.
235. Jiao, C.; Pillatsch, L.; Mulders, J.; Wall, D., Three-Dimensional Time-of-Flight Secondary Ion Mass Spectrometry and DualBeam FIB/SEM Imaging of Lithium-ion Battery Cathode. *Microsc. Microanal.* **2019,** *25*, 876-877.
236. Feng, Y.; Koo, B. M.; Seyeux, A.; Swiatowska, J.; Henry de Villeneuve, C.; Rosso, M.; Ozanam, F., ToF-SIMS Li Depth Profiling of Pure and Methylated Amorphous Silicon Electrodes After Their Partial Lithiation. *ACS Appl. Mater. Interfaces* **2022**, 35716-35725.
237. Dahbi, M.; Nakano, T.; Yabuuchi, N.; Ishikawa, T.; Kubota, K.; Fukunishi, M.; Shibahara, S.; Son, J.-Y.; Cui, Y.-T.; Oji, H.; Komaba, S., Sodium carboxymethyl cellulose as

a potential binder for hard-carbon negative electrodes in sodium-ion batteries. *Electrochem. commun.* **2014,** *44*, 66-69.
238. Chang, W. J.; Lee, G. H.; Cheon, Y. J.; Kim, J. T.; Lee, S. I.; Kim, J.; Kim, M.; Park, W. I.; Lee, Y. J., Direct Observation of Carboxymethyl Cellulose and Styrene-Butadiene Rubber Binder Distribution in Practical Graphite Anodes for Li-Ion Batteries. *ACS Appl. Mater. Interfaces* **2019,** *11*, 41330-41337.
239. Ota, H.; Akai, T.; Namita, H.; Yamaguchi, S.; Nomura, M., XAFS and TOF–SIMS analysis of SEI layers on electrodes. *J. Power Sources* **2003,** *119-121*, 567-571.
240. Veryovkin, I. V.; Tripa, C. E.; Zinovev, A. V.; Baryshev, S. V.; Li, Y.; Abraham, D. P., TOF SIMS characterization of SEI layer on battery electrodes. *Nucl. Instrum. Methods. Phys. Res. B* **2014,** *332*, 368-372.
241. Haridas, A. K.; Nguyen, Q. A.; Terlier, T.; Blaser, R.; Biswal, S. L., Investigating the Compatibility of TTMSP and FEC Electrolyte Additives for LiNi0.5Mn0.3Co0.2O2 (NMC)-Silicon Lithium-Ion Batteries. *ACS Appl. Mater. Interfaces* **2021,** *13*, 2662-2673.
242. Erickson, E. M.; Li, W.; Dolocan, A.; Manthiram, A., Insights into the Cathode-Electrolyte Interphases of High-Energy-Density Cathodes in Lithium-Ion Batteries. *ACS Appl. Mater. Interfaces* **2020,** *12*, 16451-16461.
243. Fang, R.; Xu, H.; Xu, B.; Li, X.; Li, Y.; Goodenough, J. B., Reaction Mechanism Optimization of Solid-State Li–S Batteries with a PEO-Based Electrolyte. *Adv. Funct. Mater.* **2020,** *31*, 2001812.
244. Tan, C.; Cao, D.; Zheng, L.; Shen, Y.; Chen, L.; Chen, Y., True Reaction Sites on Discharge in Li-O2 Batteries. *J. Am. Chem. Soc.* **2022,** *144*, 807-815.
245. Niesen, S.; Kappler, J.; Trück, J.; Veith, L.; Weil, T.; Soczka-Guth, T.; Buchmeiser, M. R., Influence of the Drying Temperature on the Performance and Binder Distribution of Sulfurized Poly(acrylonitrile) Cathodes. *Journal of The Electrochemical Society* **2021,** *168* (5), 050510.
246. Niesen, S.; Trück, J.; Seidl, C.; Renger, K.; Buchmeiser, M. R., Lithium-Sulfur Batteries Based on Sulfurized Poly(acrylonitrile) Cathodes: impact of Electrode Density on Cell Performance. *Journal of The Electrochemical Society* **2021,** *168* (11), 110513.
247. Niesen, S.; Fox, A.; Murugan, S.; Richter, G.; Buchmeiser, M. R., Multifunctional Self-Cross-Linked Copolymer Binder for High-Loading Silicon Anodes. *ACS Applied Energy Materials* **2022,** *5* (9), 11386-11391.
248. Krishnan, S.; Klein, A.; El-Aasser, M. S.; Sudol, E. D., Influence of Chain Transfer Agent on the Cross-Linking of Poly(n-butylmethacrylate-co-N-methylol acrylamide Latex Particles and Films. *Macromolecules* **2003,** *36*, 3511-3518.
249. Nam, J.; Kim, E.; K, K. R.; Kim, Y.; Kim, T. H., A conductive self healing polymeric binder using hydrogen bonding for Si anodes in lithium ion batteries. *Sci Rep* **2020,** *10* (1), 14966.

5 Appendix

5.1 **Publication I:** Influence of the Drying Temperature on the Performance and Binder Distribution of Sulfurized Poly(acrylonitrile) Cathodes

S. Niesen; J. M. Kappler, J. Trück; L. Veith; T. Weil; T. Soczka-Guth, M. R. Buchmeiser, Influence of the Drying Temperature on the Performance and Binder Distribution of Sulfurized Poly(acrylonitrile) Cathodes. J. Electrochem. Soc. **2021**, 168, 050510.

Author Contributions: **S.N.:** Conceptualization, Investigation (Electrode Preparation & Characterization, Electrochemical Tests), Visualization, Writing - Original Draft; **J.T:** Investigation (Electrode Preparation), Writing - Review & Editing; **J.M.K.:** Investigation (Electrode Preparation) **L.V.:** Investigation (ToF-SIMS Measurements), Writing - Review & Editing; **T.W.:** Corresponding Supervisor at Max-Planck Institute; **T.S.-G..:** Corresponding Supervisor at Mercedes-Benz AG; **M.R.B.:** Conceptualization, Writing - Review & Editing.

Reprinted with permission from the Electrochemical Society.

Journal of The Electrochemical Society, 2021 **168** 050510
1945-7111/2021/168(5)/050510/6/$40.00 © 2021 The Electrochemical Society ("ECS"). Published on behalf of ECS by IOP Publishing Limited

Influence of the Drying Temperature on the Performance and Binder Distribution of Sulfurized Poly(acrylonitrile) Cathodes

Stefan Niesen,[1,2] Julian Kappler,[1] Janina Trück,[1,2] Lothar Veith,[3] Tanja Weil,[3] Thomas Soczka-Guth,[2] and Michael R. Buchmeiser[1,4,z]

[1]*Institute of Polymer Chemistry, University of Stuttgart, 70569 Stuttgart, Germany*
[2]*Mercedes-Benz AG, RD/EBZ, 70327 Stuttgart, Germany*
[3]*Max Planck Institute for Polymer Research, 55128 Mainz, Germany*
[4]*German Institutes of Textile and Fiber Research (DITF) Denkendorf, 73770 Denkendorf, Germany*

The drying of electrodes during the manufacturing process strongly affects both the cell performance and production costs of lithium-sulfur (Li-S) batteries. Herein, we present a detailed study on the effect of temperature during the drying process on the performance and binder distribution of sulfurized poly(acrylonitrile) (SPAN) based electrodes using poly(vinylidene fluoride) (PVdF) or poly(acrylic acid) (PAA) as the binder. The electrochemical performance of the PVdF- and PAA-based cathode coatings, which were dried at three different temperatures (30 °C, 60 °C and 90 °C), is analyzed by cycling against lithium metal and utilizing reference-assisted impedance spectroscopy. Time-of-flight secondary ion mass spectrometry (ToF SIMS) is applied on both the surface and the cross-section of the electrodes to determine the binder distribution. Contrary to the PAA-based cathodes, PVdF-based electrodes exhibit binder migration to the electrode surface at elevated coating drying temperatures. The enrichment of PVdF on the surface leads to an increase in the charge transfer resistance and thereby reduces the rate capability.
© 2021 The Electrochemical Society ("ECS"). Published on behalf of ECS by IOP Publishing Limited. [DOI: 10.1149/1945-7111/abfb95]

Manuscript submitted March 10, 2021; revised manuscript received April 15, 2021. Published May 3, 2021.

Supplementary material for this article is available online

Since several countries passed legislation to lower carbon dioxide (CO_2) emissions in the transport sector, many car manufacturers have committed themselves to electrifying their fleets. Therefore, the demand for energy storage devices will rise substantially in the near future and the search for novel high-performance battery materials will intensify.[1–3] Besides state of the art lithium-ion (Li-ion) battery technology, several promising post-Li-ion technologies have emerged.[4,5] Among these, lithium-sulfur (Li-S) batteries are of particular interest as they exhibit a high theoretical capacity of 1675 mAh g_S^{-1} and consist of mostly abundant and low-cost raw materials.[6–8]

However, any large-scale commercialization of Li-S battery technology has not yet been achieved, mainly due to the insulating nature of sulfur and the dissolution of polysulfides during operation, which results in a harmful internal polysulfide shuttle.[9–13] Owing to the absence of a polysulfide shuttle, high intrinsic electrical conductivity, excellent cycling stability and compatibility with carbonate-based electrolytes, sulfurized poly(acrylonitrile) (SPAN) is a promising cathode material for Li-S batteries and thereby a desirable technology for future energy storage applications.[14–20]

Nevertheless, prior to any large-scale production of SPAN-based electrodes, several parameters need to be addressed.[21,22] One of these parameters is the drying temperature of the electrode coating. To decrease costs and overall production time, a higher electrode drying temperature is favorable.[23,24] In the field of Li-ion batteries, a detrimental effect of an increase in the drying temperature on the rate capability is known for poly(vinylidene fluoride) (PVdF) based graphite electrodes. These differences in rate capability are caused by an uneven binder distribution, which results in an additional resistance at the surface of the electrodes.[25–27] Furthermore, a negative effect of an inhomogeneous binder distribution on the adhesion force, caused by an increased coating drying temperature, was observed for graphite anodes.[28,29]

In general, the binder strongly influences the obtainable rate capability and cycling stability especially within post-Li-ion batteries and should therefore be prudently chosen.[30–32] Besides PVdF, poly(acrylic acid) (PAA) is a commonly used binder for SPAN-based cathodes.[14] Contrary to PVdF, PAA has functional groups which can interact with the electrode materials and the current collector.[33] Therefore, PVdF- and PAA-based SPAN cathodes can be expected to exhibit different coating drying behavior.

Until now, the drying process of SPAN electrode coatings was an insufficiently understood processing step during the manufacturing of Li-SPAN cells. Here, the impact of the drying temperature on the electrochemical performance was verified by cycling both PAA-and PVdF-based SPAN electrode coatings, dried at three different temperatures (30 °C, 60 °C and 90 °C), against lithium metal. Additionally, differences in the internal resistances within the obtained electrodes were identified by using reference-assisted electrochemical impedance spectroscopy (EIS). Subsequently, the binder distribution of the obtained coatings was analyzed by time-of-flight secondary ion mass spectrometry (ToF-SIMS).

Experimental

Synthesis of sulfurized poly(acrylonitrile) (SPAN).—For the synthesis of SPAN, poly(acrylonitrile) (PAN, $M_n = 54{,}900$ g mol^{-1}, $Đ = 4.4$) was placed in a quartz glass tube and mixed with excess elemental sulfur (Carl Roth, Germany). The quartz glass tube was placed into a furnace (Nabertherm, Germany) and the following two-step temperature program was used. The sample was heated to 150 °C applying a heating rate of 300 °C h^{-1} and kept at this temperature for 30 min. Then the sample was heated to 550 °C within 2 h and held at this temperature for 5 h. During the entire heating process, a nitrogen flow (200 l h^{-1}) was applied. After cooling to room temperature, elemental sulfur was removed via extensive Soxhlet extraction with toluene at 150 °C for 24 h. The obtained SPAN particles were dried under vacuum overnight. All samples had a sulfur content of 38 ± 1 wt%.

Electrode preparation and drying.—Electrode slurries were prepared by mixing the obtained SPAN particles (80 wt%), Super C65 conducting carbon (10 wt%, MTI Corporation, USA) and a polymeric binder (10 wt%). Poly(vinylidene fluoride) (PVdF, Kynar, Arkema, France) and poly(acrylic acid) (PAA, Sigma Aldrich, Germany), respectively, were used as binders. Prior to mixing, PVdF and PAA were dissolved in *N*-methyl-2-pyrrolidone (NMP, anhydrous, 99.5%, Sigma-Aldrich). The SPAN:NMP ratio was set to 1:5 (w:w). After dissolving the binder, a defined amount of SPAN and C65 was added to the binder solution and mixed twice with a

[z]E-mail: michael.buchmeiser@ipoc.uni-stuttgart.de

Journal of The Electrochemical Society, 2021 **168** 050510

planetary mixer (Thinky, Japan) at 2000 rpm for 3 min. The resulting slurry was cast on a carbon-coated aluminum foil (t = 18 μm, MTI Corporation, USA) using a film coater (Erichsen, Germany) adjusting a wet film thickness of 300 μm. The solvent was evaporated on a heated vacuum plate for 8 h at 30 °C, 60 °C or 90 °C. After drying on a heated vacuum plate, the electrodes were dried in a vacuum chamber at 60 °C for at least 2 h. The resulting areal capacity of the SPAN cathodes was 2.4 ± 0.2 mAh cm^{-2}.

Electrochemical characterization.—To verify the influence of the coating drying temperature on the rate capability of the SPAN cathodes, coin cells (CR2032, Hohsen Corporation, Japan) were assembled in an argon-filled glovebox (H_2O and O_2 concentration ⩽ 0.1 ppm, MBraun, Germany) by sandwiching two layers of glass fiber separator (Ø = 16 mm, Whatman, UK) between an SPAN electrode (Ø = 12 mm) and a lithium metal anode (Ø = 14 mm, Alfa Aesar, USA). 130 μl of a commercially available electrolyte (1 M $LiPF_6$ in EC:DEC (1:1, v:v)), Sigma Aldrich, Germany) with the addition of 10 wt% fluoroethylene carbonate (FEC, Sigma Aldrich, Germany) was used as the electrolyte.

Electrochemical testing was performed with the aid of a battery cycler (BasyTec, Germany) in a voltage range of 1.0–3.0 V vs Li/Li^+. To investigate the rate capability, all cells were cycled galvanostatically at C-rates ranging from C/4 (~0.6 mA cm^{-2}) to 4 C (~9.6 mA cm^{-2}). Each cycling experiment included a resting period of 2 h to ensure complete wetting of the separator. For the long-term cycling experiments, five preformation cycles at C/4 were applied. Specific capacity and current density were calculated based on the mass of sulfur in the cathode using a theoretical sulfur capacity of 1675 mAh g_S^{-1}.

Electrochemical impedance spectroscopy was measured in PAT-cells (EL-Cell, Germany). Cells were assembled in an argon-filled glove box by sandwiching two layers of glass fiber separator (Ø = 21.6 mm, Whatman, UK) between an SPAN electrode (Ø = 16 mm) and a lithium metal anode (Ø = 18 mm, Alfa Aesar, USA). In between the separators, a partially insulated stainless steel finger-shaped reference electrode (EL-Cell, Germany) was placed and lithiated by applying a current of 1 mA for 6 h vs the lithium metal anode. For impedance measurements, 200 μl of 1 M $LiPF_6$ in EC:DEC (1:1, v-v, Sigma Aldrich, Germany) with an additional 10 wt% fluoroethylene carbonate (FEC, Sigma Aldrich, Germany) were used as the electrolyte. Impedance spectra were recorded with a potentiostat (Biologic, France) at an open-circuit voltage (OCV) at a state-of-charge (SOC) of 50% during charging in a frequency range between 200 kHz and 50 mHz with a 10 mV voltage perturbation. Before impedance measurements, the cells were cycled for five preformation cycles at C/4. All cells were measured in a climate room at 24 °C.

Time-of-flight secondary ion mass spectrometry (ToF-SIMS).—Spectra were recorded on a TOF-SIMS 5 (ION-TOF GmbH, Germany) instrument using a 30 keV Bi_3^+ primary ion beam (current: 0.15 pA, cycle time: 150 μs, mass range 1–2070 Da) with raster scanning areas of 200 × 200 μm^2. Images were acquired using a 30 keV Bi_3^+ primary ion beam (current: 0.05 pA, cycle time: 100 μs, mass range 1–920 Da) with raster scanning areas of 150 × 150 μm^2. Mass calibration of the data sets was performed using the signals of C^-, CH^-, C_2H^-, C_4H^- and C_6H^- in the negative ion polarity and of CH_3^+, $C_2H_3^+$, $C_3H_5^+$ and $C_4H_7^+$ in the positive ion polarity.

Results and Discussion

To assess the significance of the drying process on the rate capability of PAA- and PVdF-based SPAN cathodes, the obtained electrodes were cycled at alternating rates against lithium metal. Figure 1 illustrates the discharge capacities of the PVdF- and PAA-based SPAN electrodes, dried at three different temperatures (30 °C, 60 °C and 90 °C), at various C-rates (C/4–4 C). For the PVdF-based

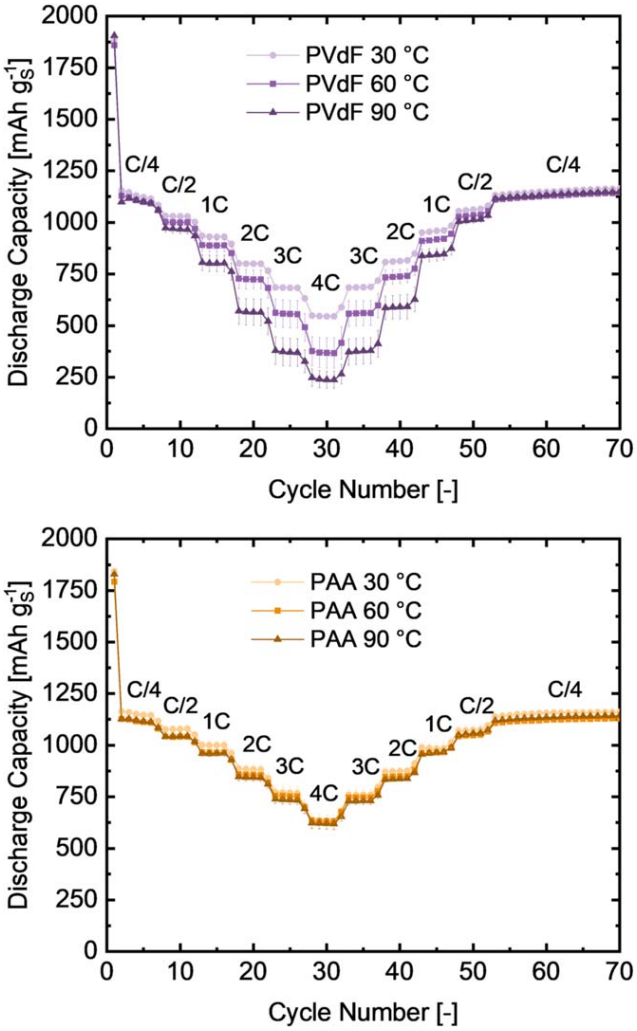

Figure 1. Galvanostatic cycling of PVdF- (upper panel) and PAA- (lower panel) based SPAN coatings dried at different temperatures (30 °C, 60 °C, 90 °C) vs lithium metal between 1−3 V vs Li/Li^+. Applied current range: C/4 (~0.6 mA cm^{-2}) to 4C (~ 9.6 mA cm^{-2}). The error bars represent the standard deviation of at least two independent measurements.

cathodes, the discharge capacities decreased with increasing coating drying temperature at C-rates higher than C/2. At 4 C, the obtainable capacity was 544 mAh g_S^{-1}, 367 mAh g_S^{-1} and 237 mAh g_S^{-1} for the PVdF coatings dried at 30 °C, 60 °C and 90 °C, respectively. At lower rates (⩽ C/2), no effect of the drying temperature on the performance of the PVdF-based cathodes was observed. The capacity of the cells at C/4 and C/2 before cycling at higher rates was identical to the capacity after cycling at higher rates. Therefore, the capacity drop at higher rates is reversible and not caused by cell degradation. In contrast to the electrodes prepared with PVdF, the coating drying temperature had no impact on the rate capability of the PAA-based electrodes. Interestingly, the rate capability of the PVdF-based cathodes dried at 30 °C, was almost identical to the rate capability of the PAA-based cathodes, which implies that the low rate capability of the PVdF-based electrodes is caused solely by an increased drying temperature (> 30 °C) and not by the nature of the binder itself. Figure 2 shows the voltage profiles of the tested electrodes, which were extracted from the third 4C cycle of the rate capability tests. With increasing coating temperature the voltage profiles of the PVdF-based electrodes are shifted to lower voltages during discharge and higher voltages during the charging of the cell. For the cathodes prepared with PAA, no shift in the voltage profiles was observed. Consequently, the loss of capacity at higher rates of

Journal of The Electrochemical Society, 2021 **168** 050510

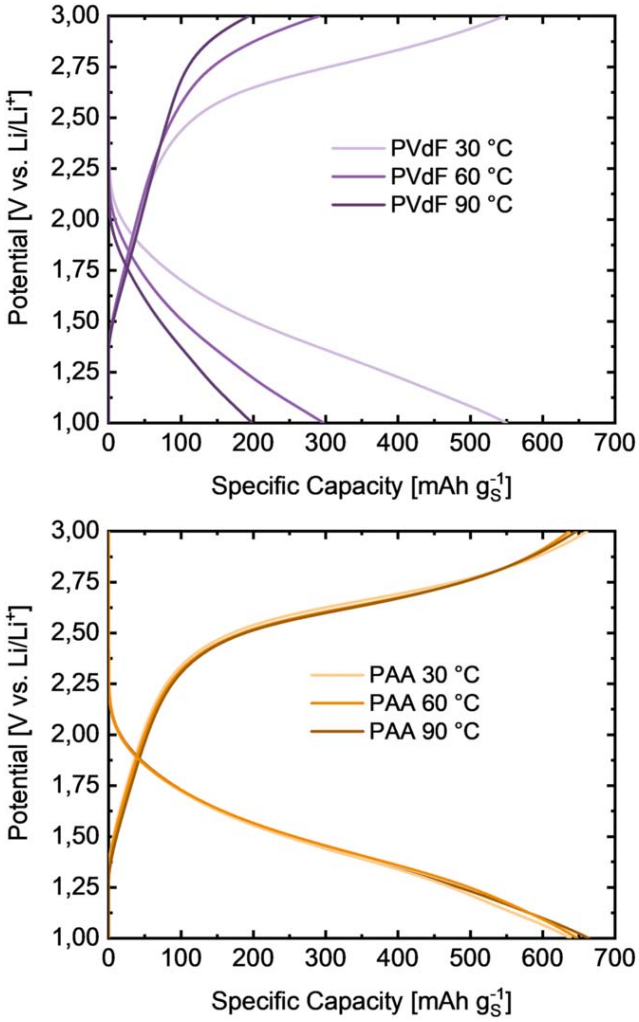

Figure 2. Voltage profiles of PVdF- (upper panel) and PAA- (lower panel) based SPAN coatings dried at different temperatures (30 °C, 60 °C, 90 °) at 4C extracted from the rate capability tests.

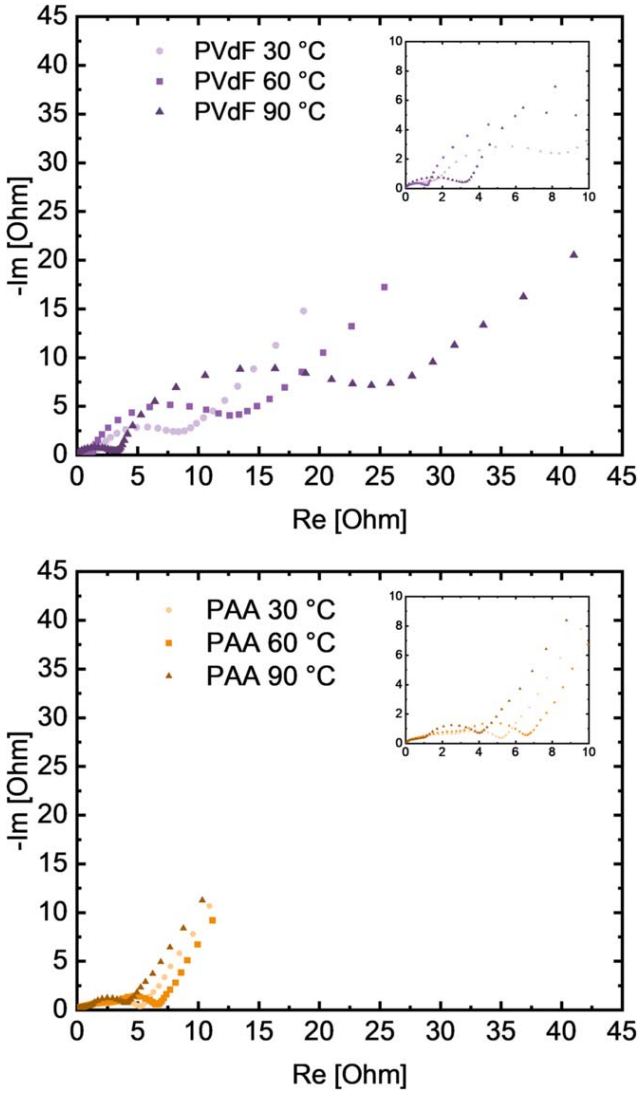

Figure 3. Nyquist plots of the SPAN cathodes with PVdF (upper panel) and PAA (lower panel) as binder dried at different coating drying temperatures (30 °C, 60 °C, 90 °C) measured in Li-SPAN cells utilizing the lithiated stainless steel finger-shaped reference electrode. For impedance measurements, cells were preformed for five cycles at C/4 ($\sim$ 0.6 mA cm^{-2}) and then charged to 50% SOC. The impedance spectra were acquired at OCV between 200 kHz and 50 mHz with an amplitude of 10 mV. For better comparability, the high-frequency resistance (R_1) was subtracted from all the measurements.

the PVdF-based coatings originates from incomplete discharge or charge of the cells, caused by an increase in overpotential at elevated coating drying temperatures.

To verify the influence of the drying process on the internal resistance of the obtained PVdF- and PAA-based cathodes, reference-assisted impedance measurements were conducted. Impedance measurements with a reference electrode in a three-electrode cell configuration allow the disentangling of the impedance signal of the anode and cathode.[34] Here, a lithiated finger-shaped stainless steel reference electrode, which was placed in the geometrical middle between anode and cathode instead of the outer edge of the cell stack, was applied. By placing the reference electrode at the center of the cell, the impedance of the cathode can be measured without artifacts caused by electric field inhomogeneity.[35] The reference electrode was lithiated by applying a small current vs the lithium metal anode. After cycling for five preformation cycles at C/4, the impedance of the cells was measured at an SOC of 50 % during the charging step. Figure 3 shows the Nyquist plots of the PVdF- and PAA-based SPAN electrode coatings, which were dried at different coating temperatures. The obtained plots were fitted with the equivalent circuit model (Fig. S1, Supporting Information (available online at stacks.iop.org/JES/168/050510/mmedia)), consisting of a high frequency resistance (R_1), two R/Q elements (R_2/Q_1, R_3/Q_2) and a Warburg element (W_1) in series. The two R/Q elements were assigned to the contact resistance between coating and current collector (R_2/Q_1) and the charge transfer resistance (R_3/Q_2). The Warburg element was applied to model Li^+ diffusion. The exact fitted data is given in Table SI (Supporting Information). Since the contact resistance (R_2) was almost identical for all measurements ($\sim$ 2 Ω), the following discussion will solely focus on distinctions in the charge transfer resistance (R_3) and differences in the high-frequency region. In the case of PVdF-based cathodes, the charge transfer resistance raised sharply with increasing coating drying temperature and was 5 Ω, 10 Ω and 14 Ω applying a coating drying temperature of 30 °C, 60 °C and 90 °C, respectively. Additionally, by comparing the angles of the high frequency branch e.g., PVdF-30 °C vs PVdF-90 °C, a coating drying temperature-induced increase in the slope of the Warburg diffusion element was observed. Contrary to the PVdF-based cathodes, the charge transfer resistances of the PAA-based cathodes remained almost constant (3 Ω−4 Ω) and no change in the angle of the high frequency region was observed within the investigated coating drying temperature range. The obtained impedance results indicate that the detrimental effect of the drying

process on the rate capability of the PVdF-based electrodes is caused by an increase in the charge transfer resistance and a more pronounced Li^+ diffusion limitation with increasing coating drying temperature.

In order to assess whether the coating drying temperature has an additional harmful effect on the cycle life of the PVdF-based cathodes, the capacity retention was evaluated by cycling the PVdF-based electrodes vs lithium metal at 1C for 500 cycles. The results of the long-term cycling tests are illustrated in Fig. S2 (Supporting Information). No impact of the temperature during the drying process on the capacity retention of the PVdF-based cathodes was observed, indicating that the drying temperature solely affects the rate capability.

To verify whether the observed distinctions in the rate capabilities, charge transfer resistances and Li^+ diffusion were caused by an inhomogeneous binder distribution, ToF-SIMS measurements were applied to analyze the binder distribution within the pristine PAA- and PVdF-based cathodes. ToF-SIMS is a powerful tool to provide fragment-specific information of surfaces.[36–38] Notably, to the best of our knowledge, this is the first time ToF-SIMS was used to elucidate the binder distribution within a battery electrode. First, ToF-SIMS measurements were carried out on the surface of the electrodes. Figure 4 illustrates the ToF-SIMS images of the surfaces of the PVdF- and PAA-based electrode coatings. The detected fragments on the electrode surfaces include the diagnostic ions CN^- (red), C_2^- (green), F^- (blue) and C_2HO^- (blue) for SPAN, C65 Carbon, PVdF and PAA, respectively. The signal intensity scales were adjusted to enable a comparison between the different drying temperatures. Reference ToF-SIMS spectra of the pure electrode materials are depicted in Figs, S3–S5 (Supporting Information).

As can be seen in Figs. 4a–4c, the F^- signal intensity (shown in blue) on the surface of the PVdF-based electrode increased sharply with increasing coating drying temperatures, suggesting a larger amount of PVdF on the surface. Especially at higher drying temperatures (> 30 °C) high PVdF signal intensities, which cover almost the entire electrode surface, were obtained. For the PAA-based electrode coatings, only a minor influence of the drying temperature on the PAA intensities on the surface of the electrodes was observed (Figs. 4d–4f). Contrary to the PVdF-based cathodes, even at the highest drying temperature (90 °C) no complete coverage of the surface by a distinct binder layer was observed for the PAA-based electrode surface. This suggests that the recognized harmful influence of the coating drying temperature on the rate capability of the PVdF-based electrodes originates from the formation of a PVdF layer on the surface.

To get a more detailed understanding of the influence of the drying temperature on the binder distribution within the PVdF- and PAA-based electrode coatings, ToF-SIMS images of electrode cross-sections (created by cutting liquid N_2-frozen electrodes with scissors) were acquired. Detected fragments were F^- for PVdF (green) and $C_3H_3O_2^-$ (green) for PAA. The O^- and AlO^- fragments (red) were used as diagnostic ions for the current collector visible on top of the images. The detected signal distributions (F^- or $C_3H_3O_2^-$) matched the expected thickness (~90 μm, previously determined with a thickness gauge) of the electrodes. The PVdF-based cathodes dried at 30 °C showed a homogenous PVdF distribution based on the detected F^- signal (Fig. 5a). At higher drying temperatures (60 °C and 90 °C), the PVdF binder became less homogenously distributed (Figs. 5b–5c). Several spots with notably high F^- intensities (bright green, exemplary spots marked with red circles) became visible in the coatings dried at elevated temperatures (> 30 °C), which indicates an agglomeration of the PVdF binder at drying temperatures higher than 30 °C. In particular, closer to the electrode surface (lower part of the images), several spots with increased F^- signal intensities became visible in the ToF-SIMS images of the PVdF-based electrode coatings dried at 60 °C and 90 °C. As can be seen by comparing Figs. 4b and 4c, the extent of the PVdF agglomeration close to the electrode surface increases notably with elevating coating drying temperature. Therefore, it can be assumed that the detected PVdF agglomerates close to or at the electrode surface are formed by the migration of the PVdF binder during the drying process at elevated drying temperatures (i.e. higher solvent evaporation rates). Since PVdF is an insulator and exhibits only poor ionic conductivity, an agglomeration of PVdF (e.g. on the surface) could potentially increase the electrical and/or ionic resistance of the electrode. Consequently, the obtained ToF-SIMS results strongly suggest that the detrimental effect of drying at elevated temperatures (> 30 °C) on the charge transfer resistance and Li^+ diffusion of PVdF-based electrodes, which led to a reduction in rate capability, is most likely caused by a migration of the PVdF binder to the

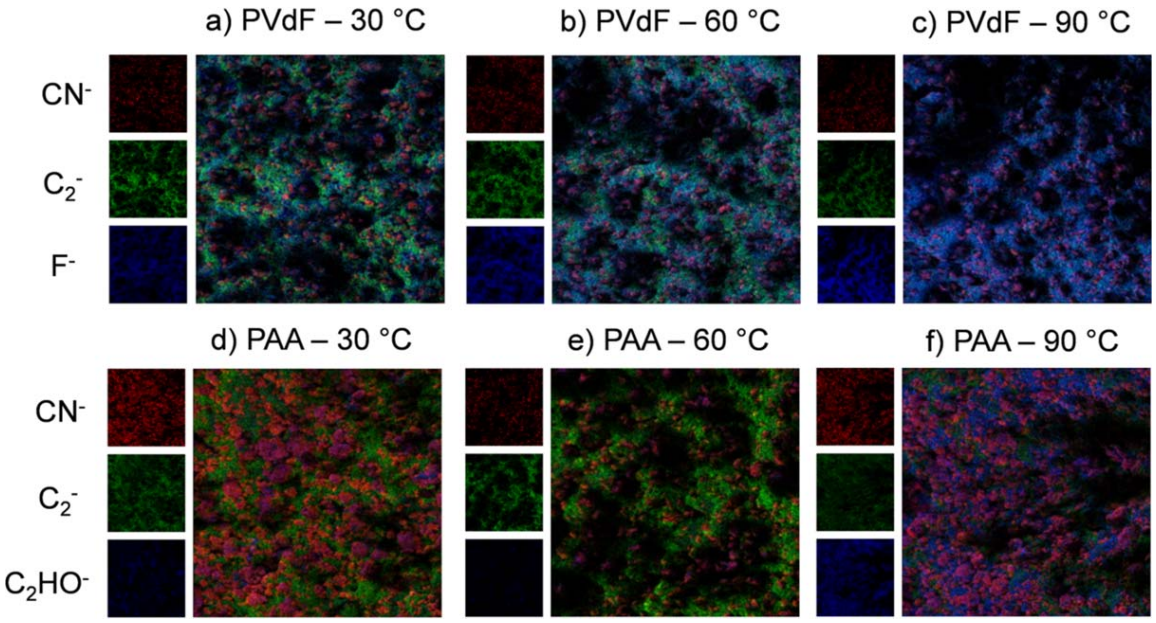

Figure 4. ToF-SIMS images of the electrode surfaces with intensity scales matched to enable for comparison within the binder type. Upper panel: pristine PVdF-based electrode coatings dried at 30 °C (a), 60 °C (b) and 90 °C (c). Lower panel: pristine PAA-based electrode coatings dried at 30 °C (d), 60 °C (e) and 90 °C (f). Detected fragments include CN^- (SPAN, red), C_2^- (C65 Carbon, green), F^- (PVdF, blue) and C_2HO^- (PAA, blue). The raster scanning area is 150 × 150 μm^2.

Journal of The Electrochemical Society, 2021 **168** 050510

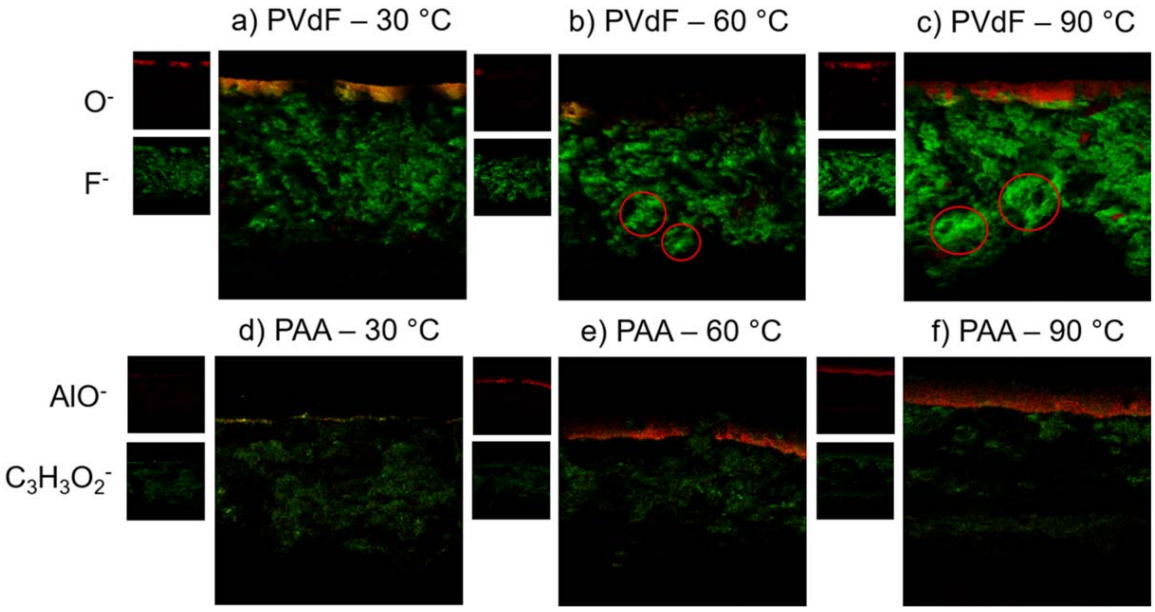

Figure 5. ToF-SIMS images of the electrode cross-sections with intensity scales matched to enable for comparison within the binder type. Upper panel: pristine PVdF-based electrode coatings dried at 30 °C (a), 60 °C (b) and 90 °C (c) with F^- (green) as the detected binder fragment. Lower panel: pristine PAA-based electrode coatings dried at 30 °C (d), 60 °C (e) and 90 °C (f) with $C_3H_3O_2^-$ (green) as the detected binder fragment. The current collector (C coated on Al) is on top of the images and detected based on the O^- (red) or AlO^- (red) fragment. The raster scanning area is 150 × 150 μm^2.

electrode surface induced by higher solvent evaporation rates. Given that the ToF-SIMS measurements were repeated several times and that the described effect of the drying temperature on the PVdF distribution was visible in all measurements, the migration of PVdF is solely caused by the drying temperature and not by a deviation in the roughness of the electrodes. The observed influence of drying temperature on the rate capability and binder distribution of the SPAN cathodes prepared with PVdF is in good agreement with studies conducted on Li-ion anodes. Jaiser et al. and Morasch et al. investigated the effect of the drying temperature on the rate capability and binder distribution of PVdF-based graphite anodes.[25,29] Both studies demonstrates that the harmful effect of an increase in the coating drying temperature on the rate capability originates from the enrichment of PVdF on the electrode surface.

In the ToF-SIMS images of the PAA-based electrode cross-sections, a mostly homogenous distribution of the C_2HO^- signal with similarly high intensity in the electrode area was observed for all the investigated drying temperatures (Figs. 5d–5f). Elevated $C_3H_3O_2^-$ intensities became visible close to the current collector in the images of the PAA-based coatings which were dried at 30 °C and 90 °C. Since the carbon-coated current collector exhibits oxygen functionalities, which can form hydrogen bonds, the increased signal intensity of the PAA-based signal ($C_3H_3O_2^-$) close to the current collector can potentially be explained by an interaction of the PAA binder with the carbon coating on the current collector.[39] Additionally, an increased ion collision-cascade efficiency on the metal current collector might also lead to elevated secondary ion intensities in its vicinity. Considering that no influence of the coating drying temperature on the rate capability and impedance was detected during the electrochemical characterization, the assumed PAA layer at the coating/current collector interface, which is visible in particular in Fig. 5d, has no detrimental effect on the performance of the PAA-based cathodes and can therefore be disregarded.

The distinction in the migration behavior between PVdF- and PAA-based electrodes during the drying process can potentially be explained by differences in the structures of the binders. In contrast to PAA, PVdF has no carboxylic acid groups which can interact via hydrogen bonds with the electrode materials (SPAN, conductive carbon) and/or current collector. It has previously been shown that the adhesion ability of binders to the electrode materials can have a strong impact on both electrode processing and performance. For example, Yoo et al. showed that the usage of hydroxyl-functionalized PVdF compared to non-functionalized PVdF as a binder for graphite anodes led to an enhanced adhesion between active material and binder and thereby to a more homogenous binder distribution.[40–42] Therefore, the inability of PVdF to form such strong interactions with the electrode materials likely promotes its mobility, which ultimately leads to a severe agglomeration and migration of PVdF towards the surface at elevated coating drying temperatures. The migration of PVdF to the surface is expected to be caused by phase separation between PVdF and other electrode materials, which itself is provoked by the more pronounced evaporation of NMP at higher drying temperatures. Besides the inability of PVdF to form sufficient adhesion with the electrode materials, a stronger interaction of PVdF and NMP (relative to PAA and NMP) could additionally be made accountable for the observed migration of PVdF. If the interaction between the binder and solvent is too strong, the binder may segregate to the surface during solvent evaporation at high drying rates. A detailed study on the migration mechanism of PVdF-based SPAN cathodes is ongoing.

Conclusions

The influence of the coating drying temperature on the electrochemical performance and binder distribution of PVdF- and PAA-based cathodes was investigated by utilizing reference-assisted impedance spectroscopy and ToF-SIMS. The rate capability of the PVdF-based electrodes decreased sharply with increasing coating drying temperature, whereas the rate capability of the PAA-based electrodes was independent of the temperature applied during the drying process. Impedance measurements of the PVdF-based cathodes revealed that the reduction in the rate capability was caused by an increase in the charge transfer resistance and a more pronounced Li^+ diffusion limitation. ToF-SIMS measurements showed that the harmful effect of an increase in the coating drying temperature on the charge transfer resistance and Li^+ diffusion of the PVdF-based electrodes originates from the enrichment of PVdF on the electrode surface.

Journal of The Electrochemical Society, 2021 **168** 050510

Acknowledgments

We gratefully acknowledge funding and support from the German Federal Ministry for Economic Affairs and Energy (BMWi, project no. S50400, *FiMaLiS*). Dralon GmbH (Germany) is gratefully acknowledged for providing the PAN particles. Furthermore, the authors thank M. Siodlaczek, A. M. Fox, S. Murugan and J. V. Musso (Institute of Polymer Chemistry, University of Stuttgart) for fruitful discussions.

ORCID

Michael R. Buchmeiser https://orcid.org/0000-0001-6472-5156

References

1. E. A. Olivetti, G. Ceder, G. G. Gaustad, and X. Fu, *Joule*, **1**, 229 (2017).
2. H. Budde-Meiwes, J. Drillkens, B. Lunz, J. Muennix, S. Rothgang, J. Kowal, and D. U. Sauer, *Proc. Inst. Mech. Eng. D*, **227**, 761 (2013).
3. N. Nitta, F. Wu, J. T. Lee, and G. Yushin, *Mater. Today*, **18**, 252 (2015).
4. J. W. Choi and D. Aurbach, *Nat. Rev. Mater.,*, **1**, 1 (2016).
5. M. Walter, M. V. Kovalenko, and K. V. Kravchyk, *New J. Chem.*, **44**, 1677 (2020).
6. A. Manthiram, Y. Fu, S. H. Chung, C. Zu, and Y. S. Su, *Chem. Rev.*, **114**, 11751 (2014).
7. G. Benveniste, H. Rallo, L. Canals Casals, A. Merino, and B. Amante, *J. Environ. Manage.*, **226**, 1 (2018).
8. Q. Pang, X. Liang, C. Y. Kwok, and L. F. Nazar, *Nat. Energy,*, **1**, 1 (2016).
9. P. T. Dirlam, R. S. Glass, K. Char, and J. Pyun, *J. Polym. Sci. A Polym. Chem.*, **55**, 1635 (2017).
10. V. S. Kolosnitsyn, E. V. Kuzmina, and E. V. Karaseva, *J. Power Sources*, **274**, 203 (2015).
11. J. Scheers, S. Fantini, and P. Johansson, *J. Power Sources*, **255**, 204 (2014).
12. R. Mukkabla and M. R. Buchmeiser, *J. Mater. Chem.*, **8**, 5379 (2020).
13. T. Ould Ely, D. Kamzabek, D. Chakraborty, and M. F. Doherty, *ACS Appl. Energy Mater.*, **1**, 1783 (2018).
14. H. M. Kim, J. Y. Hwang, D. Aurbach, and Y. K. Sun, *J. Phys. Chem. Lett.*, **8**, 5331 (2017).
15. J. Fanous, M. Wegner, J. Grimminger, Ä. Andresen, and M. R. Buchmeiser, *Chem. Mater.*, **23**, 5024 (2011).
16. J. Fanous, M. Wegner, M. B. M. Spera, and M. R. Buchmeiser, *J. Electrochem. Soc.*, **160**, A1169 (2013).
17. M. Frey, R. K. Zenn, S. Warneke, K. Müller, A. Hintennach, R. E. Dinnebier, and M. R. Buchmeiser, *ACS Energy Lett.*, **2**, 595 (2017).
18. H. Yang, J. Chen, J. Yang, and J. Wang, *Angew. Chem. Int. Ed.*, **59**, 7306 (2020).
19. S. Warneke, A. Hintennach, and M. R. Buchmeiser, *J. Electrochem. Soc.*, **165**A2093 (2018).
20. T. Lebherz, M. Frey, A. Hintennach, and M. R. Buchmeiser, *RSC Adv.*, **9**, 7181 (2019).
21. O. Gröger, H. A. Gasteiger, and J.-P. Suchsland, *J. Electrochem. Soc.*, **162**, A2605 (2015).
22. S. Dörfler, H. Althues, P. Härtel, T. Abendroth, B. Schumm, and S. Kaskel, *Joule*, **4**, 539 (2020).
23. D. L. Wood, J. D. Quass, J. Li, S. Ahmed, D. Ventola, and C. Daniel, *Dry. Technol.,*, **36**, 234 (2017).
24. D. L. Wood, J. Li, and C. Daniel, *J. Power Sources*, **275**, 234 (2015).
25. R. Morasch, J. Landesfeind, B. Suthar, and H. A. Gasteiger, *J. Electrochem. Soc.*, **165**, A3459 (2018).
26. M. Müller, L. Pfaffmann, S. Jaiser, M. Baunach, V. Trouillet, F. Scheiba, P. Scharfer, W. Schabel, and W. Bauer, *J. Power Sources*, **340**, 1 (2017).
27. B. G. Westphal and A. Kwade, *J. Energy Storage*, **18**, 509 (2018).
28. J. Kumberg, M. Müller, R. Diehm, S. Spiegel, C. Wachsmann, W. Bauer, P. Scharfer, and W. Schabel, *Energy Technol.*, **7**, 1900722 (2019).
29. S. Jaiser, M. Müller, M. Baunach, W. Bauer, P. Scharfer, and W. Schabel, *J. Power Sources*, **318**, 210 (2016).
30. H. Yuan, J.-Q. Huang, H.-J. Peng, M.-M. Titirici, R. Xiang, R. Chen, Q. Liu, and Q. Zhang, *Adv. Energy Mater.*, **8**, 1802107 (2018).
31. K. K. Rajeev, E. Kim, J. Nam, S. Lee, J. Mun, and T.-H. Kim, *Electrochim. Acta*, **333**, 135532 (2020).
32. S. Lim, R. L. Thankamony, T. Yim, H. Chu, Y. J. Kim, J. Mun, and T. H. Kim, *ACS Appl. Mater. Interfaces*, **7**, 1401 (2015).
33. J.-T. Li, Z.-Y. Wu, Y.-Q. Lu, Y. Zhou, Q.-S. Huang, L. Huang, and S.-G. Sun, *Adv. Energy Mater.*, **7**, 1701185 (2017).
34. M. Dollé, F. Orsini, A. Gozdz S., and J.-M. Tarascon, *J. Electrochem. Soc.*, **148**, A851 (2001).
35. Y. Hoshi, Y. Narita, K. Honda, T. Ohtaki, I. Shitanda, and M. Itagaki, *J. Power Sources*, **288**, 168 (2015).
36. J.-H. Song, J.-T. Yeon, J.-Y. Jang, J.-G. Han, S.-M. Lee, and N.-S. Choi, *J. Electrochem. Soc.*, **160**, A873 (2013).
37. E. M. Erickson, W. Li, A. Dolocan, and A. Manthiram, *ACS Appl. Mater. Interfaces,*, **12**, 16451 (2020).
38. T. Sui, B. Song, J. Dluhos, L. Lu, and A. M. Korsunsky, *Nano Energy*, **17**, 254 (2015).
39. M. Kuenzel, D. Bresser, G.-T. Kim, P. Axmann, M. Wohlfahrt-Mehrens, and S. Passerini, *ACS Appl. Energy Mater.*, **3**, 218 (2019).
40. C.-C. Li and Y.-S. Lin, *J. Power Sources*, **220**, 413 (2012).
41. C.-C. Li and Y. -W. Wang, *J. Electrochem. Soc.*, **158**, A1361 (2011).
42. C. W. F. M. Yoo and S. Mori, *Chem. Mater.*, **15**, 850 (2003).

Supporting Information

Influence of the Drying Temperature on the Performance and Binder Distribution of Sulfurized Poly(acrylonitrile) Cathodes

Stefan Niesen[1,3], Julian Kappler[1], Janina Trück[1,3], Lothar Veith[4], Tanja Weil[4], Thomas Soczka-Guth[3] and Michael R. Buchmeiser*[1,2]

[1]*Institute of Polymer Chemistry, University of Stuttgart, 70569, Stuttgart, Germany*

[2]*German Institutes of Textile and Fiber Research (DITF) Denkendorf, 73770 Denkendorf, Germany*

[3]*Mercedes-Benz AG, RD/EBZ, 70327 Stuttgart, Germany*

[4]*Max Planck Institute for Polymer Research, 55128 Mainz, Germany*

**Corresponding Author E-mail Address [michael.buchmeiser@ipoc.uni-stuttgart.de]*

Table S1: Fitted values of the EIS results from Figure 2. The error represents the standard deviation of at least two independent measurements.

	R_2 [Ω]	R_3 [Ω]
PAA 30°C	1.5 ± 0.1	3.3 ± 0.3
PAA 60°C	2.3 ± 0.2	4.0 ± 0.3
PAA 90°C	2.0 ± 1.0	2.7 ± 0.4
PVdF 30°C	1.7 ± 0.6	5.2 ± 0.3
PVdF 60°C	1.7 ± 0.6	9.8 ± 0.6
PVdF 90°C	2.9 ± 0.7	14.3 ± 2.4

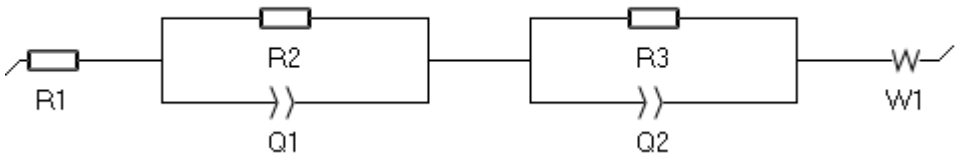

Figure S1: Equivalent circuit model used to fit the obtained impedance data.

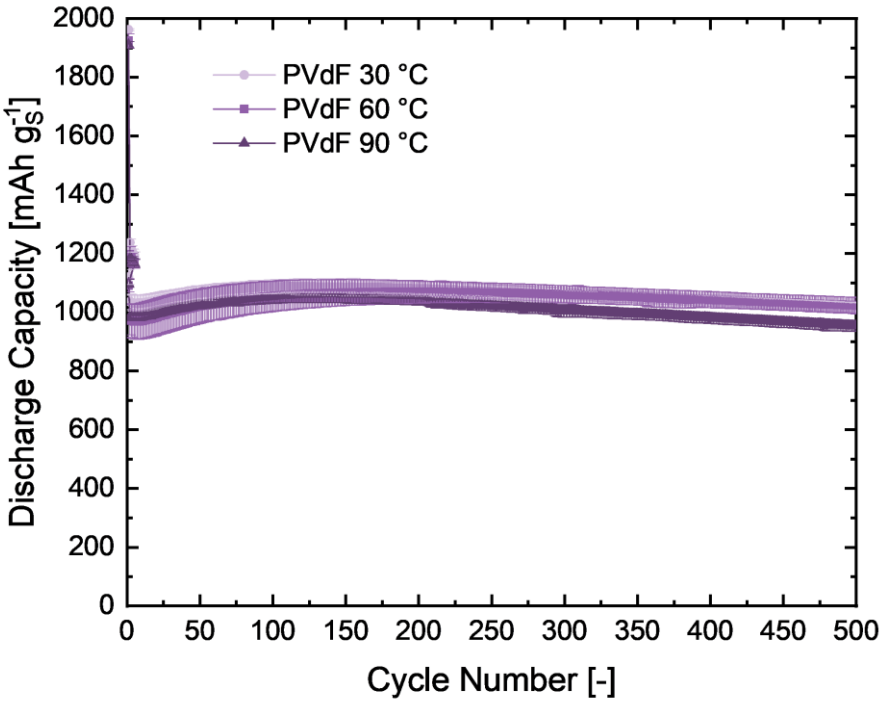

Figure S2: Galvanostatic cycling of PVdF-based SPAN coatings dried at different temperatures (30 °C, 60 °C, 90 °C) vs lithium metal between 1 - 3 V vs Li/Li^+, applied current: 1C (~ 2.4 mA cm^{-2}) after five preformation cycles at C/4 (~ 0.6 mA cm^{-2}). The error bars represent the standard deviation of at least two independent measurements.

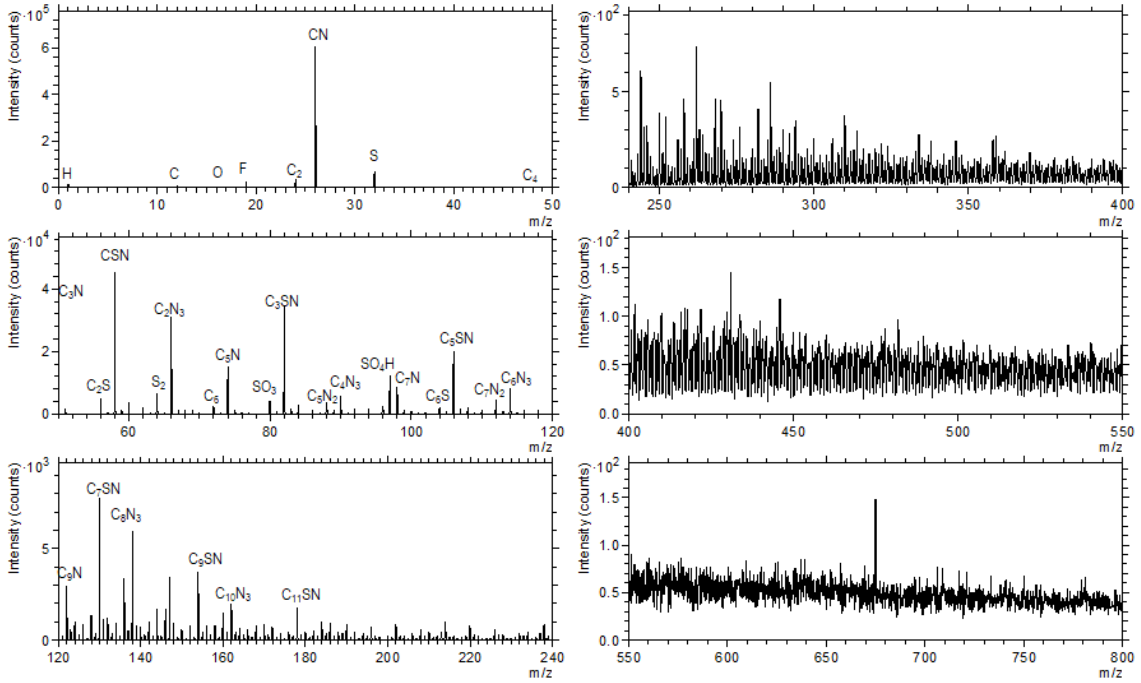

Figure S3: ToF-SIMS surface spectra of the negative fragments of SPAN.

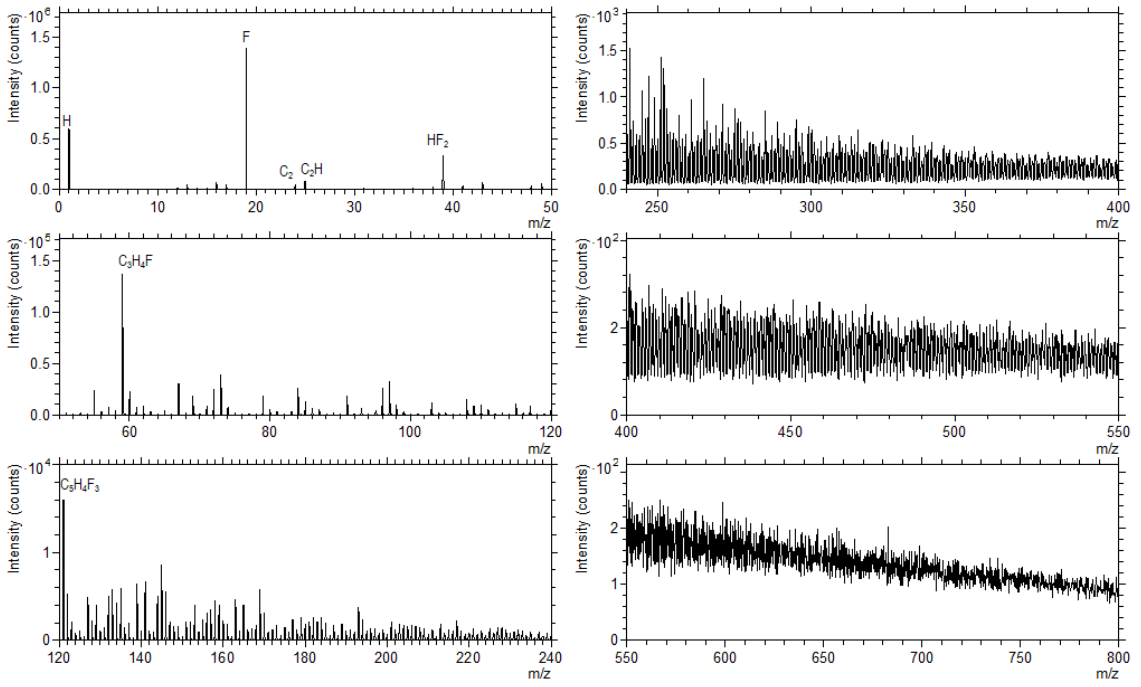

Figure S4: ToF-SIMS surface spectra of the negative fragments of PVdF.

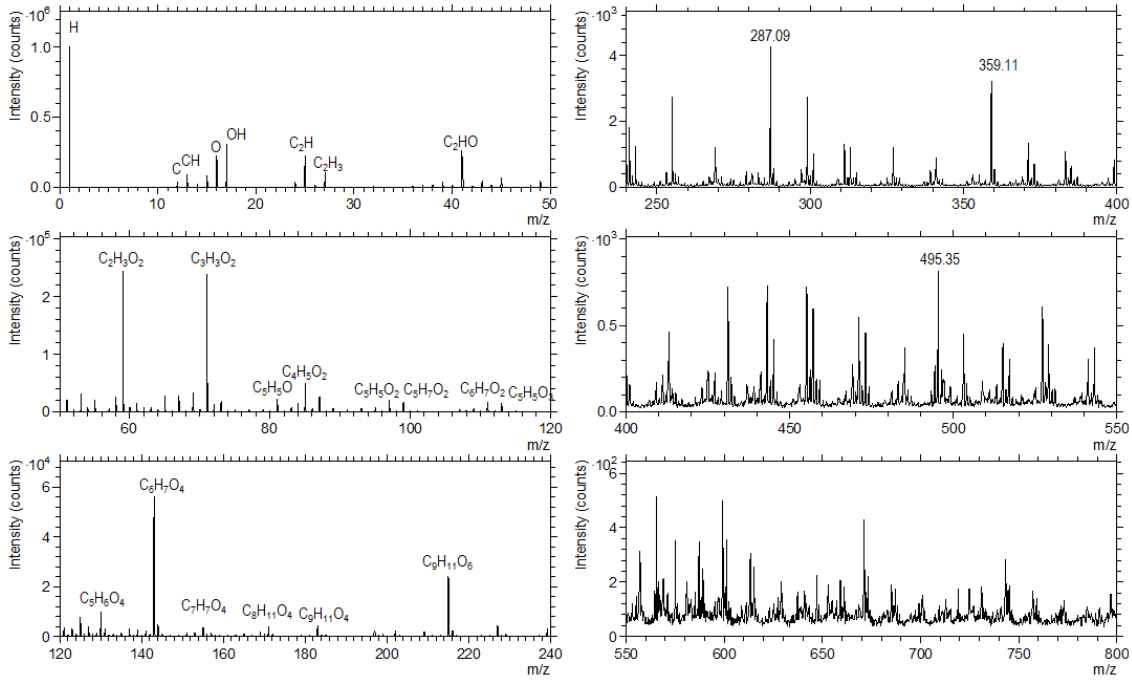

Figure S5: ToF-SIMS surface spectra of the negative fragments of PAA.

5.2 **Publication II:** Lithium-Sulfur Batteries Based on Sulfurized Poly(acrylonitrile) Cathodes: Impact of Electrode Density on Cell Performance

S. Niesen; J. Trück; C. Seidl; K. Renger; M. R. Buchmeiser, Lithium-Sulfur Batteries Based on Sulfurized Poly(acrylonitrile) Cathodes: Impact of Electrode Density on Cell Performance. J. Electrochem. Soc. **2021**, 168, 110513.

Author Contributions: **S.N.:** Conceptualization, Investigation (Electrode Preparation & Characterization, Electrochemical Tests, Calculations), Visualization, Writing - Original Draft; **J.T:** Investigation (Electrode Preparation), Writing - Review & Editing; **C.S.:** Investigation (Adhesion Tests) **K.R.:** Investigation (Calculations), Writing - Review & Editing; **M.R.B.:** Conceptualization, Writing - Review & Editing.

Reprinted with permission from the Electrochemical Society.

Journal of The Electrochemical Society, 2021 **168** 110513
1945-7111/2021/168(11)/110513/5/$40.00 © 2021 The Electrochemical Society ("ECS"). Published on behalf of ECS by IOP Publishing Limited

Lithium-Sulfur Batteries Based on Sulfurized Poly(acrylonitrile) Cathodes: impact of Electrode Density on Cell Performance

Stefan Niesen,[1,2] Janina Trück,[1,2] Christoph Seidl,[2] Katrin Renger,[2] and Michael R. Buchmeiser[1,3,z]

[1]*Institute of Polymer Chemistry, University of Stuttgart, 70569 Stuttgart, Germany*
[2]*Mercedes-Benz AG, RD/EBZ, 70327 Stuttgart, Germany*
[3]*German Institutes of Textile and Fiber Research (DITF) Denkendorf, 73770 Denkendorf, Germany*

Calendering of battery electrodes during the manufacturing process enhances the volumetric energy density by increasing the electrode density and has a substantial impact on the cell performance of Li-ion and post-Li-ion batteries. Herein, we present a detailed study on the influence of electrode density on the electrochemical performance of sulfurized poly(acrylonitrile) (SPAN) cathodes. A correlation of the density of the SPAN cathodes with electrode properties and cell performance by applying various chemical and electrochemical methods is displayed. Our results showed that while calendering reduces the electrical resistance, compressing the electrodes to densities higher than 1.05 g cm^{-3} leads to a reduction of the rate capability, which is caused by a compression-induced reduction of active reaction sites and a poor wettability of the electrode with electrolyte, both visible by an increase in the charge-transfer resistance.
© 2021 The Electrochemical Society ("ECS"). Published on behalf of ECS by IOP Publishing Limited. [DOI: 10.1149/1945-7111/ac334d]

Manuscript submitted September 16, 2021; revised manuscript received October 18, 2021. Published November 9, 2021.

Supplementary material for this article is available online

Due to the growing usage of batteries in various applications such as portable devices, electric vehicles and electrical grid storage, the demand for energy storage materials is increasing rapidly.[1–3] Unfortunately, today's state-of-the-art Li-ion batteries are expensive and based on transition metals that are harmful and carry a supply risk in the nearby future. Therefore, to meet the growing demand, alternative battery chemistries based on abundant, environmentally friendly and low-cost raw materials are needed.[4–7] Sulfur with its low price, high abundance, non-toxicity and high theoretical capacity of 1675 mAh g^{-1} is one of the most promising post-Li-ion active materials.[8–12]

Within the field of Li-S cathode materials, sulfurized poly (acrylonitrile) (SPAN) derived from the reaction of poly(acrylonitrile) with liquid sulfur is of special interest. In contrast to traditionally used Li-S active materials, the covalently bound sulfur within the SPAN structure prevents the formation and dissolution of harmful polysulfides enabling excellent capacity retention.[5,13–18]

To maximize the energy density of the Li-SPAN cells, several parameters need to be investigated and optimized. Besides increasing the active material content and enhancing the areal loading of the electrode coating, compaction of the SPAN cathodes to high electrode densities can significantly enhance the volumetric energy density, which is especially important for the application in portable devices or electric vehicles.[19–21] Higher electrode densities are not only desirable for high volumetric energy densities but also reduce electrical resistances by enhancing the particle contact and increase gravimetric energy densities due to reduction in electrolyte uptake. However, compression-induced changes in the pore structure can potentially decrease sulfur utilization, rate capability and capacity retention.[22–27] A detailed correlation between the electrode density and electrochemical performance is therefore of high importance for advancing Li-S batteries.

By combining several characterization methods, we studied the influence of the electrode density of SPAN electrodes on cell performance. The electrode density of SPAN electrodes with high active material content (90 wt% SPAN) and high areal loading (2.7mAh cm^{-2}) was adjusted by calendaring to values between 0.80 g cm^{-3} and 1.20 g cm^{-3}. Electrodes were analyzed by scanning electron microscopy (SEM), mercury intrusion measurements, multi-point resistivity measurements and electrochemical impedance spectroscopy (EIS). We correlated analytical data with rate capability and capacity retention results and thereby elucidated the impact of electrode density on the performance of SPAN cathodes.

[z]E-mail: michael.buchmeiser@ipoc.uni-stuttgart.de

Experimental

Synthesis of sulfurized poly(acrylonitrile) (SPAN).—SPAN was prepared by heating poly(acrylonitrile) (PAN, M_n = 36500 g mol^{-1}, $Đ$ = 3.6, Sigma Aldrich, Germany) and an excess amount (PAN:S = 1:5) of sulfur (Carl Roth, Germany) at 450 °C for 5 h in a nitrogen atmosphere. Elemental sulfur was removed via Soxhlet extraction with toluene at 150 °C for 24 h. The obtained SPAN particles were dried under vacuum at 250 °C for 3 h. A sulfur content of 40 ± 1 wt % was determined by elemental analysis. Data for elemental analysis and an X-ray diffraction (XRD) pattern of SPAN are depicted in the Supporting Information (available online at stacks.iop.org/JES/168/110513/mmedia) (Table SI and Fig. S1). Within the XRD pattern of the amorphous SPAN material, no elemental sulfur was visible.

Electrode preparation and calenderation.—For the preparation of the electrode slurry, SPAN particles (90 wt%), Super C65 conducting carbon (5 wt%, MTI Corporation, USA), styrene-butadiene rubber (3 wt%, MTI Corporation, USA) and carboxymethylcellulose (2 wt%, MTI Corporation, USA) were dispersed into deionized water and mixed step-wise with a planetary mixer (Thinky, Japan). The solid content of the slurry was adjusted to 40%. Afterward, the slurry was cast on a carbon-coated aluminum foil (t = 17 μm, MTI Corporation, USA) with a wet film thickness of 110 μm resulting in an areal capacity of 2.7 ± 0.2 mAh cm^{-2}. Calendering was performed with a lab calender (roller diameter = 180 mm, Ingecal, France) at ambient temperature. By adjusting the line gap between the rollers, SPAN cathodes with different electrode porosities were prepared.

Electrode characterization.—Porosities of the electrodes were calculated based on the measured coating weight, coating thickness and the following densities: 1.75 g cm^{-3} (SPAN), 2.26 g cm^{-3} (C65 Carbon), 2.00 g cm^{-3} (styrene-butadiene rubber) and 1.60 g cm^{-3} (carboxymethylcellulose). The SPAN density was measured with a pycnometer (Pycnomatic ATC, Thermo Scientific, USA), densities of the other electrode materials were acquired from supplier data. To characterize morphology changes within the electrodes, scanning electron microscopy (SEM) measurements were carried out at the German Institutes of Textile and Fiber Research (DITF) Denkendorf,

Germany, using an Auriga-type field emission scanning electron microscope from Zeiss. Before measuring, the samples were sputtered with Pt/Pd. The volume resistivities and interface resistances of the SPAN cathodes were measured with a multipoint probe system (RM2610, HIOKI Corp., Japan) at ambient temperature. The tortuosity values of the SPAN cathodes were determined by an impedance-based method developed by Landesfeind et al.[28] For these purposes, electrochemical impedance measurements of symmetrical Swagelok-type cells (cathode diameter: 12 mm) were recorded at OCV with a 10 mV voltage perturbation in a frequency range between 100 kHz and 100 mHz. 10 mM LiTFSI in EC:DEC (1:1, v–v) with an ionic conductivity of 364 μS cm^{-1} at 24 °C (Mettler Toledo InLab 720, USA) was used as electrolyte. The pore volume and pore size distribution of the coatings were determined by mercury intrusion measurements (Quantachrome POREMASTER 60-GT, USA) using 30 cm^2 of each sample.

Electrochemical characterization.—Coin cells (CR2032, Hohsen Corporation, Japan) with a lithium metal foil as counter and reference electrode (Alfa Aesar, USA) were used for cyclization experiments. 1 M $LiPF_6$ in EC:DEC (1:1, v–v) (Sigma Aldrich, Germany) with 10 wt% fluoroethylene carbonate (Sigma Aldrich, Germany) was the electrolyte. The cells were cycled with a battery cycler (BasyTec, Germany) in a potential window of 1.0–3.0 V vs Li/Li$^+$. Galvanostatic cycling was conducted at various C-rates ranging from C/4 (~0.7 mA cm^{-2}) to 3 C (~8.1 mA cm^{-2}). The current densities were calculated based on the sulfur mass in the cathode and a theoretical sulfur capacity of 1675 mAh g^{-1}. Electrochemical impedance spectroscopy was measured in PAT-cells (EL-Cell, Germany) with a potentiostat (Biologic, France) at 50% state-of-charge with a 10 mV voltage perturbation in a frequency range between 200 kHz and 100 mHz. To deconvolute the impedance signal of anode and cathode, a stainless steel finger-shaped reference electrode (EL-Cell, Germany) lithiated by applying a current of 1 mA for 6 h vs the lithium anode, was used. Cells were cycled for five preformation cycles at C/4 (~0.7 mA cm^{-2}) prior to the impedance measurements. All electrochemical testing was performed at 24 °C.

Results and Discussion

SPAN electrodes with an areal capacity of 2.7 mAh cm^{-2} were calendered to three different thicknesses by adjusting the line gap between the rollers of the calender. Table I summarizes the properties of the investigated SPAN cathodes. The coating thickness was reduced from 59 μm in the initial state to 49 μm, 43 μm, 38 μm, depending on the adjusted line gap, which facilitated an increase in electrode density from 0.80 g cm^{-3} to 0.95 g cm^{-3}, 1.05 g cm^{-3} and 1.20 g cm^{-3}, respectively. Correspondingly, the porosity calculated based on the electrode material bulk densities decreased from 56% (pristine) to 48%, 41% and 33%, respectively.

Increasing the electrode density significantly improves the volumetric energy density. Figure 1 illustrates the dependence of the volumetric energy density on the areal capacity and the electrode density. The volumetric energy densities were calculated for a multilayer Li-SPAN stacked cell based on a simplified model described by Liu et al.[20] equation and parameters used for the calculation are depicted in equation S1 and Table SII (Supporting Information). Since the calculation is based on a unit cell model, half

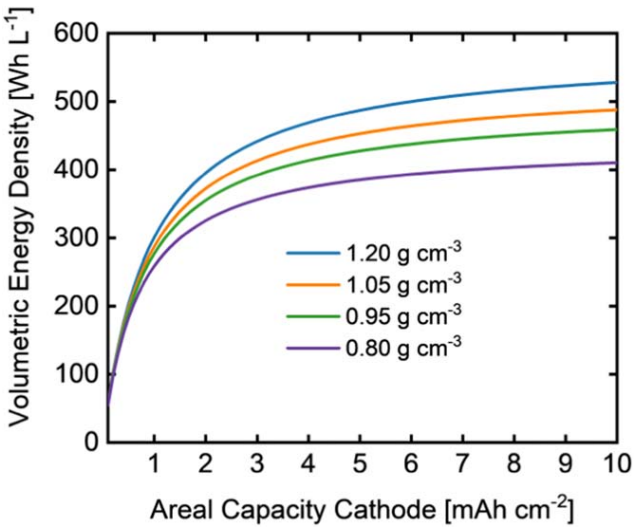

Figure 1. Dependence of the calculated theoretical volumetric energy densities on the areal capacity and the electrode density of the cathode.

of the current collector thicknesses were used for calculation. The following simplification and optimistic assumptions have been made for illustrating the effect of electrode density on the volumetric energy density: (i) the electrolyte only occupies the pores of cathode and separator, (ii) 100% excess of lithium, (iii) pouch foil, taps and other inactive cell parts are not included in the calculation and (iv) no cell swelling takes place. Notably, both sulfur-based cathodes and lithium metal anodes suffer from severe volume changes upon cycling. A previous study conducted on Li-S pouch cells revealed that the lithium metal anode masks the volume expansion/shrinkage of the sulfur-based cathode and thereby restricts the overall volume change of the cell to less than 5%.[29] As can be seen in Fig. 1, the calculated volumetric energy density of the Li-SPAN cells can be strongly enhanced by increasing the electrode density. Increasing the density of the uncompressed electrode (0.80 g cm^{-3}) to 0.95 g cm^{-3}, 1.05 g cm^{-3}, 1.20 g cm^{-3} would lead to a 10%, 16%, 30% increase in volumetric energy density, respectively. Due to the volume contribution from the non-active cell components (e.g. separator or current collector), a strong dependence of the areal capacity on the cell-level volumetric energy density becomes visible. For example, by increasing the areal loading of the highest compressed cathode from 1 mAh cm^{-2} to 3 mAh cm^{-2}, the volumetric energy would raise from 234 Wh l^{-1} to 359 Wh l^{-1}. These results underline the importance of the calendering process during the manufacturing of SPAN cathodes and the significance of high electrode loadings (>2.5 mAh cm^{-2}).

Calenderation-induced morphology changes were followed by SEM (Fig. 2). Additional cross-sectional SEM images of the analyzed SPAN cathodes are depicted in Fig. S2 (Supporting Information). With increasing electrode density a more condensed packing of the particles and a reduction of the void volume between the particles became visible. Further, increasing the electrode density led to particle agglomeration, which becomes especially visible by comparing the SEM images of the uncompressed cathode and the cathode with the highest electrode density (1.20 g cm^{-3}).

Table I. Properties of the SPAN electrodes that were calendered to various electrode densities.

Sample	Coating weight [mg]	Coating thickness [μm]	Electrode density [g cm^{-3}]	Porosity [%]
Pristine	10.1 ± 0.2	59 ± 1	0.80 ± 0.02	56 ± 1
1	10.1 ± 0.2	49 ± 1	0.95 ± 0.02	48 ± 1
2	10.1 ± 0.2	43 ± 1	1.05 ± 0.02	41 ± 1
3	10.1 ± 0.2	38 ± 1	1.20 ± 0.02	33 ± 1

Journal of The Electrochemical Society, 2021 **168** 110513

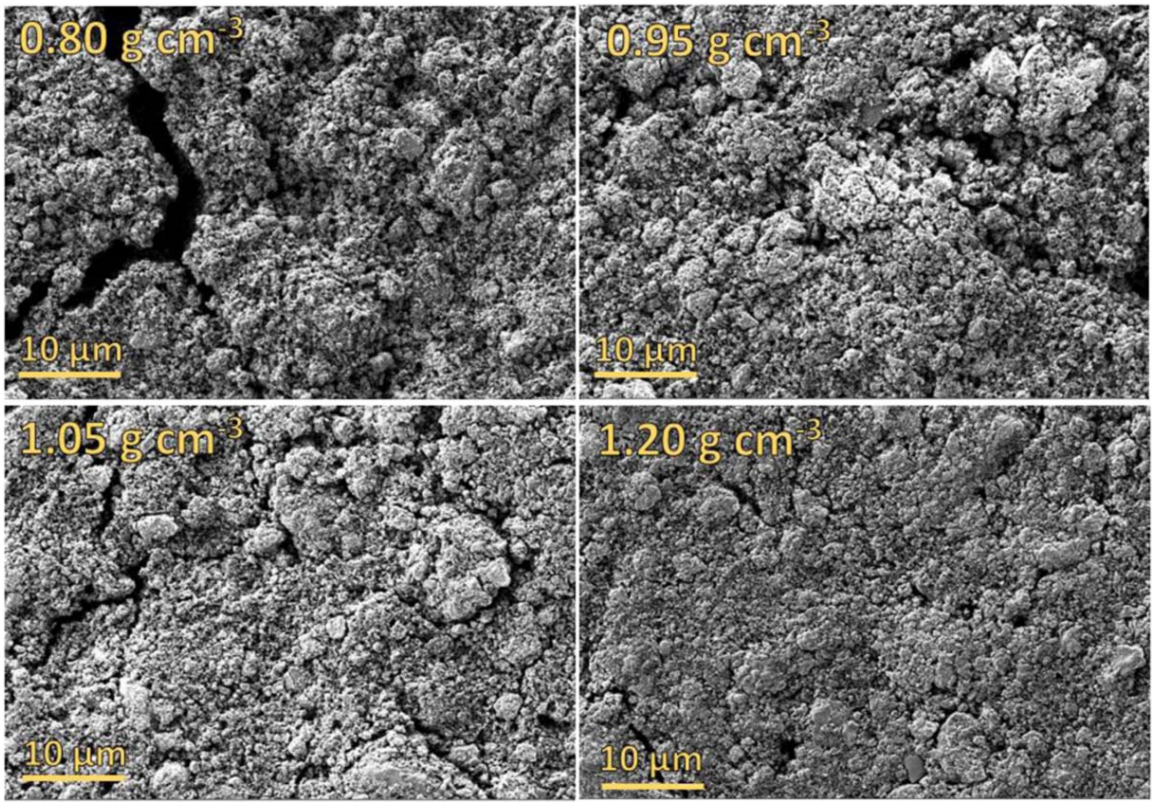

Figure 2. SEM images of SPAN cathodes at different electrode densities (0.80 g cm^{-3}, 0.95 g cm^{-3}, 1.05 g cm^{-3}, 1.20 g cm^{-3}).

The effect of electrode compression on the pore structure was further investigated by mercury intrusion porosimetry. The results of the mercury intrusion experiments are depicted in Fig. S3 and Table SIII (Supporting Information). Compressing the electrodes shifted the pore size distribution to smaller pore sizes and reduced the overall pore volume. This is especially visible for the electrodes compressed to densities higher than 1.05 g cm^{-3}. Compressing the cathodes from their pristine state (0.80 g cm^{-3}) to an electrode density of 1.20 g cm^{-3} reduced the average pore diameter from 0.43 μm to 0.22 μm and the specific pore volume by 50%. For conversion-type electrodes, high pore volumes are crucial for providing enough space for reactions to occur and ensuring suitable Li^+ transfer pathways between the particles.[24] Hence, the strong decrease in pore volume and pore size at high degrees of compression can potentially negatively affect both sulfur utilization and rate capability.

In general, it is widely accepted, that if the electrical resistance is higher than the ionic resistance of the electrode and electrolyte, the electrical resistance of the electrode dominates the overall electrochemical performance. The influence of electrode density on the electrical conductivity was evaluated with a 46 multipoint probe electrode resistance measurement system. This system enables the measurement of the electrode composite volume resistivity as well as the resistance at the interphase between the electrode composite and the current collector. As can be seen in Fig. 3a, the composite resistance slightly decreased with increasing electrode density. For example, the increase in electrode density from 0.80 g cm^{-3} to 1.20 g cm^{-3} led to a 36% reduction in the composite resistance.

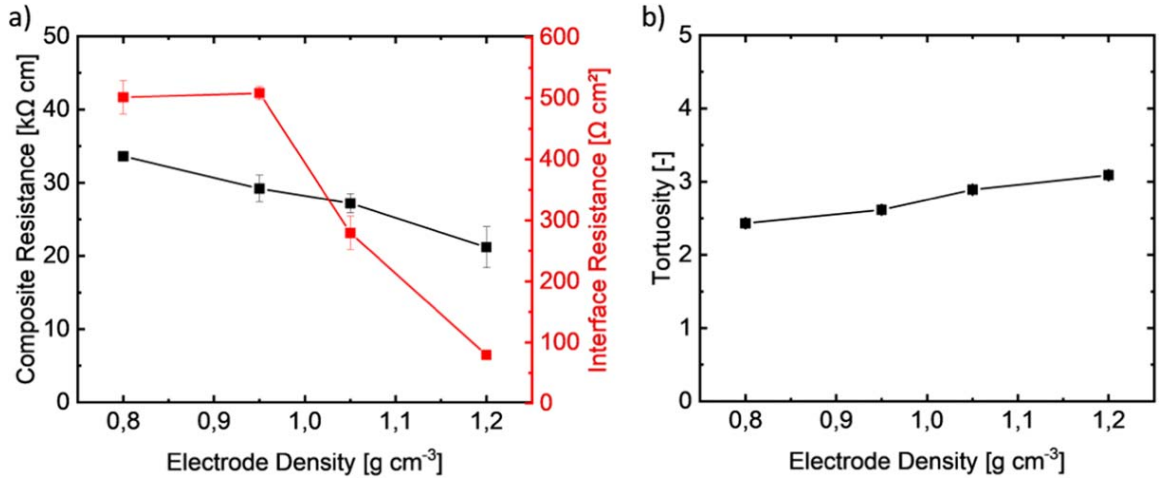

Figure 3. (a) Composite (black) and interphase resistance (red) as a function of electrode density. (b) Tortuosity values determined by EIS as a function of electrode density. The error bars represent the standard deviation of at least two independent measurements.

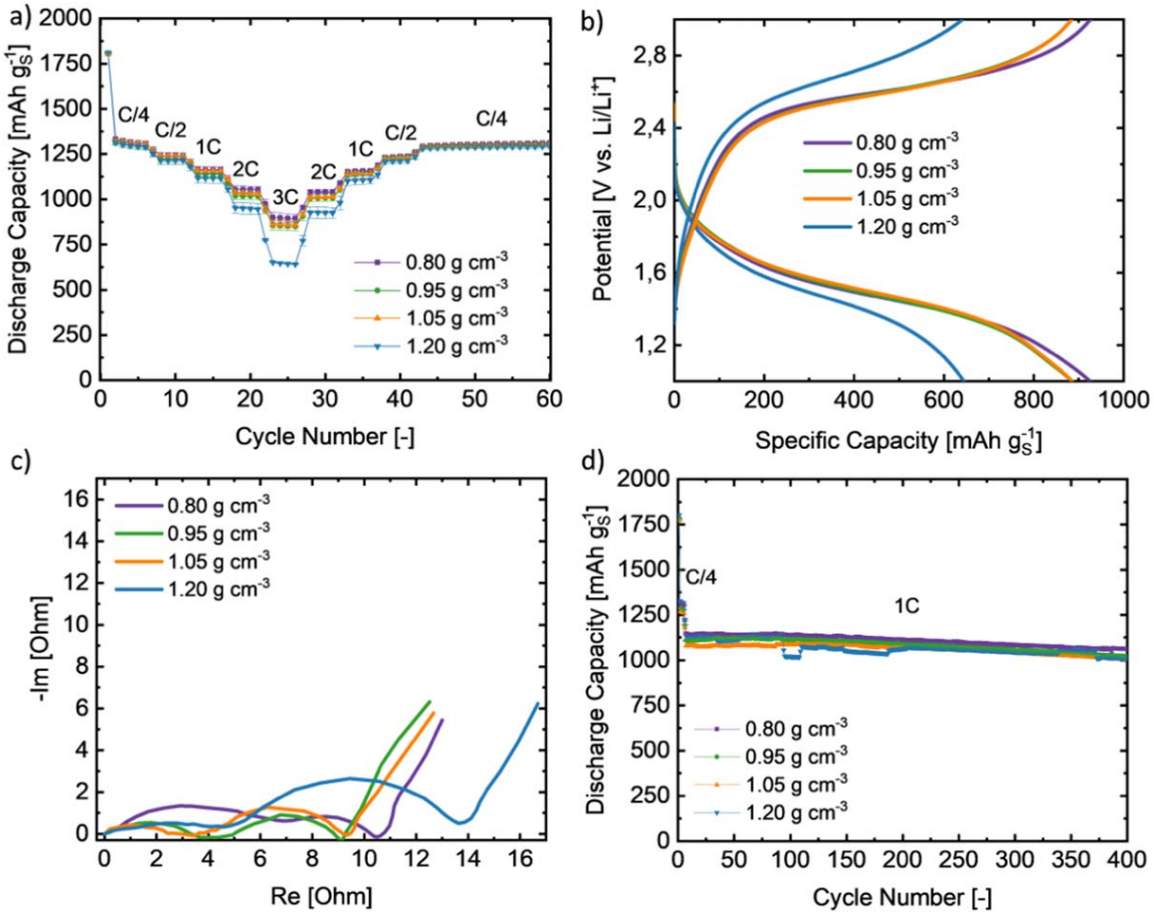

Figure 4. (a) Galvanostatic cycling of SPAN cathodes calendered to different electrode densities (0.80 g cm^{-3} (purple), 0.95 g cm^{-3} (green), 1.05 g cm^{-3} (orange), and 1.20 g cm^{-3} (blue)) vs lithium metal. Applied current range: C/4 ($\sim$ 0.7 mA cm^{-2}) to 3 C ($\sim$ 8.1 mA cm^{-2}). The error bars represent the standard deviation of at least two independent measurements. (b) Voltage profiles at 3C extracted from the rate capability tests. (c) Nyquist plots of the SPAN cathodes measured in Li-SPAN cells with a lithiated stainless steel finger-shaped reference electrode. For better comparability, the high-frequency resistance ($\sim$7−8 Ω for all measurements) was subtracted. (d) Long-term cycling of the SPAN cathodes at 1C ($\sim$2.7 mA cm^{-2}).

Compressing the cathodes to an electrode density of $\geqslant$1.05 g cm^{-3} sharply decreased the resistance between the electrode coating and the current collector (Fig. 3a). Therefore, if the overall impedance of the electrode is limited by the electrical conductivity, calendering likely enhances the sulfur utilization especially at higher C-rates.

The tortuosity is a critical structural property that directly correlates with the electrolyte conductivity and diffusion coefficient within porous electrodes. Previous studies revealed a strong correlation between electrode structure (e.g. induced by changes in composition or processing parameters), tortuosity and electrochemical performance.[30–32] Therefore, compression-induced changes in the electrode structure such as the reduction of the pore volume can potentially influence the tortuosity and thereby affect the electrochemical properties. As described by Landesfeind et al., the tortuosity can be determined by impedance measurements of symmetrical cells with electrodes in blocking conditions.[28] Figure S4 (Supporting Information) shows the Nyquist plots of the SPAN cathodes measured in a symmetrical cell configuration for different electrode densities. In the medium to high-frequency range, the electrochemical response of the electrodes was dominated by a $\sim$45° branch associated with the effective ionic resistance of the electrode and a double-layer capacitance of the electrode-electrolyte interphase at low frequencies. Since the potential of the uncycled SPAN cathodes was high ($\geqslant$3.0 V vs Li/Li$^+$) and the small voltage perturbation of the impedance measurement did not trigger any charge-transfer reactions, no resistances associated with the conversion reactions of sulfur were visible within the impedance spectra. The observed blocking behavior of the fully-charged SPAN cathodes is in good agreement with the literature.[33] By fitting the obtained impedance spectra with a transmission-line model, the effective ionic resistances of the electrodes, which correlate to the lengths of the 45° branch, can be determined. With measured effective ionic resistance, known electrode porosity and electrolyte conductivity, the tortuosity of the SPAN cathodes can be calculated. Fitted values and calculated tortuosities are summarized in Table SIIV (Supporting Information). Figure 3b shows the tortuosity values of SPAN cathodes as a function of the electrode density; these were 2.4, 2.6, 2.9 and 3.1 at an electrode density of 0.80 g cm^{-3}, 0.95 g cm^{-3}, 1.05 g cm^{-3}, and 1.20 g cm^{-3}, respectively. The only minor increase of the tortuosity suggests that compression likely has no dentrimental impact on the transport properties within the SPAN electrodes.

To quantify the impact of electrode density on the rate capability, SPAN cathodes with different densities were cycled at C-rates ranging from C/4 to 3 C against lithium metal. Figure 4a shows the results of the rate tests. At lower rates ($\leqslant$1 C), no influence of the electrode density on the discharge capacity was visible. However, at C-rates exceeding 1 C, compressing the SPAN cathodes to the highest electrode density (1.20 g cm^{-3}) resulted in a severe reduction of the obtainable capacity compared to the lower electrode densities (>1.20 g cm^{-3}). For example at 4 C, the capacity decreased from 898 mAh g_S^{-1} (0.80 g cm^{-3}) to 647 mAh g_S^{-1} (1.20 g cm^{-3}). Figure 1b shows the voltage profiles of the tested SPAN cathodes extracted from the second 4C cycle of the rate

Journal of The Electrochemical Society, 2021 **168** 110513

capability tests. The voltage curve of the cathodes calendered to 1.20 g cm^{-3} was shifted to lower potential during discharge and higher potential during charge compared to electrodes compressed to lower electrode densities. Hence, the loss of capacity of the cathode with the highest electrode density (1.20 g cm^{-3}) at higher C-rates stemmed from an enhanced overpotential leading to incomplete discharging and/or charging of the cells.

The influence of electrode density on the internal resistance within SPAN cathodes was evaluated with reference-assisted impedance spectroscopy. A lithiated stainless steel reference electrode was used to separate the impedance signals from anode and cathode. Measurements were conducted after five formation cycles at 50% state-of-charge. Nyquist plots of SPAN cathodes with different electrode densities are illustrated in Fig. 4c. For fitting the obtained impedance results, an equivalent circuit model (Fig. S5, Supporting Information) consisting of a high-frequency resistance (R_1), two R/Q elements and a constant-phase element in serial was used. The exact fitted values are shown in Table SV (Supporting Information). In the proposed circuit, the first R/Q element (R_2/Q_1) is assigned to the contact resistances within the electrodes, which includes the grain boundary resistance between the SPAN particles as well as the resistance at the coating/current collector interface. The charge-transfer resistance and its related capacitance are represented by the second R/Q element (R_3/Q_2). The constant-phase element (Q_3) represents the Li^+ diffusion process. Upon calendering, the contact resistances (R_2) slightly decreased from 8 Ω in the uncompressed state (0.80 g cm^{-3}) to ∼6 Ω in the compressed states (⩾0.95 g cm^{-3}). This is in agreement with the resistivity measurements of the SPAN coatings shown in Fig. 3 and further indicates that calendering enhanced the contact between the individual particles and reduced the contact resistance at the interphase between coating and current collector. The charge-transfer resistance (R_2) increased from ∼3 − 4 Ω (⩽1.05 g cm^{-3}) to 9 Ω (1.20 g cm^{-3}). The more than two-fold increase in the charge-transfer resistance is likely to originate from the lower rate capability of the SPAN electrodes with the highest electrode density (1.20 g cm^{-3}). It can be assumed that the earlier explained compression-induced reduction in pore volume led to a severe reduction of reaction sites, which consequently increased the charge-transfer resistance. Additionally, the compression-induced reduction of pore volume leads to a cutback in void spaces for electrolyte uptake. Since any active material that is not fully wetted with electrolyte may become electrochemically inert, insufficient wetting of the electrode can reduce electrochemical performance. In addition, hindered or slow electrolyte infiltration can suppress reaction kinetics.[24,34,35] Based on the calculated porosities (Table I), an increase in electrode density from its pristine state (0.80 g cm^{-3}) to 1.20 g cm^{-3} reduces the possible electrolyte uptake by 41%. In view of that, the lower rate capability of the electrode with the highest density can additionally be ascribed to the poor wettability of the electrode with electrolyte.

The influence of electrode density on the capacity retention was evaluated by cycling the SPAN cathodes vs lithium metal at 1C. As can be seen in Fig. 4d, the capacity decay did not depend on the density of the SPAN cathodes. All cells showed a decay of ∼8% after cycling for 400 cycles (0.05% per cycle). Calculated coulombic efficiencies extracted from the cycling test at 1C are depicted in Fig. S6 (Supporting Information). The achieved coulombic efficiencies were independent of the SPAN electrode density. The obtained results indicate that reducing the porosity of the SPAN electrodes has no detrimental effect on the capacity retention and the coulombic efficiency of the Li-SPAN cells.

Conclusions

In this work, we analyzed the influence of the electrode density of SPAN electrodes on the electrochemical performance of the resulting Li-S cells in detail. The pristine cathodes (0.80 g cm^{-3}) were calendered to three different densities (0.95 g cm^{-3}, 1.05 g cm^{-3}, 1.20 g cm^{-3}) and investigated with various chemical and electrochemical methods. It was found that while calendering decreased the electrical resistance, compressing the SPAN cathodes to higher electrode densities (>1.05 g cm^{-3}) resulted in a reduction of the rate capability. Reference-assisted electrochemical impedance spectroscopy revealed that the reduction in the rate capability is caused by a severe increase in the charge-transfer resistance, which in turn is rooted by a reduction of the overall pore volume. Based on the obtained results, we recommend compressing the SPAN electrodes to a density of 1.05 g cm^{-3}, which would increase the volumetric energy density of a multi-layer Li-SPAN cell by 16%. Future work focuses on verifying the gained knowledge in practical multi-layer Li-SPAN pouch cells.

Acknowledgments

We gratefully acknowledge funding and support from the German Federal Ministry for Economic Affairs and Energy (BMWi, project no. 3ETE009A, *EVOLi^{2}S*). We thank J. Kappler and S. Murugan (Institute of Polymer Chemistry, University of Stuttgart) for fruitful discussions. Furthermore, the authors thank Mr U. Hageroth (German Institutes of Textile and Fiber Research (DITF), Denkendorf) for the SEM measurements.

ORCID

Michael R. Buchmeiser https://orcid.org/0000-0001-6472-5156

References

1. T. Kim, W. Song, D.-Y. Son, L. K. Ono, and Y. Qi, *J. Mater. Chem. A*, **7**, 2942 (2019).
2. N. Nitta, F. Wu, J. T. Lee, and G. Yushin, *Mater. Today*, **18**, 252 (2015).
3. G. E. Blomgren, *J. Electrochem. Soc.*, **164**, A5019.
4. C. Helbig, A. M. Bradshaw, L. Wietschel, A. Thorenz, and A. Tuma, *Clean. Prod.*, **172**, 274 (2018).
5. R. Mukkabla and M. R. Buchmeiser, *J. Mater. Chem. A*, **8**, 5379 (2020).
6. E. A. Olivetti, G. Ceder, G. G. Gaustad, and X. Fu, *Joule*, **1**, 229 (2017).
7. S. H. Chung and A. Manthiram, *Adv. Mater.*, **31**, 1901125 (2019).
8. J. W. Choi and D. Aurbach, *Nat. Rev. Mater.*, **1**, 1 (2016).
9. G. Benveniste, H. Rallo, L. Canals Casals, A. Merino, and B. Amante, *J. Environ. Managem.*, **226**, 1 (2018).
10. L. Yang, Q. Li, Y. Wang, Y. Chen, X. Guo, Z. Wu, G. Chen, B. Zhong, W. Xiang, and Y. Zhong, *Ionics*, **26**, 5299 (2020).
11. X.-Q. Zhang, C. Liu, Y. Gao, J.-M. Zhang, and Y.-Q. Wang, *Nano*, **15**, 2030002 (2020).
12. A. Manthiram, S. H. Chung, and C. Zu, *Adv. Mater.*, **27**, 1980 (2015).
13. J. Wang, J. Yang, J. Xie, and N. Xu, *Adv. Mater.*, **14**, 963 (2002).
14. J. Fanous, M. Wegner, J. Grimminger, Ä. Andresen, and M. R. Buchmeiser, *Chem. Mater.*, **23**, 5024 (2011).
15. J. Fanous, M. Wegner, M. B. M. Spera, and M. R. Buchmeiser, *J. Electrochem. Soc.*, **160**, A1169 (2013).
16. M. Frey, R. K. Zenn, S. Warneke, K. Müller, A. Hintennach, R. E. Dinnebier, and M. R. Buchmeiser, *ACS Energy Lett.*, **2**, 595 (2017).
17. X. Wang, Y. Qian, L. Wang, H. Yang, H. Li, Y. Zhao, and T. Liu, *Adv. Funct. Mater,*, **29**, 1902929 (2019).
18. P. Wang, J. Trück, S. Niesen, J. Kappler, K. Küster, U. Starke, F. Ziegler, A. Hintennach, and M. R. Buchmeiser, *Batteries & Supercaps*, **3**, 1239 (2020).
19. O. Gröger, H. A. Gasteiger, and J.-P. Suchsland, *J. Electrochem. Soc.*, **162**, A2605 (2015).
20. Y. T. Liu, S. Liu, G. R. Li, and X. P. Gao, *Adv. Mater.*, **33**, 2003955 (2021).
21. S. Dörfler, H. Althues, P. Härtel, T. Abendroth, B. Schumm, and S. Kaskel, *Joule*, **4**, 539 (2020).
22. A. C. Ngandjong, T. Lombardo, E. N. Primo, M. Chouchane, A. Shodiev, O. Arcelus, and A. A. Franco, *J. Power Sources*, **485**, 229320 (2021).
23. P. Titscher, P. Schön, M. Horst, U. Krewer, and A. Kwade, *Energy Technol.*, **6**, 1139 (2018).
24. D. Lu, Q. Li, J. Liu, J. Zheng, Y. Wang, S. Ferrara, J. Xiao, J. G. Zhang, and J. Liu, *ACS Appl. Mater. Interfaces*, **10**, 23094 (2018).
25. C. Meyer, H. Bockholt, W. Haselrieder, and A. Kwade, *J. Mater. Process. Technol.*, **249**, 172 (2017).
26. E. N. Primo, M. Touzin, and A. A. Franco, *Batteries & Supercaps*, **4**, 834 (2021).
27. N. Kang, Y. Lin, L. Yang, D. Lu, J. Xiao, Y. Qi, and M. Cai, *Nat. Commun.*, **10**, 4597 (2019).
28. J. Landesfeind, J. Hattendorff, A. Ehrl, W. A. Wall, and H. A. Gasteiger, *J. Electrochem. Soc.*, **163**, A1373 (2016).
29. S. Waluś, G. Offer, I. Hunt, Y. Patel, T. Stockley, J. Williams, and R. Purkayastha, *Energy Stor. Mater.*, **10**, 233 (2018).
30. T. DuBeshter, P. K. Sinha, A. Sakars, G. W. Fly, and J. Jorne, *J. Electrochem. Soc.*, **161**, A599 (2014).
31. T. Lebherz, M. Frey, A. Hintennach, and M. R. Buchmeiser, *RSC Adv.*, **9**, 7181 (2019).
32. J. Landesfeind, A. Eldiven, and H. A. Gasteiger, *J. Electrochem. Soc.*, **165**, A1122 (2018).
33. R F. L. Raccichini, J. W Dibden, J. R Owen, and N Garcia.Araez, *J. Electrochem. Soc.*, **165**, A2741 (2018).
34. H. Zheng, L. Tan, G. Liu, X. Song, and V. S. Battaglia, *J. Power Sources*, **208**, 52 (2012).
35. J. Smekens, R. Gopalakrishnan, N. Steen, N. Omar, O. Hegazy, A. Hubin, and J. Van Mierlo, *Energies*, **9**, 104 (2016).

Supporting Information

Lithium-Sulfur Batteries Based on Sulfurized Poly(acrylonitrile) Cathodes: Impact of Electrode Density on Cell Performance

Stefan Niesen[1,3], Janina Trück[1,3], Christoph Seidl[3], Katrin Renger[3] and Michael R. Buchmeiser*[1,2]

[1]*Institute of Polymer Chemistry, University of Stuttgart, 70569 Stuttgart, Germany*
[2]*German Institutes of Textile and Fiber Research (DITF) Denkendorf, 73770 Denkendorf, Germany*
[3]*Mercedes-Benz AG, RD/EBZ, 70327 Stuttgart, Germany*
[*]*Corresponding Author E-mail Address: [michael.buchmeiser@ipoc.uni-stuttgart.de]*

Table S1: Elemental analysis data of SPAN.

C [wt%]	H [wt%]	N [wt%]	S [wt%]
40.5	0.78	15.3	39.1

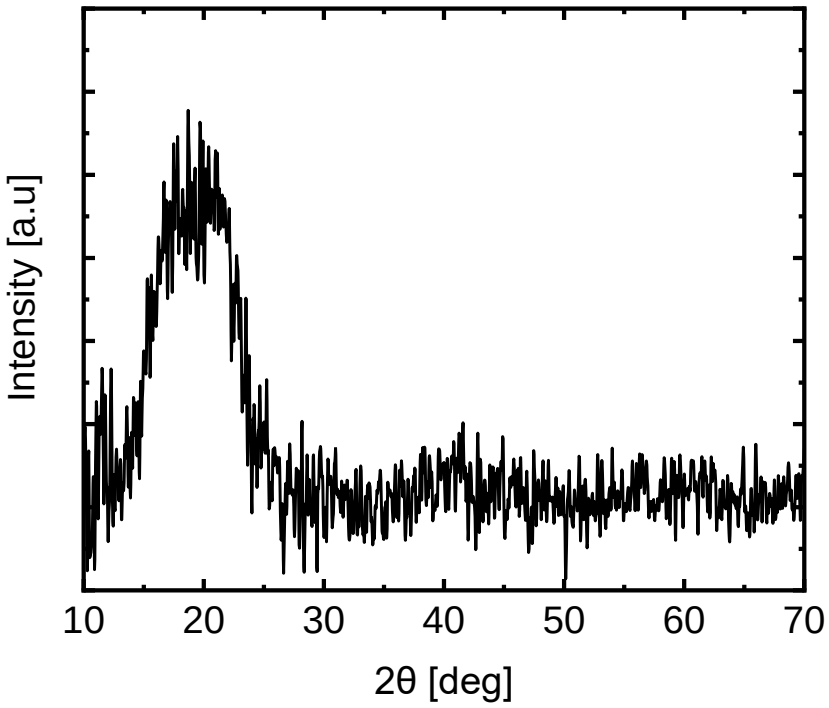

Figure S1: XRD pattern of SPAN.

$$E_v = \frac{U \cdot x \cdot c_{areal}}{d_{cathode} + d_{Li} + d_{Al} + d_{Cu} + d_{separator}} \qquad \text{(Equation S1)}$$

in which E_v is the volumetric energy density, U is the cell voltage, c_{areal} is the areal capacity (mAh cm^{-2}), x is the capacity utilization, d_i is the thickness of cathode, lithium anode, aluminum foil, copper foil and separator.

Table S2: Parameters used for calculating the volumetric energy densities of Li//SPAN stacked cells.

Li // SPAN (90 wt%)	
Capacity utilization	80 % (536 mAh g^{-1}_{SPAN})
Cell voltage	1.69 V
Anode current collector thickness	8 µm
Cathode current collector thickness	12 µm
Separator thickness	20 µm
Lithium excess	100 %

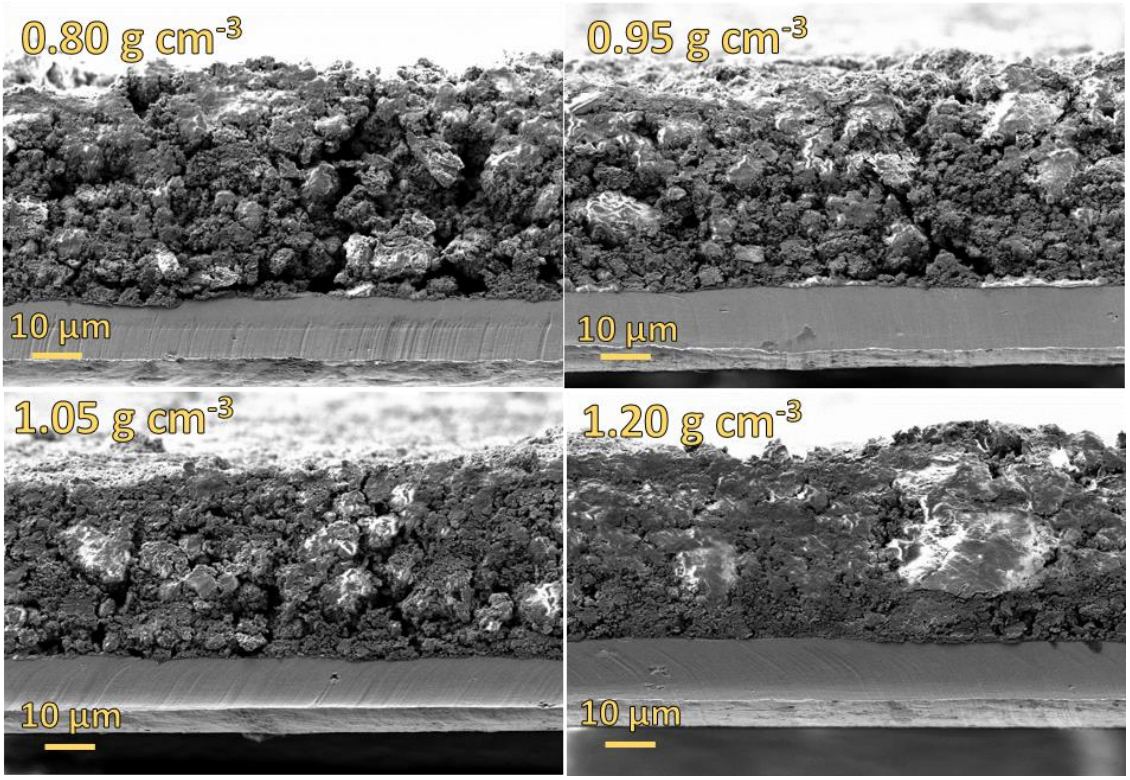

Figure S2: Cross-sectional SEM images of SPAN cathodes with different electrode densities (0.80 g cm^{-3}, 0.95 g cm^{-3}, 1.05 g cm^{-3}, 1.20 g cm^{-3}).

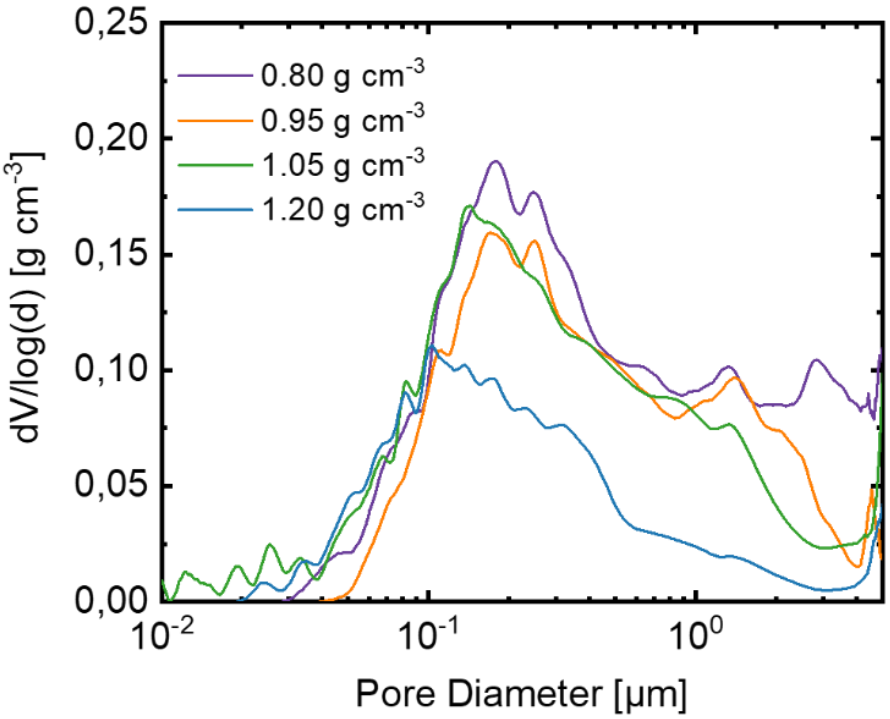

Figure S3: Pore size distribution of SPAN cathodes with different electrode densities (0.80 g cm^{-3}, 0.95 g cm^{-3}, 1.05 g cm^{-3}, 1.20 g cm^{-3}).

Table S3: Determined specific pore volume and average pore diameter of SPAN cathodes with different electrode densities (0.80 g cm^{-3}, 0.95 g cm^{-3}, 1.05 g cm^{-3}, 1.20 g cm^{-3}).

Electrode density [g cm^{-3}]	**Spec. pore volume [cm^3 g^{-1}]**	**Av. Pore diameter [µm]**
0.80	0.24	0.43
0.95	0.19	0.43
1.05	0.22	0.32
1.20	0.12	0.22

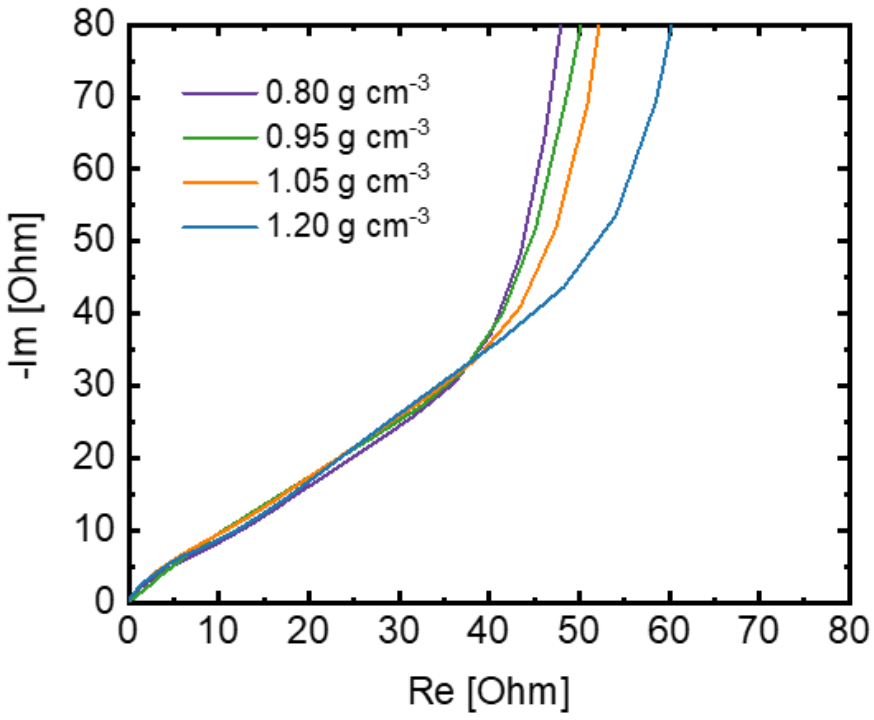

Figure S4: Nyquist plots of SPAN cathodes with different electrode densities (0.80 g cm^{-3}, 0.95 g cm^{-3}, 1.05 g cm^{-3}, 1.20 g cm^{-3}), subtracted by the high-frequency-resistance. Measured in symmetrical Swagelok-type cells using 10 mM LiTFSI in EC:DEC (1:1, v:v) as electrolyte.

Table S4: Porosities, effective ionic resistances obtained from EIS measurements of symmetrical cells (Figure S2) and calculated tortuosity values of the investigated SPAN cathodes. The error represents the standard deviation of at least two independent measurements.

Electrode density [g cm^{-3}]	**Porosity [%]**	**Effective ionic resistance [Ω]**	**Tortuosity [-]**
0.80	56 ± 1	127.2 ± 2.9	2.4 ± 0.1
0.95	47 ± 1	135.2 ± 4.8	2.6 ± 0.1
1.05	41 ± 1	147.7 ± 1.9	2.9 ± 0.1
1.20	33 ± 1	174.3 ± 1.3	3.1 ± 0.1

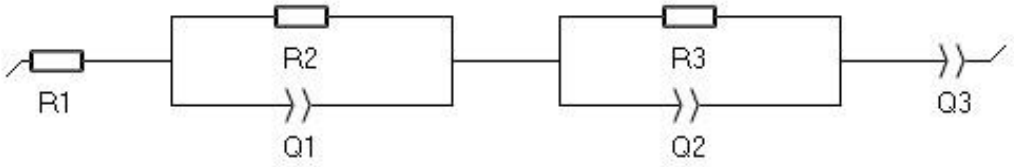

Figure S5: Equivalent circuit model used to fit the impedance data in Figure 4c

Table S5: Fitted resistances of the SPAN cathodes. Measured in Li-SPAN with lithiated stainless-steel reference electrode cells at 50 % SOC.

Electrode density [g cm^{-3}]	**R_1 [Ω]**	**R_2 [Ω]**	**R_3 [Ω]**
0.80	7.6	8.3	2.9
0.95	7.1	6.0	4.8
1.05	8.3	5.8	4.4
1.20	6.5	5.2	9.4

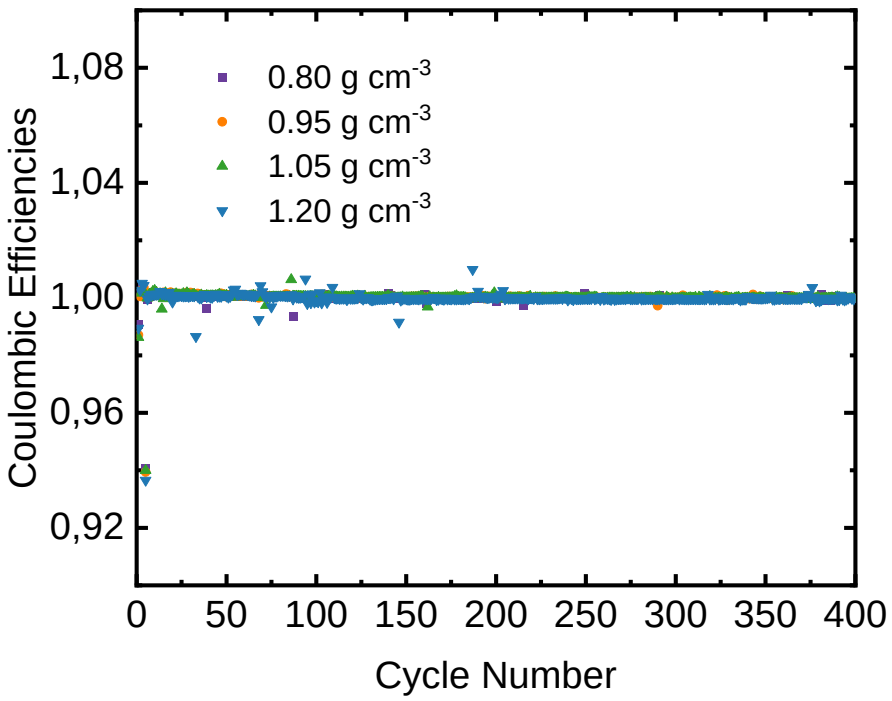

Figure S6: Coulombic efficiencies extracted from the long-term cycling test at 1C (Figure 4d).

5.3 **Publication III:** Multifunctional Self-Cross-Linked Copolymer Binder for High-Loading Silicon Anodes

S. Niesen; A. Fox; S. Murugan; G. Richter; M. R. Buchmeiser, Multifunctional Self-Cross-Linked Copolymer Binder for High-Loading Silicon Anodes. ACS Appl. Energy Mater. **2022**, 5, 11386-11391.

Author Contributions: **S.N.:** Conceptualization, Investigation (Polymer Synthesis & Characterization, Electrode Preparation & Characterization, Electrochemical Tests), Visualization, Writing - Original Draft; **A.F.:** Investigation (Polymer Synthesis and Characterization), Writing - Review & Editing; **S.M.:** Investigation (Electrode Synthesis and Characterization), Writing - Review & Editing; **G.R.:** Investigation (SEM Measurements of Electrodes); **M.R.B.:** Conceptualization, Writing - Review & Editing.

Reprinted with permission from the American Chemical Society.

ACS APPLIED ENERGY MATERIALS

www.acsaem.org Article

Multifunctional Self-Cross-Linked Copolymer Binder for High-Loading Silicon Anodes

Stefan Niesen, Alina Fox, Saravanakumar Murugan, Gunther Richter, and Michael R. Buchmeiser*

Cite This: *ACS Appl. Energy Mater.* 2022, 5, 11386–11391 Read Online

ACCESS | Metrics & More | Article Recommendations | Supporting Information

ABSTRACT: Due to its ultra-high capacity and moderately low potential, silicon (Si) shows potential in replacing graphite-based anodes. Unfortunately, Si suffers from severe intrinsic volume expansions that restrict its practical use. Herein, we present a tailored copolymer, poly(acrylamide)-*co*-poly(hydroxymethylacrylate), p(AM-*co*-HMA), as a multifunctional binder for Si anodes, which forms a 3D network structure via a thermally induced self-cross-linking reaction. The formed cross-linked binder structure provides both covalent and hydrogen bonds and thereby improves both the adhesion between the individual electrode components and the current collector as well as the adhesion between the individual Si particles. Overall, the p(AM-*co*-HMA)-based binder offers superior electrochemical performance for high-loading Si anodes compared to traditionally applied binder systems.

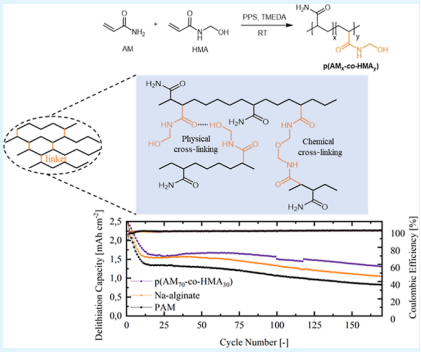

KEYWORDS: *self-cross-linkable binder, silicon anodes, 3D network structure, silicon nanoparticles, N-(hydroxymethyl)-acrylamide, lithium-ion battery*

1. INTRODUCTION

Driven by the urgent need for large-scale batteries as power sources for hybrid/full electric vehicles, the increase of the energy density of lithium-ion batteries (LIBs) has become a central research question. Particularly, the development of novel anode and cathode materials has been the focus of many researchers as the energy density of LIBs is mainly limited by the capacity of the currently used active materials.[1] For instance, silicon (Si) has been widely studied as a replacement for traditionally used graphite due to its high theoretical capacity (3579 mA h g^{-1}). Additional merits of Si are its abundance and moderately low electrochemical potential (~0.4 V vs Li/Li^+), which is a good compromise between an acceptable cell voltage and restricted Li plating. Nevertheless, the application of anodes with high Si content is quite challenging as Si strongly expands during lithium insertion (up to 300%). The severe volume changes break the electrical contact between the particles and lead to continuous solid electrolyte interphase (SEI) formation. As a result, Si anodes suffer from rapid capacity decay, which is especially severe for electrodes with high active material loadings.[2−5] As smaller Si particles can better compensate the volume changes that occur during discharge/charge, Si nanoparticles have intensively been investigated.[6,7] Additional active material modifications studied to constrain volume changes include the coating of Si particles with a protective layer (e.g., carbonaceous materials, metal oxides) or embedding Si in a carbon matrix.[8−11] Further attention has been devoted to the introduction of functional binders that can buffer large volume changes. It has been reported that the state-of-the-art binders applied in LIB electrodes, such as poly(vinylidene difluoride) (PVDF), are not capable of withstanding the severe volume expansion of Si particles. It has been further demonstrated that Si anodes prepared with polymeric binders containing polar moieties (e.g., hydroxyl or carboxyl groups), such as poly(acrylic acid) (PAA) or sodium alginate (Na-alginate), exhibit far superior electrochemical performance than Si electrodes prepared from non-polar PVdF. Contrary to non-polar binders, those having functional groups possess enhanced adhesion due to their ability to form hydrogen bonds between polar groups and the partially hydrolyzed SiO_2 surface layer on the Si particles.[12−18] Nonetheless, non-cross-linked binders are not capable of fully compensating the volume expansions as the Si particles tend to slip between the polymer chains. Consequently, Si particles embedded in the polymer matrix cannot recover their pristine state after continuous expansion/shrinkage, which results in a loss of structural integrity and capacity fading.[19,20] To address this issue, cross-linked binders, which form a 3D network structure around the Si particles, have been introduced. Koo et al. were the first to develop a cross-linked binder for Si anodes.

Received: June 14, 2022
Accepted: August 18, 2022
Published: August 31, 2022

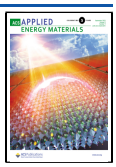

ACS Publications © 2022 The Authors. Published by American Chemical Society

They in situ cross-linked PAA and carboxymethylcellulose (CMC) by heating the electrodes under vacuum. The cross-linked PAA/CMC binder possessed higher mechanical strain resistance and superior cycling performance relative to Si anodes prepared from PVdF or PAA alone.[21] Other cross-linked binder systems prepared via an in-situ condensation reaction or radical polymerization include, for example, poly(acrylamide)/Na-alginate,[22] in situ cross-linked poly(acrylamide),[23] PAA/borax,[24] PAA/poly(ethylene imine),[25] poly(ethylene oxide)/PAA,[26] and poly(ethylene glycol)/PAA.[27] Despite promising progress, their applicability is limited as most cross-linked binder systems are based on two or more components, which enhances complexity during production. Additionally, most reported binder studies utilized Si anodes with low active material loadings (<0.7 mg_{si} cm^{-2}), which further limits their practical use.

Herein, we present an easy to prepare self-cross-linkable copolymer based on acrylamide (AM) and *N*-(hydroxymethyl)-acrylamide (HMA) as binders for high loading Si anodes (≥1 $mg_{silicon}$ cm^{-2}). Our novel binder design combines two main functionalities in one polymer backbone. Both the functional groups of AM and HMA can form hydrogen bonds. This ensures strong interaction between the binder and the Si particles as well as good adhesion between the electrode materials and the current collector. In addition, HMA can form a 3D network structure via a thermal-induced self-condensation.

2. EXPERIMENTAL SECTION

2.1. Synthesis of Poly(acrylamide-*co*-*N*-(hydroxymethyl)-acrylamide). The p(AM-*co*-HMA) copolymer was synthesized by redox copolymerization of acrylamide (AM, Sigma Aldrich, Germany) and *N*-(hydroxymethyl)-acrylamide (HMA, TCI, Japan) in deionized water. To initiate the polymerization, potassium persulfate (PPS, Sigma Aldrich, Germany) and *N*,*N*,*N*′,*N*′-tetramethylethylenediamine (TMEDA, Sigma-Aldrich, Germany) were used. Depending on the prepared sample, different AM to HMA ratios were added to a flask filled with 17 mL of deionized water. After the monomers were completely dissolved, PPS (0.5 mol %) and TMEDA (0.5 mol %) were added. For synthesizing p(AM-*co*-HMA) in different molar ratios, both the initiator and total monomer concentration were kept constant. Poly(acrylamide) (PAM) was synthesized from acrylamide via the same method. Table S1 (Supporting Information) summarizes the amounts of monomers used to prepare the p(AM_x-*co*-HMA_y) copolymers and PAM. Polymerization were carried out under a nitrogen atmosphere at 30 °C for 2 h. The formed polymers were precipitated in a water/acetone mixture, filtered, washed with acetone, and dried under vacuum.

2.2. Electrode Preparation. Si nanoparticles from PlasmaChem (100 nm, USA) were used. TEM images of the Si nanoparticles are shown in Figure S1 (Supporting Information). The electrode slurries were prepared by suspending Si nanoparticles (60 wt %, PlasmaChem, USA), carbon C65 (20 wt %, MTI Corporation, USA), and the binder (20 wt %) in deionized water (solid content: 20%). The dispersion was mixed with a planetary mixer (Thinky, Japan). Besides, the synthesized p(AM-*co*-HMA) copolymers and PAM, sodium alginate (Na-alginate, Sigma-Aldrich, Germany) was used as the binder. The resulting slurries were cast onto a copper foil (MTI Corporation, USA). To initiate the cross-linking reaction and to dry the electrodes, the electrode sheets were heated in a vacuum oven at 120 °C for 12 h. The resulting electrodes had a Si mass loading of 1.0 ± 0.1 mg cm^{-2} corresponding to an areal capacity of 3.6 ± 0.4 mA h cm^{-2}.

2.3. Physical Characterization. NMR measurements were conducted on a Bruker Avance III 400 (Germany). The cross-linking reaction of the p(AM-*co*-HMA) copolymer was monitored by attenuated total reflectance infrared (ATR-IR) spectroscopy. The adhesion strength of the Si anodes was measured by utilizing an adhesion strength testing machine. The electrode was fixed between parallel plates using a double-sided adhesion tape (3 M, USA). The area of the measurement surface was 6.45 cm^2. A compression stress of 2000 N was applied for 60 s to ensure proper adhesion of the tape to the electrode surface. The pull-off phase was set to 1000 mm min^{-1}. The surface morphologies of the electrodes were measured with a scanning electron microscope (GeminiSEM 500, Zeiss, Germany) before and after cycling.

2.4. Electrochemical Characterization. To evaluate the electrochemical performance of the Si anodes, coin-type (CR2016, Hohsen Corporation, Japan) half cells were assembled with a Si working electrode and a lithium metal counter electrode. 1 M $LiPF_6$ in ethylene carbonate (EC):diethyl carbonate (DEC, 1:1, v/v) (Sigma Aldrich, Germany) with 10 wt.% fluoroethylene carbonate (FEC, Sigma-Aldrich, Germany) was used as an electrolyte. Cells were cycled in a potential window of 0.005−1.5 V during the formation cycles (C/20) and 0.01−1.2 V in the following cycles. Galvanostatic cycling was performed at C-rates ranging from C/10 (~0.4 A g^{-1}) to 1C (~3.6 A g^{-1}). Electrochemical impedance spectroscopy (EIS) measurements were conducted in Swagelok-type half cells with a 10 mV voltage perturbation in a frequency range of 200 kHz to 100 mHz. All electrochemical tests were performed at 24 °C.

3. RESULTS AND DISCUSSION

The different p(AM-*co*-HMA) copolymers were synthesized by redox copolymerization of AM and HMA (Scheme 1a). The

Scheme 1. (a) Synthesis of p(AM-*co*-HMA) by Redox Copolymerization; (b) Cross-Linking Reaction of HMA via the Condensation of Two Methylol Groups; And (c) Schematic Illustration of the Physical and Chemical Cross-Linking Occurring in the p(AM-*co*-HMA) Copolymer after Heat Treatment

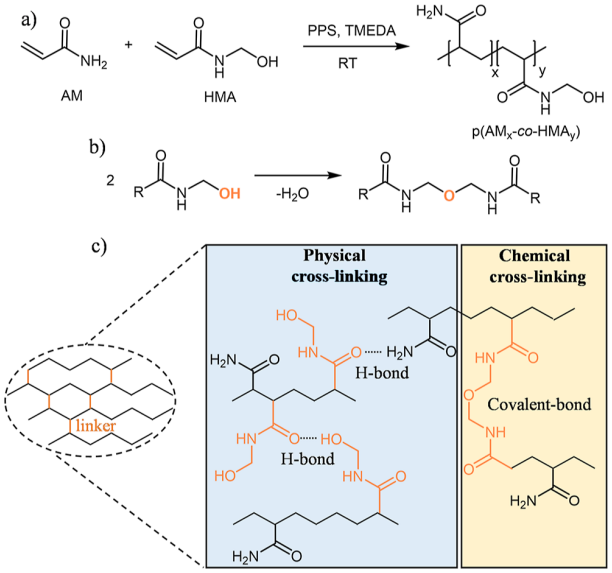

monomer ratios were varied to prepare the following three copolymers: p(AM_{90}-*co*-HMA_{10}), p(AM_{70}-*co*-HMA_{30}), p-(AM_{60}-*co*-HMA_{40}), as well as the PAM homopolymer. The ^1H and ^{13}C NMR spectra of p(AM-*co*-HMA) and PAM can be found in the Supporting Information (Figures S2−S5). The characteristic proton and carbon signals of the AM and HMA segments were identified. In addition to the protons of the polymer backbone (signals a and b), a singlet at δ = 4.65 ppm (signal c), corresponding to a CH_2 group, was visible in the ^1H NMR spectrum of the p(AM-*co*-HMA) copolymer (Figures S2

and S3). In contrast to the ^{13}C NMR spectrum of the PAM homopolymer, two additional signals were observed in the spectrum of the p(AM_{70}-*co*-HMA_{30}) sample, which correspond to the carbonyl group (signal d) and the CH_2 group (signal e) of the HMA segment (Figures S4 and S5).

The main reason to introduce hydroxymethyl groups into the copolymer was to allow for the generation of covalent links between the individual polymer chains by thermally induced cross-linking. As previously reported, the polymer's hydroxymethyl groups self-cross-link at temperatures above 90 °C. At these temperatures, two methylol groups condense to form a bis(methylene) ether (Scheme 1b).[28,29] Besides chemical cross-linking, physical cross-linking can occur in the p(AM-*co*-HMA) copolymer by forming hydrogen bonds between the polar groups of two individual polymer chains, which further stabilizes the network structure and ensures good adhesion to the electrode materials (Scheme 1c). AM was chosen as the second monomer as it is water-soluble and known to form hydrogen bonds. Previous works showed that cross-linking between the HMA groups and CMC can occur.[30,31] In contrast to these reports, cross-linking of the binder system outlined here solely takes place between two HMA groups.

The self-cross-linking behavior of the p(AM-*co*-HMA) copolymer was confirmed by ATR-IR spectroscopy. For comparison, the copolymer film was measured before and after heat treatment (120 °C for 12 h). The occurrence of the cross-linking reaction was verified by determining the transmittances of the 3250−3686 cm^{-1} band attributed to the −OH stretching and the 1600−1850 cm^{-1} band (C═O stretching). As visible in Figure 1a, the peak intensity of the −OH group

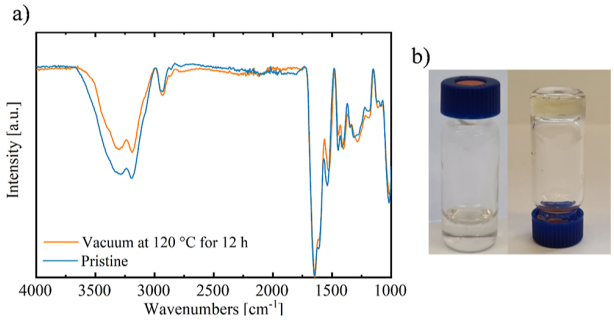

Figure 1. (a) FT-IR spectra of a p(AM-*co*-HMA)-based film before (blue) and after heating at 120 °C under vacuum (orange). (b) Optical images of p(AM-*co*-HMA) in ethylene glycol before (left) and after heating at 100 °C (right).

significantly reduced after heat treatment while the peak intensity of the C═O band remained constant. This decrease in intensity of the peak for the −OH group confirms the self-cross-linking reaction involving the condensation of two −OH groups (Scheme 1b). Cross-linking was further confirmed by heating a solution of p(AM-*co*-HMA) to 100 °C. As visible in Figure 1b, the solution turned into a highly viscous gel, which further proves the occurrence of a thermal-induced cross-linking reaction.

To evaluate the electrochemical performance of the p(AM-*co*-HMA) copolymers, electrodes with Si nanoparticles (60 wt. %) were fabricated and cycled against the Li metal. Si electrodes containing widely used Na-alginate and PAM were prepared as control samples. Before electrochemical testing, the surface morphologies of the pristine Si electrodes were evaluated with the aid of scanning electron microscopy (SEM). In the SEM images of the p(AM-*co*-HMA)-based Si anodes, a smoother surface morphology as well as fewer cracks were observed compared to the reference electrodes (Figure 2). Further, the influence of the binder on the adhesion of the electrode coatings was examined by conducting adhesion tests. For all tests, p(AM_{30}-*co*-HMA_{70}) and Na-alginate-based electrode sheets were used. Both electrode sheets showed no complete delamination of the coating from the Cu current collector. However, the electrode sheets with p(AM_{30}-*co*-HMA_{70}) as the binder remained almost completely intact whereas large parts of the Na-alginate-based coating were detached from the copper foil (as visible in Figure S6 of the Supporting Information). We attribute the better coating quality and the higher adhesion of the p(AM-*co*-HMA)-based electrode coating to its cross-linked structure, which is formed via the self-cross-linking of the HMA comonomer and which indeed enhances the binding strength between the Si particles and adhesion of the coating to the Cu current collector.

The cycling performance at C/5 (~0.7 A g^{-1}) of the p(AM-*co*-HMA)-based electrodes as well as the reference electrodes is outlined in Figure 3a. As visible in Figure 3b, all cells exhibited specific capacities ≥3500 mA h g_{Si}^{-1} and high ICEs (~89%) in the initial formation cycle (C/20). The electrodes prepared with Na-alginate, PAM, and p(AM_{90}-*co*-HMA_{10}) showed higher first cycle capacities (1st C/5 cycle) but suffered from a more severe capacity decay compared to the p(AM_{70}-*co*-HMA_{30})- and p(AM_{60}-*co*-HMA_{40})-based anodes (Figure 3a). In particular, the capacity drop during the first 10 cycles was far lower in electrodes prepared from the p(AM-*co*-HMA) copolymers as the binder containing large amounts of HMA (≥30 mol %). The reduction of the initial capacity drop resulted in a strongly improved cycling performance of the cells containing p(AM_{70}-*co*-HMA_{30}) or p(AM_{60}-*co*-HMA_{40}) as the binder. After 50 cycles, the capacity retention was 70, 67, 45, and 39% for p(AM_{70}-*co*-HMA_{30}), p(AM_{60}-*co*-HMA_{40}), Na-alginate, and PAM, respectively. The obtained cycling results point out that copolymerization of the self-cross-linkable HMA (content ≥30 mol %) into the polymeric binder strongly reduces the capacity fading especially during the first few cycles. In addition, the long-term cycling performance of p(AM_{70}-*co*-HMA_{30}), Na-alginate, and PAM at a higher rate (C/2, ~1.8 A g^{-1}) was evaluated (Figure 3e). Like at C/5, the C/2 tests revealed a lower capacity decay of the p(AM_{70}-*co*-HMA_{30}) anodes relative to the reference electrodes.

To obtain more detailed insights into the effect of the binder on the capacity drop in the initial cycles, EIS measurements were conducted on electrodes containing p(AM_{70}-*co*-HMA_{30}), Na-alginate, and PAM after 10 C/5 cycles. The obtained EIS results were fitted with the equivalent circuit model as shown in Figure S7 (Supporting Information) consisting of a high-frequency resistance (R_1), two R/Q elements (R_2/Q_1 and R_3/Q_2), and a Warburg element (W_1) connected in series. The R/Q elements were assigned to the SEI layer resistance (R_2/Q_1) and the charge-transfer resistance (R_3/Q_2) of the Si anode. The Warburg element was used to model lithium-ion diffusion. As visible in Figure 3c, all cells showed two semi-circles at high to medium frequencies, which represent the SEI layer resistance and charge transport inside the active material, as well as an inclined line at lower frequencies (Warburg element). The exact fitted values are shown in Table S2 (Supporting Information). As both the SEI layer resistance and the charge-transfer resistance can be linked to the interphase of

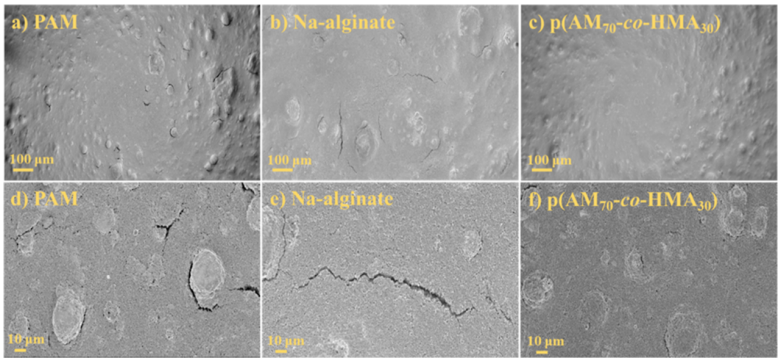

Figure 2. Surface morphologies of Si anodes prepared with (a,d) PAM, (b,e) Na-alginate, and (c,f) p(AM_{70}-*co*-HMA_{30}) before cycling. The scale bars in the images are either 100 or 10 μm in size.

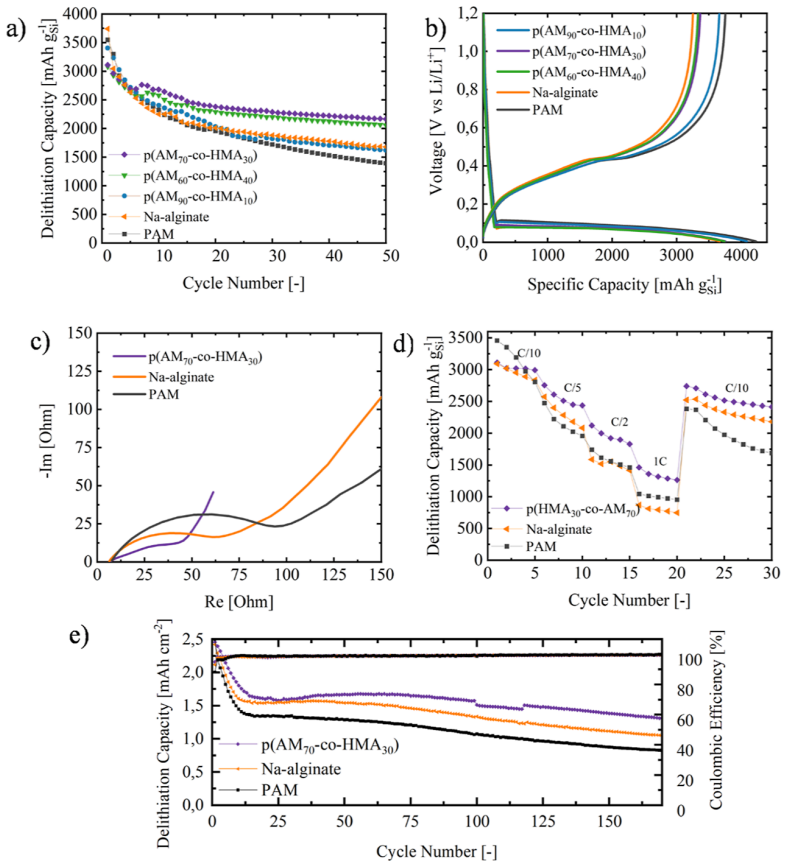

Figure 3. (a) Electrochemical performance of the tested Si anodes at C/5 (~0.7 A g^{-1}) measured after one formation cycle at C/20. (b) Charge/discharge curves of the formation cycle. (c) Nyquist plots of the Si anodes after cycling for 10 cycles at C/5. (d) Rate capability of the Si anodes. (e) Cycling performance and Coulombic efficiency of the Si electrodes at C/2 (1.8 A g^{-1}) after two formation cycles at C/20.

the Si particles, we labeled the sum of R_2 and R_3 as the interfacial resistance. Because the fitted high-frequency resistances (R_1, ~5−9 Ω) were very small compared to the interfacial resistances, the following discussion will solely focus on the differences in the $R_2 + R_3$ values. The Si anodes fabricated with p(AM_{70}-*co*-HMA_{30}) as a binder showed a far lower interfacial resistance ($R_2 + R_3$) relative to the reference electrodes (Na-alginate, PAM). The values for $R_2 + R_3$ were 45, 82, and 103 Ω for p(AM_{70}-*co*-HMA_{30}), Na-alginate, and PAM, respectively. Generally, irreversible volume changes of the Si particles result in a loss of electrical and ionic contact as well as the formation of a thick SEI layer. Both effects lead to an increase in the SEI layer resistance and the charge-transfer resistance.[32] Consequently, the reduced interphase resistance of the p(AM_{70}-*co*-HMA_{30})-based anodes relative to the reference electrodes can be attributed to a more stable binder network structure, which helps to restrict irreversible morphology changes of the active material particles and thereby positively affect the capacity retention.

The rate capabilities of the p(AM_{70}-*co*-HMA_{30})-based anode and the reference electrodes were assessed by cycling the cells at rates ranging from C/10 (~0.4 A g^{-1}) to 1C (~3.6 A g^{-1}).

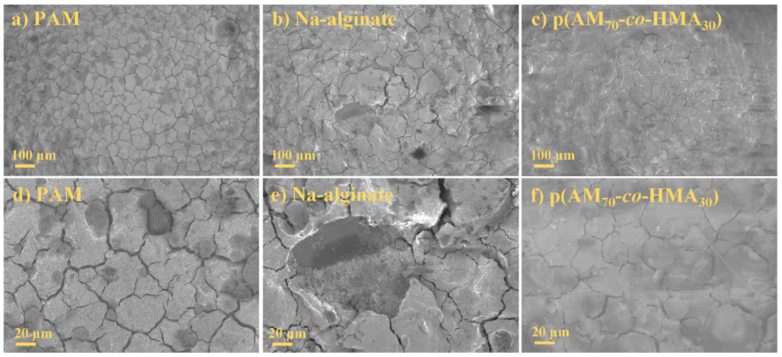

Figure 4. Surface morphology of Si anodes prepared from (a,d) PAM, (b,e) Na-alginate, and (c,f) p(AM_{70}-*co*-HMA_{30}) after cycling at C/5 (~0.7 A g^{-1}) for 10 cycles. The scale bars in the images are either 100 or 20 μm in size.

Remarkably, the electrodes containing p(AM_{70}-*co*-HMA_{30}) as the binder exhibited far superior cycling performance at higher rates (≥C/2) than the reference electrodes (Figure 3d). For instance, at a high current density of 3.6 A g^{-1}, electrodes prepared with p(AM_{70}-*co*-HMA_{30}) maintained a delithiation capacity of 1316 mA h g_{Si}^{-1}, while the Na-alginate- and PAM-based anodes reached a capacity of 795 and 991 mA h g_{Si}^{-1}, respectively. The improved rate capability of the p(AM_{70}-*co*-HMA_{30})-based anodes at higher rates (≥C/2) likely originated from a lower internal resistance relative to the reference electrodes. At lower rates (<C/2), a more severe capacity loss was visible for the reference electrodes relative to the p(AM_{70}-*co*-HMA_{30})-based anodes, which is in good agreement with the cycling test at C/5 and the EIS measurements.

For a better understanding of the improved capacity retention in the initial cycles achieved by using the self-cross-linkable p(AM_{70}-*co*-HMA_{30}) binder, Si anodes prepared with different binders were characterized by SEM after cycling for ten cycles at C/5. As shown in Figure 4, the SEM images of the reference electrodes (Na-alginate, PAM) showed huge cracks and active material fragmentation, whereas in the images of the Si anodes prepared with p(AM_{70}-*co*-HMA_{30}) only minor cracks were observed.

In addition, the electrode thicknesses after 10 cycles at C/5 were measured with a thickness gauge. As can be seen in Figure S8 (Supporting Information), the Si anodes prepared with p(AM_{70}-*co*-HMA_{30}) (8%) showed a far reduced irreversible expansion compared to the Na-alginate- (20%) and PAM-based electrodes (34%). The less detectable morphology changes of the p(AM_{70}-*co*-HMA_{30})-based samples can be explained by the formation of a cross-linked binder network structure, which can accommodate volume changes and limit the movement of Si particles. As a result, the morphology of the electrodes was preserved. This led to the observed reduced capacity fading of the p(AM_{70}-*co*-HMA_{30})-based anodes compared to the reference electrodes.

4. CONCLUSIONS

In summary, we introduced an easy to prepare self-cross-linkable copolymer for use as the binder for high-loading Si anodes. We showed that Si anodes prepared with a copolymer consisting of AM and HMA (≥30 wt %) as the binder exhibited far superior cycling performance compared to electrodes fabricated with conventional binder systems (e.g., Na-alginate). Our novel binder design improved both the capacity retention and rate capability. The enhanced electrochemical performance of the p(AM-*co*-HMA) binder can be attributed to the formation of a 3D binder network, which is induced by the self-cross-linking reaction of the HMA monomer. The chemically and physically formed cross-linked polymer matrix compensates the volume changes of the Si particles and thereby helps to maintain the mechanical integrity of the electrodes during cycling. To further advance Si anodes toward practical application, current work focuses on novel copolymer designs based on self-cross-linkable HMA.

■ ASSOCIATED CONTENT

Supporting Information

The Supporting Information is available free of charge at https://pubs.acs.org/doi/10.1021/acsaem.2c01867.

Experimental details, ^{1}H and ^{13}C NMR spectra of PAM and p(AM-*co*-HMA); adhesions tests of Na-alginate- and p(AM-*co*-HMA)-based Si anodes; fitted resistances of impedance measurements from Figure 3c; and thickness changes after cycling (PDF)

■ AUTHOR INFORMATION

Corresponding Author

Michael R. Buchmeiser − *Institute of Polymer Chemistry, University of Stuttgart, 70569 Stuttgart, Germany; German Institutes of Textile and Fiber Research (ITCF) Denkendorf, 73770 Denkendorf, Germany;* orcid.org/0000-0001-6472-5156; Email: michael.buchmeiser@ipoc.uni-stuttgart.de

Authors

Stefan Niesen − *Institute of Polymer Chemistry, University of Stuttgart, 70569 Stuttgart, Germany; Mercedes-Benz AG, RD/EBZ, 70327 Stuttgart, Germany*

Alina Fox − *Institute of Polymer Chemistry, University of Stuttgart, 70569 Stuttgart, Germany; Mercedes-Benz AG, RD/EBZ, 70327 Stuttgart, Germany*

Saravanakumar Murugan − *Institute of Polymer Chemistry, University of Stuttgart, 70569 Stuttgart, Germany*

Gunther Richter − *Max Planck Institute for Intelligent Systems, 70569 Stuttgart, Germany*

Complete contact information is available at: https://pubs.acs.org/10.1021/acsaem.2c01867

Notes

The authors declare no competing financial interest.

■ ACKNOWLEDGMENTS

The authors thank Peter Haberzettl (Mercedes-Benz AG) for conducting the adhesion tests, Hilda David (Max Planck Institute for Intelligent Systems, Stuttgart) for the SEM measurements and Dr. Robert Lawitzki (Institute for Material Science, University of Stuttgart) for the TEM measurements. Moreover, all authors thank N. Keim, J. Kappler, and Dr. J. V. Musso (all Institute of Polymer Chemistry, University of Stuttgart) for fruitful discussions.

■ REFERENCES

(1) Gröger, O.; Gasteiger, H. A.; Suchsland, J.-P. Review—Electromobility: Batteries or Fuel Cells? *J. Electrochem. Soc.* **2015**, *162*, A2605.
(2) Ma, D.; Cao, Z.; Hu, A. Si-Based Anode Materials for Li-Ion Batteries: A Mini Review. *Nano-Micro Lett.* **2014**, *6*, 347−358.
(3) Zhang, C.; Wang, F.; Han, J.; Bai, S.; Tan, J.; Liu, J.; Li, F. Challenges and Recent Progress on Silicon-Based Anode Materials for Next-Generation Lithium-Ion Batteries. *Small Struct.* **2021**, *2*, 2100009.
(4) Zuo, X.; Zhu, J.; Müller-Buschbaum, P.; Cheng, Y.-J. Silicon based lithium-ion battery anodes: A chronicle perspective review. *Nano Energy* **2017**, *31*, 113−143.
(5) Zhao, Y. M.; Yue, F. S.; Li, S. C.; Zhang, Y.; Tian, Z. R.; Xu, Q.; Xin, S.; Guo, Y. G. Advances of polymer binders for silicon-based anodes in high energy density lithium-ion batteries. *InfoMat* **2021**, *3*, 460−501.
(6) Kasavajjula, U.; Wang, C.; Appleby, A. J. Nano- and bulk-silicon-based insertion anodes for lithium-ion secondary cells. *J. Power Sources* **2007**, *163*, 1003−1039.
(7) Keller, C.; Desrues, A.; Karuppiah, S.; Martin, E.; Alper, J. P.; Boismain, F.; Villevieille, C.; Herlin-Boime, N.; Haon, C.; Chenevier, P. Effect of Size and Shape on Electrochemical Performance of Nano-Silicon-Based Lithium Battery. *Nanomaterials* **2021**, *11*, 307.
(8) Qi, C.; Li, S.; Yang, Z.; Xiao, Z.; Zhao, L.; Yang, F.; Ning, G.; Ma, X.; Wang, C.; Xu, J.; Gao, J. Suitable thickness of carbon coating layers for silicon anode. *Carbon* **2022**, *186*, 530−538.
(9) Gattu, B.; Epur, R.; Jampani, P. H.; Kuruba, R.; Datta, M. K.; Kumta, P. N. Silicon−Carbon Core−Shell Hollow Nanotubular Configuration High-Performance Lithium-Ion Anodes. *J. Phys. Chem. C* **2017**, *121*, 9662−9671.
(10) Jiang, S.; Yang, Z.; Liu, Y.; Johnson, N.; Bloom, I.; Zhang, L.; Zhang, Z. Engineering the Si Anode Interface via Particle Surface Modification: Embedded Organic Carbonates Lead to Enhanced Performance. *ACS Appl. Energy Mater.* **2021**, *4*, 8193−8200.
(11) Fox, A. M.; Vrankovic, D.; Buchmeiser, M. R. Influence of the Silicon-Carbon Interface on the Structure and Electrochemical Performance of a Phenolic Resin-Derived Si@C Core-Shell Nanocomposite-Based Anode. *ACS Appl. Mater. Interfaces* **2022**, *14*, 761−770.
(12) Hochgatterer, N. S.; Schweiger, M. R.; Koller, S.; Raimann, P. R.; Wöhrle, T.; Wurm, C.; Winter, M. Silicon/Graphite Composite Electrodes for High-Capacity Anodes: Influence of Binder Chemistry on Cycling Stability. *Electrochem. Solid State Lett.* **2008**, *11*, A76−A80.
(13) Mazouzi, D.; Karkar, Z.; Reale Hernandez, C.; Jimenez Manero, P.; Guyomard, D.; Roué, L.; Lestriez, B. Critical roles of binders and formulation at multiscales of silicon-based composite electrodes. *J. Power Sources* **2015**, *280*, 533−549.
(14) Xu, J.; Zhang, L.; Wang, Y.; Chen, T.; Al-Shroofy, M.; Cheng, Y. T. Unveiling the Critical Role of Polymeric Binders for Silicon Negative Electrodes in Lithium-Ion Full Cells. *ACS Appl. Mater. Interfaces* **2017**, *9*, 3562−3569.
(15) So, Y.; Bae, H. S.; Kang, Y. Y.; Chung, J. Y.; Park, N. K.; Kim, J.; Jung, H. T.; Won, J. C.; Ryou, M. H.; Kim, Y. H. Eco-Friendly Water-Processable Polyimide Binders with High Adhesion to Silicon Anodes for Lithium-Ion Batteries. *Nanomaterials* **2021**, *11*, 3164.
(16) Liu, J.; Zhang, Q.; Wu, Z. Y.; Wu, J. H.; Li, J. T.; Huang, L.; Sun, S. G. A high-performance alginate hydrogel binder for the Si/C anode of a Li-ion battery. *Chem. Commun.* **2014**, *50*, 6386−6389.
(17) Lestriez, B.; Bahri, S.; Sandu, I.; Roue, L.; Guyomard, D. On the binding mechanism of CMC in Si negative electrodes for Li-ion batteries. *Electrochem. Commun.* **2007**, *9*, 2801−2806.
(18) Magasinski, A.; Zdyrko, B.; Kovalenko, I.; Hertzberg, B.; Burtovyy, R.; Huebner, C. F.; Fuller, T. F.; Luzinov, I.; Yushin, G. Toward efficient binders for Li-ion battery Si-based anodes: polyacrylic acid. *ACS Appl. Mater. Interfaces* **2010**, *2*, 3004−3010.
(19) Preman, A. N.; Lee, H.; Yoo, J.; Kim, I. T.; Saito, T.; Ahn, S.-k. Progress of 3D network binders in silicon anodes for lithium ion batteries. *J. Mater. Chem. A* **2020**, *8*, 25548−25570.
(20) Chen, Z.; Zhang, H.; Dong, T.; Mu, P.; Rong, X.; Li, Z. Uncovering the Chemistry of Cross-Linked Polymer Binders via Chemical Bonds for Silicon-Based Electrodes. *ACS Appl. Mater. Interfaces* **2020**, *12*, 47164−47180.
(21) Koo, B.; Kim, H.; Cho, Y.; Lee, K. T.; Choi, N. S.; Cho, J. A highly cross-linked polymeric binder for high-performance silicon negative electrodes in lithium ion batteries. *Angew. Chem., Int. Ed. Engl.* **2012**, *51*, 8762−8767.
(22) Gendensuren, B.; Oh, E.-S. Dual-crosslinked network binder of alginate with polyacrylamide for silicon/graphite anodes of lithium ion battery. *J. Power Sources* **2018**, *384*, 379−386.
(23) Woo, H.; Park, K.; Kim, J.; Yun, A. J.; Nam, S.; Park, B. 3D Meshlike Polyacrylamide Hydrogel as a Novel Binder System via in situ Polymerization for High-Performance Si-Based Electrode. *Adv. Mater. Interfaces* **2019**, *7*, 1901475.
(24) Wang, S.; Duan, Q.; Lei, J.; Yu, D. Y. W. Slime-inspired polyacrylic acid-borax crosslinked binder for high-capacity bulk silicon anodes in lithium-ion batteries. *J. Power Sources* **2020**, *468*, 228365.
(25) Chuang, Y.-P.; Lin, Y.-L.; Wang, C.-C.; Hong, J.-L. Dual Cross-Linked Polymer Networks Derived from the Hyperbranched Poly(ethyleneimine) and Poly(acrylic acid) as Efficient Binders for Silicon Anodes in Lithium-Ion Batteries. *ACS Appl. Energy Mater.* **2021**, *4*, 1583−1592.
(26) Hu, Y.; Shao, D.; Chen, Y.; Peng, J.; Dai, S.; Huang, M.; Guo, Z.-H.; Luo, X.; Yue, K. A Physically Cross-Linked Hydrogen-Bonded Polymeric Composite Binder for High-Performance Silicon Anodes. *ACS Appl. Energy Mater.* **2021**, *4*, 10886−10895.
(27) Jiao, X.; Yuan, X.; Yin, J.; Boorboor Ajdari, F.; Feng, Y.; Gao, G.; Song, J. Multiple Network Binders via Dual Cross-Linking for Silicon Anodes of Lithium-Ion Batteries. *ACS Appl. Energy Mater.* **2021**, *4*, 10306−10313.
(28) Yin, H.-E.; Lee, C.-F.; Chiu, W.-Y. Preparation of thermally curable conductive films PEDOT:P(SS-NMA) and their performances on weather stability and water resistance. *Polymer* **2011**, *52*, 5065−5074.
(29) Laysandra, L.; Chuang, C.-H.; Kobayashi, S.; Au-Duong, A.-N.; Cheng, Y.-H.; Li, Y.-T.; Mburu, M. M.; Isono, T.; Satoh, T.; Chiu, Y.-C. Design of Self-Cross-Linkable Poly(n-butyl acrylate)-co-poly[N-(hydroxymethyl)acrylamide] Amphiphilic Copolymers toward Elastic and Self-Healing Properties. *ACS Appl. Polym. Mater.* **2020**, *2*, 5432−5443.
(30) Ma, L.; Zhang, Y.; Wang, X.; Tang, R.; Zheng, X.; Dong, Y.; Kong, G.; Hou, Z.; Wei, L. Poly (acrylic acid-co-N-methylol acrylamide-co-butyl acrylate) copolymer grafted carboxymethyl cellulose binder for silicon anode in lithium ion batteries. *J. Appl. Electrochem.* **2020**, *51*, 131−141.
(31) Wei, L.; Hou, Z. High performance polymer binders inspired by chemical finishing of textiles for silicon anodes in lithium ion batteries. *J. Mater. Chem. A* **2017**, *5*, 22156−22162.
(32) Nam, J.; Kim, E.; K.K, K. R.; Kim, Y.; Kim, T. H. A conductive self healing polymeric binder using hydrogen bonding for Si anodes in lithium ion batteries. *Sci. Rep.* **2020**, *10*, 14966.

Supporting Information

Multifunctional Self-Cross-Linked Copolymer Binder for High-Loading Silicon Anodes

Stefan Niesen[1,3], Alina Fox[1,3], Saravanakumar Murugan[1], Gunther Richter[4], Michael R. Buchmeiser*[1,2]

[1]*Institute of Polymer Chemistry, University of Stuttgart, 70569, Stuttgart, Germany*
[2]*German Institutes of Textile and Fiber Research (DITF) Denkendorf, 73770 Denkendorf, Germany*
[3]*Mercedes-Benz AG, RD/EBZ, 70327 Stuttgart, Germany*
[4]*Max Planck Institute for Intelligent Systems, 70569 Stuttgart, Germany*
Email: michael.buchmeiser@ipoc.uni-stuttgart.de

Table S1: Mass of AM and HMA used to prepare the p(AM_x-*co*-HMA_y) copolymers and PAM.

Polymer	Mass of AM	Mass of HMA
p(AM_{90}-*co*-HMA_{10})	1.42 g (20 mmol)	0.20 g (2 mmol)
p(AM_{70}-*co*-HMA_{30})	1.01 g (15 mmol)	0.67 g (7 mmol)
p(AM_{60}-*co*-HMA_{40})	0.94 g (13 mmol)	0.89 g (9 mmol)
PAM	1.56 g (22 mmol)	-

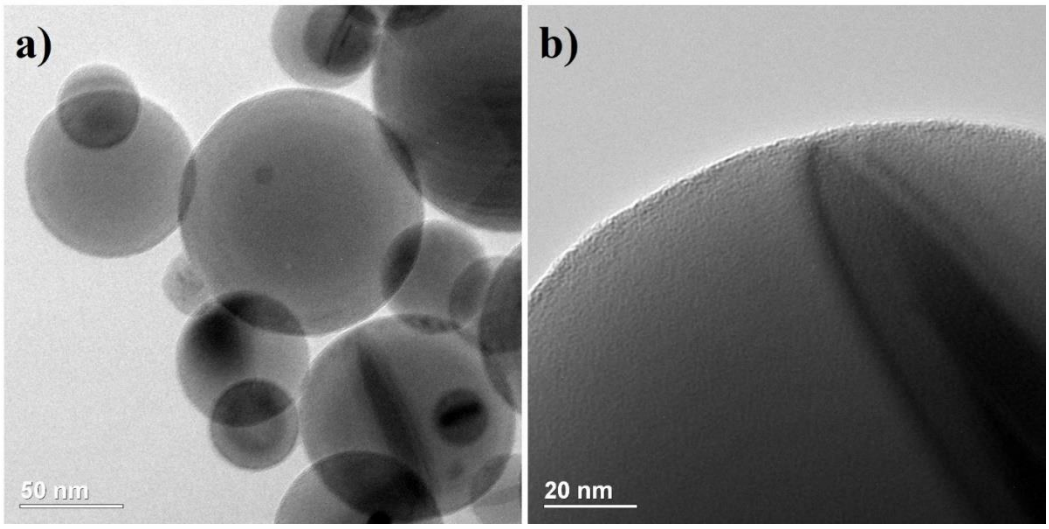

Figure S1: TEM images of Si nanoparticles at a) low and b) high magnitude.

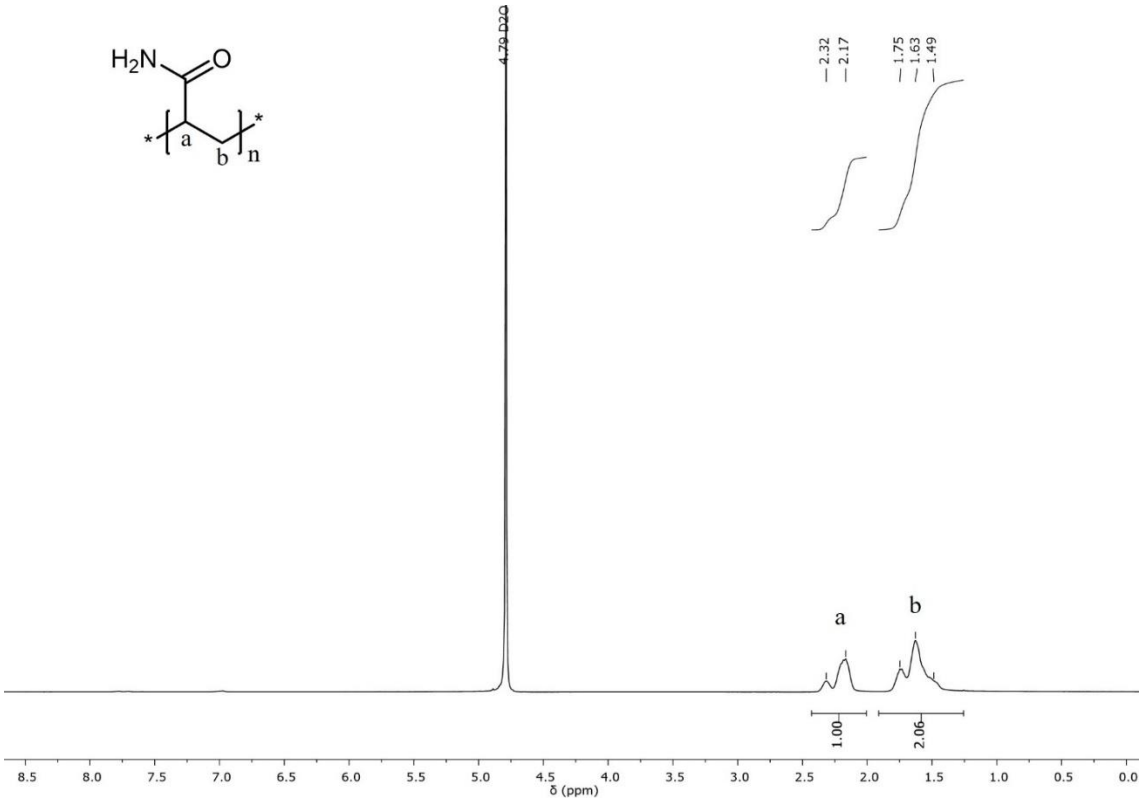

Figure S2: ^{1}H NMR spectrum of PAM in D_2O.

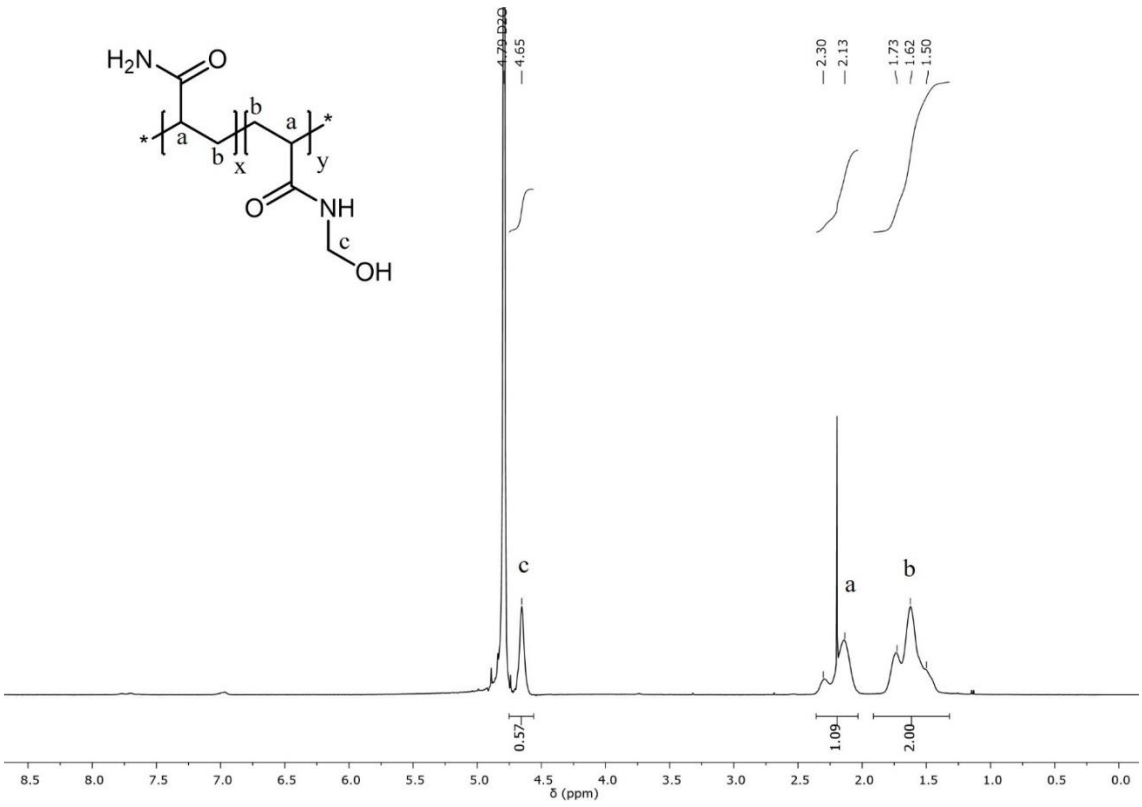

Figure S3: ^{1}H NMR spectrum of p(AM-*co*-HMA) in D_2O

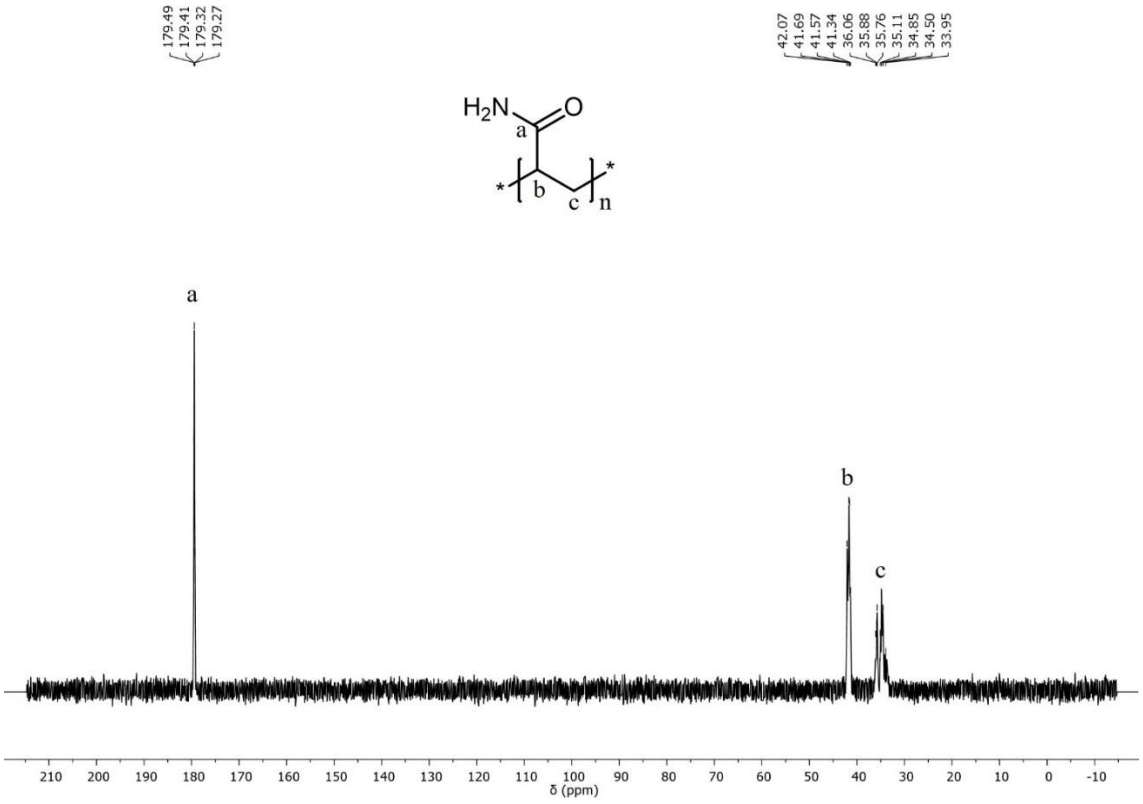

Figure S4: ^{13}C NMR spectrum of PAM in D_2O.

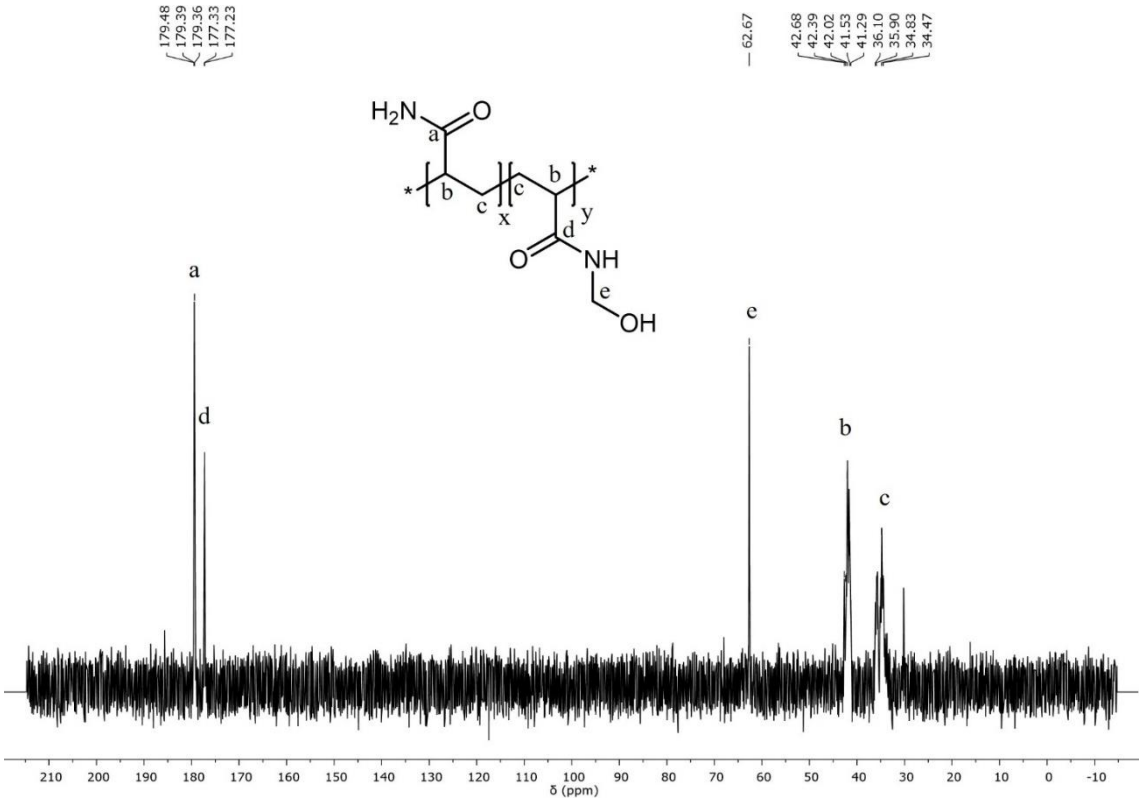

Figure S5: ^{13}C NMR spectrum of p(AM-*co*-HMA) in D_2O.

Figure S6: Optical images of the Si coatings prepared with Na-alginate (upper panel) and p(AM$_{70}$-*co*-HMA$_{30}$) (lower panel) after conducting a 180° peel test.

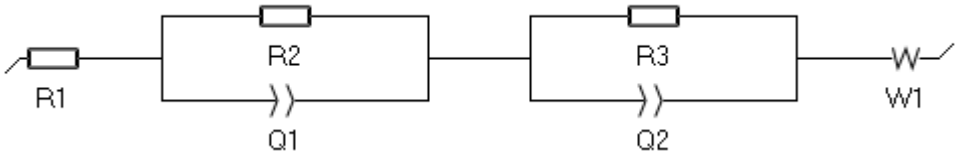

Figure S7: Equivalent circuit model used to fit the impedance data in Figure 4c.

Table S2: Fitted resistances of the Si anodes prepared with various binders. Measured in half-cells after cycling for ten cycles at C/5.

Sample	**R_1 [Ω]**	**R_2 [Ω]**	**R_3 [Ω]**
PAM	4.7	1.2	101.9
Na-alginate	8.5	2.6	79.5
p(AM$_{70}$-*co*-HMA$_{30}$)	7.0	3.2	41.5

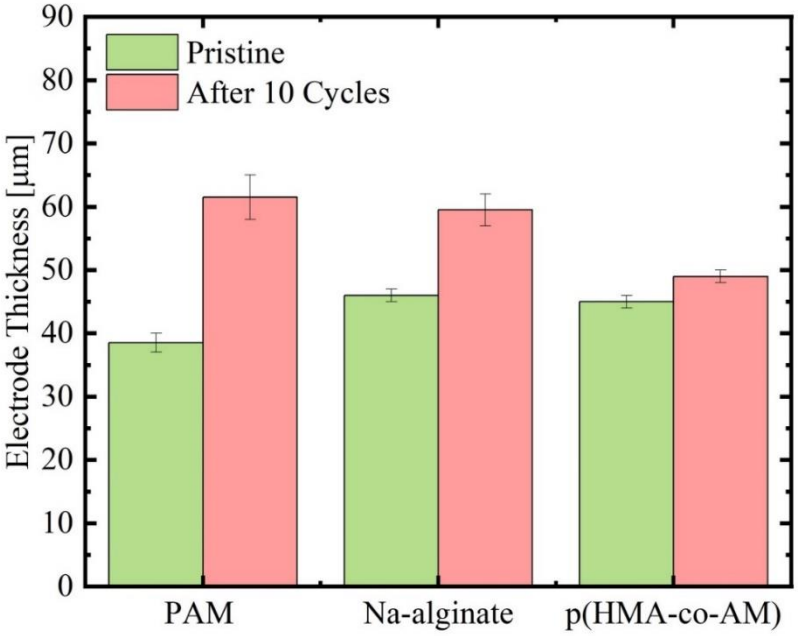

Figure S8: Thickness of Si anodes prepared with PAM, Na-alginate and p(AM_{70}-*co*-HMA_{30}) as binder before and after cycling for ten cycles at C/5.